Ecological insights through single-cell measurements of marine bacteria

by

Cherry Gao

B.Sc. Interdepartmental Honours in Immunology
McGill University (2012)

Submitted to the Department of Biological Engineering
in partial fulfillment of the requirements for the degree of

Doctor of Philosophy
at the
Massachusetts Institute of Technology

September 2020

Signature of Author: …….
Cherry Gao
Department of Biological Engineering
August 14, 2020

Certified by: ……..…
Roman Stocker
Thesis Supervisor
Professor of Civil and Environmental Engineering

Accepted by: …….
Douglas A. Lauffenburger
Thesis Committee Chair
Ford Professor of Biological Engineering, Chemical Engineering, and Biology

Ecological insights through single-cell measurements of marine bacteria

by

Cherry Gao

Submitted to the Department of Biological Engineering on August 14, 2020
in partial fulfillment of the requirements for the degree of
Doctor of Philosophy in Biological Engineering

Abstract

Bacteria in the ocean, though invisible to the naked eye, play an indispensable role in facilitating life on Earth by driving chemical reactions that are essential to the planet's habitability. Some marine bacteria, however, cause disease outbreaks that are capable of rapid and massive destruction of ecosystems. Although individual bacterial cells are ~1 μm in size, their collective action enables large-scale nutrient fluxes throughout the marine food web, as well as wreak havoc in marine systems with major socioeconomic consequences for humans. In this Thesis, I seek to connect single-cell measurements of behavior and metabolism of marine bacteria to ecological processes that shape global biogeochemical cycles and influence ecosystem health. In particular, I focus on the impact of microbial activities on two globally-relevant contexts: (1) the biogeochemical cycling of sulfur, a chemical element that is essential to life, and (2) coral disease, which threatens the reef ecosystems that support marine biodiversity and provide food security for many human coastal communities. In **Chapter 1**, I describe the development of synthetic biology tools for the construction of fluorescent reporters in a marine bacterium (*Ruegeria pomeroyi*). These engineered reporter strains enabled the investigations in **Chapter 2**, which presents the first single-cell measurements of the transcriptional response of *R. pomeroyi* to different concentrations of dimethylsulfoniopropionate (DMSP), a pivotal compound in the oceans' carbon and sulfur cycles and a key chemical currency in marine microbial interactions. These measurements revealed the importance of microscale DMSP hotspots in marine sulfur cycling. In **Chapter 3**, I describe the simultaneous measurements of behavior (through microscopy) and gene expression (through RNA sequencing) of a coral pathogen, *Vibrio coralliilyticus*, to investigate the sequence of microscopic events preceding infection. The Appendix describes the methodology of tracking single cells over time through quantitative microscopy and high-throughput image analysis. The application of new tools from biological engineering to marine microbial ecology presents an unprecedented opportunity to understand the connections between single-cell behaviors, and ecosystem- and global-scale processes.

Thesis Supervisor: Roman Stocker
Title: Professor of Civil and Environmental Engineering

Acknowledgements

I would like to acknowledge the guidance and support of my Thesis Supervisor, Roman Stocker. Roman's dynamic leadership inspired me to straddle not only scientific fields, but also continents and academic institutions. He has been a terrific role model from whom I have learned how to approach problems with scientific rigor and communicate discoveries effectively. I would like to thank the members of my globally-distributed Thesis Committee, Doug Lauffenburger, Katharina Ribbeck, and Justin Seymour, for their guidance delivered sometimes locally, and sometimes remotely. The close mentorship of Jean-Baptiste Raina and Vicente Fernandez has been indispensable throughout my PhD, and I am extremely thankful to have had JB and Vicente as my mentors.

I am deeply grateful to the National Science Foundation for supporting my graduate studies through the Graduate Research Fellowships Program. I would like to acknowledge the training programs that granted me the incredible opportunities to gain field experiences in oceanography research, first at the University of Hawaii (C-MORE Summer Course on Microbial Oceanography), and second at Palmer Station in Antarctica (NSF Advanced Training Program in Antarctica for Early-Career Scientists). I am also grateful to the Department of Biological Engineering for the unwavering commitment to support students, including myself.

I am privileged to have been a part of many enriching communities at both MIT and at ETH Zurich. I would like to thank my invaluable friends in the Stocker lab and Parsons (Building 48), whose curiosity, intelligence, and humor have made each day of my PhD journey a joy, including during the COVID-19 pandemic. I also thank the Sidney Pacific Graduate Community, Graduate Student Council Sustainability Subcommittee, MIT Concert Choir, Akademischer Chor Zürich, ETH Entrepreneur Club, MIT Sandbox Innovation Fund, The Martin Trust Center for MIT Entrepreneurship, and the MIT Delta V accelerator for enabling my personal growth and granting me the freedom to explore.

Most importantly, I would like to thank my family for their love, support, and encouragement throughout my life and time at MIT. I dedicate this PhD Thesis to my mother and father, who have sacrificed so much to make my dreams a reality.

Table of Contents

Abstract 3
Acknowledgements 4
Table of Contents 5
Introduction 7

Microorganisms in the ocean facilitate life (and death) on Earth. 7
Bacterial catabolism of dimethylsulfoniopropionate in the global sulfur cycle 8
Mucus is the host-pathogen interface in coral disease. 9
Single-celled measurements in marine microbial ecology 10

Chapter 1. Genetic engineering of *Ruegeria pomeroyi* DSS-3 12

1.1 Overview of engineered strains of DSS-3 13
1.2 Plasmid vectors for engineering DSS-3 16
1.3 Transformation of DSS-3 17
1.4 Constitutive fluorescent protein expression in DSS-3 19
1.5 Single-color protein fusion reporter 23
1.6 Single-color promoter fusion reporter 26
1.7 Tri-color promoter fusion designs 28
1.8 Conclusions 38
1.9 Acknowledgements 38

Chapter 2. Single-cell bacterial transcription measurements reveal the importance of dimethylsulfoniopropionate (DMSP) hotspots in ocean sulfur cycling 40

2.1 Abstract 40
2.2 Introduction 41
2.3 Results and Discussion 42
2.4 Methods 50
2.5 Figures 64
2.6 Supplementary Figures and Tables 71
2.7 Supplementary Tables 91

2.8 Supplementary Notes 93
2.9 Acknowledgements 97
2.10 Author contributions 98

Chapter 3. Coral mucus rapidly induces chemokinesis and genome-wide transcriptome shifts toward pathogenesis in a bacterial coral pathogen 99

3.1 Abstract 99
3.2 Introduction 100
3.3 Materials and methods 101
3.4 Results 106
3.5 Discussion 112
3.6 Figures 116
3.7 Supplementary Methods 124
3.8 Supplementary Figures 129
3.9 Supplementary Tables 147
3.10 Supplementary Discussion 160
3.11 Acknowledgements 165
3.12 Author contributions 166

Conclusions and Future Directions 167

Appendix. Quantitative microscopy and image analysis 170

A1. Image analysis for cellular fluorescence quantification 170
A2. Image analysis for phytoplankton-bacteria co-incubation experiment 175
A3. Video analysis for cell segmentation, swimming track reconstruction, and speed calculation 178
A4. Motile and non-motile cell determination 180

References 181

Introduction

Microorganisms in the ocean facilitate life (and death) on Earth.

Marine microorganisms facilitate life on Earth by driving chemical reactions that are essential to the planet's habitability. However, a minority of microorganisms in the ocean can be harmful, and their toxic blooms or infections of marine animals are capable of rapid and massive destruction of ecosystems. Photosynthesis by single-celled marine phytoplankton sequesters carbon and produces oxygen on a scale equivalent to terrestrial plants[1,2], and thus is responsible for creating the largest carbon sink on Earth located in the deep ocean[2,3], as well as the production of much of the world's oxygen. In a process called the microbial loop[4,5], microbes play an indispensable role in the ocean food web by recycling waste products of other organisms back into nutrients, thus forming critical links in the global cycling of essential elements including carbon, nitrogen, phosphorous, and sulfur. Some of these microbial metabolisms, however, can cause the rapid expansion of a single microbial species whose local domination over other organisms can be deleterious in some contexts, such as disease and algal blooms. Thus, understanding and potentially harnessing microbial processes in the ocean have important implications on the future of our climate, marine-sourced food security, and ecosystem health.

The majority of the ocean's biomass is concentrated in single-celled microorganisms (eukaryotes and prokaryotes), whose contribution to biomass far surpasses that of fish, crustaceans (e.g., Antarctic krill), and megafauna (e.g., whales) combined[6]. Of the total biomass in the ocean (~6 gigatons of carbon), 27% is estimated to comprise of prokaryotes (bacteria and archaea; ~1.6 gigatons of carbon)[6], which are capable of diverse metabolic modes. Although these metabolic activities are carried out by individual cells, their collective action across ~10^{29} prokaryotic cells in the open ocean[6,7] enables large-scale nutrient fluxes throughout the marine food web, as well as wreak havoc through disease outbreaks that cause marine animal mortalities worldwide. Thus, individual cellular metabolic activities have major consequences at the global and ecosystem scales. In this Thesis, I focus on understanding the interplay between microbial metabolisms and large-scale consequences in two globally-relevant contexts: the biogeochemical cycling of sulfur

(**Chapters 1 and 2**), a chemical element that is essential to life, and coral disease (**Chapter 3**), which threatens the reef ecosystems that support marine biodiversity and provide food security for millions of humans[8].

Bacterial catabolism of dimethylsulfoniopropionate in the global sulfur cycle.

The centerpiece of ocean sulfur cycling, dimethylsulfoniopropionate (DMSP), is a ubiquitous organosulfur compound in the marine environment. Up to 10% of the carbon fixed by phytoplankton cells in the ocean is converted to DMSP[9], resulting in a global DMSP production exceeding one billion tons per year[10]. DMSP is an important currency in the ecological and metabolic exchanges between phytoplankton and heterotrophic bacteria[11], as it represents a major nutrient source that fulfills much of the sulfur and carbon demand of bacteria (up to 95% and 15%, respectively[12,13]).

Heterotrophic marine bacteria catabolize DMSP via two competing catabolic pathways[14] with distinct consequences for global sulfur and carbon cycles: the demethylation pathway leads to the incorporation of both carbon and sulfur into bacterial biomass, whereas the cleavage pathway results in the incorporation of carbon only and the release of sulfur in the form of the climatically-active gas dimethylsulfide (DMS). DMS represents a significant source of marine sulfate aerosols, which are a precursor of cloud condensation nuclei. Thus, the production of DMS via bacterial cleavage of DMSP is implicated in climate regulation through modification of cloud albedo (reflection of solar radiation)[15,16] and therefore the Earth's atmospheric temperatures. However, the environmental factors that govern the utilization of one pathway over the other, and ultimately the production and release of DMS into the atmosphere, have remained elusive, marking a major gap in the mechanistic link between individual microbial processes and global-scale carbon and sulfur biogeochemical cycles.

The marine bacterium *Ruegeria pomeroyi* encodes both DMSP degradation pathways in a single cell, offering a unique opportunity to study the regulation of these metabolic pathways within the same organism. In **Chapters 1** and **2**, I investigate the effect of different ecologically-relevant concentrations of DMSP on the bacterial utilization of the demethylation vs. cleavage pathways.

The development of a synthetic biology toolbox in *R. pomeroyi* (**Chapter 1**) enabled the construction of a suite of fluorescent reporter strains that visually report the expression of *dmdA* and *dddW*, the genes encoding the enzymes responsible for the first steps of demethylation and cleavage pathways, respectively.

Mucus is the host-pathogen interface in coral disease.

While many species of marine bacteria, such as *R. pomeroyi*, are important drivers of life-enabling chemical transformations, a minority of these bacteria are pathogens that cause disease outbreaks in ecosystems which are critical for human socioeconomic activities, such as coral reefs. Coral reefs are currently threatened by sea surface temperature rise and ocean acidification. One major consequence of these environmental changes is the rise of opportunistic bacterial pathogens[17–19] such as *Vibrio coralliilyticus*, which becomes virulent against their coral host, *Pocillopora damicornis*, at high temperatures (above 27 °C)[20]. Increasing prevalence of bacterially-mediated coral disease outbreaks due to rising seawater temperatures has caused coral mortality and the collapse of reef ecosystems worldwide[17–19]. Uncovering the sequence of events in bacteria that lead to coral pathogenicity is critical in protecting these important ecosystems.

To fight against infections, corals are equipped with innate and adaptive-like immunity[21], and cultivate a beneficial microbiome which may contribute to their resilience against pathogens[22,23]. Due to their sessile lifestyle, corals rely on the viscosity and movement of mucus—a part of the innate immunity that covers the coral surface—to concentrate a large population of bacteria (the coral microbiome)[24,25], and to transport trapped particulates towards the gastrovascular cavity for consumption, or away from the coral body into the reef wasters as waste products[26]. However, recent studies have found that the pathogen *V. coralliilyticus* increases swimming speed in, and chemotaxis efficiency towards, the mucus of heat-stressed corals[27,28]. Thus, mucus represents a critical chemical signal that dictates pathogen behaviors, and potentially, disease outcomes.

To date, infection studies of *V. coralliilyticus* have uncovered several virulence genes that are necessary for coral infection. These virulence genes include motility, chemotaxis, colonization, and host damage genes[29–36]. However, the sequence of behavioral and molecular events that lead

to pathogenicity by *V. coralliilyticus* remain a major open question. Thus, uncovering the temporal evolution of pathogen behavior in the moments leading up to infection marks a critical missing link in understanding the environmental factors that dictate coral disease outcome. In **Chapter 3**, I describe single-cell experiments to understand the behavior and gene expression of a bacterial coral pathogen in the context of its host mucus.

Single-celled measurements in marine microbial ecology.

For bacteria, the majority of the ocean is a food desert that is dotted by ephemeral nutrient hotspots produced by larger organisms such as eukaryotic phytoplankton[37]. Due to leakage and diffusion, elevated DMSP concentrations may exist in the immediate area surrounding phytoplankton cells, representing nutrient oases for starved marine bacteria. Similarly, the diffusion of mucus from corals into the surrounding seawater provides nutrient-rich hotspots in the otherwise oligotrophic (nutrient-poor) reef waters. In both cases, the success of bacteria in finding and utilizing these nutrient opportunities relies on their ability to sense and respond rapidly to changes in their surrounding environment.

Bacterial behaviors and interactions, due to their small cell size and the ephemeral nature of nutrient distributions in the marine environment, occur at spatial lengths of micrometers and timescales of seconds to minutes[38–40]. Thus, to effectively study bacteria in the ocean, one must utilize methods that enable the observation of these rapid and microscopic behaviors and activities. However, traditional marine microbial ecology studies have relied on large-volume sampling schemes in which precise manipulation of the environment and high temporal and spatial resolution measurements are difficult to impossible. Recent studies have chartered the way towards studying natural populations of marine microbes at their length and time scales through the utilization of single-cell techniques in genomics[41–44], behavioral observations[45], and in-situ microscopy imaging[46,47], which have enabled our understanding of the spatiotemporal heterogeneity that govern microbial ecology in the ocean. Furthermore, recent advances in biological engineering tools, including synthetic biology, microfluidics, and microscopy offer the ability to precisely manipulate, measure, and model individual bacterial activities at the appropriate scales.

In September 2013, the then Head of the Department of Biological Engineering at MIT, Doug Lauffenburger, defined biological engineering to the incoming class of PhD students as a cycle to "design, build, and test" biological systems "using 'omics technology and other tools in molecular and cellular life sciences". In this context, this Thesis describes my endeavor in harnessing the biological engineering toolbox towards the investigation of marine microbial processes with ecosystem-level and global implications. In **Chapter 1**, I describe the development of a synthetic biology toolbox in a DMSP-degrading marine bacterium, *R. pomeroyi*, that enabled the iterative design-build-test cycle towards the creation of a suite of fluorescent reporter strains. In **Chapter 2**, I present the application of these *R. pomeroyi* fluorescent reporter strains to perform single-cell transcriptional measurements in different concentrations of DMSP, which led to the discovery of the importance of microscale DMSP hotspots in marine sulfur cycling. In **Chapter 3**, I describe the simultaneous measurements of behavior (video microscopy) and gene expression (transcriptomics) of a coral pathogen to investigate the sequence of microscopic events leading up to infection. In the Appendix, I describe the quantitative microscopy methods and image analysis software development that enabled these single-cell investigations. The application of new tools from biological engineering to marine microbial ecology presents an unprecedented opportunity to understand the connections between single-cell behaviors, and ecosystem- and global-scale processes.

Chapter 1.

Genetic engineering of *Ruegeria pomeroyi* DSS-3

This Chapter describes the development of genetic engineering tools in the marine bacterium *R. pomeroyi* DSS-3, and the intermediate engineering steps that led to the design and construction of the final fluorescent reporters for quantitative DMSP pathway gene expression used in **Chapter 2**. This Chapter describes my "design, build, test" cycle of genetic engineering in DSS-3, including failed attempts and lessons learned, which I record here in the hopes of reducing time and resources spent towards successful engineering of DSS-3 by future researchers.

DSS-3 was first isolated from the coast of Georgia, USA, by selection for enrichment in DMSP-amended seawater[48,49]. The DSS-3 genome was sequenced in 2004 (ref. 50), which facilitated the generation of the first cloning protocols[51] and genetic experiments involving knockouts and complementation of genes, transposon mutagenesis, and RNA-seq and microarray measurements[10,52–55]. In this Chapter, I first discuss the plasmid vectors (**Section 1.2**) and transformation protocols (**Section 1.3**) that were tested in DSS-3, and their outcomes. The establishment of these genetic engineering protocols in our laboratory environment enabled the construction of the first fluorescent strain of DSS-3 (**Section 1.4**). Next, different fluorescent reporters of DMSP degradation gene expression (*dmdA* and *dddW*) were built and tested iteratively (**Sections 1.5–1.7**). The work described in this Chapter represents, to our knowledge, the first (i) transformation of DSS-3 with large (up to 14.833 kb) plasmids; (ii) usage of a synthetic promoter (PA1/04/03) for constitutive expression in DSS-3; (iii) demonstration of fluorescent protein expression in DSS-3; and (iv) establishment of triparental mating protocol in DSS-3 with helper plasmid pRK600.

1.1 Overview of engineered strains of DSS-3

Several fluorescent strains of DSS-3 were constructed and tested with microscopy to assess their fluorescence signal outputs. **Figure 1.1** shows a list of engineered plasmids transformed into DSS-3 that are discussed in this Chapter. Additional reporter strains are discussed in **Chapter 2**. All engineered plasmids transformed into DSS-3 that are discussed in both **Chapters 1** and **2** are listed in **Table 1.1**.

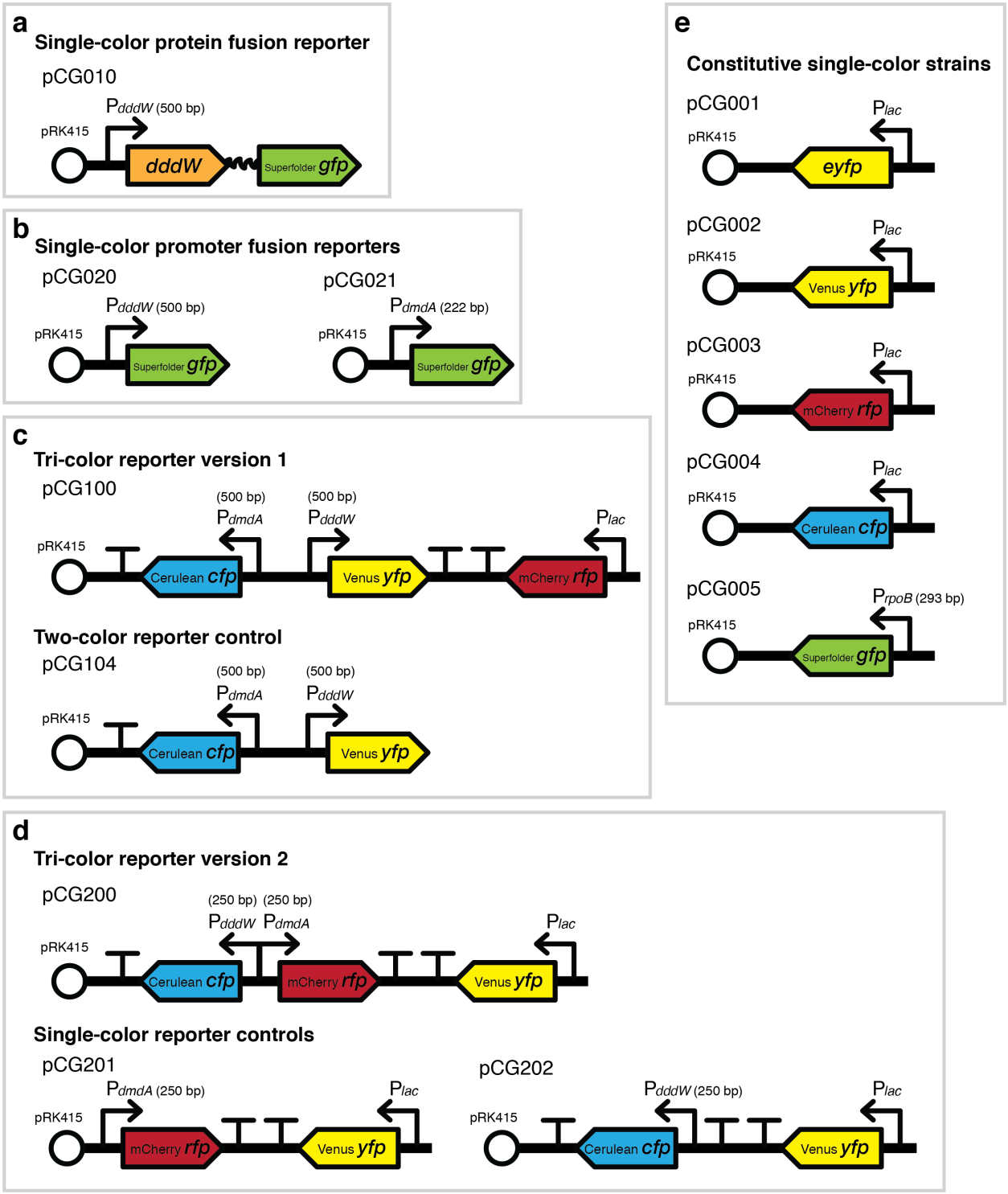

Figure 1.1 | Overview of unpublished engineered plasmids transformed into *R. pomeroyi* DSS-3. All constructs were cloned into the plasmid vector pRK415 in the multiple cloning site (MCS). Open circles, origins of replication; black arrows, promoters; colored arrows, fluorescent protein genes; jagged line, 9-amino acid linker; T, terminators.

Table 1.1 | List of all engineered plasmids transformed into *R. pomeroyi* DSS-3.

Strain / Plasmid	Description	Construct	Accession
pCG001	single-color constitutive	P_{lac}::EYFP	MT889351
pCG002	single-color constitutive	P_{lac}::YFP Venus	MT889352
pCG003	single-color constitutive	P_{lac}::RFP mCherry	MT889353
pCG004	single-color constitutive	P_{lac}::CFP Cerulean	MT889354
pCG005	single-color constitutive	P_{rpoB}::sfGFP	MT889355
pCG010	single-color protein fusion	*dddW*::sfGFP	MT889356
pCG020	single-color promoter fusion	P_{dddW}::sfGFP	MT889357
pCG021	single-color promoter fusion	P_{dmdA}::sfGFP	MT889358
pCG100	tri-color reporter v1	P_{dmdA}::CFP, P_{dddW}::YFP, P_{lac}::RFP	MT889359
pCG104	two-color reporter	P_{dmdA}::CFP, P_{dddW}::YFP	MT889360
pCG200	tri-color reporter v2	P_{dmdA}::RFP, P_{dddW}::CFP, P_{lac}::YFP	MT889361
pCG201	two-color reporter	P_{dmdA}::RFP, P_{lac}::YFP	MT889362
pCG202	two-color reporter	P_{dddW}::CFP, P_{lac}::YFP	MT889363
Regular / pCG301	tricolor reporter v3	P_{dmdA}::mTFP1, P_{dddW}::mKate2, $P_{A1/04/03}$::YFP	MN744962
pCG302	single-color reporter	P_{dmdA}::mTFP1	MN744963
pCG303	single-color reporter	P_{dddW}::mKate2	MN744964
Goofy / pCG401	tricolor reporter v4	P_{dmdA}::mKate2, P_{dddW}::mTFP1, $P_{A1/04/03}$::YFP	MN744965
pCG402	single-color reporter	P_{dmdA}::mKate2	MN744966
pCG403	single-color reporter	P_{dddW}::mTFP1	MN744967
pCG101	single-color constitutive	$P_{A1/04/03}$::mKate2	MN744959
pCG102	single-color constitutive	$P_{A1/04/03}$::YFP	MN744960
pCG103	single-color constitutive	$P_{A1/04/03}$::mTFP1	MN744961
pZS2-200	modified pZS2-123 for cloning aid only	replaced promoters (P_{dmdA}, P_{dddW}, P_{lac})	MN744968

Top section lists unpublished constructs which were cloned into the plasmid vector pRK415 (discussed in this Chapter). Bottom section lists published constructs cloned into plasmid vector pBBR1MCS-KanR (discussed in Chapter 2). GenBank accession numbers are provided.

1.2 Plasmid vectors for engineering DSS-3

In this Thesis, two plasmid vectors were utilized to genetically engineer DSS-3. First, pRK415 (GenBank EF437940) is a broad-host-range, 10.69 kb expression vector with a tetracycline resistance cassette[56], which has been used in gene knockout and complementation studies in DSS-3 (refs. 10, 52). The large size of pRK415 led to several challenges, including low electroporation efficiency and the potential effect of the burden of DNA replication on cell physiology. Furthermore, linearization of the vector backbone, which is necessary for insertion of e.g., fluorescent protein genes, was performed through restriction enzymes, since vector linearization through high-fidelity PCR amplification was difficult. The restriction enzyme method led to low yield of linearized vectors (posing a challenge for final plasmid construction through Gibson assembly), and fragments of the lacZ gene (encoding β-galactosidase) and its promoter (P_{lac}) from the multiple cloning site (MCS) remained at the 5' and 3' ends of the insert, which may have an effect on the expression of the DNA. Furthermore, the selection antibiotic of pRK415, tetracycline (administered at 20 μg/ml on agar plates and 3 μg/ml for liquid culture), is light-sensitive and thus may result in increased false-positive transformants.

I later converted to using a different plasmid vector, pBBR1MCS-KanR (GenBank U23751), which is a 5.144 kb vector. The pBBR1MCS series of plasmid vectors contain different antibiotic-resistance cassettes (kanamycin, tetracycline, ampicillin, or gentamycin), has been highlighted as a genetic tool for engineering Roseobacters[57], and has previously been used for complementation of a knocked out gene in DSS-3 (ref. 54). After testing different concentrations of kanamycin on wildtype DSS-3, 50 μg/ml was determined to be a selective concentration of the antibiotic, and pBBR1MCS-KanR was chosen for subsequent cloning work. The smaller size of pBBR1MCS-KanR vector backbone enabled the PCR amplification of the entire vector backbone without the MCS, thus eliminating the effect of any residual β-galactosidase gene on fluorescent reporter expression and performance (see **Chapter 2** for detailed methods on cloning with pBBR1MCS-KanR).

1.3 Transformation of DSS-3

1.3.1 Electroporation

Electroporation has previously been utilized by others to transform DSS-3 (refs. 51, 52, 58, 59). Briefly, electrocompetent DSS-3 was prepared from a 500-ml liquid culture in 1/2 YTSS medium, grown overnight at room temperature until OD_{600} 0.1–0.5 (see below for a note on optical density). Growth was stopped by incubating on ice for 30 min. Cells were washed three times with sterile 10% glycerol (250 ml, 150 ml, then 100 ml) with gentle centrifugation (5000 × *g* for 10 min) at 4 °C. After the final centrifugation, concentrated electrocompetent cells were resuspended in 1 ml 10% glycerol, aliquoted in 100 µl, and kept frozen at –80 °C until electroporation.

Prior to electroporation, plasmids were methylated using the M.SssI CpG Methyltransferase (New England Biolabs), and DNA was purified using the DNA Clean & Concentrator kit (Zymo Research). Electroporation was performed on 100 µl electrocompetent DSS-3 with 5 µl of methylated and cleaned DNA in a 2 mm cuvette, using the Gene Pulser Xcell (BioRad) electroporator with the following settings: 1.8 kV, 25 µF, 200 Ω. Post-electroporation recovery was initiated with the addition of 1 ml pre-warmed (30 °C) 1/2 YTSS to cells, which were subsequently transferred to 14-ml growth tubes.

Electroporation is a relatively high-cost and time-consuming transformation procedure that is extremely sensitive to chemical and environmental variability and human error. I experienced a period of time during which all DSS-3 electroporation attempts failed and did not yield any positive transformation colonies on selection plates. This was a laboratory-specific phenomenon, since electroporation of the same plasmids in another laboratory (Prof. Mary Ann Moran's group at University of Georgia) led to positive DSS-3 transformants. Although the exact cause of this series of failed electroporation remains unknown, several steps can be taken to identify the problematic step should a future researcher encounters the same problem.

First, positive transformant yield seems to decrease with the duration of storage of electrocompetent cells at –80 °C. In my experience, electrocompetent cells should be prepared

less than 1 week before electroporation if possible, and should not be used after 2 months of storage at –80 °C. If viability of frozen electrocompetent cells is questioned, one should streak out an aliquot on an agar plate to confirm that the frozen cells can form viable colonies.

Second, the optical density at which cultures are harvested for electrocompetent cell preparation has an effect on transformation efficiency. In one electroporation troubleshooting experiment with pCG201 (12.746 kb), electrocompetent cells that were harvested at OD_{600} of 0.1 yielded the largest number of transformed cells, followed by OD_{600} 0.19, 0.33, then 0.49. In the same experiment, OD_{600} of 0.07 yielded no colonies.

Third, methylation of DNA should be confirmed with a BstUI (New England Biolabs) restriction enzyme digestion. If DNA is methylated, it should be protected from BstUI digestion. Unsuccessful methylation of DNA may result from old S-adenosylmethionine (SAM).

Finally, if the plasmid is large (11–15 kb in this case), an initial recovery period of 4–6 h in 1/2 YTSS at 30 °C should be followed by an extended recovery period overnight in the presence of dilute selection antibiotic (3 μg/ml tetracycline for pRK415-based plasmids). Following extended recovery, all cells should be plated on a selection agar plate (centrifuge first to remove most liquid). In my case, these recovery and plating procedures yielded 10–30 colonies on the selection plate 3 days after plating.

1.3.2 Triparental mating

Challenges with the electroporation protocol led me to start utilizing a tri-parental conjugation (mating) method to transform DSS-3 in the last few years of this Thesis (detailed methods in **Section 2.4.4**). The tri-parental conjugation method was successful for transforming plasmids with both pRK415 and pBBR1MCS vector backbones.

1.3.3 Genomic integration

Genomic integration of fluorescent reporters into the DSS-3 genome using the mini-Tn7 transposon system[60,61] was briefly explored but failed to yield positive integration results. In this system, the simultaneous delivery of the helper plasmid (pUX-BF13) and the delivery plasmid

(carrying the DNA fragment for insertion) into a bacterial cell leads to a single-copy insertion of the desired DNA fragment into a neutral part of the genome that is believed to not affect the host (*att*Tn7 site located downstream of the *glmS* gene). For a genomic integration trial in DSS-3, the helper plasmid and the delivery plasmid (AKN132 from ref. 60 which carries a P1/04/03-DsRed expression cassette with gentamycin resistance in a pUC-based plasmid carrying the ColE1 origin of replication) were extracted by miniprep from *E. coli*. Following methylation and column purification in separate vessels, the two plasmids were combined for electroporation into DSS-3. After recovery of 3.5 h or overnight in liquid 1/2 YTSS at 30 °C, cells were plated on 1/2 YTSS gentamicin (10 µg/ml) selection plates. Even after 6 days of incubation, plates showed no colonies.

The failure of these genomic integration trials in DSS-3 may be due to two reasons: (i) the ColE1 origin of replication in the delivery plasmid is not compatible in DSS-3, and/or (ii) the insertion site (*att*Tn7) sequence encoded in the delivery plasmid does not match the sequence in the DSS-3 genome, leading to failed insertion. According to correspondence with the authors of ref. 60, the exact sequence of the delivery plasmid has been lost. Thus, further exploration of genomic integration with the mini-T7n would require some effort, including re-sequencing the 6.3 kb plasmid. Furthermore, genomic integration of a single copy of the fluorescent reporter construct, while eliminating the quantification challenge of variable copy number of a plasmid-based reporter, would most likely lead to low fluorescence signal that would mask low-level gene expression (as see in **Chapter 2**). Thus, I quickly moved on from genomic integration and focused solely on reporter construction in plasmids.

1.4 Constitutive fluorescent protein expression in DSS-3

To test whether fluorescent protein expression and subsequent microscopy imaging are possible in DSS-3, different colors of fluorescent proteins and constitutive promoters were inserted in the multiple cloning site (MCS) of pRK415 and subsequently electroporated into DSS-3.

1.4.1 *lac* promoter in pRK415

The 70-bp *lac* promoter (P_{lac}) in pRK415 controls the expression of the *lacZ* gene (encoding β-galactosidase) which is also the MCS of the plasmid. Thus, I first tested this pRK415 *lac* promoter to achieve constitutive fluorescence in DSS-3. The gene encoding EYFP (enhanced yellow fluorescent protein) was inserted in the MCS through double digestion using restriction enzymes (New England Biolabs) HindIII (5' end of EYFP) and PstI (3' end) to create the first engineered plasmid of this Thesis, pCG001 (
Table 1.1). Similarly, Venus YFP, mCherry RFP, and Cerulean CFP were inserted into the MCS using EcoRI (5' end) and PstI (3' end) to create pCG002, pCG003, and pCG004, respectively. Plasmids were electroporated into DSS-3 as described above.

Fluorescence microscopy imaging of transformed DSS-3 confirmed the presence of fluorescence signals in appropriate color channels (**Figure 1.2**), thus confirming that the expression of fluorescent proteins (across the color spectrum) is possible in DSS-3, and that the *lac* promoter in pRK415 induces constitutive expression in DSS-3. However, the fluorescence signals were weak, and required high exposure times (1 second) and gain setting on the camera for detection. A 5-h induction with the addition of 0.5 mM IPTG (activator of the *lac* promoter) during the exponential stage of growth of pCG002-transformed DSS-3 did not lead to detectable increase in fluorescence signal (not shown). These results suggest that the *lac* promoter, and possibly ribosomal binding site (RBS), of pRK415 MCS is only weakly active in DSS-3.

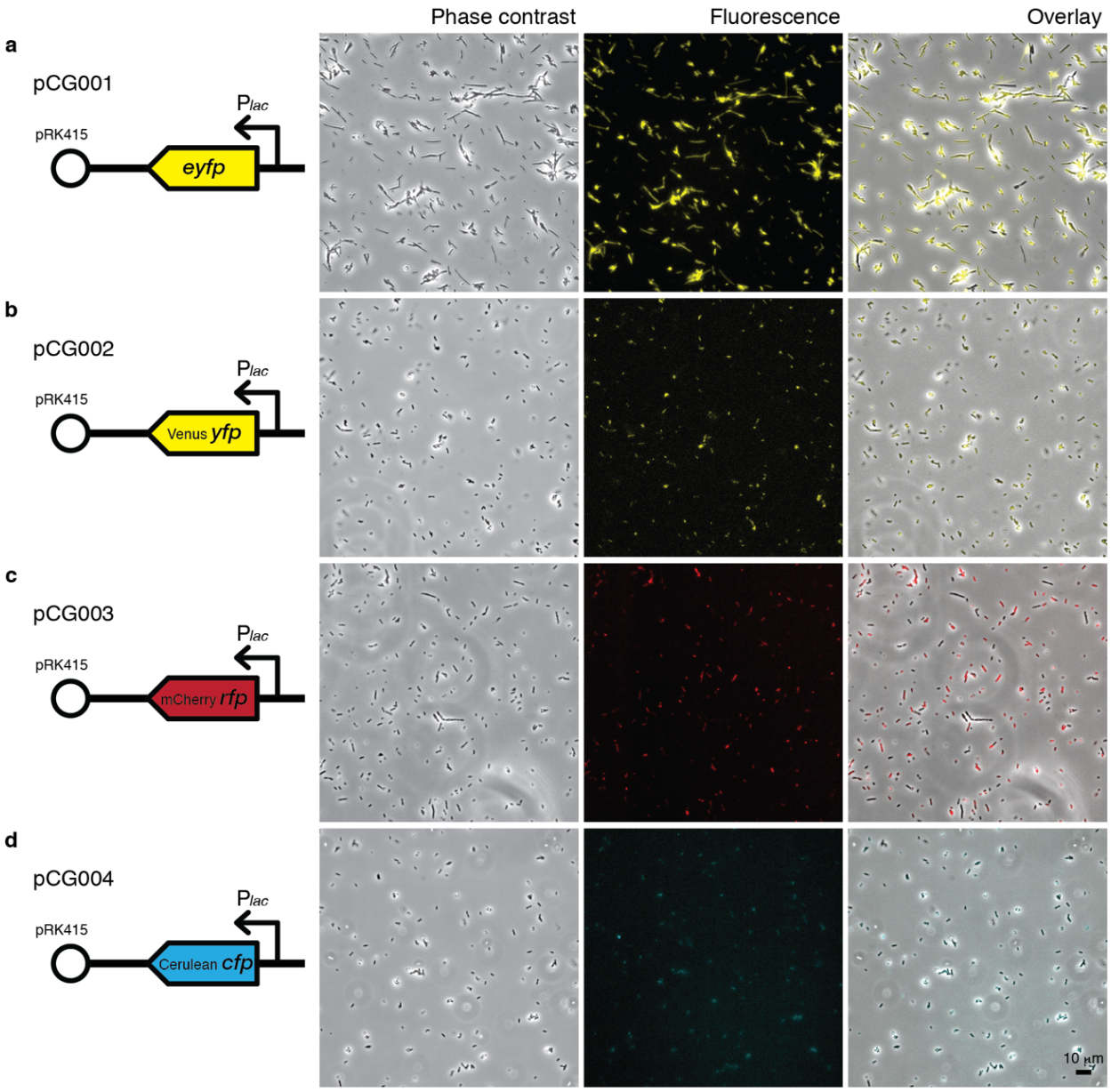

Figure 1.2 | Microscopy images of constitutively fluorescent DSS-3 (*lac* promoter of pRK415). All cells were imaged after overnight growth (30 °C) in liquid 1/2 YTSS amended with 3 µg/ml tetracycline, using a 40× objective. (**a**) pCG001 (EYPF) images were acquired with an electron multiplying CCD (EMCCD) camera (iXon3 885; Andor Technology; 8 µm pixel; exposure 100 ms; gain 58), with fluorescence excitation from a metal halide white light source (Lumen 200) and a filter cube with 450±50 nm excitation, 485 nm bandpass, and 515 nm long-pass emission filters. (**b–d**) pCG002 (Venus YFP), pCG003 (mCherry RFP), and pCG004 (Cerulean CFP) images were acquired with an sCMOS camera (Andor Zyla 4.2; 6.5 µm pixel; exposure 1 second; gain 1), with fluorescence excitation from single-color LED light source (Lumencor) at 508 nm (**b**), 555 nm (**c**), 440 nm (**d**) and a tri-color ECFP/EYFP/mCherry filter cube (Chroma 69308). Different brightness adjustments of fluorescence images were used between fluorescence only and overlay images. Scale bar, 10 µm.

1.4.2 Promoter of a housekeeping gene (*rpoB*)

I next searched within the DSS-3 genome for housekeeping genes whose promoters may be suitable candidates of constitutive promoters. In particular, *rpoB* (SPO3508), which encodes the β subunit of RNA polymerase, was stably expressed in a microarray study of DSS-3 (ref. 62). The 293-bp sequence upstream of *rpoB*, which is arranged in an operon with *rpoC* (SPO3507) downstream was cloned out of the DSS-3 genome, and fused with the superfolder GFP (sfGFP) gene in the MCS of pRK415 to construct pCG005. Fluorescence microscopy of the overnight culture of the DSS-3 strain containing pCG005 showed extremely low fluorescence signals (not shown), thus leading to the conclusion that the 293-bp sequence may not contain the correct promoter sequence for *rpoB*, or that *rpoB* is expressed at a very low level.

1.4.3 Strong, constitutive, modified *lac* promoter: PA1/04/03

The modified *lac* promoter, PA1/04/03, was originally derived from *Escherichia coli*[63] but has been used for fluorescence tagging in diverse species of Gram-negative bacteria, including *Vibrio anguillarum*[64], *Marinobacter adhaerens*[65], *Caulobacter crescentus*[66], *Pseudomonas putida*[60], and the Roseobacter *Phaeobacter gallaeciensis*[67]. Thus, I cloned the sequence containing PA1/04/03 and the downstream putative RBS from the pXGFPC-2 P*lac*::mKate2 plasmid (used in *C. crescentus* by ref. 66) and fused this sequence to genes of mKate2 RFP, Venus YFP, and mTFP1 to construct pCG101, pCG102, and pCG103, respectively. The PA1/04/03 promoter yielded strong constitutive fluorescence in DSS-3 which was even visible macroscopically on a culture plate (**Figure 1.3**). These constitutively fluorescent strains were used in the final experiments described in **Chapter 2**.

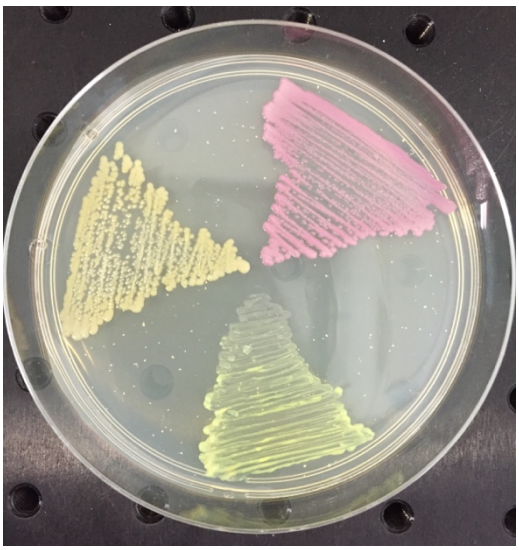

Figure 1.3 | Photograph of a culture plate containing constitutively fluorescent DSS-3. The plasmids contain the PA1/04/03 promoter with genes of fluorescent proteins mKate2 (pCG101), Venus YFP (pCG102), and mTFP1 (pCG103).

1.5 Single-color protein fusion reporter

After confirming that fluorescent protein expression is possible in DSS-3, I investigated the feasibility of reporting DMSP degradation gene (*dmdA* and *dddW*) expression by fluorescence emission in DSS-3. A protein fusion approach was chosen to preserve the 1:1 stoichiometry between the DMSP enzyme and the fluorescent protein (**Figure 1.4**). The fluorescent protein, superfolder GFP (sfGFP) was chosen for its superior performance in protein fusions[68]. I opted to first work with the cleavage gene, *dddW*, whose expression was dramatically upregulated (~70×) in DSS-3 incubated in DMSP[55]. A similarly large upregulation in my engineered reporter strain would yield measurable fluorescence signal output.

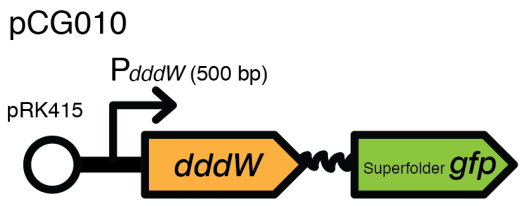

Figure 1.4 | Protein fusion reporter construct in DSS-3 containing the putative promoter of *dddW*, and the *dddW* gene (SPO0453) fused to sfGFP with a 9-amino acid peptide linker.

The plasmid pCG010 (12.387 kb) contained the putative promoter (500 bp) and gene sequence of *dddW* (456 bp) followed by a 9-amino acid linker (5'–Gly Gly Ser Gly Gly Ser Ser Gly Gly–3') and the gene sequence of superfolder *gfp* (714 bp), inserted in the pRK415 vector backbone (linearized by a PstI restriction digest) at the MCS through a 3-fragment Gibson assembly. The peptide linker, which was encoded in PCR primers as Gibson overhangs, were designed to be flexible and minimize steric hinderance between the two connected proteins (DddW and sfGFP) for proper protein folding. Glycine (Gly) confers flexibility to the peptide linker and has the smallest side chain, and the interspersed serine (Ser) improves the solubility of the multi-Gly chain[69]. To facilitate the protein fusion between DddW and sfGFP, the stop codon of *dddW* and the start codon of superfolder *gfp* were omitted.

Incubation of the DddW-sfGFP protein fusion reporter with 2.5 mM DMSP led to upregulation of fluorescence within 65 min (**Figure 1.5**). Negative control in glucose did not show signal increase. These results suggest that the 500-bp sequence upstream of *dddW* contains a DMSP-responsive promoter that controls the expression of the DMSP cleavage gene. Furthermore, the protein fusion construct allowed the proper folding of sfGFP, which enabled the detection of its fluorescence signal.

However, fluorescence signals were weak and required high exposure time (1 sec) and gain (200) on a sensitive camera (EMCCD) to enable visualization. The expression of a fusion protein, in addition to the replication of a large plasmid, is likely energetically burdensome, which could lead to slow cellular processes such as protein production. Furthermore, the implications of more than doubling the genetic materials encoding *dddW* on downstream processes in DMSP catabolism is unclear. Thus, a more streamlined reporter design may promoter fusions, which I explore in the next section.

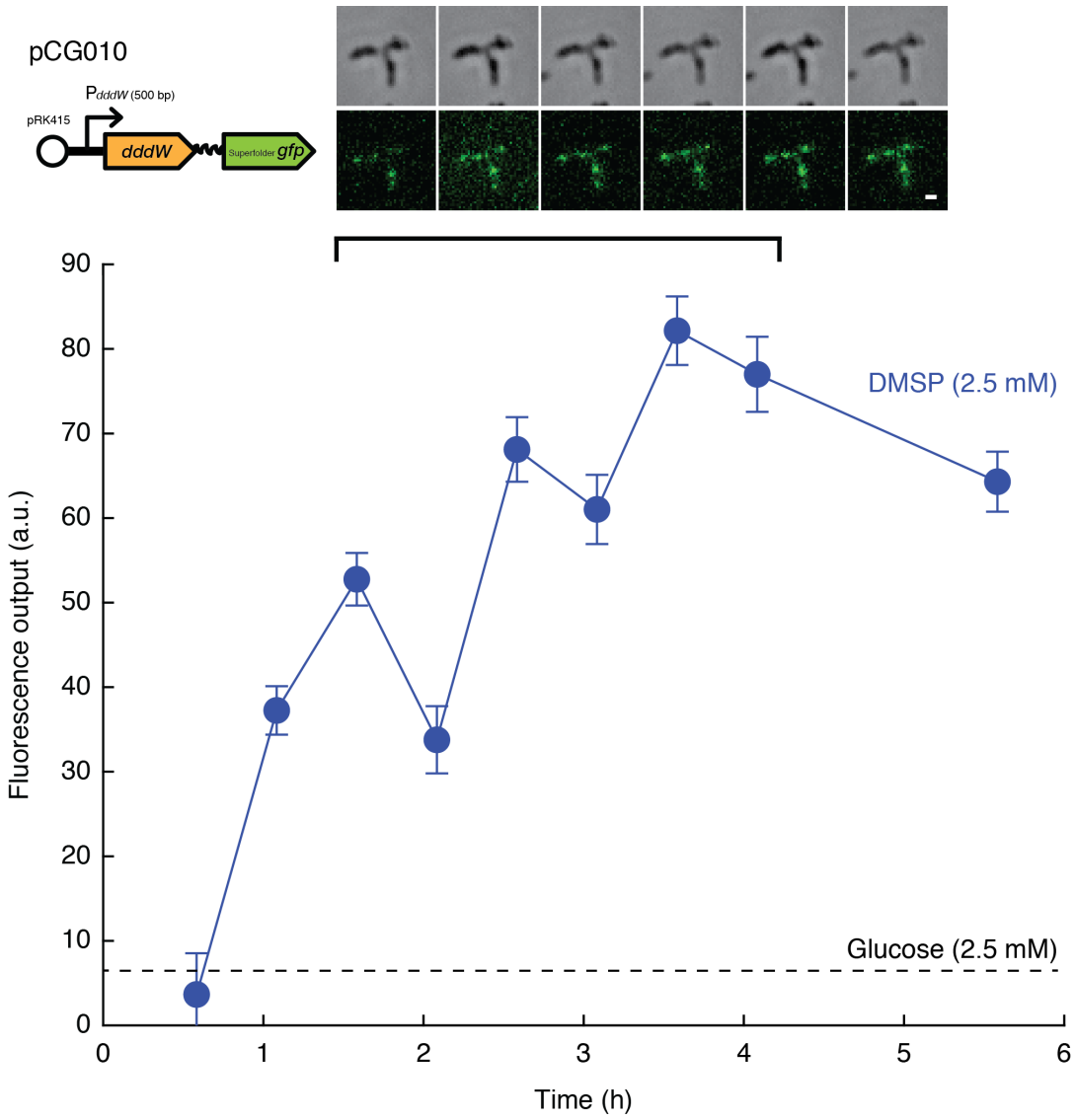

Figure 1.5 | Fluorescence of the single-color DddW-sfGFP protein fusion reporter strain of DSS-3 incubated in 2.5 mM DMSP. All cells were grown overnight (30 °C) in glucose-amended (2.5 mM) MBM with tetracycline (4 µg/ml) to OD_{600} 0.26 and washed in non-amended MBM before treatment (0 h) with 2.5 mM DMSP (dark blue) or glucose (black dotted) dissolved in MBM. One image per time point was acquired with an EMCCD camera (iXon3 885; Andor Technology; 8 µm pixel; exposure 1 sec; gain 200) and 40× objective, with fluorescence excitation from a metal halide white light source (Lumen 200) and the EGFP filter cube (Chroma 49002). Sample phase and fluorescence (false-colored) microscopy images of three cells are shown at time points 3–8 (black bar). Each displayed fluorescence image is an average of 5 frames taken consecutively as described above (each frame 1 sec exposure) to reduce background noise. Data points and error bars are average ± s.e.m. fluorescence outputs of cells after background subtraction. Glucose fluorescence was measured in the first 5 time points and averaged (dotted black line). Mean ± s.d. cell number in DMSP at time points 2–9 was 655±196; glucose at time points 2–5 was 456±124. Scale bar, 1 µm.

1.6 Single-color promoter fusion reporter

Promoter fusion, in which the expression of a fluorescent protein is controlled by the promoter of the gene of interest (*dddW* or *dmdA*), was explored next as a more efficient reporter design than protein fusion (**Figure 1.6**). Plasmids pCG020 (11.879 kb) and pCG021 (11.574 kb) contained the sfGFP gene fused to the putative promoter-containing 500-bp sequence upstream of *dddW* and 222-bp sequence upstream of *dmdA*, respectively, in the MCS of the pRK415 vector backbone (linearized by a PstI restriction digest) through 3-fragment Gibson assembly. The 222-bp sequence upstream of *dmdA* avoids an overlap with an upstream gene (SPO1912) encoded in the opposite direction.

Figure 1.6 | Single-color promoter fusion reporter construct in DSS-3, each encoding sfGFP under the control of putative promoters of DMSP catabolism genes, *dmdA* (SPO1913) and *dddW* (SPO0453). Due to a cloning error, the sfGFP gene in pCG020 contains an extra leucine (Leu) before the stop codon.

Time-lapse fluorescence microscopy of a DMSP incubation experiment (**Figure 1.7**) revealed that the demethylation (P_{dmdA}::sfGFP) reporter strain significantly upregulated fluorescence signals starting at 110 min for both DMSP concentrations (1 mM and 1 μM) compared to glucose negative control (one-tailed *t*-test at each time point, $p < 0.01$). The cleavage (P_{dddW}::sfGFP) reporter strain showed faster significant upregulation (within 20 min) but only at the higher concentration of DMSP (1 mM) compared to glucose (one-tailed *t*-test at each time point, $p < 0.01$). Furthermore, fluorescence signals at the first time point in glucose were 47.65 ± 4.39 a.u. for demethylation compared to 1.98 ± 0.16 a.u. for cleavage, suggesting that demethylation is expressed at a higher baseline level than cleavage pathway in the absence of DMSP. These results agree with the results that were later obtained with the final, tri-color reporter strains (described in **Chapter 2**). The differences in the fluorescence outputs (y-axis values) between the two reporter strains is likely due to the large differences in the number of

cells in the incubation experiment rather than differences in expression levels of the two genes. The larger number of cells (1700 cells quantified at 65-min time point in glucose) of the cleavage (*dddW*) reporter likely led to faster depletion of DMSP, and thus fluorescence signals plateaued earlier and at lower signal values than the demethylation (*dmdA*) reporter (335 cells at 65 min in glucose) (**Figure 1.7**).

These results confirmed that the promoter fusion reporter design (**Figure 1.7**) yields stronger fluorescence signals than the protein fusion design (**Figure 1.5**). Strong fluorescence outputs are desirable for achieving a high signal-to-noise ratio, which is important for quantification of signals. Furthermore, these results confirmed that the 500-bp and 222-bp upstream of *dddW* and *dmdA*, respectively, contain DMSP-responsive promoters.

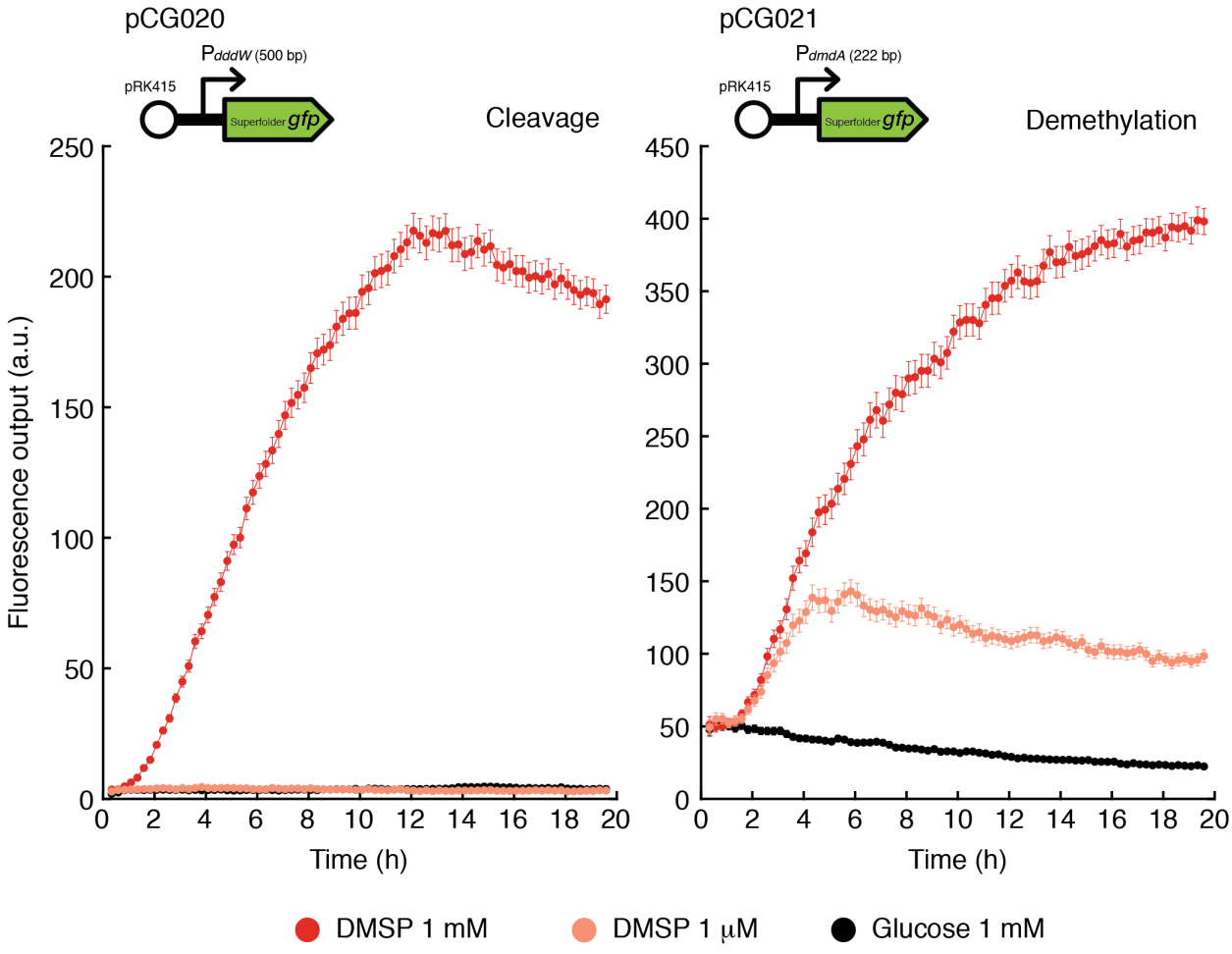

Figure 1.7 | Fluorescence of single-color promoter fusion reporter strains of DSS-3 incubated in 1 mM or 1 µM DMSP. All cells were grown overnight (30 °C) in glucose-amended (1 mM) MBM with tetracycline (3 µg/ml) and washed in non-amended MBM before treatment (0 h) with DMSP (1 µM, 1 mM) or glucose (1 mM) dissolved in MBM. One pair of phase contrast and fluorescence images per time point and treatment condition was acquired with an sCMOS camera (ORCA-Flash 4.0 V3; Hamamatsu Photonics; 6.5 µm pixel; exposure 300 ms) and 40× objective, with fluorescence excitation from a single-color LED light source (470 nm; Lumencor) and the EGFP filter cube (Chroma 49002). Data points and error bars are average ± s.e.m. fluorescence outputs of cells after background subtraction. Number of cells at t = 65 min (fourth time point) in the glucose condition was 1,700 for the cleavage reporter, and 335 for the demethylation reporter.

1.7 Tri-color promoter fusion designs

After validating the feasibility of constitutive fluorescence expression (**Section 1.4**) and promoter-fusion reporter construction (**Section 1.6**) in DSS-3, I next combined these designs to build a tri-color promoter fusion reporter strain that would enable the gene expression quantification of both DMSP pathway genes (*dmdA* and *dddW*) within a single cell. The third, constitutively expressed fluorescent protein enabled the quantification of fluorescence signal as a proxy of gene expression by providing a normalization factor to account for plasmid number and metabolic activity differences in cells. Below, I describe the two iterations of tri-color reporter designs that preceded the final versions (strains Regular and Goofy) that were published and described in **Chapter 2**.

1.7.1 Fluorescent protein choice

As of June 2020, FPbase lists 778 fluorescent proteins spanning the entire visible spectrum and each possessing different biochemical properties (www.fpase.org, ref. 70). The three fluorescent proteins incorporated into tri-color reporters were carefully chosen to optimize for maximum spectral separation (to minimize spectral leakage), fast maturation (to be as close to real-time as possible), monomeric structure (to preserve stoichiometry of the three fluorescent proteins), and high quantum yield (to enable detection of low gene expression). For tri-color reporter versions 1 and 2, this led to the choice of Cerulean CFP, Venus YFP, and mCherry RFP. In versions 3 and 4, the final reporter designs described in **Chapter 2**, contained mTFP1, Venus YFP, and mKate2 RFP.

1.7.2 Tri-color reporter version 1 (challenge of spectral leakage)

I drew inspiration from a tri-color promoter fusion plasmid that was built in the synthetic biology community by the Elowitz group[71], pZS2-123, which contains three fluorescent proteins (Cerulean CFP, Venus YFP, and mCherry RFP) fused to different inducible promoters. The three promoter fusion cassettes were separated by terminators to prevent transcriptional read-through[71]. A modified tri-color promoter fusion scaffold, with the promoters swapped out for putative promoters of *dddW* and *dmdA* (500 bp upstream of each gene), was integrated into the MCS of pRK415, which led to a 14.833 kb plasmid (pCG100), transformed into DSS-3 by electroporation. A two-color version, pCG104 (13.631 kb), was also constructed as a control to ensure that the inclusion of the third color (mCherry RFP) does not interfere with the promoter activity patterns measured through CFP and YFP fluorescence signals.

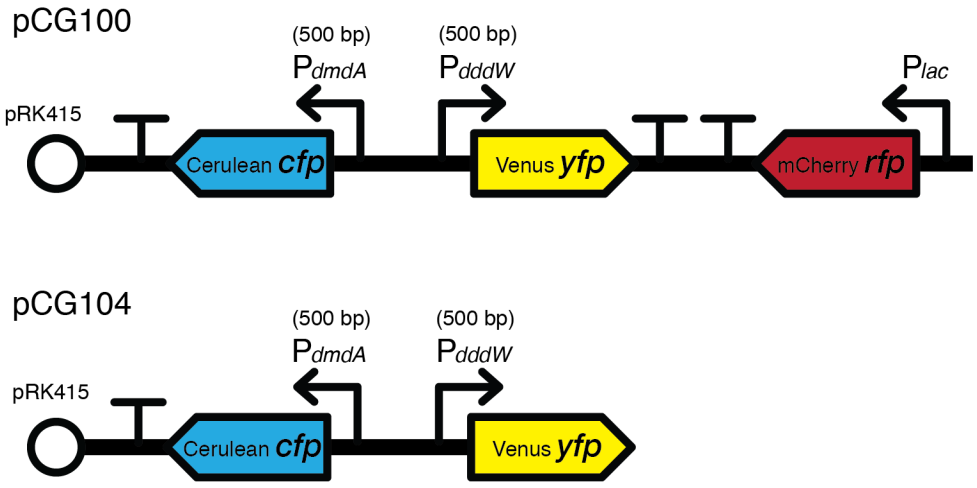

Figure 1.8 | Tri-color reporter version 1 and the two-color reporter control in DSS-3, containing promoter fusions. The 500-bp upstream sequences of the two genes involved in DMSP catabolism (*dmdA* and *dddW*) were used as putative promoters. The third color (RFP) was expressed with a constitutive promoter, P_{lac}, located at the MCS of pRK415.

Time-lapse fluorescence microscopy of this DSS-3 tri-color reporter strain incubated in different concentrations of DMSP revealed the concentration-dependent upregulation of both pathways (**Figure 1.9**). In the lowest four DMSP concentrations tested (2.3 µM–0.46 mM), the time point, as well as the magnitude of fluorescence, at which signals plateaued were concentration-dependent. In the highest DMSP concentrations tested, 1.23 mM and 0.9225 mM, the

fluorescence signal did not plateau within the experimental duration (5.75 h). However, the temporal patterns of fluorescence signals of the demethylation (P_{dmdA}::CFP) and cleavage (P_{dddW}::YFP) reporters of the tri-color strain were almost identical, albeit different magnitudes of fluorescence signal values (*y*-axis, **Figure 1.9**), which may point to substantial spectral leakage between yellow and cyan fluorescence color channels. The two-color reporter (pCG104) strain showed similar fluorescence patterns (data not shown). This highlighted the need for better spectral separation of fluorescent proteins, which may be achieved through better optical setups of the microscope (e.g., limiting the excitation and emission wavelength ranges, and increasing detector sensitivity to increase the signal-to-noise ratio) to differentiate signals from different colors of fluorescent proteins. Furthermore, the fluorescence signals from the constitutively expressed P_{lac}::RFP cassette of the tri-color strain were barely detectable, highlighting the need for a stronger constitutive promoter. Overall, experiments with the tri-color reporter version 1 showed the feasibility of integrating three promoter fusion reporter cassettes into a single plasmid in DSS-3, and the dose-dependence of fluorescence signals of DMSP pathway reporters.

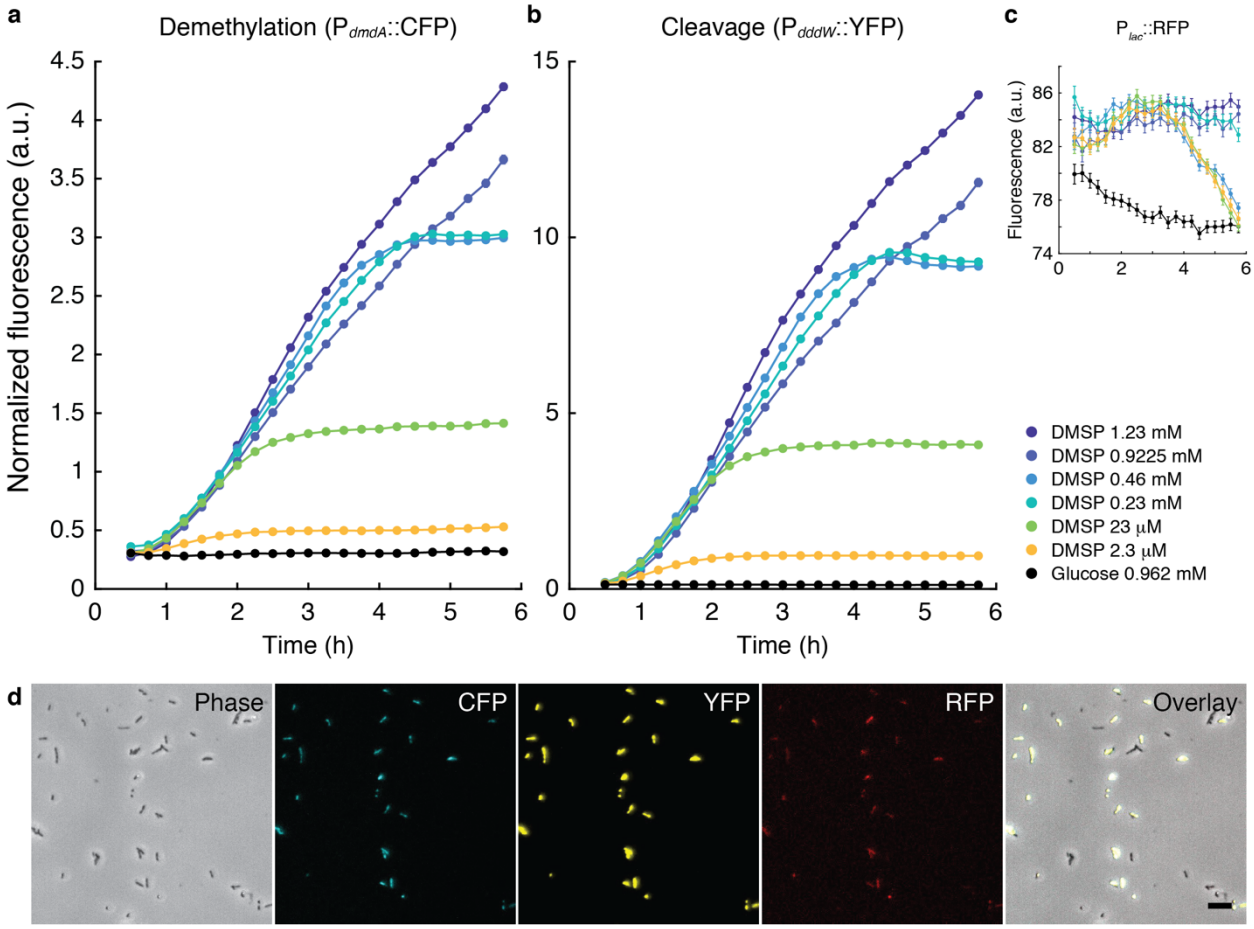

Figure 1.9 | Fluorescence of tri-color reporter (version 1) strain of DSS-3 incubated in different concentrations of DMSP (2.3 µM–1.23 mM). All cells were grown overnight (23.1 °C) in glucose-amended (1 mM) MBM with tetracycline (3 µg/ml) and washed in non-amended MBM before treatment (0 h) with DMSP or glucose dissolved in MBM. At each time point, images at 20 different *xy* positions were acquired for each experimental condition with an sCMOS camera **(**Andor Zyla 4.2; 6.5 µm pixel; exposure 200 ms for CFP and YFP, 400 ms for RFP; gain 4) and 40× objective with fluorescence excitation from single-color LED light source (Lumencor) with 100% power at 440 nm (**a**), 508 nm (**b**), 555 nm (**c**) and a tri-color ECFP/EYFP/mCherry filter cube (Chroma 69308). Only cells with constitutive RFP fluorescence intensities of greater than 25 a.u. were deemed RFP-positive and included for analyses. (**a**,**b**) Each cell's CFP and YFP signals (after background subtraction) were normalized by the average RFP intensity at the same time point. Data points and error bars are mean ± s.e.m. normalized fluorescence of cells. (**c**) Mean ± s.e.m. of RFP fluorescence of cells after background subtraction. Mean ± s.d. number of RFP-positive cells across experimental conditions at the fourth time point (1.25 h) was 6900 ± 1583. (**d**) Sample microscopy images at 4 h (15th time point) of incubation with 1.23 mM DMSP. Scale bar, 2 µm. Number of cells at t = 65 min (fourth time point) in the glucose condition was 1,700 for the cleavage reporter, and 335 for the demethylation reporter.

1.7.3 Tri-color reporter version 2 (challenge of reporter cassette arrangement)

In the second iteration of tri-color reporters of DMSP degradation gene expression in DSS-3, several changes were made: (i) the colors of fluorescent proteins fused to the promoters of *dddW* and *dmdA* were changed, to simultaneously spectrally distance the two reporters as well as to assign a different color to each promoter compared to version 1, (ii) the 231-bp inter-promoter space between P_{dddW} and P_{dmdA} of pCG100 was eliminated such that the promoters are now back-to-back, and (iii) only the 250-bp sequence was used as putative promoters of both *dmdA* and *dddW*. I previously showed that the 222-bp sequence upstream of *dmdA* was sufficient for activation by DMSP (**Figure 1.7**). Furthermore, bacterial promoters are typically shorter than 100 bp, containing two hexamer sequences at –10 and –35 bp upstream of the start of the gene[72]. Thus, I reasoned that shortening the putative promoter sequences of *dmdA* and *dddW* would still lead to functional reporters. As a result, pCG200 was 13.972 kb, representing a 5.8% reduction in size (862 bp) compared to pCG100. Two-color reporter controls were also built, this time separating *dmdA* (pCG201) and *dddW* (pCG202) reporters into to two plasmids but both containing the constitutive P_{lac}::YFP cassette to enable normalization to account for plasmid copy number and metabolic activity variation.

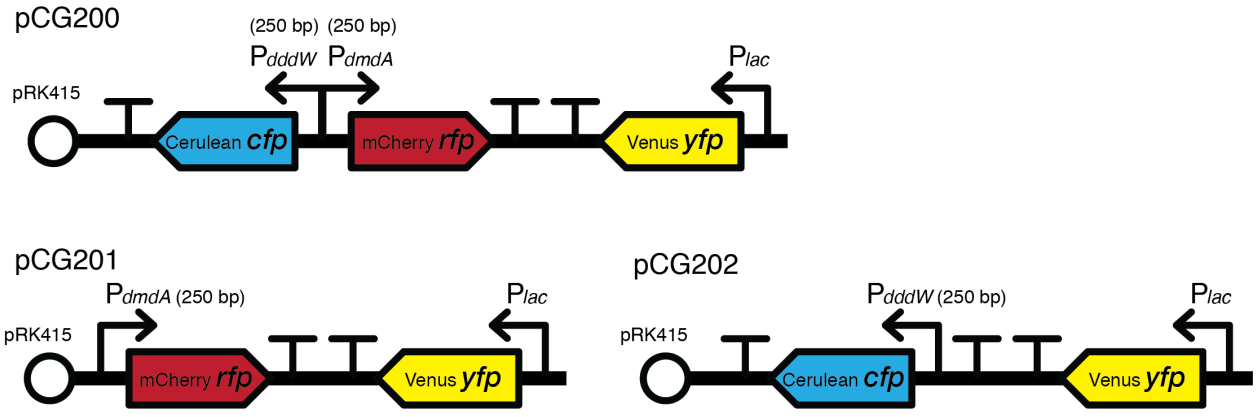

Figure 1.10 | Tri-color reporter version 2 and the two-color reporter control in DSS-3, containing promoter fusions. In an effort to decrease the size of the final plasmids, only the 250-bp upstream sequences of the two DMSP catabolism genes (*dmdA* and *dddW*) were used as putative promoters, without a spacer region between the two promoters. The third color (RFP) was expressed with a constitutive promoter, P_{lac}, located at the MCS of pRK415.

Comparisons of fluorescence signals of tri-color reporter versions 1 and 2 incubated in 1 mM DMSP revealed that the direction and spacing of reporter cassettes on the DNA scaffold has a large impact on the accuracy of the reporters (**Figure 1.11**). As previously shown in Figure 1.9, tri-color reporter version 1 (pCG100) showed signal increase of both *dmdA* and *dddW* reporters in DMSP, which plateaued at ~6–7 h (**Figure 1.11**a–c). In contrast, tri-color reporter version 2 (pCG200) showed contrasting behaviors of *dddW* and *dmdA* reporters, whereby the *dddW* reporter signal increased as shown previously, but the *dmdA* reporter fluorescence decreased in DMSP in a temporal pattern that mimicked that of constitutive YFP (**Figure 1.11**d–f). Furthermore, the *dmdA* reporter displayed high baseline fluorescence (362.48 ± 22.07 a.u. at the fourth time point, 62 min), suggesting that the back-to-back arrangement of promoters is causing bidirectional gene expression response that is not responsive to DMSP for *dmdA* (**Figure 1.11**d). The *dmdA* two-color reporter control (pCG201) containing solely the *dmdA* reporter and the constitutively expressed YFP showed the expected increase of the *dmdA* reporter (**Figure 1.11**g), suggesting that the absence of a spacer region between the putative promoters of *dmdA* and *dddW* caused the inappropriate behavior of the tri-color version 2. Furthermore, the *dddW* two-color reporter control (pCG202) was unresponsive to DMSP (**Figure 1.11**k), and showed a fluorescence signal pattern that mimicked that of background noise (**Figure 1.11**h). This lack of *dddW* signal may be caused by the sequential positioning of the putative promoter of *dddW* and transcriptional terminators, whose effect may be overpowering and inactivating the *dddW* promoter in the context of pCG202. Importantly, all constitutively expressed fluorescent proteins showed similar temporal patterns (**Figure 1.11**c,f,i,l), suggesting that the activity of the P_{lac} cassette is insulated from the rest of the DNA scaffold, perhaps due to the double transcriptional terminators. Taken together, the tri-color reporter version 2 revealed the importance of preserving the original direction and spacing of reporter cassettes on the DNA scaffold for successful reporting of *dmdA* and *dddW* promoter activities.

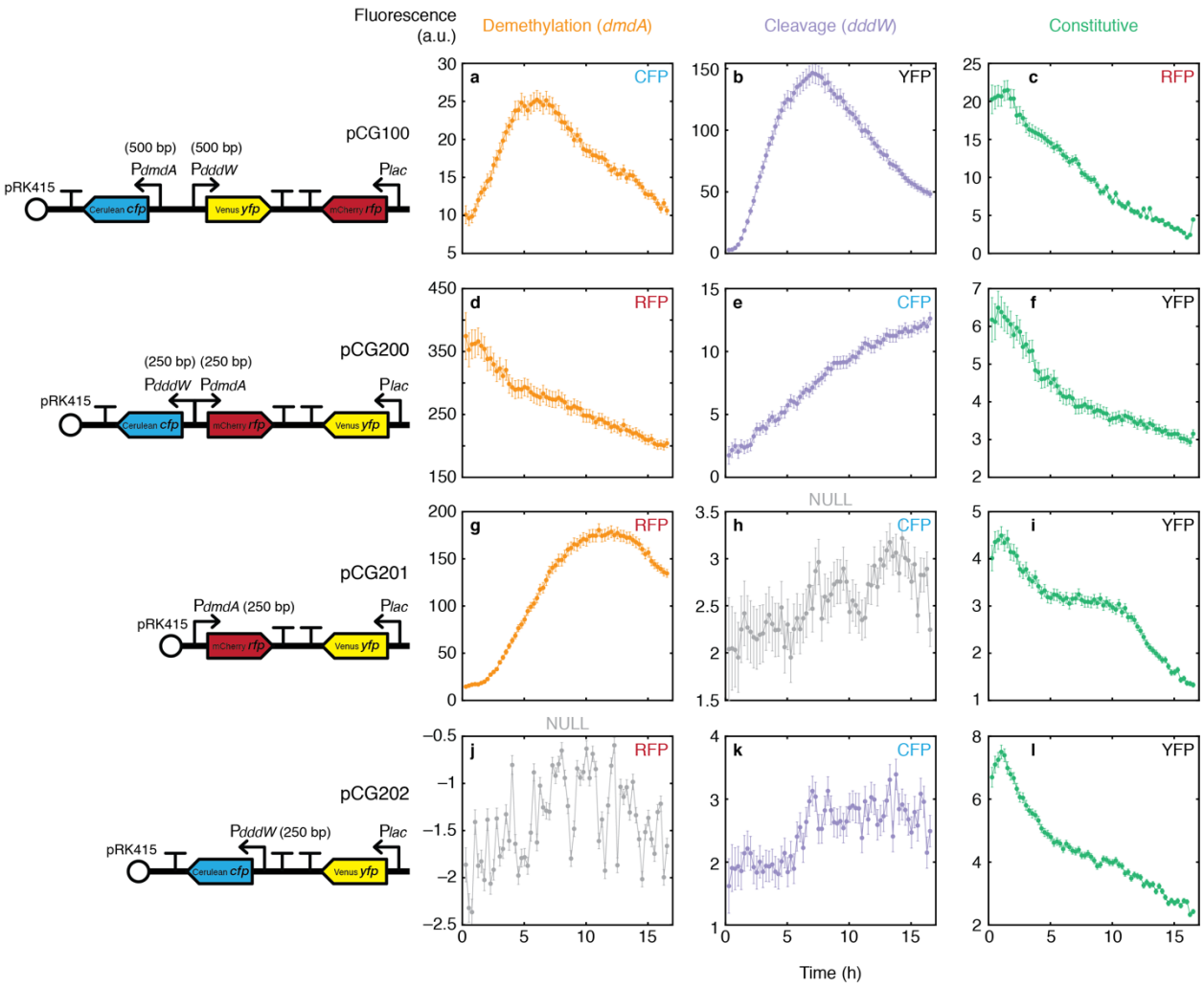

Figure 1.11 | Fluorescence signal comparisons of DSS-3 tri-color reporter versions 1 and 2 incubated in DMSP (1 mM). All cells were grown overnight (30 °C) in glucose-amended (1 mM) MBM with tetracycline (3 µg/ml) and washed in non-amended MBM before treatment (0 h) with 1 mM DMSP. At each time point (15-min intervals), phase contrast and fluorescence images at one *xy* position per experimental condition were acquired with an sCMOS camera (ORCA-Flash 4.0; Hamamatsu Photonics; 6.5 µm pixel; exposure 1 sec) and 40× objective, with fluorescence excitation from a single-color LED light source (Lumencor) at 100% power and different filter cubes used for imaging different fluorescent proteins: mCherry (Chroma 49008), 575 nm excitation; EYFP (Chroma 49003), 513 nm excitation; ECFP (Chroma 49001), 440 nm excitation. All cells detected in phase contrast images, regardless of their fluorescence intensities, were included for analyses. Data points and error bars are mean ± s.e.m. of fluorescence of cells after background subtraction. Fluorescence signals detected in all three channels (RFP, YFP, CFP) of four reporter constructs were quantified (number of cells at fourth time point, 62 min): pCG100 (**a–c**, 564 cells); pCG200 (**d–f**, 614 cells); pCG201 (**g–i**, 1,150 cells); pCG202 (**j–k**, 1,431 cells).

1.7.4 Final tri-color reporter versions (strains Regular and Goofy)

Several improvements were made in the final versions of the tri-color reporters (pCG301 and pCG401). First, a smaller plasmid vector, pBBR1MCS-KanR, was used, which resulted in 7.974 kb tri-color reporter plasmids that were easier to engineer and transform into DSS-3. Second, the usage of the strong constitutive PA1/04/03 promoter enabled me to quantitatively correct fluorescence signals for spectral leakage. Third, the lengths of putative promoters were determined through observations of responses in previous reporter designs in the presence of DMSP (500 bp for *dddW* and 222 bp for *dmdA*). Finally, I explored the fluorescent protein palette and identified mKate2 RFP and mTFP1 as superior replacements for mCherry RFP and Cerulean CFP (**Figure 1.12**). While excitation spectra of the two RFPs are similar, mKate2 emission spectra are slightly farther red, leading to greater separation of excitation and emission. Furthermore, mKate2 has shorter maturation time and higher quantum yield than mCherry. Similarly, mTFP1 emission and excitation wavelengths are well-separated, and its quantum yield is higher than that of Cerulean. Furthermore, the mTFP1 emission spectra does not show two peaks as Cerulean does. Taken together, mKate2 and mTFP1 are brighter and possess cleaner spectral profiles, for which signal detection optimization was easier. Details of methods and experiments with the final tri-color reporter strains of DSS-3 are available in **Chapter 2**.

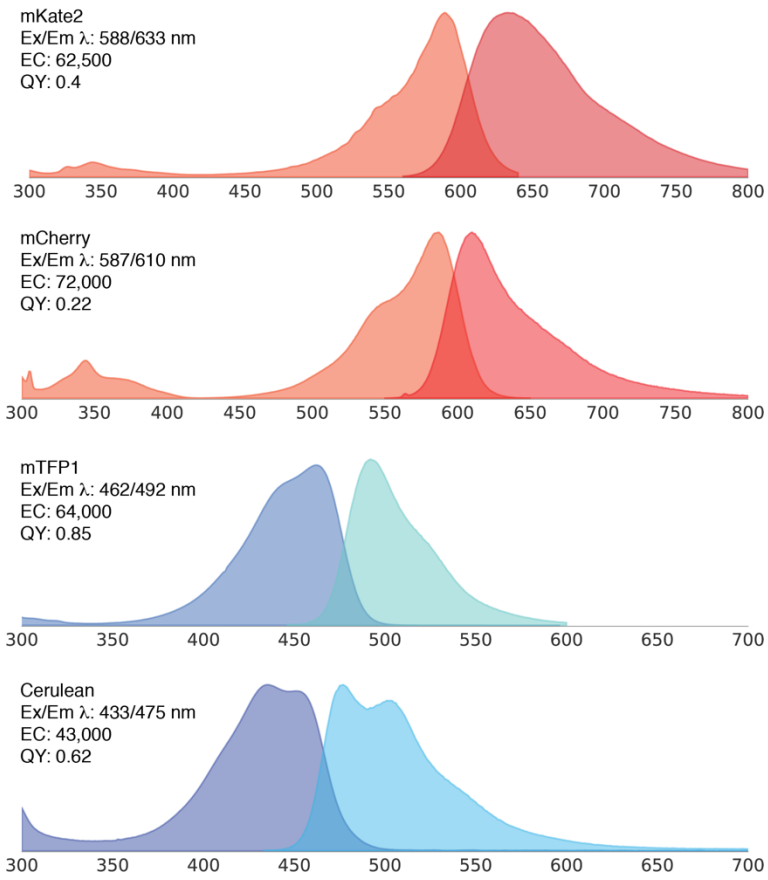

Figure 1.12 | Excitation and emission spectra of fluorescent proteins mKate2, mCherry, mTFP1, and Cerulean (adapted from FPbase[70]).

1.7.5 Fluorescence off-kinetics

Once fluorescent proteins are expressed in a cell, fluorescence signals are detectable for a long time due to the proteins' stability (half-lives of hours to more than a day[73]). To characterize the decay of fluorescence signals, or off-kinetics, of the DSS-3 fluorescent reporters upon the sudden withdrawal from DMSP, single-color reporter strains of DSS-3 (transformed with pCG302, P_{dmdA}::mTFP1 or pCG303, P_{dddW}::mKate2, described in **Chapter 2**) were first incubated with 10 mM DMSP for 3 hours, and subsequently washed and resuspended in 10 mM succinate.

In both strains, the rate of fluorescence signal increase slowed within 37 minutes of transfer from DMSP to succinate, and started to decrease within 97 minutes for P_{dddW}::mKate2 and within 157 minutes for P_{dmdA}::mTFP1 (**Figure 1.13**). The delay in the onset of fluorescence plateau and

decay upon withdrawal from DMSP may be due to the slow maturation times of the fluorescent proteins, which may continue to fold even in the absence of DMSP. Even after 3.5 hours of incubation in succinate and in the absence of DMSP, fluorescence signals did not return to baseline levels. It is possible that the cells continue to express *dmdA* and *dddW* genes in the hours following DMSP exposure and withdrawal. However, a more likely explanation is that the stability of fluorescent proteins causes the fluorescence signal to decouple from gene expression levels. This represents a major limitation of the fluorescence reporter system, which is likely unsuitable for measurements of gene expression downregulation.

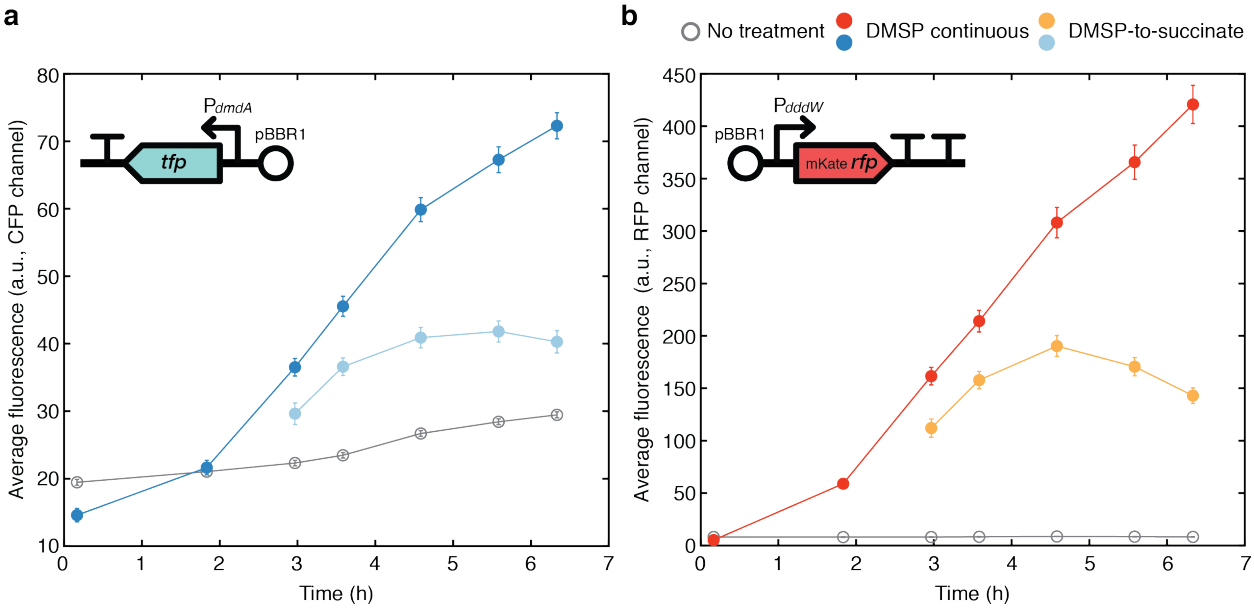

Figure 1.13 | Fluorescence off-kinetics. DSS-3 strains reporting *dmdA* (**a**) or *dddW* (**b**) promoter activities were used. All cells were grown overnight (30 °C) in succinate-amended (10 mM) MBM with kanamycin (25 µg/ml). Overnight cultures were directly loaded into microfluidic observation chambers (60 µm height) for the "no treatment" condition (open circles). For DMSP incubation, cells were washed in non-amended MBM before treatment (at $t = 0$ h) with 10 mM DMSP. DMSP-treated cells were either placed in the observation chambers (red, blue), or placed in 1.5-ml Eppendorf tubes and incubated in a shaker at 30 °C, and subsequently washed and resuspended in 10 mM succinate at ~3 h. Cells were subjected to antibiotic pressure throughout the entire experiment (kanamycin, 25 µg/ml), and time-lapse observations were conducted at 30 °C on a caged incubator-equipped microscope. At each time point, phase contrast and fluorescence images at two *xy* positions per experimental condition were acquired with an sCMOS camera (Andor Zyla 4.2; 6.5 µm pixel; exposure 200 ms for fluorescence, 9.8 ms for phase contrast) and 40× objective, with fluorescence excitation from a single-color LED light source (Lumencor) at 100% power and different filter cubes used for imaging different fluorescent proteins:

ECFP cube (Chroma 49001) with 440 nm excitation for TFP fluorescence measurements (**a**); and mCherry cube (Chroma 49008) with 555 nm excitation for mKate RFP fluorescence measurements (**b**). All cells detected in phase contrast images, regardless of their fluorescence intensities, were included for analyses. Data points and error bars are mean ± s.e.m. of fluorescence of cells after background subtraction. Number of cells included in fluorescence signal quantification at the fourth time point, 3.6 h: **a**, 4872 cells (no treatment), 1833 cells (DMSP continuous), 1684 cells (DMSP-to-succinate) cells; **b**, 5212 cells (no treatment), 1895 cells (DMSP continuous), 1741 cells (DMSP-to-succinate).

1.8 Conclusions

Like any genetic engineering efforts in relatively novel model organisms, the "design, build, test" cycle of engineering of DSS-3 was a multi-year effort spanning two laboratory environments as a result of a move from MIT to ETH Zurich. Careful calibrations of protocols were necessary for each laboratory environment due to the sensitivity of cloning procedures to chemical and environmental variations. In this Chapter, I first discussed the challenges that I encountered with plasmid vectors and transformation protocols of DSS-3, and suggested potential solutions to them. I then demonstrated the feasibility of constitutively expressing fluorescent proteins across the visible spectrum in DSS-3, using a constitutive promoter or through promoter fusions with genes of interest. Finally, I arrived at the final tri-color fluorescent reporter design which enabled the first semi-real-time measurements of DMSP pathway expression at the single-cell level, which I discuss in **Chapter 2**.

1.9 Acknowledgements

The work in this Chapter would not have been possible without the critical tips and conversations during the protocol troubleshooting stage. I would like to thank Prof. C.A. Voigt and his group members for teaching me how to clone and for demonstrating the great potential of synthetic biology. I also thank Prof. C.R. Reisch for crucial conversations that led me to the pBBR1MCS plasmids and the tri-parental mating protocol that finally got me out of a troubleshooting rut. I thank Prof. A. Persat for a key conversation that led me to pivot towards a tri-color reporter design, and Dr. A.S. Burns for his assistance in troubleshooting the electroporation protocol. Finally, I thank the generous scientists who shared their plasmids to

enable my cloning work: Prof. C.R. Reisch (pRK415, pRK600), Prof. S. Molin (miniTn7 plasmids), Prof. M.E. Kovach (pBBR1MCS series), Dr. F. Moser (sfGFP, EYFP), Dr. G. D'Souza (mTFP1, mKate2).

Chapter 2.

Single-cell bacterial transcription measurements reveal the importance of dimethylsulfoniopropionate (DMSP) hotspots in ocean sulfur cycling

Work presented in this chapter has been published as "Cherry Gao, Vicente I. Fernandez, Kang Soo Lee, Simona Fenizia, Georg Pohnert, Justin R. Seymour, Jean-Baptiste Raina & Roman Stocker. Single-cell bacterial transcription measurements reveal the importance of dimethylsulfoniopropionate (DMSP) hotspots in ocean sulfur cycling. *Nature Communications* **11,** 1942 (2020). https://doi.org/10.1038/s41467-020-15693-z"

2.1 Abstract

Dimethylsulfoniopropionate (DMSP) is a pivotal compound in marine biogeochemical cycles and a key chemical currency in microbial interactions. Marine bacteria transform DMSP via two competing pathways with considerably different biogeochemical implications: demethylation channels sulfur into the microbial food web, whereas cleavage releases sulfur into the atmosphere. Here, we present single-cell measurements of the expression of these two pathways using engineered fluorescent reporter strains of *Ruegeria pomeroyi* DSS-3, and find that external DMSP concentration dictates the relative expression of the two pathways. DMSP induces an upregulation of both pathways, but only at high concentrations (>1 μM for demethylation; >35 nM for cleavage), characteristic of microscale hotspots such as the vicinity of phytoplankton cells. Co-incubations between DMSP-producing microalgae and bacteria revealed an increase in cleavage pathway expression close to the microalgae's surface. These results indicate that bacterial utilization of microscale DMSP hotspots is an important determinant of the fate of sulfur in the ocean.

2.2 Introduction

Up to 10% of the carbon fixed by phytoplankton cells in the ocean is converted to dimethylsulfoniopropionate (DMSP)[9], resulting in a global production of this compound that exceeds one billion tons per year[10]. DMSP is an important currency in the ecological and metabolic exchanges between phytoplankton and heterotrophic bacteria[11], as it represents a major nutrient source that contributes significantly to the sulfur and carbon demand of bacteria (up to 95% and 15%, respectively[12,13]). DMSP is utilized by marine bacteria via two competing catabolic pathways[14]: the demethylation pathway leads to the incorporation of both carbon and sulfur into bacterial biomass, whereas the cleavage pathway results in the utilization of carbon but the release of sulfur in the form of the climatically-active gas dimethylsulfide (DMS). The environmental factors that govern the utilization of one pathway over the other, and ultimately the production and release of DMS to the atmosphere, have remained elusive, marking a major gap in the mechanistic link between microbial processes and global-scale carbon and sulfur biogeochemical cycles.

The water-column concentration of DMSP has been hypothesized to be an important factor regulating the choice of degradation pathway by bacteria (DMSP Availability Hypothesis[14]) and it has been speculated that bacteria control the fate of sulfur from DMSP by adjusting the relative expression of the demethylation and cleavage pathways (Bacterial Switch Hypothesis[74]). Concentrations of DMSP in bulk seawater are typically low, ranging from a few nanomolar (global oceanic average: 16.91 ± 22.17 nM[75]) up to 200 nM during phytoplankton blooms[76]. However, much higher DMSP concentrations are expected to occur in the vicinity of individual DMSP-producing organisms, such as phytoplankton cells, which can have intracellular DMSP concentrations of hundreds of millimolar[77]. Efforts to elucidate the environmental drivers of microbial catabolism of DMSP have to date been limited to measurements in large-volume batch cultures[78,79] and seawater samples[80]. As a consequence, an understanding of the influence of microscale heterogeneity in DMSP concentrations on the microbial choice of degradation pathway is lacking.

Here, we report that the external concentrations of DMSP that are relevant for controlling the expression of degradation pathways by a model copiotrophic bacterium are unexpectedly high, and are characteristic of DMSP hotspots. This finding was enabled by the development of the first single-cell, time-resolved measurements of DMSP degradation pathway expression and their application to study the response of bacteria to different concentrations of DMSP.

2.3 Results and Discussion

2.3.1 Construction and validation of fluorescent reporter bacteria.

To examine the relative expression of bacterial DMSP catabolism genes at the single-cell level, we genetically transformed *Ruegeria pomeroyi* DSS-3, a model Alphaproteobacterium from the Roseobacter clade. Like many members of the Roseobacter clade, which plays a central role in DMSP cycling[81], *R. pomeroyi* harbors both DMSP catabolic pathways[50]. We transformed *R. pomeroyi* cells with a custom-built tricolor promoter-fusion plasmid designed to simultaneously report metabolic activity and the expression of the genes encoding the two DMSP degradation pathway enzymes through different fluorescence emission (Fig. 1a,b). In the engineered plasmid, the promoter regions of DMSP-dependent demethylase (DmdA) and DMSP lyase (DddW), which catalyze the first steps of the demethylation and cleavage pathways, respectively, control the expression of fluorescent proteins (Methods). Out of the three functional DMSP lyases (DddP, DddQ, and DddW)[82] encoded in the *R. pomeroyi* DSS-3 genome, DddW was chosen in this study due to its strong upregulation response to DMSP reported in previous transcriptomic studies[55,78], which suggests that it is the primary DMSP lyase in this bacterium. However, some of the cleavage dynamics, controlled by DddP and DddQ, may be missed by our approach.

Construction of promoter-fusion reporter strains, followed by quantitative single-cell time-lapse microscopy, has been commonly adopted to utilize fluorescence signal dynamics as a proxy for native gene expression behaviors[83–85]. To control for signal bias caused by the choice of fluorescent protein fused to each promoter region, we constructed two *R. pomeroyi* reporter strains (Goofy and Regular), for which we interchanged the color of fluorescent proteins fused to the *dmdA* and *dddW* promoter regions (Fig. 1a,b and Supplementary Fig. 1). The choice of fluorescent protein led to some differences in the temporal evolution of fluorescence signal, but

did not affect our overall conclusions (Supplementary Fig. 2). A comparison of fluorescence signal output by tricolor and single-color reporter strains confirmed that promoter fusion cassettes induce fluorescent protein expression whether encoded alone or together (Supplementary Fig. 2).

To confirm that the strains specifically report *dmdA* and *dddW* gene expression, and to test for non-specific responses, the engineered bacteria were incubated with seven different carbon sources. Rich medium (5% 1/2YTSS), propionate, acetate, succinate, and glucose did not elicit any fluorescence response (Supplementary Fig. 3). Glucose was chosen as the most suitable negative control for subsequent experiments for the following reasons: it elicited no non-specific DMSP gene transcription responses (Supplementary Fig. 3); its molecular weight is similar to DMSP; and the metabolic pathways of glucose and organosulfur compounds are distinct. The only carbon sources that led to an increase in cell fluorescence were DMSP (activating both *dmdA* and *dddW* promoters) and acrylate, a known *dmdA* inducer[53] (activating only *dmdA*, but not *dddW*), thus confirming the validity of our reporter construct design (Supplementary Fig. 3).

2.3.2 Time-lapse DMSP incubation experiments in microfluidic chips.

A custom microfluidic chip containing nine observation chambers was employed for the simultaneous incubation of an engineered reporter strain with a range of concentrations of DMSP as a sole amended carbon source (Fig. 1c). The absence of fluid flow in the observation chambers enabled us to monitor the expression of DMSP degradation pathways in a time-resolved manner at the single-cell level (Fig. 1d). Images in phase contrast and fluorescence (in red, yellow, and teal channels) were acquired every 45 min for 24 h at six or seven positions per observation chamber (Fig. 2), encompassing 218 ± 120 (mean ± s.d.) cells per field of view (at t = 45 min) per condition (Supplementary Fig. 4). Microscope and camera settings were optimized to minimize phototoxicity and photobleaching while maximizing fluorescence signal capture.

Low levels of expression of both pathways occurred even in the absence of DMSP (Supplementary Fig. 5 and Supplementary Note 1), with baseline *dmdA* expression 1.0–6.7 times higher than *dddW* expression (Fig. 3). High variability of fluorescence output amongst replicate experiments at ≥10 μM DMSP (Supplementary Fig. 6), likely caused by slight differences in

subculture growth phase, prevented the comparison of pathway reporters within each color (Supplementary Fig. 5). Thus, across-color ratio calculation, which enabled comparisons of pathway expression within the same experiment, was employed in our study (Fig. 3). Importantly, the across-color ratios (0.15–1.0; Fig. 3) and within-color ratios (0.3–0.5; Supplementary Fig. 5) in glucose showed consistent results.

No significant upregulation beyond these baseline levels of either pathway was detected at DMSP concentrations below 1 µM (i.e., 100 nM and 500 nM) compared to negative controls (two-tailed *t*-tests, $n = 259–2125$ cells, $p > 0.01$) (Supplementary Fig. 7). At 1 µM DMSP, significant upregulation was only observed in some replicate experiments (Supplementary Fig. 8). Only one out of six replicate experiments of the demethylation pathway (*dmdA*) was upregulated at 1 µM DMSP, while the cleavage pathway (*dddW*) showed more consistent significant upregulation (four out of six replicate experiments) at 1 µM DMSP compared to glucose negative controls (two-tailed *t*-tests, $n = 1284–9362$ cells, $p < 0.01$) (Supplementary Fig. 8). At higher concentrations (≥10 µM), all replicate experiments exhibited upregulation (Supplementary Fig. 6). These results suggest that 1 µM approximates the threshold DMSP concentration above which bacteria start to increase *dmdA* gene expression beyond baseline levels. Consistent with existing evidence that points to demethylation as the major fate of DMSP in seawater[86], our results also suggest that DMSP at typical bulk seawater concentrations (16.91 ± 22.17 nM[75]) is primarily degraded through the higher baseline expression levels of the demethylation pathway by Roseobacters (such as *R. pomeroyi*), which are major players in marine organic sulfur cycling[81].

Both pathways were consistently and significantly upregulated compared to negative controls upon incubation with DMSP concentrations between 10 µM and 1 mM, which led to upregulation of 1.6–6.0-fold (*dmdA*) and 8.0–112.6-fold (*dddW*) compared to glucose at 24 h (Fig. 2a,b and Supplementary Figs. 6, 9; averages of $n = 6$ replicates). The rates of upregulation, expressed as the slope of the exponential phase of the fluorescence kinetics curves, were similar across different DMSP concentrations (10 µM–1 mM, Fig. 2a,b and Supplementary Fig. 6), suggesting that upon exposure to DMSP concentrations at or above 10 µM, cells are stimulated

to initially increase the expression of both demethylation and cleavage pathways at a conserved rate.

While the rate of upregulation was conserved across DMSP concentrations, maximum gene expression levels of *dddW* and *dmdA* increased with DMSP concentration (Fig. 2c,d). Due to the stability of fluorescent proteins (half-lives of hours to more than a day[73]), the fluorescence signal is expected to persist even after gene expression returns to baseline levels. We therefore used the magnitude of the end-point fluorescence signal (averaged over the last five time points, i.e., 20.4–24 h) as a proxy for maximum gene expression levels of *dddW* and *dmdA*. Normalized maximum gene expression levels of both pathways increased approximately linearly with DMSP concentration between 1 and 75 μM DMSP (0.07–0.77 a.u. for *dmdA*; 0.02–0.62 a.u. for *dddW*; Fig. 2c,d). This increase plateaued above 100 μM (Fig. 2c,d), possibly as a result of the gene expression machinery becoming saturated and unable to respond as sensitively to DMSP at these high concentrations (Supplementary Note 2).

To determine how consumption of DMSP in the chambers may have affected our conclusions, we performed a larger-volume (8 ml) experiment in which we directly measured DMSP concentration and cell fluorescence, for selected timepoints (0, 2, 8, 24 h) and initial DMSP concentrations (1 μM, 75 μM, 1 mM). DMSP concentration decreased over time, due to uptake by bacteria (Supplementary Fig. 10). Consistent with results from the microfluidic chip experiments (Fig. 2), the initial rate of increase in the fluorescent signal was conserved between the 75 μM and 1 mM conditions, but decreased as the DMSP concentration diminished due to bacterial uptake (Supplementary Fig. 10). The saturation of the fluorescence signal coincided temporally with the depletion of DMSP (at 8 h, for the 75 μM condition; Supplementary Fig. 10). These results suggest that cells initially increase gene expression at a rate that is independent of DMSP concentration, but halt their gene upregulation when the DMSP supply is exhausted.

Rather than expressing only one pathway at any given DMSP concentration, as implied by the Bacterial Switch Hypothesis[74], we observed that bacteria express both pathways simultaneously, but modulate the ratio of cleavage and demethylation according to DMSP concentration (Fig. 3). Overall, the cleavage-to-demethylation expression ratio increased with DMSP concentration up

to 100 μM, above which it started to plateau (Fig. 3b). Baseline expression levels that are biased towards demethylation were represented by cleavage-to-demethylation ratios of 0.15–1.0 in the glucose negative controls (Fig. 3). At high DMSP concentrations between 10 μM and 1 mM, bacteria gradually skewed their gene expression towards the cleavage pathway, with the cleavage-to-demethylation ratio increasing from 1.89 ± 0.29 at 10 μM to 8.10 ± 0.60 at 1 mM (Fig. 3, strain Regular). Similar ratio values were obtained with strain Goofy (Fig. 3). These results indicate that the cleavage pathway becomes more strongly expressed than the demethylation pathway above a transition concentration of DMSP that lies between 1 and 10 μM. We propose that at this transitional concentration, the sulfur needs of the bacteria are completely met through the demethylation pathway, and excess organic sulfur at higher DMSP concentrations is released as DMS via cleavage.

2.3.3 Raman microspectroscopy.

The effect of sulfur satiation on cleavage pathway expression was more directly observed via single-cell Raman microspectroscopy. Measurements with deuterium-labelled DMSP revealed that bacteria that were satiated in sulfur through prior exposure to methionine (also an organic sulfur source) maintained uptake of DMSP but skewed gene expression towards the cleavage pathway (Supplementary Fig. 11). Bacterial sulfur demand has been proposed as a factor that regulates the fate of DMSP[14,74,79]. Since different elements of the DMSP molecule are harvested by the bacteria through demethylation (both carbon and sulfur) and cleavage (carbon only), our observations are consistent with the hypothesis that cells favor the cleavage pathway when they no longer require additional sulfur but continue to harvest carbon from DMSP.

2.3.4 Co-incubation of phytoplankton and engineered bacteria.

While uptake of DMSP was detected at all concentrations tested (Supplementary Fig. 10), upregulation of DMSP degradation genes was observed only in relatively high concentrations (≥1 μM in microfluidic chip experiments; Fig. 2). DMSP is not homogeneously distributed in the water column, but often occurs as point sources of high concentration surrounding DMSP-producing organisms[87]. Bacterial exploitation of these enriched microenvironments[37] can influence DMSP transformation rates and microbial pathway choice in the ocean. To determine DMSP degradation gene expression in the context of microscale hotspots, we exposed the *R.*

pomeroyi fluorescent reporter strains to an ecologically relevant point source of DMSP: a unicellular phytoplankton. Concentration gradients of nutrients, often including DMSP, are present in the microenvironment directly surrounding phytoplankton cells (the phycosphere[87]). We co-incubated the reporter strains with the unicellular dinoflagellate *Breviolum* CCMP2459, which belongs to a family containing some of the most prolific producers of DMSP (Symbiodiniaceae; with intracellular DMSP concentrations of 36–7590 mM)[77]. Co-incubations were performed on agarose pads, which immobilized both phytoplankton and bacterial cells for ease of observation. After 24 h of co-incubation in the dark, high-magnification (100× objective) epifluorescence microscopy images of the phycosphere surrounding individual *Breviolum* cells were acquired (Fig. 4a,b and Supplementary Fig. 12). To avoid alterations to the phycosphere due to microscopy light-induced cellular stress, images were acquired at a single time point (24 h). Only teal fluorescence was quantified to represent bacterial pathway expression (due to spectral leakage in the red fluorescence channel by photosynthetic pigments, e.g., chlorophyll and carotenoids), with strain Regular reporting demethylation (*dmdA*; n = 15 *Breviolum* cells) and strain Goofy reporting cleavage (*dddW*; n = 18 *Breviolum* cells) (Fig. 4). Fluorescence intensities of bacteria were averaged across *Breviolum* cells as a function of distance from the phytoplankton cell (Supplementary Note 3).

R. pomeroyi gene expression patterns reflected the spatial locations of the bacteria within the phycosphere of *Breviolum* cells. According to modeled DMSP diffusion assuming a leakage rate of 11% of intracellular DMSP per day (Supplementary Note 4), the steady-state concentration at the surface of a *Breviolum* cell (radius = 3.3 ± 0.9 μm, mean ± s.d.) was 197 nM and decayed exponentially with distance, r, from the center of the phytoplankton cell (Supplementary Fig. 13). In line with the predicted DMSP concentration profile within the phycosphere, bacteria that were nearest to the surface of *Breviolum* cells, but far enough not to be affected by spectral interference from photosynthetic pigments (r = 7.4 μm), were the most metabolically active, exhibiting YFP fluorescence intensities that were on average double (1.4 ± 0.5 a.u., Goofy; 0.4 ± 0.2 a.u., Regular) those exhibited by bacteria located at r = 18.6 μm (0.7 ± 0.3 a.u., Goofy; 0.2 ± 0.05 a.u., Regular), beyond which YFP intensities did not change with distance (Fig. 4c,d).

The expression of the cleavage pathway (*dddW*) also increased with decreasing distance from a *Breviolum* cell. The *dddW* expression levels ($3.4 \pm 1.1 \times 10^{-2}$ a.u., raw TFP signal) were highest near the surface of *Breviolum* ($r = 7.4$ µm; modeled DMSP concentration = 89 nM) (Fig. 4d) and decreased to baseline levels ($2.4 \pm 0.4 \times 10^{-2}$ a.u., raw TFP signal) at $r \geq 18.6$ µm (modeled DMSP concentration = 35 nM). These results differ from our previous microfluidic experiments where exposure to pure DMSP at <1 µM did not lead to *dddW* fluorescence upregulation (Supplementary Fig. 7). This discrepancy may be due to the presence of compounds in algal exudates that positively influence the regulation of *dddW* expression, or by the greater sensitivity of the camera setup used in the *Breviolum* experiment. In contrast, the demethylation pathway (*dmdA*) was not expressed above baseline levels at any distance from the *Breviolum* cells (Fig. 4c), but its expression, normalized by the average baseline YFP intensity (proxy for metabolic activity), was still higher than that of the cleavage pathway throughout the phycosphere (Fig. 4e). As a result, relative pathway expression was skewed towards demethylation at all distances from a *Breviolum* cell (Fig. 4f), but with decreasing distance, and thus increasing DMSP concentration, the cleavage-to-demethylation pathway ratio increased in a pattern consistent with the microfluidic observations (Fig. 3a).

These results suggest that within the phycosphere of a small phytoplankton cell slowly exuding DMSP, elevated production of DMS due to cleavage by marine bacteria occurs close to the surface of the phytoplankton cell, but most of the DMSP within the phycosphere is degraded through the demethylation pathway. However, in the scenario of a lysing phytoplankton cell that releases its intracellular DMSP at once, for example at the demise of a phytoplankton bloom, DMSP within the phycosphere can reach micro- or millimolar concentration for seconds to minutes[88]. Matching these time scales, bacterial gene expression (transcription and translation) can theoretically be upregulated within a few minutes[89], although limitations in fluorescence signal detection prevented the observation of such early responses in the present study. Furthermore, oligotrophic DMSP degraders such as SAR11[90,91] likely employ regulatory mechanisms that differ from copiotrophic bacteria such as *R. pomeroyi*. In general, the results from our microfluidic experiments suggest that in the vicinity of lysing phytoplankton cells (>10 µM) or in other microenvironments with similarly high DMSP levels[92], both DMSP degradation genes increase expression, with cleavage more so than demethylation. These microscale

dynamics are consistent with macroscale patterns of elevated DMS production that are observed during the decline of phytoplankton blooms[93] and following high rates of viral-induced phytoplankton lysis[94].

Taken together, our observations reveal that the metabolic machinery of DMSP-degrading copiotrophic bacteria may be adapted for encounters with DMSP hotspots. Baseline expression of both pathways was detected even in the absence of DMSP (Supplementary Fig. 5), possibly owing to promoter leakage of *dmdA* and *dddW*, which likely allows bacteria to be poised for the next encounter with DMSP. Upregulation of DMSP degradation genes, beyond baseline levels, was only observed at high DMSP concentrations that are characteristic of hotspots: above 1 μM for *dmdA* (Fig. 2a and Supplementary Fig. 6) and above 35 nM for *dddW* (Fig. 4b,d and Supplementary Fig. 13). Furthermore, K_m values of DMSP degradation enzymes (5.4 mM for DmdA[95] and 4.50–8.68 mM for DddW[96]) are orders of magnitude above the mean seawater concentrations of DMSP (16.91 ± 22.17 nM[75]), further supporting the notion that bacteria are adapted to exploit sporadic encounters with DMSP hotspots[97] as we observed by single-cell imaging.

Identifying the environmental determinants of microbial DMSP cycling is key in understanding their effects on global climate and biogeochemical cycles. Two interconnected concepts, the DMSP Availability Hypothesis[14] and the Bacterial Switch[74], were proposed nearly two decades ago to explain the interplay between the two DMSP degradation pathways and the factors leading to the production of DMS, but have remained largely hypothetical. The present study offers the first direct evidence that the ambient concentration of DMSP regulates the relative (i.e., cleavage-to-demethylation ratios; Figs. 3 and 4), rather than mutually exclusive, expression of demethylation and cleavage pathways. We observed that elevated concentrations of DMSP (>10 μM), which are typically found in microscale hotspots, shift bacterial DMSP degradation towards cleavage and are ultimately expected to increase the bacterial production and release of DMS. Thus, we propose that the concentrations of DMSP that are most relevant for the bacterial production of DMS, and ultimately for global sulfur cycling and for the production of DMS-derived cloud condensing nuclei, may not be the levels present in bulk seawater, but instead those existing in microscale hotspots. This points to the importance of understanding the relative

contribution of DMSP catabolism rates in hotspots compared to the bulk seawater, and the need to develop more realistic microscale methods to quantify the utilization and fate of this ubiquitous and important marine compound.

2.4 Methods

2.4.1 Construction of tricolor fluorescent reporter strains.

Tricolor fluorescent reporters were constructed in the marine model organism *Ruegeria pomeroyi* DSS-3 (wildtype strain a gift from Prof. M. A. Moran, University of Georgia) to visually report expression of DMSP degradation genes (*dddW* and *dmdA*). DddW was chosen due to its strong upregulation response to DMSP reported in previous transcriptomic studies[55,78], which suggests that DddW is the primary DMSP lyase in *R. pomeroyi* DSS-3. Three fluorescent proteins were chosen for brightness, monomeric structures, and spectral separation: mTFP1 (teal)[98]; mVenus-Q69M (yellow)[99], which is the mVenus YFP[100] modified with a Q69M mutation to reduce environmental sensitivity; and mKate2 (far-red)[101]. To control for bias caused by the choice of color of fluorescent protein (RFP or TFP) fused to each promoter region, we constructed two *R. pomeroyi* reporter strains (Goofy and Regular) in which we interchanged the fluorescent proteins fused to *dmdA* and *dddW* promoter regions (Fig. 1a,b).

Three promoter fusion cassettes were inserted into a single vector backbone (pBBR1MCS-2, a 5.144 kb, broad-host-range, medium copy number plasmid with a kanamycin resistance cassette and origin of replication pBBR1, originally isolated from *Bordetella bronchiseptica*)[102,103] to enable gene expression readouts from individual cells (Supplementary Fig. 14): a *dmdA* promoter reporter cassette; a *dddW* promoter reporter cassette; and a constitutively expressed *yfp* cassette (Fig. 1a,b). The 500 bp sequence upstream of the *dddW* gene and 222 bp upstream of the *dmdA* gene in the *R. pomeroyi* DSS-3 genome were determined as putative promoter regions and used to construct promoter reporter cassettes. A strong, constitutive synthetic promoter $P_{A1/04/03}$ (an *E. coli lac* promoter derivative)[60,63] controlled the expression of YFP, whose intensity was utilized as a proxy for cell viability, plasmid copy number, and metabolic activity (Supplementary Fig. 15). Transcriptional terminators (RNAI, TSAL, TR2-17, TL17, BS7, T7TE+) and spacer regions between promoter fusion cassettes were cloned from plasmid pZS2-

123[71]. As an intermediate step in the construction of the tricolor reporter strains, a derivative of pZS2-123 (with its original promoters replaced with 500 bp sequence upstream of *dmdA* or *dddW* genes), pZS2-200, was built using restriction enzymes: AvrII, XmaI, XhoI, BamHI, XmnI, and SalI (New England Biolabs).

2.4.2 Construction of control reporter strains.

Truncated versions of the tricolor reporters (Supplementary Fig. 1), each of which contained one of the promoter fusion cassettes, were built to test the effect of including three promoter fusion cassettes within one DNA construct (Supplementary Fig. 2). We also constructed constitutively fluorescent, single-color *R. pomeroyi* strains (Supplementary Fig. 1) to quantify spectral leakage amongst fluorescent protein colors, and to calculate the spectral leakage correction matrix, *B* (Supplementary Note 1 and Supplementary Fig. 16).

2.4.3 DNA assembly.

All *R. pomeroyi* strains and plasmids engineered in this study are listed in Supplementary Table 1 and Supplementary Fig. 1. For assembly of the promoter fusion cassettes into the pBBR1MCS-2 vector, DNA fragments containing overlapping regions (~30 bp) were amplified with 25 cycles of PCR using KAPA HiFi HotStart ReadyMix (Kapa Biosystems) with primers listed in Supplementary Table 2. Putative promoter regions of *dmdA* and *dddW* were amplified from *R. pomeroyi* DSS-3 genomic DNA isolated with DNeasy Blood & Tissue Kits (Qiagen). Plasmids that were used as PCR templates (Supplementary Table 3) were isolated using the QIAprep Spin Miniprep Kit (Qiagen). Primers for vector backbone amplification were designed to eliminate the multiple cloning site (MCS) within the *lacZα* gene in the pBBR1MCS-2 vector to prevent fusion with the β-galactosidase α-peptide. Two extra stop codons (TAATAA) were added to each fluorescent protein gene sequence through primer design.

DNA fragments were assembled using NEBuilder HiFi DNA Assembly Master Mix (New England Biolabs). Assembled plasmids were transformed into electrocompetent *E. coli* (NEB 10-beta; New England Biolabs) through electroporation (Gene Pulser Xcell, Bio-Rad), positive colonies were picked on X-Gal/IPTG Luria Broth (LB) plates, and correct assembly of DNA

fragments was confirmed through sequencing of purified plasmids using diagnostic primers listed in Supplementary Table 2.

2.4.4 Transformation of *Ruegeria pomeroyi* through conjugation.

Reporter plasmids were transformed into *R. pomeroyi* DSS-3 through a triparental conjugation method, which was found to be ideal due to the large sizes of our reporter plasmids (up to 7.974 kb). Overnight liquid culture of wildtype *R. pomeroyi* was prepared in half-strength YTSS (1/2 YTSS) containing (500 ml^{-1}) 2 g yeast extract (BD Biosciences), 1.25 g tryptone (BD Biosciences), 10 g sea salts (Sigma-Aldrich). In addition, overnight liquid cultures of helper *E. coli* containing the pRK600 plasmid[104] (15 µg ml^{-1} chloramphenicol) and donor *E. coli* containing a constructed reporter plasmid (50 µg ml^{-1} kanamycin) were prepared in LB. *E. coli* cultures were washed twice in 1/2 YTSS medium to eliminate antibiotics. The following mixture was concentrated and resuspended in a final volume of 100 µl 1/2 YTSS medium: 2 ml overnight culture of *R. pomeroyi*, 200 µl of washed overnight culture of helper *E. coli*, and 200 µl of washed overnight culture of donor *E. coli*. 50 µl of this bacterial mixture was spotted on a 1/2 YTSS plate, and incubated overnight at 30 °C to allow mating to occur. Selection for plasmid-containing *R. pomeroyi* was achieved by re-streaking onto a 1/2 YTSS plate amended with kanamycin (50 µg ml^{-1}) and potassium tellurite (50 µg ml^{-1}; Fluorochem). Like many marine microorganisms[105,106], *R. pomeroyi* was found in this study to be resistant to potassium tellurite, while *E. coli* is known to be sensitive to the oxide mineral. Successfully transformed *R. pomeroyi* were confirmed through colony PCR and sequencing.

2.4.5 Bacterial culture preparation for experiments.

A frozen glycerol stock of each *R. pomeroyi* reporter strain was streaked onto a half-strength YTSS (1/2 YTSS) culture plate containing (500 ml^{-1}) 7.5 g agar (Bacto Agar, BD Biosciences), amended with 50 µg ml^{-1} kanamycin sulfate (Sigma-Aldrich), and incubated at 30 °C for 48–72 hours. A single colony was picked from the plate to inoculate 1 ml of 1/2 YTSS liquid medium amended with 25 µg ml^{-1} kanamycin for overnight culture (~19 h) in the dark at 30 °C on an orbital shaker (200 rpm). When overnight cultures reached visible turbidity, subcultures were prepared by washing (6300 × *g*, 3 min) and diluting (1/75 vol/vol) overnight culture cells to a final volume of 1.5 ml in marine basal medium (MBM) consisting of 0.07 M Tris HCl (pH 7.5),

0.24 mM K_2HPO_4, 13.4 mM NH_4Cl, 0.073 mM FeEDTA, 2% (wt/vol) sea salts, and 0.1% (vol/vol) vitamin solution[107]. D-glucose (10 mM) was provided as a sole amended carbon source in MBM, and kanamycin (25 μg ml^{-1}) was added for plasmid retention. Initial OD_{700} of 10 mM glucose MBM subcultures ranged from 0.04 to 0.05. After a 4-hour incubation in similar conditions as overnight cultures, OD_{700} decreased to 0.03 to 0.04, probably due to a decrease in cell size as cells transitioned from rich medium (elongated cells) to MBM (shortened cells).

To prepare for the low DMSP concentration (≤1 μM) experiment (Supplementary Fig. 7), several colonies of strain Regular cells on an agar plate were resuspended directly into MBM amended with 1 mM succinate and 50 μg ml^{-1} kanamycin, and grown overnight at 30 °C in the light. The overnight culture was diluted (1/50 vol/vol) into fresh 1 mM succinate MBM with kanamycin (50 μg ml^{-1}) and incubated for an additional 4 h. Similar to other time-lapse experiments, OD_{700} was 0.3 before initiation of incubation with DMSP.

2.4.6 Carbon sources test.

To assess the validity of engineered reporter strains, as well as to identify an appropriate negative control carbon source, *R. pomeroyi* reporter strains Regular and Goofy were incubated with a range of carbon sources, and their fluorescence response and growth were measured (Supplementary Fig. 3). Carbon sources chosen for this experiment were utilized in previous studies to cultivate *R. pomeroyi*. MBM solutions amended with 10 mM of the following carbon sources were prepared: DMSP (Tokyo Chemical Industry), sodium succinate dibasic hexahydrate (Sigma-Aldrich), sodium propionate (Sigma-Aldrich), sodium acetate (Sigma-Aldrich), sodium acrylate (Sigma-Aldrich), or D-glucose (Sigma-Aldrich). MBM solutions were filter sterilized (0.2 μm) after dissolution of carbon sources. The 5% 1/2 YTSS was prepared with a dilution (1/20 vol/vol) of the rich medium in non-carbon amended MBM.

Several colonies of *R. pomeroyi* reporter strains on agar plates were washed and resuspended in non-carbon amended MBM. Resuspended cells (2 μl) were seeded into 0.75 ml of each carbon source MBM solution amended with 25 μl ml^{-1} kanamycin. Incubations were performed in 2-ml microcentrifuge tubes (Eppendorf) in the dark at 30 °C with 200 rpm orbital shaking for 18.5 h before microscopy imaging.

Glucose was chosen as the most suitable negative control for the following reasons: it elicited no non-specific DMSP gene transcription response (Supplementary Fig. 3); its molecular weight is similar to DMSP; and the metabolic pathways of glucose and organosulfur compounds are distinct. The low DMSP concentration (≤1 μM) experiment (Supplementary Fig. 7) was the only instance in which succinate was used as the negative control, as it had been utilized in previous studies[53,108]. While succinate was also suitable as negative control (Supplementary Fig. 3), it produced slightly higher non-specific fluorescence response than glucose; thus, glucose, unless otherwise noted, was utilized as the negative control for all other experiments.

2.4.7 Growth curves.

Growth curves of *R. pomeroyi* strains Regular and Goofy in different carbon sources (Supplementary Fig. 3) were measured in a flat-bottom 96-well plate (Thermo Fisher Scientific), containing 200 μl of carbon source-amended MBM per well in the absence of antibiotics. Each carbon source was prepared in triplicates, with corresponding blank wells in duplicates. Each well was inoculated with 2 μl of bacteria, grown overnight in 1/2 YTSS amended with 25 μg ml^{-1} kanamycin, and washed and resuspended without dilution in non-carbon amended MBM. Optical density was measured at 700 nm (OD_{700}) to avoid spectral interference from fluorescence. The plate was incubated at 25 °C, and OD_{700} was measured every 1 h (3 min of fast orbital shaking before each time point) for 56 h using a Synergy HTX Multi-Mode Microplate Reader (BioTek Instruments).

2.4.8 Microfluidic device fabrication.

The microfluidic device containing 9 parallel observation chambers (Fig. 1c) was fabricated using soft lithography[109]. A mold for the observational chamber geometry was fabricated with SU8 on a silicon wafer. The microfluidic device was then created by casting polydimethylsiloxane (PDMS) (SYLGARD 184 Silicone Elastomer Kit; Dow Corning) onto the mold. The cured PDMS was then removed from the mold, perforated with inlet and outlet holes with a biopsy punch (1.5 mm diameter), and permanently fixed to a glass coverslip (60 mm × 24 mm; 0.17 ± 0.005 mm precision thickness; Carl Roth) by plasma bonding. Depth of each observation chamber was ~60 μm.

2.4.9 Microscopy.

All experiments were performed using an inverted epifluorescence TE2000 microscope (Nikon) controlled through Nikon Elements software (unless otherwise specified). A Spectra X LED light source (Lumencore) provided single wavelength excitation illumination for fluorescence imaging (100% LED power unless otherwise indicated). The Perfect Focus System (Nikon) was engaged to maintain focus in time-lapse experiments. Three filter cubes (Chroma) were used for fluorescence imaging: a custom filter cube optimized for mKate2 RFP (ET580/25x excitation filter, T600lpxr band-pass filter, and ET645/75m emission filter), Chroma 49003 for YFP, and Chroma 49013 for TFP. Unless otherwise indicated, the excitation filter of each cube was removed for imaging to maximize fluorescence signal captured. At each field of view, phase contrast and fluorescence images were captured sequentially in the following order: phase contrast, red fluorescence channel (575 nm excitation), yellow fluorescence channel (508 nm excitation), teal fluorescence channel (440 nm excitation). Bacteria were introduced into microfluidic devices, allowed to settle for 20–30 min, and imaged at the plane of the glass coverslip surface.

Images were acquired with an electron multiplying CCD (EMCCD) camera (iXon$_3$ 885; Andor Technology) (1004 × 1002 pixels; 8 μm pixel size) for the following experiments: time-lapse DMSP experiments in microfluidic chips; large-volume DMSP concentration measurement experiment (Supplementary Fig. 10); carbon sources test (Supplementary Fig. 3); DMSP uptake experiment (Supplementary Fig. 11); and phytoplankton co-incubation (Fig. 4 and Supplementary Fig. 12). For time-lapse DMSP experiments in microfluidic chips and the large-volume DMSP concentration measurement experiment, a 40× objective (CFI S Plan Fluor ELWD ADM 40X, correction collar adjusted to 0.17; Nikon) was used with electron multiplier gain at 3×, and the following exposure times: phase contrast (20 ms, 5% white LED power), red (100 ms), yellow (100 ms), and teal (200 ms). Imaging conditions for the carbon sources test were identical, except exposure time for teal fluorescence imaging was 100 ms. Time-lapse imaging for the DMSP uptake experiment was done in parallel with, but on a different microscope from, Raman microspectroscopy measurements (see below). Only phase contrast and teal fluorescence were acquired, with microscopy setup as described above. For phytoplankton co-incubation imaging, an oil-immersion 100× objective (CFI Plan Apo Lambda DM 100X Oil;

Nikon) was used, without electron multiplier gain, with the following exposure times (total 240 ms per image) and LED powers: phase contrast, 60 ms, 10%; red, 100 ms, 100%; yellow, 40 ms, 50%; and teal, 40 ms, 100%.

Finally, images for the low DMSP concentration (≤1 μM) experiment (Supplementary Fig. 7) were acquired with an sCMOS camera (Zyla 4.2; Andor Technology) (2048 × 2048 pixels; 6.5 μm pixel size). A 40× objective (described above) was used, with the following camera exposure times: phase contrast, 9.8 ms, 10% white LED power; and all fluorescence channels, 200 ms.

2.4.10 Image analysis.

Analysis of fluorescence images was performed in MATLAB (MathWorks) using an automated image segmentation and fluorescence quantification software developed in-house. Detailed descriptions of image processing and analysis methodologies for microfluidic and agarose pad co-incubation experiments are provided in Supplementary Notes 1 and 3, respectively. Briefly, cells were segmented by pixel intensity thresholding in phase contrast images. Background subtraction and spectral leakage correction were performed to enable accurate quantification of cellular fluorescence. Thresholding on YFP fluorescence intensity (proxy for metabolic activity) was applied to only include viable cells for further analyses. Finally, fluorescence signals in red and teal channels of each cell were normalized by the mean YFP signal at each time point of each experimental condition.

2.4.11 DMSP pathway expression time-lapse experiment.

Each replicate experiment represents a biological replicate performed on a single microfluidic device containing nine observation chambers (Fig. 1c). For each replicate experiment, one of the two *R. pomeroyi* reporter strains (Regular or Goofy) was prepared for experimentation as described above. At the end of subculture incubation, cells were washed and concentrated by 4.5× in non-carbon amended MBM amended with kanamycin (10 μg ml^{-1}), and distributed into 9 separate microcentrifuge tubes (Eppendorf) representing each treatment condition. For each tested concentration of glucose or DMSP, a 10× concentrated stock solution was prepared in non-carbon amended MBM amended with kanamycin (10 μg ml^{-1}). To initiate incubation, 10× stock solutions were diluted to 1× final concentration in the cell-containing MBM, resulting in a

4.05× cumulative concentration of subcultured cells. Each observation chamber was populated with 12.5 µl of treated cells. Inlet and outlet holes of observation chambers were sealed with clear tape to minimize evaporation. Since PDMS is a gas-permeable material, oxygen is not expected to be limited in our experimental setup. Cells in observation chambers were allowed to settle onto the glass coverslip surface with gravity for 20–30 min before initiation of image capture. Phase contrast and fluorescence images were captured at 7 positions, determined manually before start of imaging, per observation chamber every 45 min for ~24 h. Replicate experiment 3 of strain Regular (Supplementary Figs. 4, 6, 15) contained 6 imaging positions (instead of 7) per observation chamber. All fluorescence kinetic experiments, except the low DMSP concentration (≤1 µM) experiment, were conducted at room temperature (21 °C) and in the dark. In the low DMSP concentration (≤1 µM) experiment only (Supplementary Fig. 7), 1 mM succinate was used as negative control, all experimental conditions contained 50 µg ml^{-1} kanamycin, and fluorescence was monitored by microscopy with image acquisition every 30 min for 7.4 h with a cage incubator set to 30 °C.

2.4.12 Cultivation of phytoplankton.

The dinoflagellate Breviolum (strain CCMP2459, formally within genus Symbiodinium[110]) was chosen for its prolific production of DMSP. Breviolum cells were grown in sterile plastic culture flasks (Nunclon EasyFlasks, 25 cm^3 volume; Thermo Fisher Scientific) under a diel light cycle (14 h light:10 h dark, (100 µmol m^{-2} s^{-1})) in 30 ml f/2 medium at 22 °C. Cells at 22 days post-inoculation (a 1:100 dilution into fresh medium) were harvested for experimentation at 14:00 in the afternoon. Cellular concentration was determined by counting in a microfluidic observation chamber (21 cells $µl^{-1}$).

2.4.13 Phytoplankton-bacteria co-incubation experiment.

Co-incubations between *Breviolum* cells and *R. pomeroyi* reporter strains Regular or Goofy were performed on agarose pads, which immobilized the algal cells and allowed them to establish their phycospheres (i.e., the immediate regions surrounding unicellular algae cells) through steady exudation. For agarose pad preparation, low melting temperature agarose (Promega) was combined with 1/2 YTSS medium at 15 mg ml^{-1}, and gently dissolved in a microwave. After partial cooling, kanamycin was added at 25 µg ml^{-1} final concentration. Rubber gaskets (0.5 mm

thickness) were manually cut into square frames (~2 cm × 2 cm inner square area) and placed on glass coverslips (22 mm × 50 mm; VWR). The inner square areas of rubber gaskets were filled with ~500 µl melted agarose-kanamycin mixture. Agarose pads were allowed to cool and solidify for 1.5 hours before seeding with *R. pomeroyi* strains.

Bacteria were first seeded onto agarose pads and allowed to grow for 24 h without phytoplankton. Overnight cultures of *R. pomeroyi* strains grown in 1/2 YTSS were washed and concentrated three-fold in non-carbon amended MBM amended with 10 µg ml^{-1} kanamycin. 10 µl of this concentrated cell mixture was spotted onto the center of each agarose pad, and loosely covered with a plastic lid (without contacting the agarose) to minimize evaporation. *R. pomeroyi* strains were allowed to grow in patches of monolayer cells on the agarose pads for 24 h at 30 °C in the light before *Breviolum* cells were added to initiate co-incubation.

In preparation for co-incubation with bacteria, *Breviolum* cells were washed and concentrated 20-fold in fresh f/2 medium amended with 10 µg ml^{-1} kanamycin. Prepared *Breviolum* cells (10 µl) were spotted onto the middle of each agarose pad containing monolayer growth of *R. pomeroyi*. Co-incubation agarose pads were incubated at room temperature (21 °C) in the dark, loosely covered with a plastic lid without contacting the agarose, for 24 h before imaging. Prior to imaging, a glass coverslip (60 mm × 24 mm; 0.17 ± 0.005 mm precision thickness; Carl Roth) was placed onto the agarose pads carefully to avoid agitation of established phycospheres, and flipped onto the oil immersion objective for imaging. Only one time point (24 h) was taken for microscopy, to avoid microscopy light-induced cell stress that could alter the phycosphere profile.

To calculate the spectral leakage correction matrix ($B_{agarose}$; Supplementary Note 1), different colors of single-color constitutive control strains of *R. pomeroyi* (Supplementary Fig. 1) were grown on separate agarose pads for 24 h without phytoplankton, and imaged as described above.

2.4.14 Large-volume DMSP concentration measurement experiment.

To estimate the DMSP concentration evolution in microfluidic observation chambers over time, a large-volume (8 ml) experiment was performed to allow sampling for DMSP concentration

measurements (Supplementary Fig. 10). The experiment, while larger in volume by ~800-times compared to microfluidic experiments, preserved cell-to-volume ratio at all steps in the protocol. Three representative initial concentrations of DMSP were chosen, each of which was incubated in triplicates: 1 µM, 75 µM, and 1 mM.

R. pomeroyi (strain Regular) was grown and prepared as described above, with modifications as described below. Three biological replicates (i.e., three different colonies as inocula) of overnight cultures were prepared in 2.5 ml of 1/2 YTSS rich medium per replicate. Overnight culture cells were washed and concentrated ten-fold in non-carbon amended MBM. For each biological replicate, 153 µl of concentrated overnight culture was used to inoculate subculture flasks containing 115 ml of 10 mM glucose MBM amended with 25 µg ml^{-1} kanamycin. This led to a cumulative dilution factor of 1/75 (vol/vol) of overnight culture for subculture preparation, consistent with microfluidic experiments. Subcultures were incubated in the dark at 30 °C on an orbital shaker (200 rpm) for 4 h, at the end of which OD_{700} was measured to be 0.02–0.04. A volume of 110 ml of subcultured cells per biological replicate was washed and concentrated five-fold in non-carbon amended MBM. 7.2 ml of this concentrated cells was allocated into each treatment flask of each biological replicate (150-ml glass Erlenmeyer flasks). The addition of 800 µL concentrated DMSP solution stocks (10× concentration, i.e., 10 µM, 750 µM, and 10 mM) and kanamycin (final concentration = 10 µg ml^{-1}) marked the initiation of incubation, with a starting volume of 8 ml. Final cumulative concentration from subcultured cells was 4.5× (nearly consistent with microfluidic experiments). One replicate of blank control flasks (i.e., without cells) representing each DMSP concentration condition was also prepared. All experimental flasks were sealed and incubated in the dark at room temperature (21.4–22.8 °C) and in the absence of agitation.

At each sampling time point, incubation flasks were swirled to resuspend sunken cells. From each flask, a 1.5-ml sample was taken for DMSP concentration measurement, and an additional 10-µl sample was placed in a microfluidic observation chamber for microscopy observation (imaged as described above). The first time point (0 h) was taken from the blank control flasks, for measurement of initial DMSP concentration. Subsequent time points, at which samples were

taken from blank control flasks as well as from all replicate experimental conditions, were approximately 2, 8, and 24 h after the start of incubation with DMSP.

Each sample was immediately centrifuged at 2500 × *g* for 3 min to remove cells from solution. 1 ml of the supernatant was placed in an acid-washed 5-ml glass scintillation vial containing 3 ml methanol (>99.9%, HPLC gradient grade; VWR International). Sample vials were sealed and stored in the dark at 4 °C until DMSP concentration measurement using ultra-high-pressure liquid chromatography/high-resolution mass spectrometry (UHPLC/HRMS).

2.4.15 Ultra-high-pressure liquid chromatography/high-resolution mass spectrometry (UHPLC/HRMS).

To prepare samples for DMSP concentration measurements, 50 µl of each sample (processed and stored as described above) was diluted with 100 µl of a mixture of acetonitrile and water (9:1 v/v), centrifuged (4500 × *g*, 5 min), and the supernatant was used for UHPLC/HRMS measurements. All UHPLC/HRMS results were obtained on a Dionex Ultimate 3000 system (Thermo Scientific) coupled to a Q Exactive Plus Orbitrap mass spectrometer (Thermo Scientific).

UHPLC/HRMS quantification followed a previously reported protocol[108]: the eluent consisted of high-purity water with 2% acetonitrile and 0.1% formic acid (solvent A) and 90% acetonitrile with 10% 5 mmol l^{-1} aqueous ammonium acetate (solvent B). The flow rate was set to 0.60 ml min^{-1}. A linear gradient was used for separation with 100% solvent B (1 min), 20% B (6.5 min), 100% B (7.1 min) and 100% B (10 min). The LC separation column (SeQuant ZIC-HILIC column (5 mm, 2.1 × 150 mm) equipped with a SeQuant ZIC-HILIC guard column (5 mm, 2.1 × 20 mm)) was kept at 25 °C. Electrospray ionization was performed in positive mode ionization, recording the mass range from 75 to 200 m/z, with the following parameters: capillary temperature 380 °C; spray voltage 3,000 V; sheath gas flow 60 arbitrary units; and aux gas flow 20 arbitrary units. The injection volume was 2 µl.

Calibration curves for DMSP were recorded in triplicate using synthetic standards prepared as described in a previous study[108]. Calibration curve for DMSP: area [DMSP] = 470,540*c* [DMSP

in nM] with $r = 0.9999$. Data analyses were performed using the software Thermo Xcalibur version 3.0.63.

2.4.16 Pre-exposure to sulfur experiment with Raman microspectroscopy.

Raman microspectroscopy was utilized to infer uptake of DMSP at the single-cell level by measuring the deuterium-labelling status of cells incubated with deuterated DMSP ([$^2H_6$]-DMSP), in which the two CH_3 groups of the DMSP molecule were labeled with deuterium in a protocol previously reported[111] (Supplementary Fig. 11). Three incubation conditions were tested to probe the effect of sulfur satiation (due to pre-exposure of *R. pomeroyi* to 10 mM methionine) on DMSP uptake and cleavage pathway expression: [$^2H_6$]-DMSP without pre-exposure to methionine; [$^2H_6$]-DMSP with pre-exposure to methionine; and non-labeled DMSP without pre-exposure to methionine (negative control for Raman microspectroscopy signal).

The P_{dddW}::mTFP1 single-color *R. pomeroyi* reporter strain (cleavage pathway promoter-fusion with TFP) was used to avoid spectral interference with Raman microspectroscopy measurements (see below). An overnight culture in rich medium was prepared as described above. Two subculture conditions, with or without 10 mM L-methionine (Sigma-Aldrich), were prepared in 10 mM glucose MBM amended with 25 μg ml^{-1} kanamycin, and incubated for 4 h as described above. Subcultured cells were washed, concentrated three-fold, and resuspended in the appropriate solution for incubation: 1 mM [$^2H_6$]-DMSP MBM or 1 mM unlabeled DMSP MBM. All incubation conditions contained final concentrations of 1% methanol (solvent in which [$^2H_6$]-DMSP was dissolved) and 10 μg ml^{-1} kanamycin. Treated cells were incubated at room temperature (22.8 °C) in the dark for 5.5 hours before imaging and Raman microspectroscopy measurements.

We utilized a commercial confocal Raman microspectroscope (LabRAM HR Evolution; HORIBA Scientific) based on an inverted microscope (Eclipse Ti; Nikon) with two cameras: an sCMOS camera (ORCA-Flash 4.0; Hamamatsu Photonics; field of view of 221.867 μm × 221.867 μm; camera #1) for fluorescence and brightfield measurements with high sensitivity; and a CMOS camera (UI-3580LE; IDS Imaging Development Systems GmbH; camera #2) for positioning the Raman laser (532-nm neodymium-doped yttrium garnet—Nd:YAG) onto each

cell. After incubation of cells with deuterated or non-deuterated DMSP as described above, a 4 µl-droplet of cells was placed on a CaF_2 coverslip (25 mm × 15 mm × 0.2 mm; Crystran) which was chosen to avoid background Raman signal noise[112]. A thin liquid column containing cells was achieved by separating the bottom (CaF_2) and top (glass, 18 mm × 18 mm, no. 1 thickness) coverslips with 0.17 mm-thick glass coverslips placed along two opposing edges of the setup. As the Raman measurements took place at the surface of the CaF_2 coverslip (i.e., 170 µm away from glass), this arrangement generated sufficient thickness of liquid sample in the *z*-direction to prevent interference from the glass material of the top coverslip[113]. The coverslip setup was secured onto the microscope stage with the CaF_2 surface interfacing with the 60× water-immersion objective (Plan Apo IR 60XC 1.27 WI; Nikon), and was left undisturbed for 10 min to allow cells to settle to the bottom surface with gravity.

To measure the expression of the cleavage pathway, a fluorescence image in the teal channel (filter cube Chroma 49013 with excitation (445/30 nm) and emission (500/40 nm) filters installed to minimize interference with the Raman measurements performed with the 532 nm laser) was first acquired with camera #1 (50 ms exposure). A matching brightfield image (2 ms exposure, white LED light source) was also captured to visualize all cells. After fluorescence and brightfield image capture, the system was shifted to the Raman configuration (i.e., Raman laser and camera #2).

Single-cell Raman measurements were performed (1.5-s exposure time; 150-µm pinhole size) by manually moving the *xy*-stage to align the Raman laser (532 nm, 400 mW power), as well as to focus it (confirmed via inspection with camera #2), onto each cell. For each experimental condition sample, Raman measurements of as many cells as possible were taken within 30 min (n = 32–52 cells per treatment condition). Each cell's Raman measurement and fluorescence signal were retrospectively matched using the brightfield image as the reference.

To determine the presence of DMSP uptake by cells, the DMSP uptake index (P_{DMSP}) was computed for each cell:

$$P_{DMSP} = \frac{I_{2040-2300}}{I_{2400-2450}}$$

where $I_{2040\text{-}2300}$ (numerator) and $I_{2400\text{-}2450}$ (denominator) represent the integrated intensities in the Raman spectrum regions between the wavenumbers 2040 and 2300 cm^{-1} (the C–D peak whose intensity is affected by deuterium[114]) and between 2400 and 2450 cm^{-1} (reference region where background intensity was low), respectively.

2.5 Figures

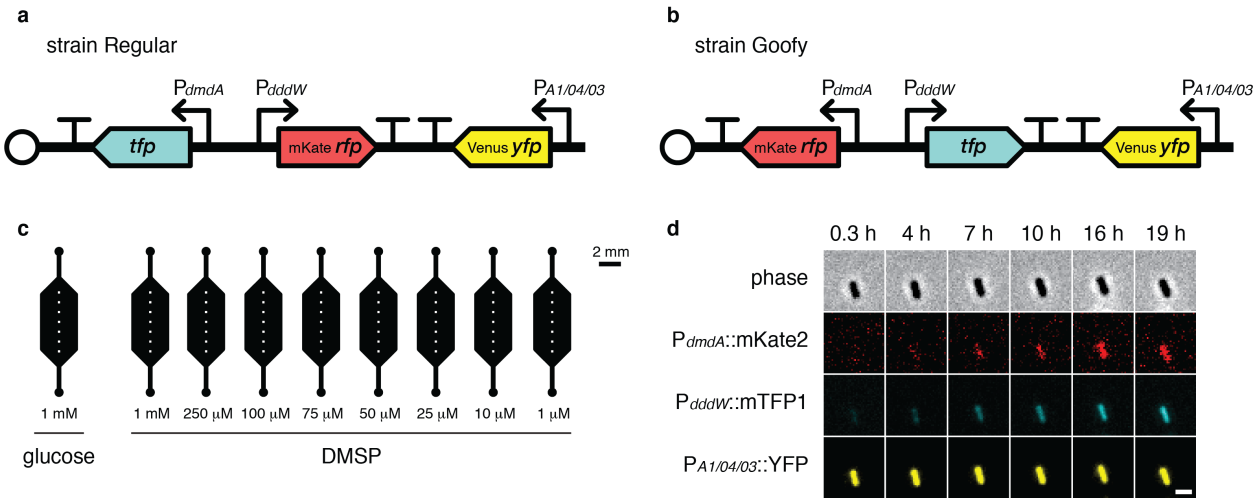

Figure 2.1 | Single-cell measurements of DMSP degradation pathway expression. a,**b**, Plasmids transformed into *R. pomeroyi* DSS-3 contain three components: *dmdA* reporter (222 bp promoter region); *dddW* reporter (500 bp promoter region); and constitutive *yfp* expression (strong, synthetic promoter $P_{A1/04/03}$). YFP signal was used as a proxy for plasmid copy number and metabolic activity. Transcriptional terminators (represented by T) were placed between promoter fusion cassettes to prevent transcriptional read-through. To control for spectral bias caused by fluorescent protein choice (RFP or TFP), we constructed two *R. pomeroyi* reporter strains—Regular (**a**) and Goofy (**b**)—in which the colors of fluorescent proteins fused to *dmdA* and *dddW* promoter regions were interchanged. Vector backbone: pBBR1MCS-2 with origin of replication pBBR1 (open circles). **c**, Schematic of a single microfluidic device used for time-lapse DMSP experiments. Each time-lapse DMSP experiment used one microfluidic device containing nine observation chambers for parallel incubation of a single reporter strain (Regular or Goofy; **a**,**b**) with different concentrations of DMSP. Glucose was used as negative control. White squares in each observation chamber represent the seven fields of view (200 µm × 200 µm) imaged at each time point. **d**, Representative phase contrast and fluorescence images of a single cell (strain Goofy) over time in the presence of 1 mM DMSP. Scale bar, 2 µm.

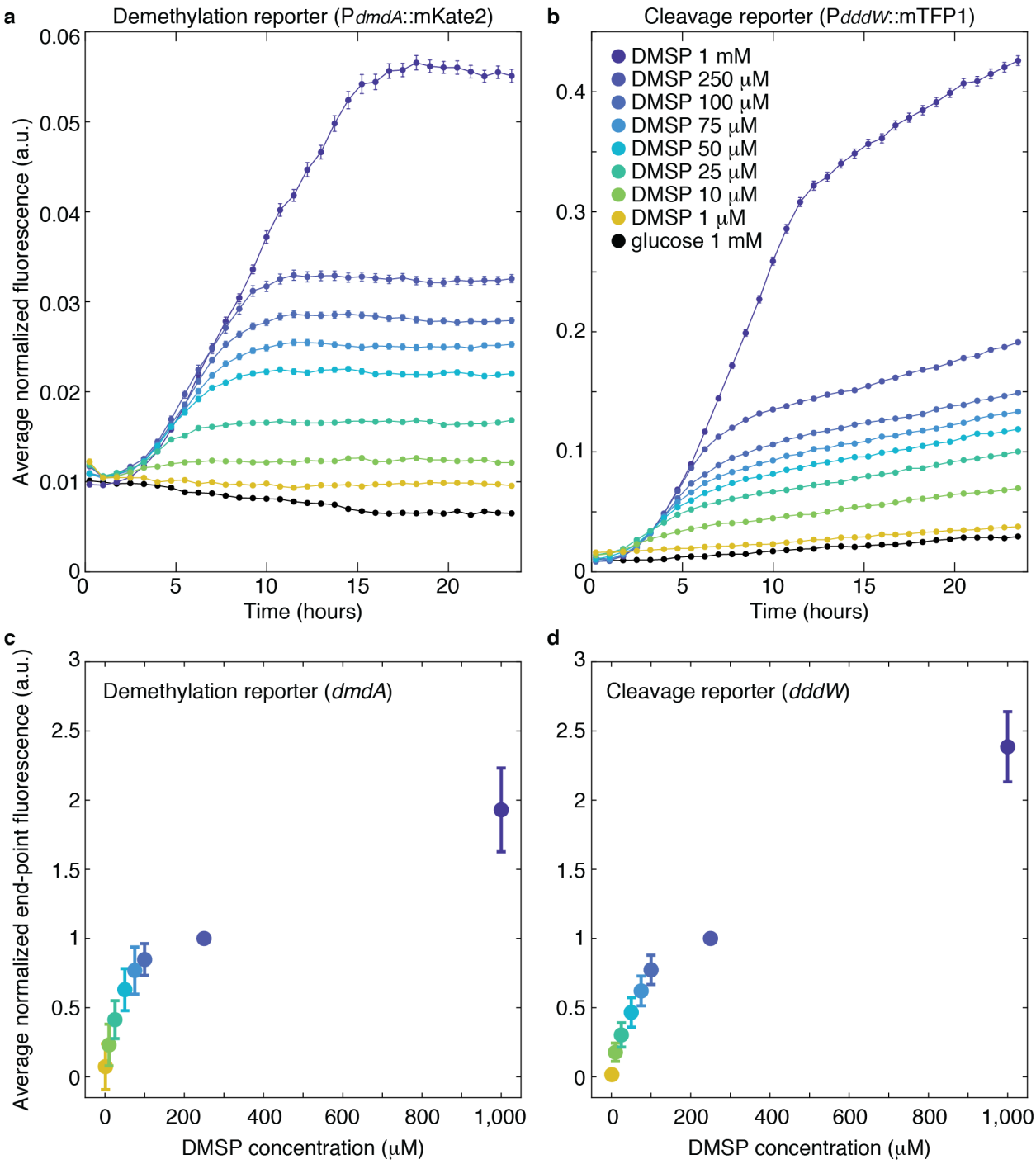
a
Demethylation reporter (P*dmdA*::mKate2)
Average normalized fluorescence (a.u.)
Time (hours)
b
Cleavage reporter (P*dddW*::mTFP1)
DMSP 1 mM
DMSP 250 μM
DMSP 100 μM
DMSP 75 μM
DMSP 50 μM
DMSP 25 μM
DMSP 10 μM
DMSP 1 μM
glucose 1 mM
Time (hours)
c
Demethylation reporter (*dmdA*)
Average normalized end-point fluorescence (a.u.)
DMSP concentration (μM)
d
Cleavage reporter (*dddW*)
DMSP concentration (μM)

Figure 2.2 | DMSP concentration-dependent upregulation of *dmdA* and *dddW*. a,**b**, Mean fluorescence signals of *dmdA* (**a**) and *dddW* (**b**) reporters in response to different concentrations of DMSP. One representative replicate experiment of reporter strain Goofy is shown (data from additional replicate experiments (n = 3 for each reporter strain) are shown in Supplementary Fig. 6). Spectral leakage correction, background subtraction, and a threshold on YFP intensity were applied (see Methods and Supplementary Note 1). RFP and TFP signals of each cell were normalized by the mean YFP signal at each time point of each experimental condition. Data points and error bars represent means ± s.e.m. of cells (error bars may be smaller than markers). **c**,**d**, Average end-point fluorescence levels of *dmdA* (**c**) and *dddW* (**d**) reporters. For each replicate experiment, baseline signal (glucose) was subtracted at each time point, fluorescence signals over the final five time points (~20.4–24 h) were averaged, then normalized by the corresponding end-point fluorescence signal at 250 μM DMSP. Data points and error bars represent means ± s.d. of six total replicates (n = 3 for strain Regular and n = 3 for strain Goofy combined).

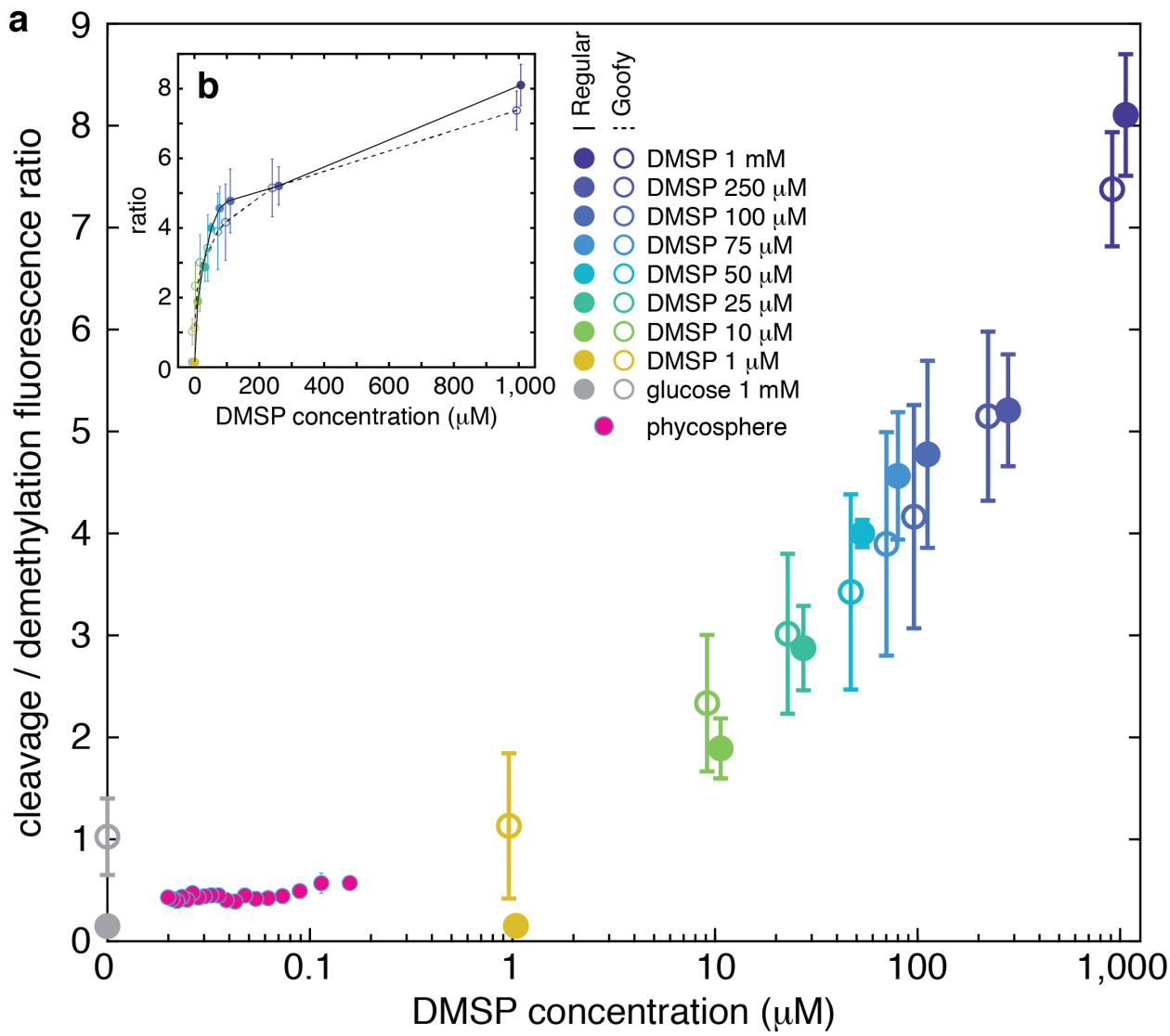
a
b
cleavage / demethylation fluorescence ratio
DMSP concentration (μM)
ratio
DMSP concentration (μM)
Regular
Goofy
DMSP 1 mM
DMSP 250 μM
DMSP 100 μM
DMSP 75 μM
DMSP 50 μM
DMSP 25 μM
DMSP 10 μM
DMSP 1 μM
glucose 1 mM
phycosphere

Figure 2.3 | DMSP concentration modulates relative expression of *dddW* and *dmdA*. a, Cleavage-to-demethylation pathway ratio was calculated at each DMSP concentration for strains Regular (RFP/TFP) and Goofy (TFP/RFP). High variability of fluorescence output amongst replicate experiments at ≥10 μM DMSP prevented the comparison of pathway reporters within each color (Supplementary Fig. 5). Average fluorescence signals at time points at which *dmdA* expression is mid-exponential for each DMSP concentration (shown in Supplementary Fig. 6), or at the second time point for glucose and 1 μM DMSP conditions, were used for ratio calculation. Close agreement between strains Regular and Goofy at ≥10 μM DMSP suggests that fluorescence ratios are close to true pathway expression ratios. The deviation between strains Regular and Goofy of ratios in glucose and 1 μM DMSP may be due to low fluorescence signals; importantly, ratios calculated within-color (0.3–0.5; Supplementary Fig. 5) and across-color (0.15–1.0; Fig. 3) in glucose showed consistent results (similar values at 1 μM DMSP). Pathway ratios from the phycosphere experiment (also shown in Fig. 4f) were calculated using TFP signals of reporter strains (reporting either *dmdA* or *dddW* expression in strains Regular or Goofy, respectively) normalized by constitutive YFP signals, and were plotted against modeled phycosphere DMSP concentrations (Supplementary Fig. 13). Data points and error bars of DMSP concentration experiments are slightly offset in the x-direction for presentation clarity, and represent means ± s.d. of replicate experiments (n = 3 for strain Regular; n = 3 for strain Goofy). Error bars of the phycosphere experiment represent the variance of the ratio of normalized cleavage and demethylation fluorescence signals (Supplementary Note 3). Error bars may be smaller than markers. **b**, Inset represents the same data as **a**, plotted on a linear scale on the x-axis to show the saturating relationship between DMSP concentration and cleavage-to-demethylation ratio.

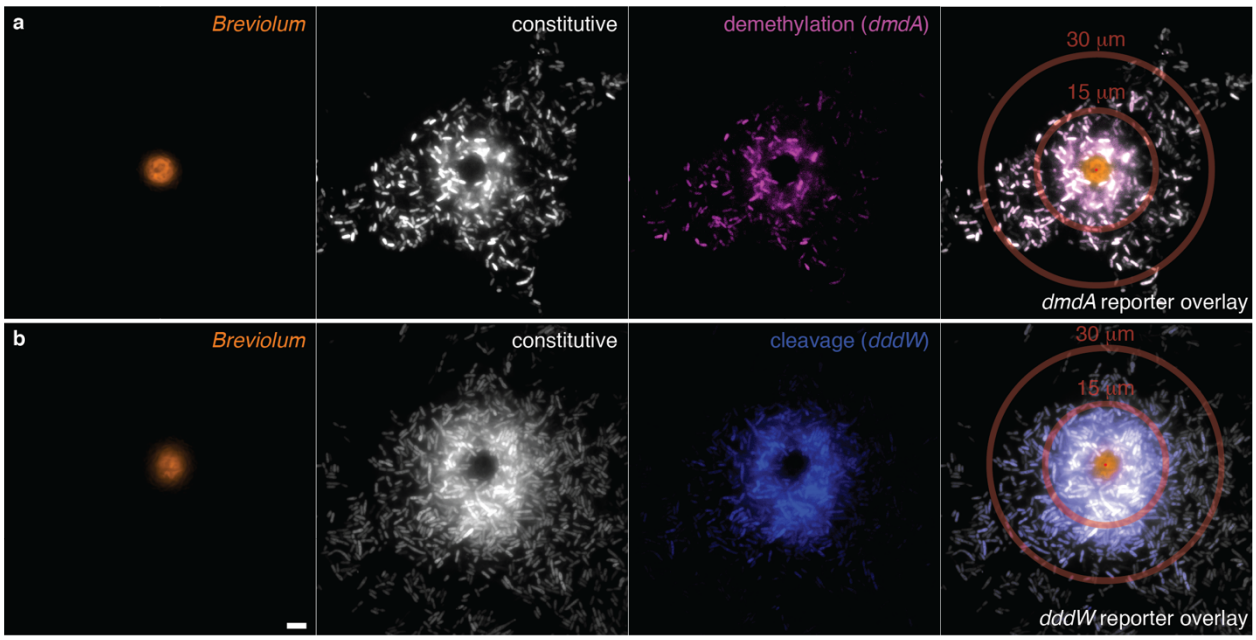
a
Breviolum
constitutive
demethylation (dmdA)
30 μm
15 μm
dmdA reporter overlay
b
Breviolum
constitutive
cleavage (dddW)
30 μm
15 μm
dddW reporter overlay

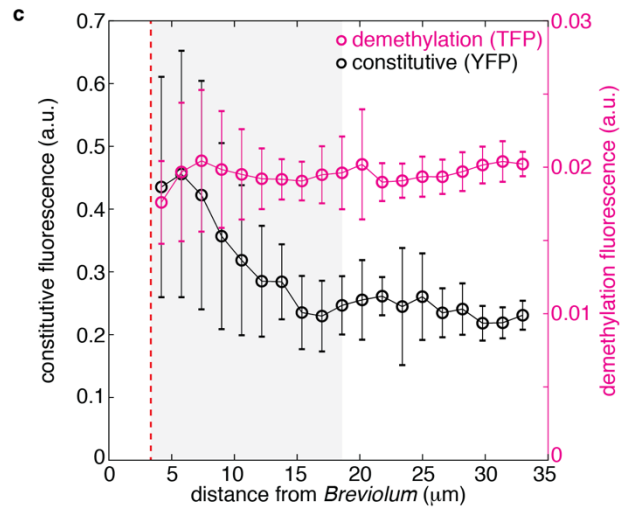
c
demethylation (TFP)
constitutive (YFP)
constitutive fluorescence (a.u.)
demethylation fluorescence (a.u.)
distance from Breviolum (μm)

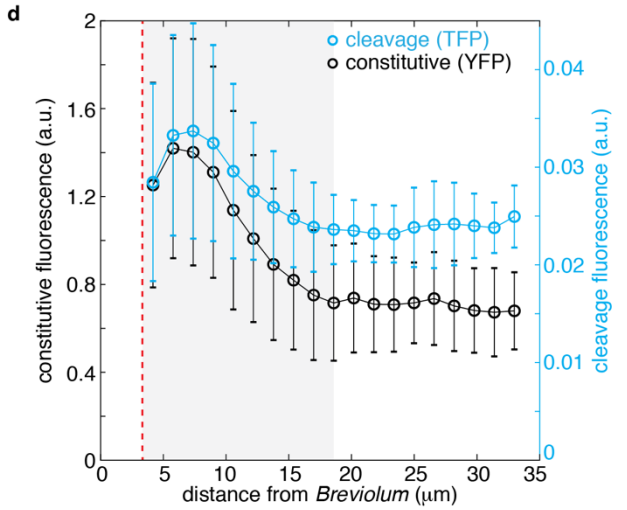
d
cleavage (TFP)
constitutive (YFP)
constitutive fluorescence (a.u.)
cleavage fluorescence (a.u.)
distance from Breviolum (μm)

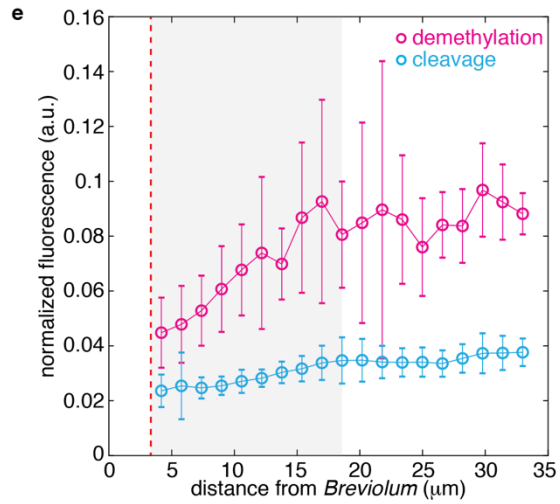
e
demethylation
cleavage
normalized fluorescence (a.u.)
distance from Breviolum (μm)

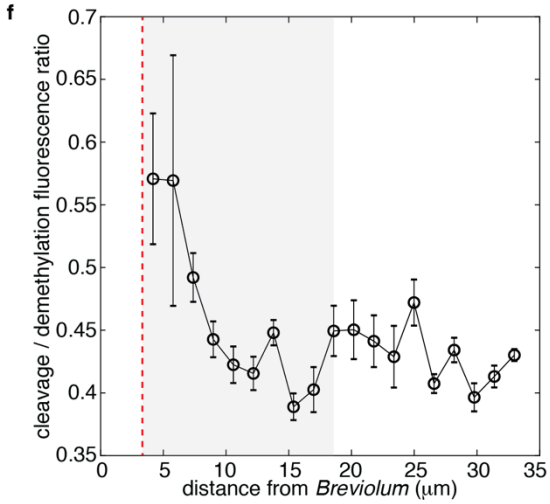
f
cleavage / demethylation fluorescence ratio
distance from Breviolum (μm)

Figure 2.4 | Gene expression patterns in a natural DMSP hotspot. a,**b**, Representative images of co-incubation between DMSP-producing microalgae, *Breviolum* CCMP2459 (photosynthetic pigment, orange), and engineered bacteria, *R. pomeroyi*, constitutively expressing YFP (white) and fluorescently reporting *dmdA* (**a**, demethylation, strain Regular-TFP, magenta) or *dddW* (**b**, cleavage, strain Goofy-TFP, blue) expression. Fluorescence signals are false-colored. Representative concentric rings (widths, 20 pixels = 1.6 μm) that bin distances from the center (red dots) of *Breviolum* cells for fluorescence quantification are shown at 15 and 30 μm. Scale bar, 5 μm. **c**,**d**, Quantification of YFP (constitutive) and TFP (*dmdA* (**c**), or *dddW* (**d**)) fluorescence at each distance (*r*) from the center of *Breviolum* cells (mean radius = 3.3 μm, red dotted line; *n* = 33). Fluorescence upregulation of YFP (**c**,**d**) and TFP (*dddW*; **d**) were detectable up to *r* = 18.6 μm (gray shading), at which modeled DMSP concentration was 35 nM (Supplementary Fig. 13). YFP of the cleavage pathway reporter (**b**,**d**) was brighter than that of the demethylation pathway reporter (**a**,**c**), probably due to differences in metabolic activity levels in each bacterial culture. Bacteria nearest to the surface of the phytoplankton (*r* = 4.2 μm, the first concentric ring) appeared dimmer than expected, possibly due to spectral interference from photosynthetic pigments. Data points and error bars represent mean ± s.d. of images (*n* = 15 *Breviolum* cells for *dmdA* (**c**); *n* = 18 for *dddW* (**d**)), calculated at each concentric ring (image analysis methods in Supplementary Note 3). **e**, TFP fluorescence of each cell-containing pixel normalized by the average YFP fluorescence of cell-containing pixels within the corresponding concentric circle to remove the effect of metabolic activity differences on fluorescence intensities. Direct comparisons between demethylation and cleavage after normalization revealed that demethylation expression was higher than cleavage expression at all distances from the phytoplankton. Data points and error bars represent mean ± s.d. of normalized fluorescence of images, calculated at each concentric ring. **f**, Average normalized TFP intensity (**e**) of strain Goofy (*dddW*, *n* = 18) divided by that of strain Regular (*dmdA*, *n* = 15) at each distance from the phytoplankton. Error bars represent the variance of the ratio of normalized cleavage and demethylation fluorescence signals (Supplementary Note 3).

2.6 Supplementary Figures and Tables

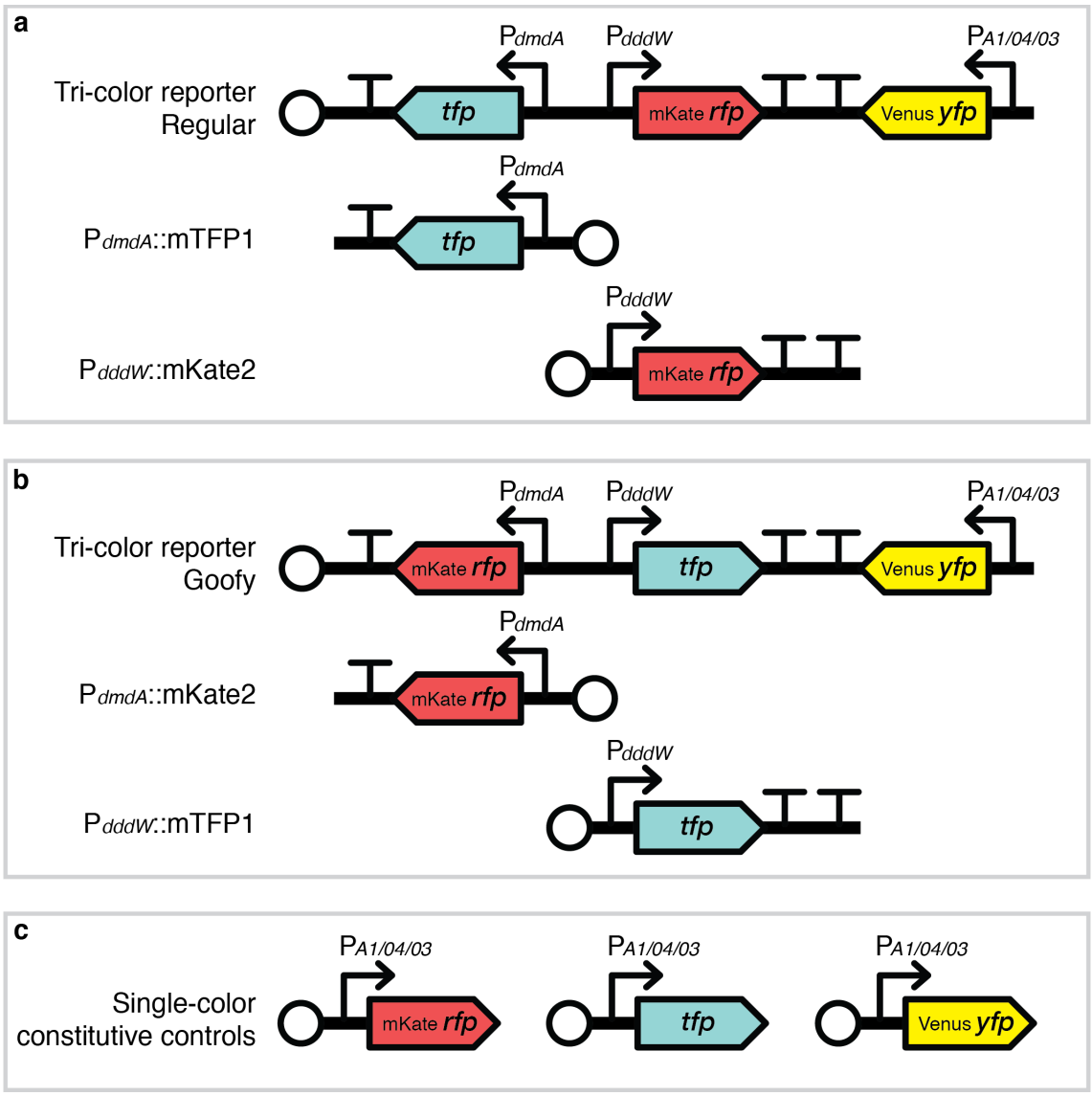

Supplementary Figure 2.1 | All engineered fluorescent *R. pomeroyi* DSS-3 strains used in this study. Two tricolor reporter strains, Regular (**a**) and Goofy (**b**), with interchanged colors of fluorescent proteins fused to *dmdA* and *dddW* promoter regions were built to control for spectral bias during fluorescence intensity quantification. Four single-color reporter strains, representing truncated versions Regular and Goofy, were built to verify that incorporating three promoter fusion cassettes within one DNA construct did not affect our conclusions (Supplementary Fig. 2): P_{dmdA}::mTFP1 and P_{dddW}::mKate2 (truncated Regular, **a**) and P_{dmdA}::mKate2 and P_{dddW}::mTFP1 (truncated Goofy, **b**). Finally, a spectral leakage correction matrix, *B* (Supplementary Note 1), was calculated using images of constitutively fluorescent single-color control strains (**c**). Vector backbone: pBBR1MCS-2 with origin of replication pBBR1 (open circles).

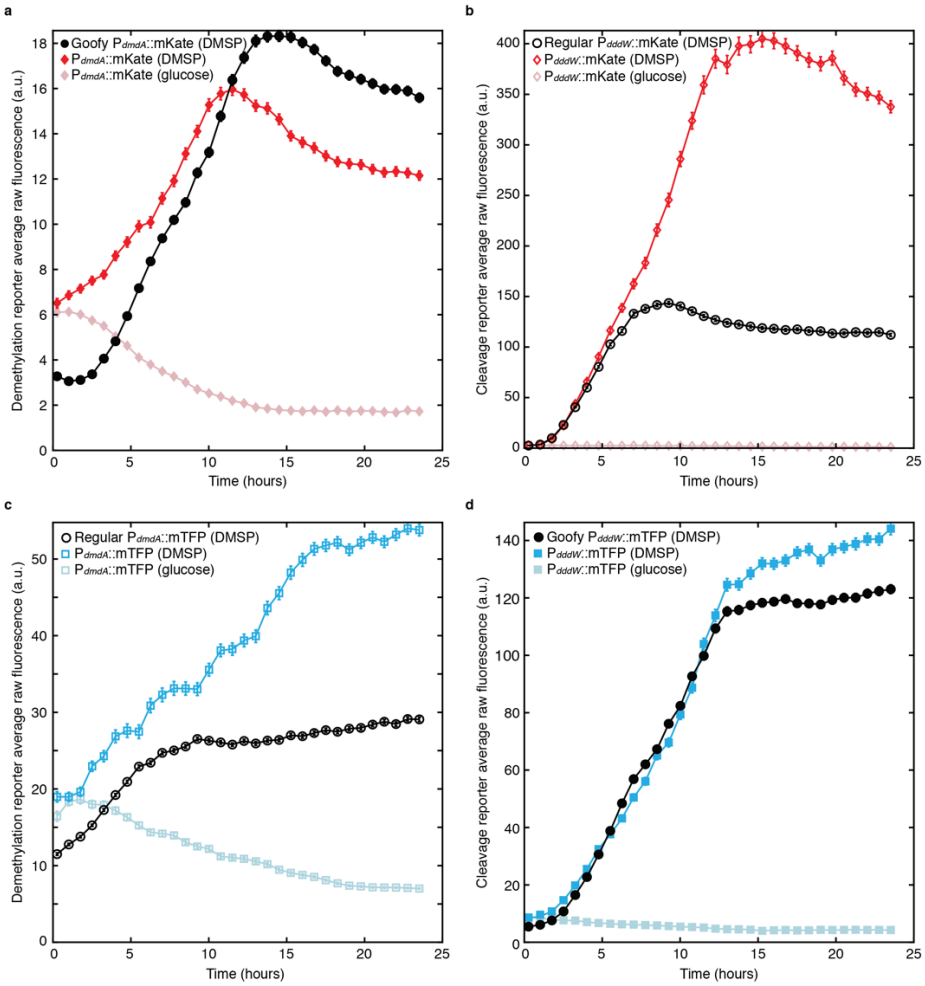

Supplementary Figure 2.2 | Tricolor and truncated single-color reporter strains yield similar fluorescence responses in the presence of DMSP. To confirm that the incorporation of three promoter fusion cassettes within one DNA construct (*i.e.*, in tricolor reporter strains Regular and Goofy) did not affect our overall conclusions, four single-color reporter strains, representing truncated versions of tricolor reporter strains Regular and Goofy, were incubated with DMSP or glucose (1 mM), and their fluorescence signals were recorded: P_{dmdA}::mKate2 (**a**); P_{dddW}::mKate2 (**b**); P_{dmdA}::mTFP1 (**c**); and P_{dddW}::mTFP1 (**d**). Tricolor reporters Goofy (**a,d**) and Regular (**b,c**) were also incubated with DMSP in the same experiment for comparison. Image segmentation and background subtraction were performed as described in Methods. For tricolor reporters only, spectral leakage correction and YFP thresholding (at 25 a.u.) were performed, but normalization by constitutive YFP was not (*i.e.*, raw fluorescence). While absolute magnitudes and slopes of fluorescence responses were not identical between tricolor and truncated single-color reporter strains (probably due to slight differences in physiological states in different bacterial cultures), and the choice of fluorescent protein led to slight differences in the temporal evolution of fluorescence signals, the general patterns of fluorescence kinetics were preserved (*i.e.*, initial lag, followed by linear increase that flattens after ~8–17 h; further discussion in Supplementary Note 2). These conserved behaviors validate the tricolor

reporters' design and accuracy of their fluorescence signals in reporting *dmdA* and *dddW* expression dynamics and relative expression levels. Data points and error bars represent mean ± s.e.m. of raw fluorescence intensities of cells.

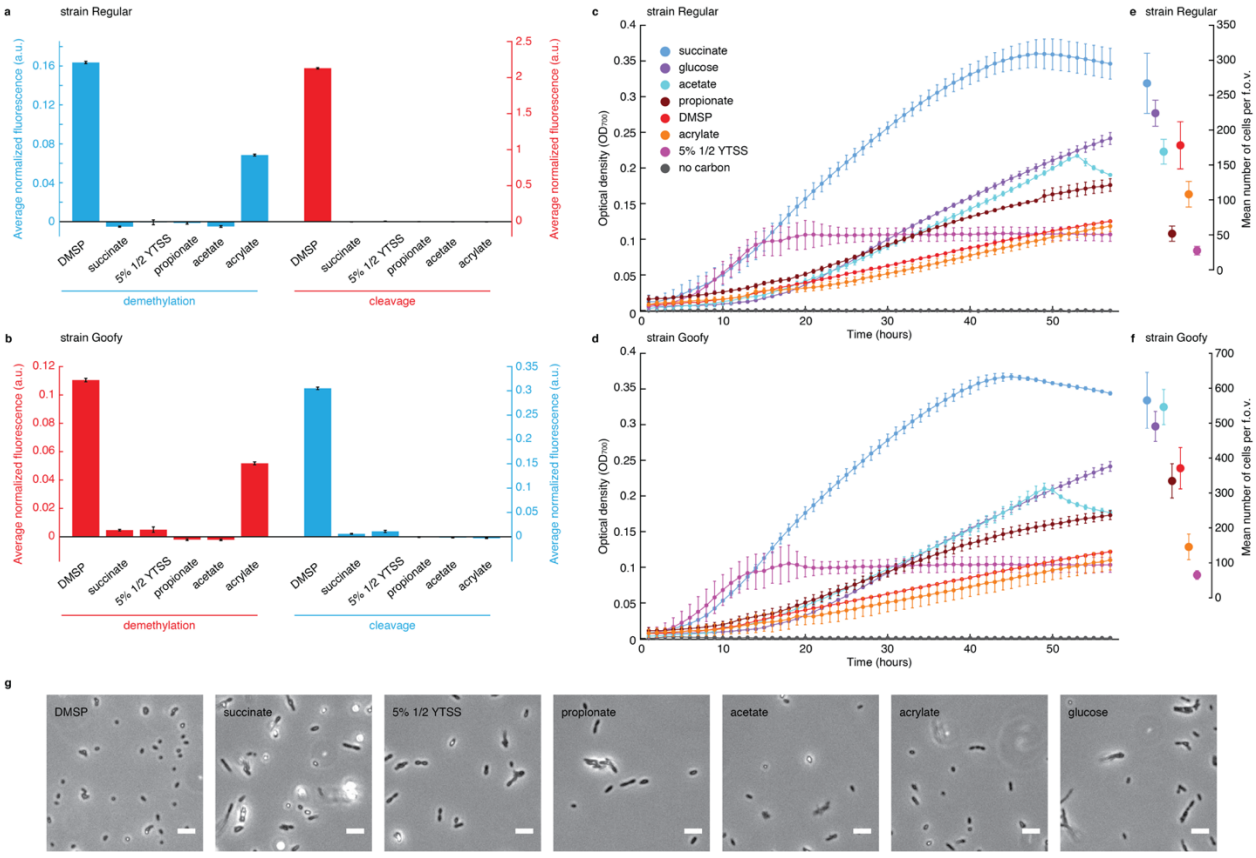

Supplementary Figure 2.3 | Fluorescence response and growth of engineered *R. pomeroyi* reporters in diverse carbon sources. **a** and **b** Mean fluorescence intensities of strains Regular (**a**) and Goofy (**b**) after incubation with DMSP; succinate; 5% rich media (1/2 YTSS); propionate; acetate; acrylate; or glucose provided as sole amended carbon sources for 18.5 h in the presence of antibiotic pressure (25 µM kanamycin; 30 °C; continuously shaken). All carbon sources were provided at 10 mM concentration except rich media (1/2 YTSS). YFP threshold of 10 a.u. was applied, and each cell's teal and red fluorescence were normalized by its own yellow fluorescence. After spectral leakage correction and background fluorescence subtraction, mean fluorescence values of glucose (used as negative controls in experiments) were subtracted from each cell's signals in corresponding color channels before calculation of mean; thus, some mean fluorescence values were negative. Bars and error bars represent mean ± s.e.m. of fluorescence signals of cells. **c** and **d** Growth curves of *R. pomeroyi* reporter strains incubated with different organic compounds as sole amended carbon sources in the absence of antibiotic pressure (25 °C). Data points and error bars represent mean ± s.d. of blank-subtracted triplicate wells. **e** and **f** Average number of YFP-positive cells per field of view (f.o.v.; 200 µm × 200 µm) in images acquired for fluorescence quantification (**a**,**b**). Example phase microscopy images are shown in **g** (strain Regular; scale bars, 5 µm). Relative growth yields according to optical density (**c**,**d**; OD_{700}) were consistent with cell counts (**e**,**f**) except in DMSP, due to their smaller cell size compared to bacteria grown in other carbon sources. Data points and error bars represent mean ± s.d. of cell number in a field of view.

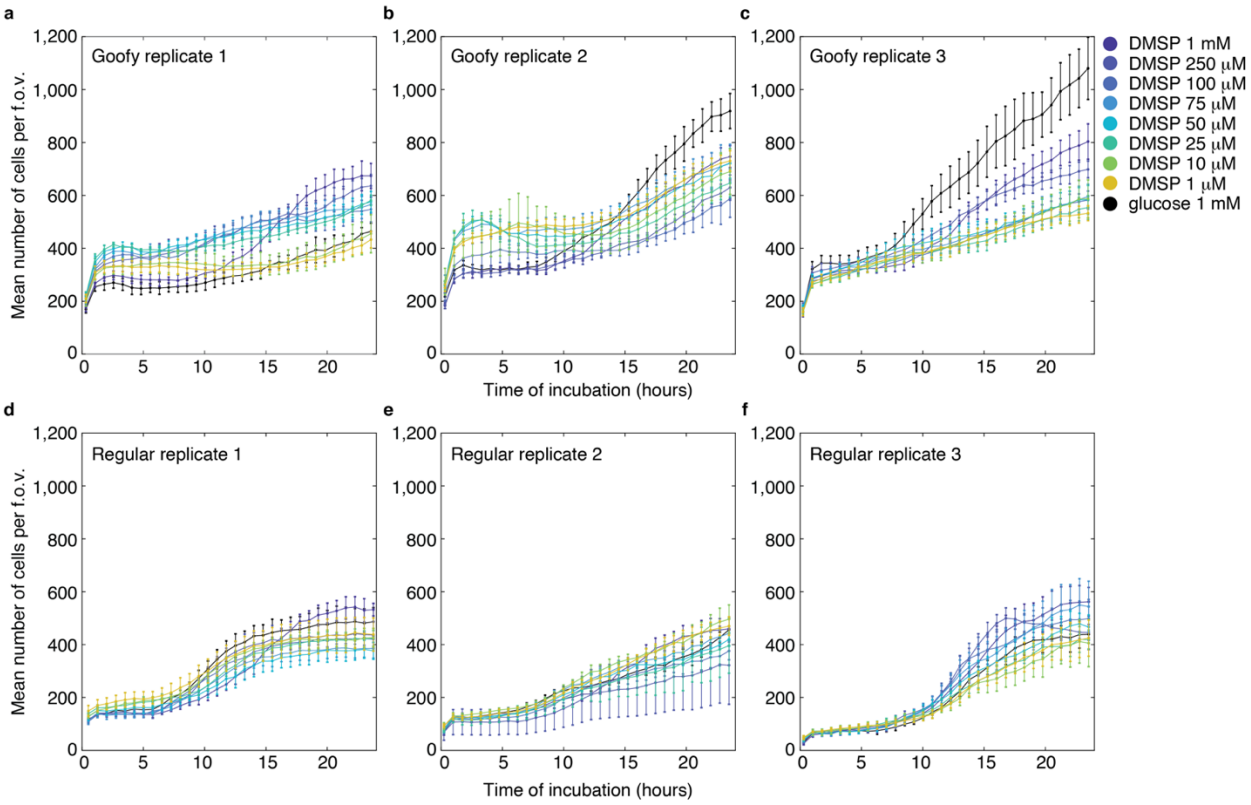

Supplementary Figure 2.4 | Number of cells in time-lapse DMSP experiments performed in microfluidic chips (all replicate experiments). Mean number of cells per field of view (f.o.v.; 200 µm × 200 µm) in time-lapse DMSP experiments. Images were acquired at seven different fields of view per observation chamber (Fig. 1c) except strain Regular replicate experiment 3 (**f**), in which six fields of view were taken. Only cells that passed the YFP intensity threshold were included in the analysis. The large increase in cell number between the first and second time points is likely attributed to cells settling into the field of view due to gravity. On average, the number of cells in a field of view at the second time point was 218 ± 120 (mean ± s.d.) across replicate experiments. Replicate experiments correspond to those presented in Supplementary Fig. 6. Data points and error bars represent mean ± s.d. across seven (or six for **f**) fields of view.

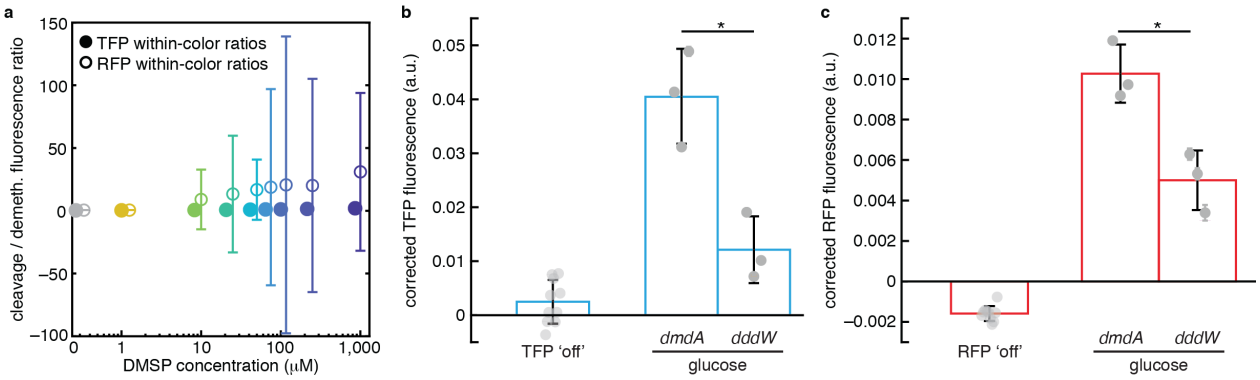

Supplementary Figure 2.5 | Within-color comparisons of demethylation (*dmdA*) and cleavage (*dddW*) pathway reporters. **a** Cleavage-to-demethylation fluorescence ratios were calculated within each color (TFP/TFP (●) or RFP/RFP (○)) similarly to Fig. 3. At ≥10 μM DMSP, the variability amongst replicate experiments resulted in large variance (error bars) for RFP within-color ratios (though not TFP, probably due to the relatively small signal values of TFP (Supplementary Fig. 6)). This result prevented within-color comparisons of pathway reporters except in glucose (**b**,**c**) and 1 μM DMSP (similar values). Thus, across-color ratio calculation, which enabled comparisons of pathway expression within the same experiment, was employed in our study for consistency (Fig. 3). Error bars represent the variance of the cleavage-to-demethylation ratio calculated using Eq. S6 (Supplementary Note 3; $n = 3$ for each reporter). **b** and **c** Average baseline fluorescence of demethylation and cleavage reporters incubated in glucose (cells aggregated over three time points, ~2.5–4h). In glucose, baseline demethylation expression was significantly higher than that of cleavage (two-tailed *t*-tests; * $p \leq 0.05$; ratios 0.3 in TFP, **b**; 0.5 in RFP, **c**). Importantly, this higher baseline demethylation expression was conserved in both within-color and across-color ratios (0.15–1.0; Fig. 3). Fluorescence signals in glucose were significantly higher than the theoretical 'off' intensities of TFP ($2.5 \pm 4.1 \times 10^{-3}$ a.u.) and RFP ($-1.6 \pm 0.37 \times 10^{-3}$ a.u.), indicating that *dmdA* and *dddW* are expressed at a baseline level even in the absence of DMSP (two-tailed *t*-tests, $p \leq 0.01$). Some theoretical 'off' intensities were slightly overcorrected to below zero due to background subtraction and spectral leakage correction (Supplementary Note 1). Each grey symbol represents a replicate experiment (symbols and error bars = mean ± s.e.m. of fluorescence signals of cells), and each bar represents the average of replicate experiments (bars and error bars = mean ± s.d. of replicate experiments, $n = 3$).

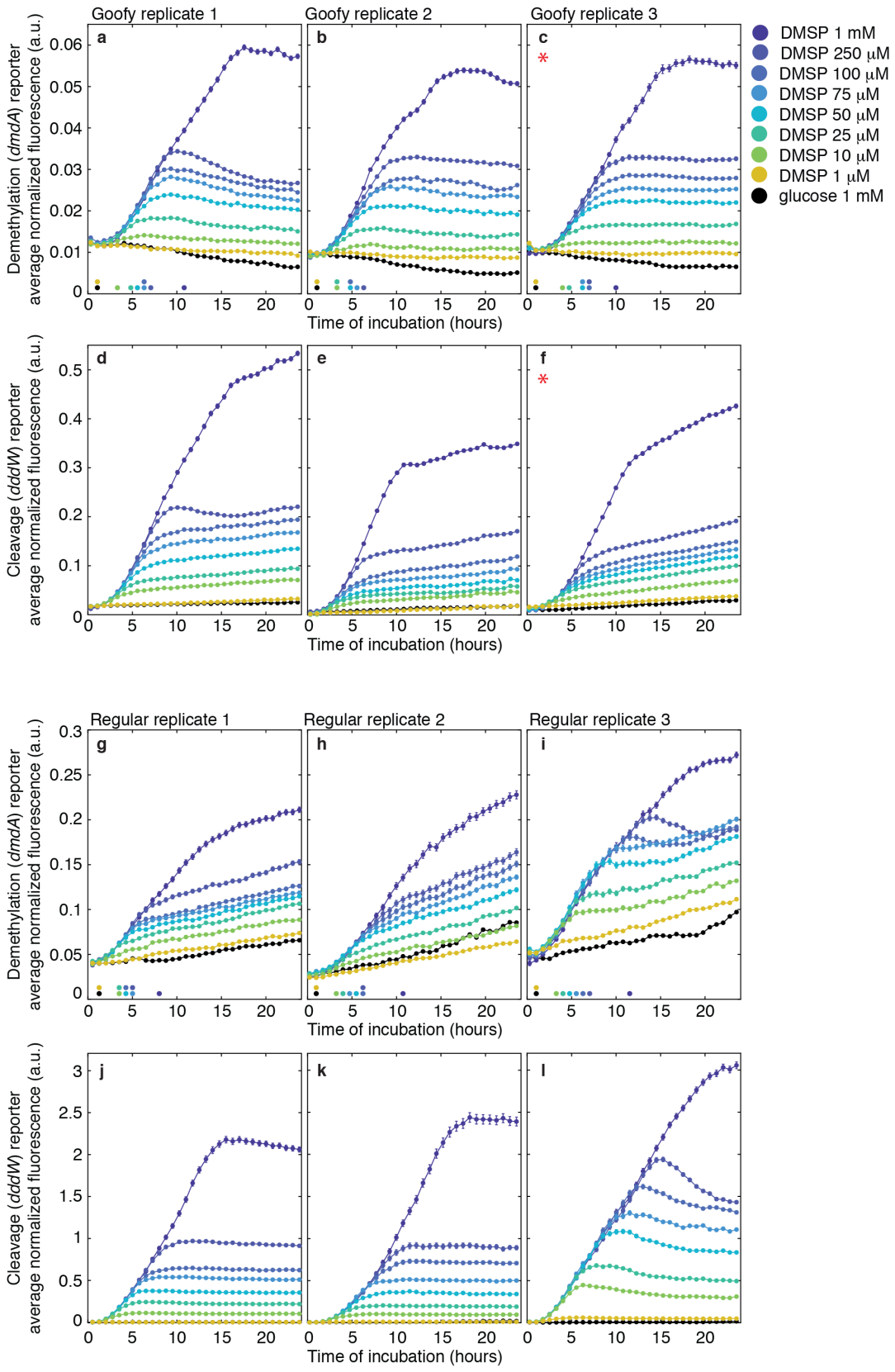
Goofy replicate 1
Goofy replicate 2
Goofy replicate 3
a
b
c
*
d
e
f
*
Demethylation (dmdA) reporter average normalized fluorescence (a.u.)
Cleavage (dddW) reporter average normalized fluorescence (a.u.)
Time of incubation (hours)
DMSP 1 mM
DMSP 250 μM
DMSP 100 μM
DMSP 75 μM
DMSP 50 μM
DMSP 25 μM
DMSP 10 μM
DMSP 1 μM
glucose 1 mM
Regular replicate 1
Regular replicate 2
Regular replicate 3
g
h
i
j
k
l

Supplementary Figure 2.6 | Demethylation and cleavage pathway expression measurements in time-lapse DMSP experiments performed in microfluidic chips (all replicate experiments). Results from all replicate experiments (n = 3 for strain Goofy (**a–f**); n = 3 for strain Regular (**g–l**)). In strain Goofy, *dmdA* was reported by RFP (**a–c**) and *dddW* by TFP (**d–f**). In strain Regular, *dmdA* was reported by TFP (**g–i**) and *dddW* by RFP (**j–l**). The time points of mid-exponential in *dmdA* expression, used for cleavage-to-demethylation ratio calculation (shown in Fig. 3), are represented as colored dots at the appropriate time points on the x-axis in demethylation pathway plots (**a–c**, **g–i**). Red asterisks (*) identify the replicate experiment shown in Fig. 2 (**c**,**f**). While the magnitudes of end-point fluorescence intensities, and the timepoints of mid-exponential and saturation of fluorescence kinetics curves, were not the same across replicate experiments and strains, other aspects (*e.g.*, concentration-dependence of end-point fluorescence intensities, and the preservation of slopes of the fluorescence curves across concentrations) were consistent (further discussion in Supplementary Note 2). Data points and error bars represent mean ± s.e.m. of fluorescence signals of cells.

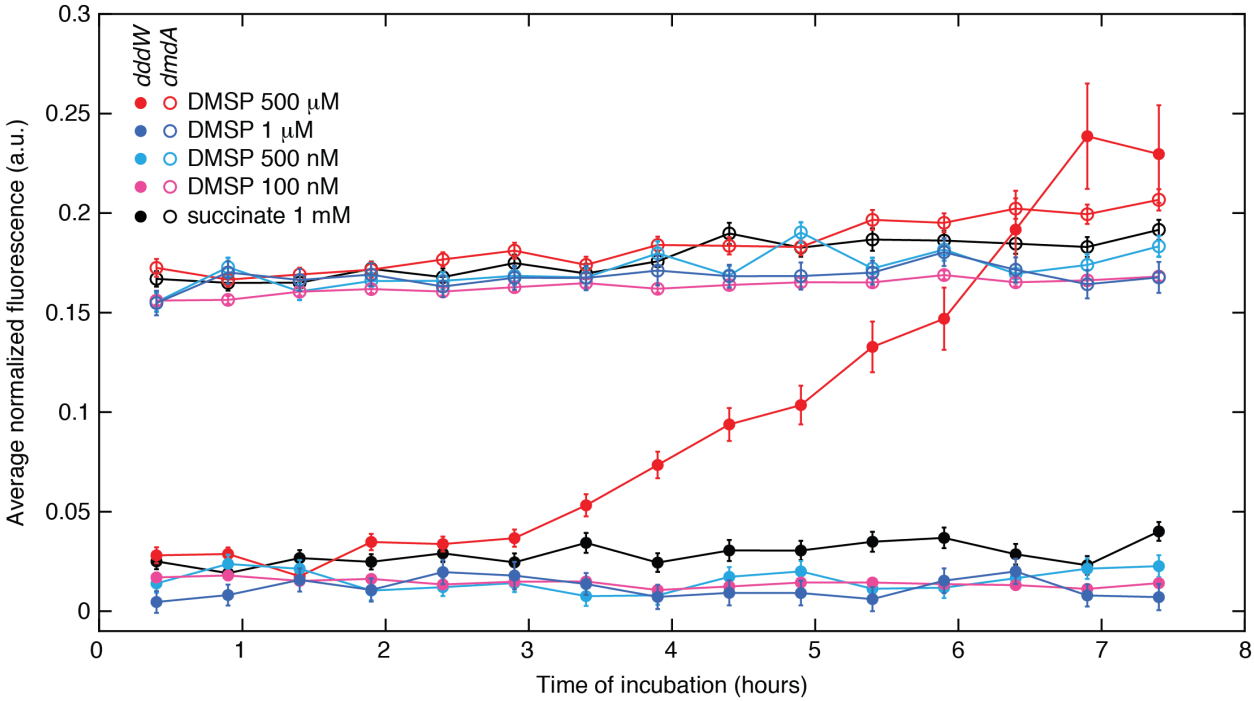

Supplementary Figure 2.7 | Fluorescence response to DMSP concentrations below 1 μM was undetectable in the microfluidic chip experimental setup. Lower DMSP concentration experiment (≤1 μM): *R. pomeroyi* reporter strain Regular was incubated with succinate (negative control) or DMSP (at 100 nM, 500 nM, 1 μM, or 500 μM) in observation chambers of a microfluidic chip in the presence of 50 μg/ml kanamycin. TFP (*dmdA* reporter; open circles) and RFP (*dddW* reporter; closed circles) fluorescence of each cell were normalized by its own YFP intensity (constitutive expression). Each experimental condition was imaged at 4–10 different positions, with each field of view containing 25–200 cells that passed the constitutive YFP fluorescence intensity threshold. No cell division was observed over the experimental duration. Fluorescence signal upregulation above baseline was either absent, or not detectable, in DMSP concentrations at and below 1 μM compared to succinate (two-tailed *t*-test at 6.4 h, $p > 0.01$). Data points and error bars represent mean ± s.e.m. of normalized fluorescence intensities of cells. This represents the only experiment in which succinate was used as negative control. Succinate, which did not elicit a fluorescence reporter response (Supplementary Fig. 3) and possesses a molecular weight that is similar to DMSP, was initially used as negative control in some early experiments. All other experiments presented in this manuscript used glucose as the negative control.

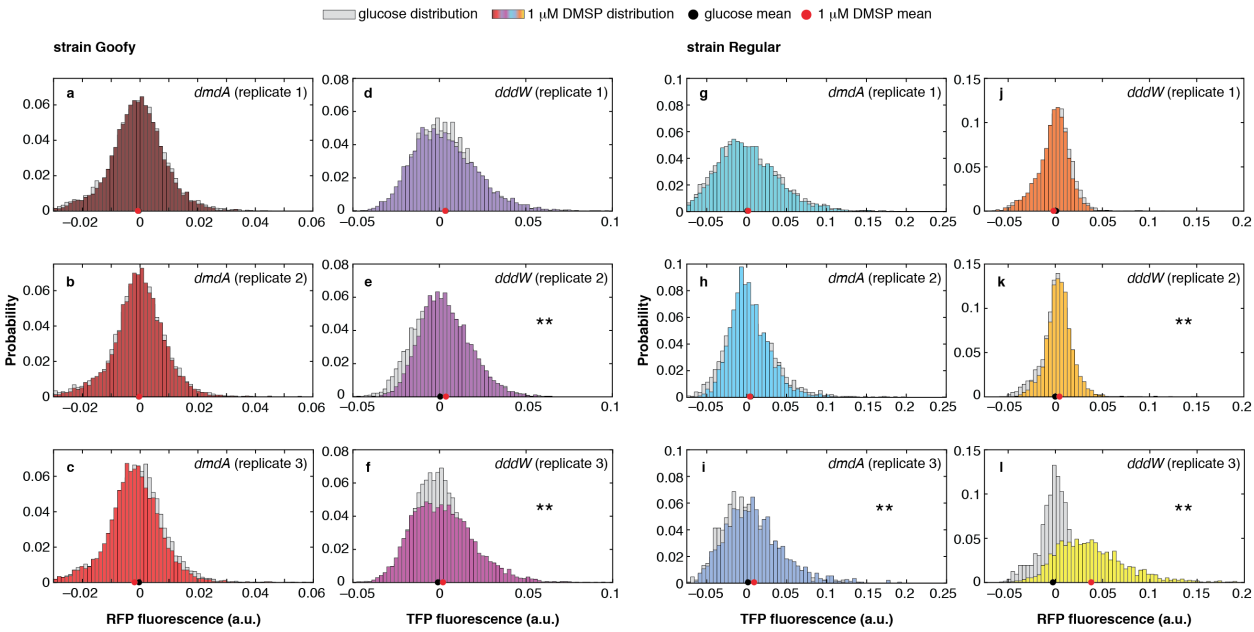

Supplementary Figure 2.8 | Onset of *dmdA* and *dddW* upregulation at 1 μM DMSP in microfluidic experiments. Probability distributions of fluorescence signals of *dmdA* (**a–c, g–i**) or *dddW* (**d–f, j–l**) reporters (strain Goofy (**a–f**) or Regular (**g–l**)) incubated with 1 mM glucose or 1 μM DMSP in microfluidic chip experiments (cells aggregated across three time points, ~2.5–4 h). Mean fluorescence of the first time point was subtracted from the fluorescence of each cell in appropriate color channels. Two-tailed *t*-test was performed on fluorescence data within each replicate experiment to determine statistically significant upregulation of *dmdA* or *dddW* in DMSP compared to glucose (glucose, n = 1,284–7,191 cells; DMSP, n = 1,488–9,362 cells; **, significant upregulation with $p < 0.01$). Only one (**i**) out of six replicate experiments showed significant upregulation of the demethylation pathway (*dmdA*) at 1 μM DMSP compared to glucose, while at higher concentrations (≥10 μM) all experiments exhibited upregulation of *dmdA* (Supplementary Fig. 6). These results suggest that 1 μM approximates the threshold DMSP concentration above which bacteria increase *dmdA* gene expression beyond baseline levels.

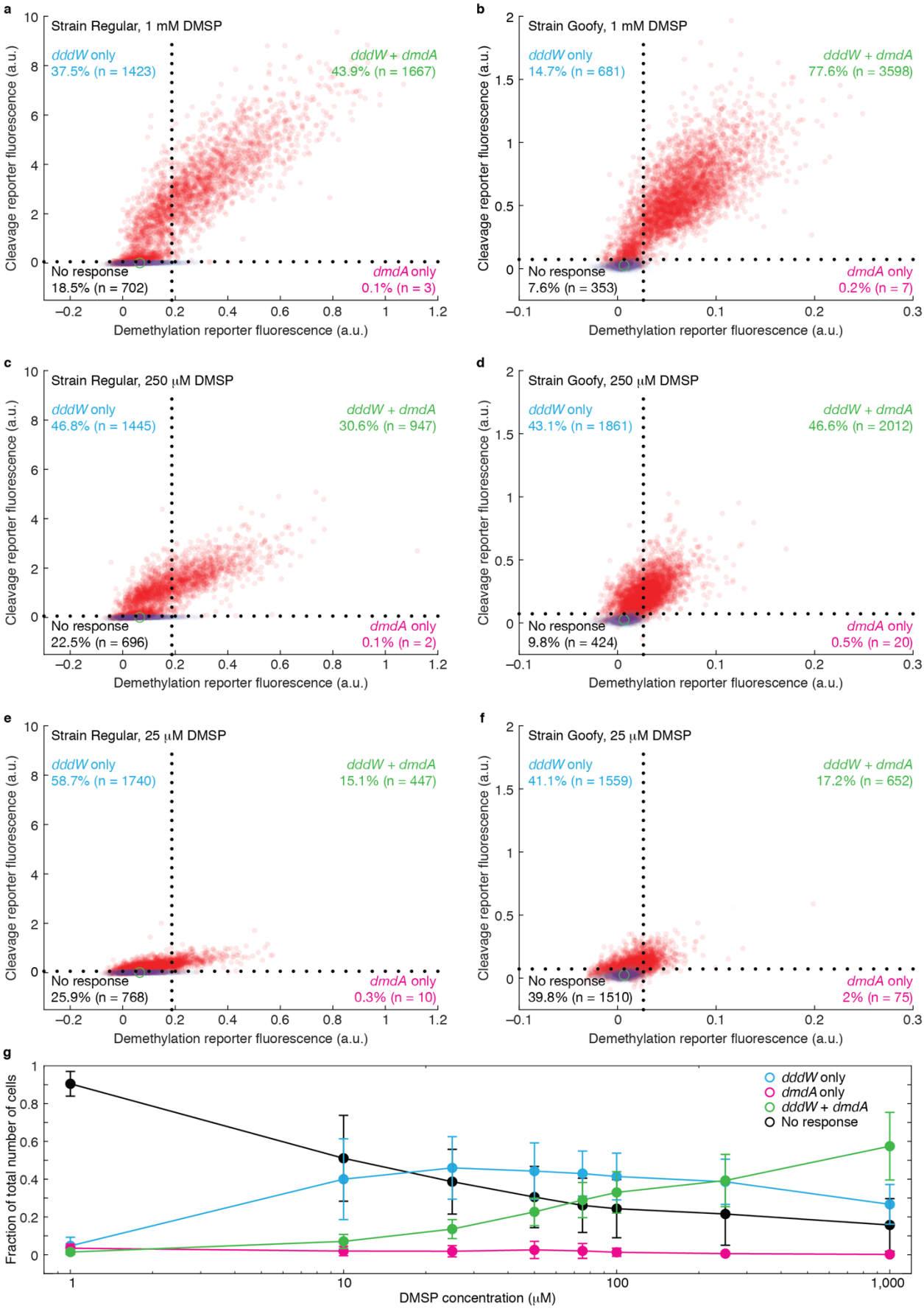
a
Strain Regular, 1 mM DMSP
dddW only
37.5% (n = 1423)
dddW + dmdA
43.9% (n = 1667)
No response
18.5% (n = 702)
dmdA only
0.1% (n = 3)
b
Strain Goofy, 1 mM DMSP
dddW only
14.7% (n = 681)
dddW + dmdA
77.6% (n = 3598)
No response
7.6% (n = 353)
dmdA only
0.2% (n = 7)
c
Strain Regular, 250 μM DMSP
dddW only
46.8% (n = 1445)
dddW + dmdA
30.6% (n = 947)
No response
22.5% (n = 696)
dmdA only
0.1% (n = 2)
d
Strain Goofy, 250 μM DMSP
dddW only
43.1% (n = 1861)
dddW + dmdA
46.6% (n = 2012)
No response
9.8% (n = 424)
dmdA only
0.5% (n = 20)
e
Strain Regular, 25 μM DMSP
dddW only
58.7% (n = 1740)
dddW + dmdA
15.1% (n = 447)
No response
25.9% (n = 768)
dmdA only
0.3% (n = 10)
f
Strain Goofy, 25 μM DMSP
dddW only
41.1% (n = 1559)
dddW + dmdA
17.2% (n = 652)
No response
39.8% (n = 1510)
dmdA only
2% (n = 75)
Cleavage reporter fluorescence (a.u.)
Demethylation reporter fluorescence (a.u.)
g
Fraction of total number of cells
DMSP concentration (μM)
dddW only
dmdA only
dddW + dmdA
No response

Supplementary Figure 2.9 | Upregulation of demethylation (*dmdA*) and cleavage (*dddW*) at the single-cell level. **a–f**, Fluorescence of *dmdA* and *dddW* reporters at ~23 h (time point 30) from representative microfluidic chip experiments are shown (also in Supplementary Fig. 6): replicate experiment 1 of strain Regular (**a**,**c**,**e**) and replicate experiment 1 of strain Goofy (**b**,**d**,**f**). Each data point represents fluorescence signals of a single cell. Blue dots represent cells that have been incubated with 1 mM glucose, while red dots represent cells that have been incubated with DMSP at 1 mM (**a**,**b**), 250 μM (**c**,**d**), or 25 μM (**e,f**). Dotted lines mark two standard deviations from the mean (green circle) of the glucose population, representing cutoffs for defining the four populations: cells that upregulated (1) *dddW* only (cyan), (2) *dmdA* only (magenta), (3) both pathways (green), and (4) neither pathways (no response, black). **g**, Fractions of total number of cells at ~23 h (time point 30) in each of the four populations, averaged across all replicate experiments of both reporter strains (Goofy and Regular). At DMSP concentrations ranging between 10–100 μM, the '*dddW* only' population (cyan) represented the majority of responsive cells. At DMSP concentrations ranging from 250 μM–1 mM, cells that upregulate both pathways (green) formed the majority. Data points and error bars represent mean ± s.d. of replicate experiments (n = 6). Heterogeneity in DMSP degradation gene upregulation is discussed in Supplementary Note 2.

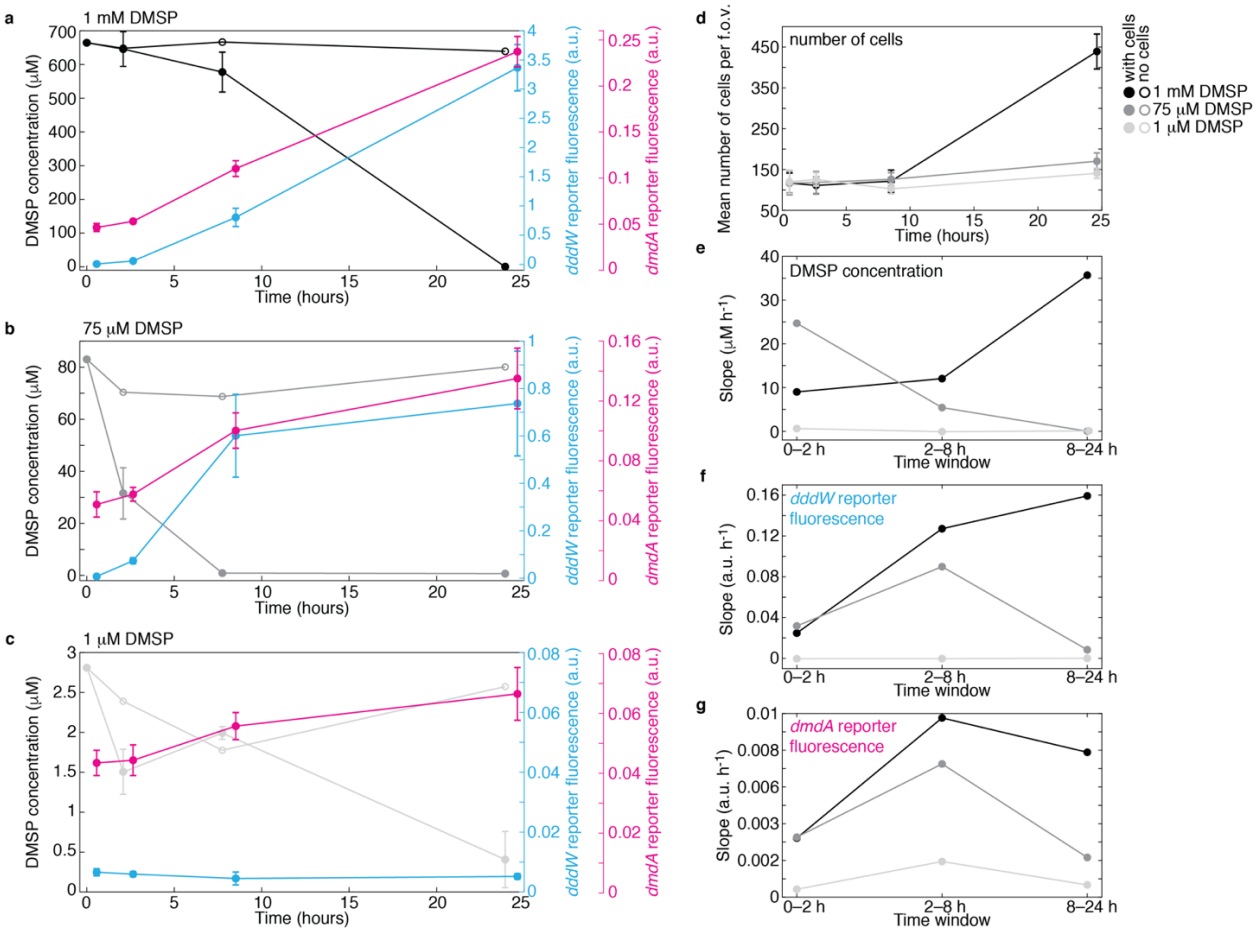
a
1 mM DMSP
b
75 μM DMSP
c
1 μM DMSP
DMSP concentration (μM)
dddW reporter fluorescence (a.u.)
dmdA reporter fluorescence (a.u.)
Time (hours)
d
number of cells
Mean number of cells per f.o.v.
with cells
no cells
1 mM DMSP
75 μM DMSP
1 μM DMSP
Time (hours)
e
DMSP concentration
Slope (μM h-1)
0–2 h
2–8 h
8–24 h
Time window
f
dddW reporter fluorescence
Slope (a.u. h-1)
g
dmdA reporter fluorescence

Supplementary Figure 2.10 | Concentrations of DMSP in time-lapse experiments decrease over time due to cell uptake. **a–c** DMSP concentration measurements in a large-volume (8 ml) experiment with engineered *R. pomeroyi* (strain Regular) incubated with 1 mM DMSP (**a**), 75 μM DMSP (**b**), or 1 μM DMSP (**c**). Small differences between measured and expected initial concentrations are attributed to experimental or measurement errors. Samples were taken for DMSP concentration measurements (left y-axis, black) and fluorescence microscopy (right y-axes, cyan and magenta) at approximately 0, 2, 8, and 24 h after the start of incubation. Consistent with our microfluidic chip experiments, both pathways increased expression when bacteria were incubated with 75 μM and 1 mM DMSP, but 1 μM DMSP led to little or no response in either pathway. Data points and error bars represent mean ± s.d. of three biological replicates for DMSP concentration measurements and fluorescence intensities. Specifically, mean fluorescence intensities of cells within a field of view, then across fields of views, were calculated before averaging across the three biological replicates (n = 90–151 average number of cells per field of view at 0 h; seven fields of views per condition at 0 h; two fields of views per condition at subsequent time points). Each cell's fluorescence signals were normalized by its own constitutive-YFP signal. **d** Mean number of cells per field of view (f.o.v.; 200 μm × 200 μm), counted in images taken for fluorescence intensity quantification at each sampling time point. Growth was observed in all DMSP concentrations. At 1 mM DMSP, a burst of growth during the last two time points (between 8 and 24 h after start of incubation), coincided with the largest DMSP concentration decrease (**a**). Data points and error bars represent mean ± s.d. across three biological replicates of average number of cells per f.o.v. **e–g** Rates of change in DMSP concentration (**e**), cleavage (*dddW*) reporter fluorescence (**f**), and demethylation (*dmdA*) reporter fluorescence (**g**). Slopes between pairwise time points were calculated for each DMSP concentration condition. The 1 mM condition (black) is marked by an initial period (0–8 h) of slow DMSP concentration decay (**e**) but rapid pathway upregulation (**f**,**g**). This initial period is followed by fast DMSP uptake (8–24 h; **e**) coinciding with rapid increase in cell number (**d**) and continued increase in pathway expression (**f**,**g**). In contrast, the 75 μM condition (dark grey) is marked by a rapid initial decline in DMSP concentration during the first time points (0–2 h; **e**), followed by a period of fast pathway expression increase (2–8 h; **f**,**g**), which plateau at the same time as DMSP is depleted (8–24 h; **b**). Differences in rates of DMSP uptake, growth, and pathway expression between 75 μM and 1 mM DMSP conditions point to potentially different physiological adaptations corresponding to low and high nutrient conditions.

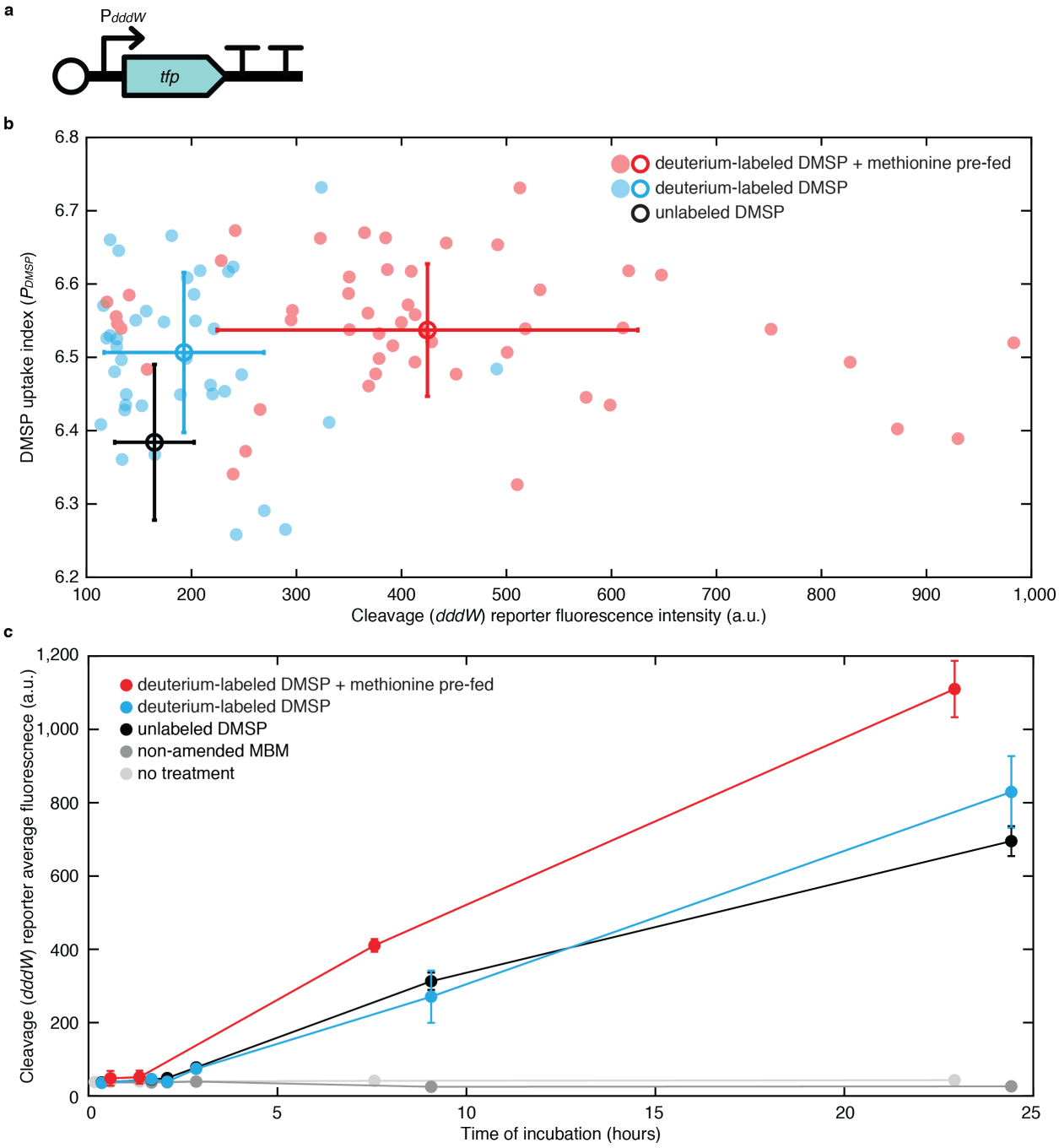
a
P*dddW*
tfp
b
deuterium-labeled DMSP + methionine pre-fed
deuterium-labeled DMSP
unlabeled DMSP
DMSP uptake index (P_{DMSP})
Cleavage (*dddW*) reporter fluorescence intensity (a.u.)
c
deuterium-labeled DMSP + methionine pre-fed
deuterium-labeled DMSP
unlabeled DMSP
non-amended MBM
no treatment
Cleavage (*dddW*) reporter average fluorescnece (a.u.)
Time of incubation (hours)

Supplementary Figure 2.11 | Cells satiated in sulfur maintain DMSP uptake but increase cleavage pathway expression. **a** The P_{dddW}::mTFP1 single-color *R. pomeroyi* reporter strain (cleavage pathway promoter-fusion with TFP) was used to avoid spectral interference with Raman microspectroscopy measurements. **b** Raman microspectroscopy measurements were performed at 5.5 h after incubation initiation. The reporter strain (**a**) was incubated with 1 mM deuterium-labeled DMSP ([$^2H_6$]-DMSP), either with or without prior exposure to 10 mM L-methionine (an alternative sulfur source to DMSP). All DMSP and methionine were dissolved in marine basal medium (MBM). The DMSP uptake index, P_{DMSP}, was calculated as the ratio of integrated intensities at Raman spectrum regions between the Raman wavenumbers 2040 and 2300 cm^{-1} (C-D peak) and between 2400 and 2450 cm^{-1} (reference region where background intensity was low) (Methods). Each filled-circle data point represents the P_{DMSP} value and the background-subtracted, raw TFP fluorescence signal of a single cell, measured by the Raman microspectroscopy setup (Methods) (n = 43 cells treated with deuterium-labeled DMSP only (cyan); n = 50 cells pre-fed with methionine and treated with deuterium-labeled DMSP (red)). For clarity of presentation, individual cell data points for unlabeled DMSP condition are not shown. Empty circles and error bars represent mean ± s.d. of fluorescence (horizontal) and DMSP uptake index (vertical) of cells in each experimental condition. **c** Fluorescence response of cells incubated with deuterium-labeled DMSP (red and cyan), unlabeled DMSP (black), non-carbon amended MBM (dark grey), or no treatment (light grey) in observation chambers, monitored over time by microscopy (start of incubation at 0h). All conditions except 'no treatment' contained a final concentration of 1% methanol (solvent in which [$^2H_6$]-DMSP was dissolved). At each time point, seven images were taken at different positions within each observation chamber (n = 330 ± 325 (mean ± s.d.) cells per image). Following image segmentation and background subtraction (Methods), the mean cellular fluorescence was calculated for each image, then averaged across images. Results confirmed that DMSP, unlabeled (black) or deuterium-labeled (cyan), elicit the same fluorescence response. Pre-feeding with methionine (red) led to faster upregulation and higher fluorescence signals of the cleavage (*dddW*) reporter cells compared to control cells (*i.e.*, not pre-fed with methionine). Data points and error bars represent mean ± s.d. of average cellular fluorescence of seven images.

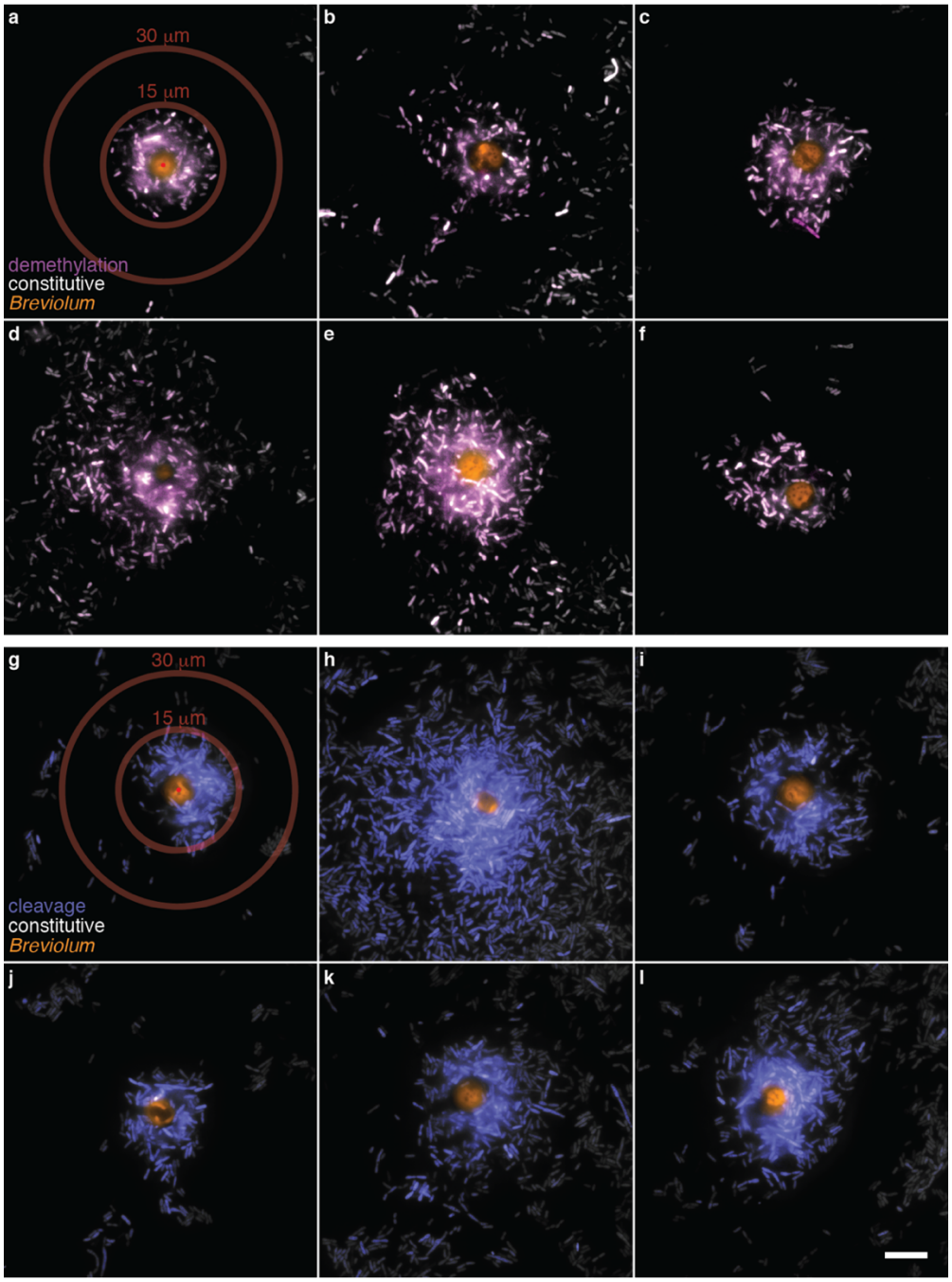

Supplementary Figure 2.12 | Images of phytoplankton-bacteria co-incubation experiment. Representative images of the agarose pad co-incubation experiment (also shown in Fig. 4) with DMSP-producing phytoplankton, *Breviolum* CCMP2459, surrounded by *R. pomeroyi* bacteria fluorescently reporting *dmdA* (**a–f**, strain Regular; out of 15 total images) or *dddW* (**g–l**, strain Goofy; out of 18 total images) gene expression. Fluorescence signals are false-colored orange for photosynthetic pigments of phytoplankton, white for YFP (constitutive expression), magenta for *dmdA* reporter (TFP; **a–f**), and blue for *dddW* reporter (TFP; **g–l**). Representative concentric rings (widths of 20 pixels = 1.6 µm), used to bin distances from the center of *Breviolum* cells (red dots; **a**,**g**) for quantification of fluorescence signals, are shown for distances 15 and 30 µm. Scale bar, 15 µm.

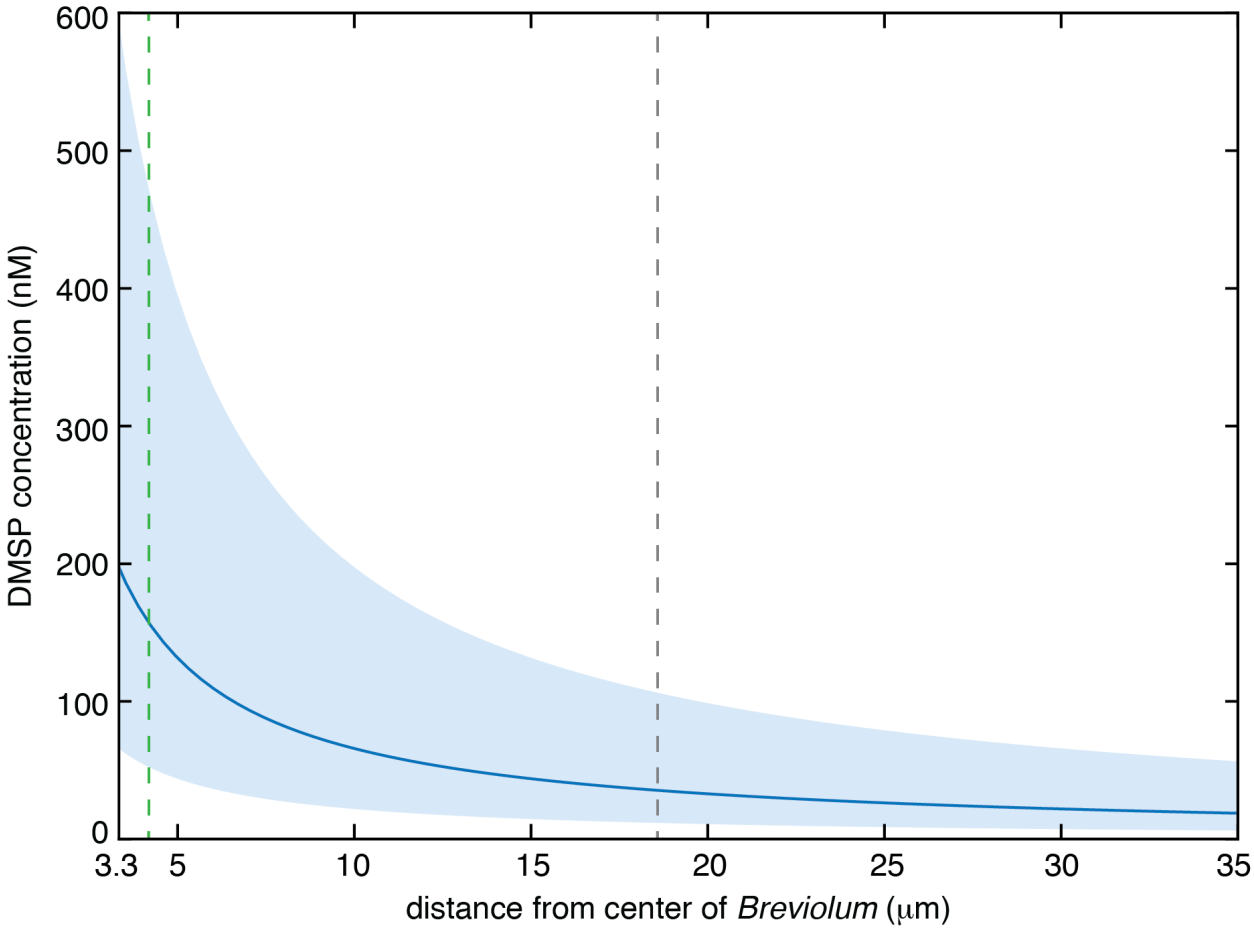

Supplementary Figure 2.13 | Model of DMSP concentration in a phycosphere. Concentration profile of DMSP within a phycosphere predicted using Eq. S7 (Supplementary Note 4). The dark blue line shows modeled DMSP concentrations at distances (r) from the center of a *Breviolum* cell, with a radius of 3.3 μm (average radius in our co-incubation experiment; lower x-axis limit). Modeled DMSP concentration at the surface of the cell (r = 3.3 μm) was 197 nM. Green dotted line marks the distance of the first concentric ring at which bacterial fluorescence was quantified (r = 4.2 μm; modeled DMSP concentration = 157 nM). Grey dotted line represents the distance within the phycosphere beyond which bacterial fluorescence signals were observed to return to baseline levels (r = 18.6 μm; modeled DMSP concentration = 35 nM). Shaded regions show two further cases in which modeled DMSP concentrations are 3-fold greater (upper boundary of the shaded region) or 3-fold smaller (lower boundary) than in the baseline case.

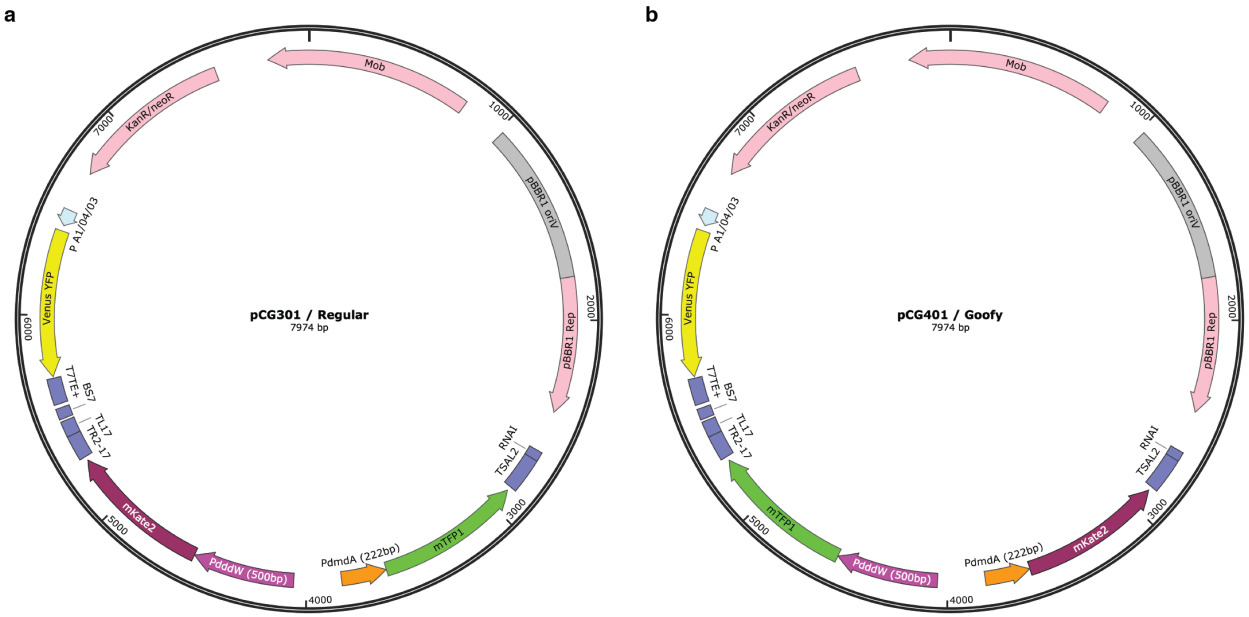

Supplementary Figure 2.14 | Plasmid maps of tricolor reporter constructs, pCG301 (**a**, strain Regular) and pCG401 (**b**, strain Goofy).

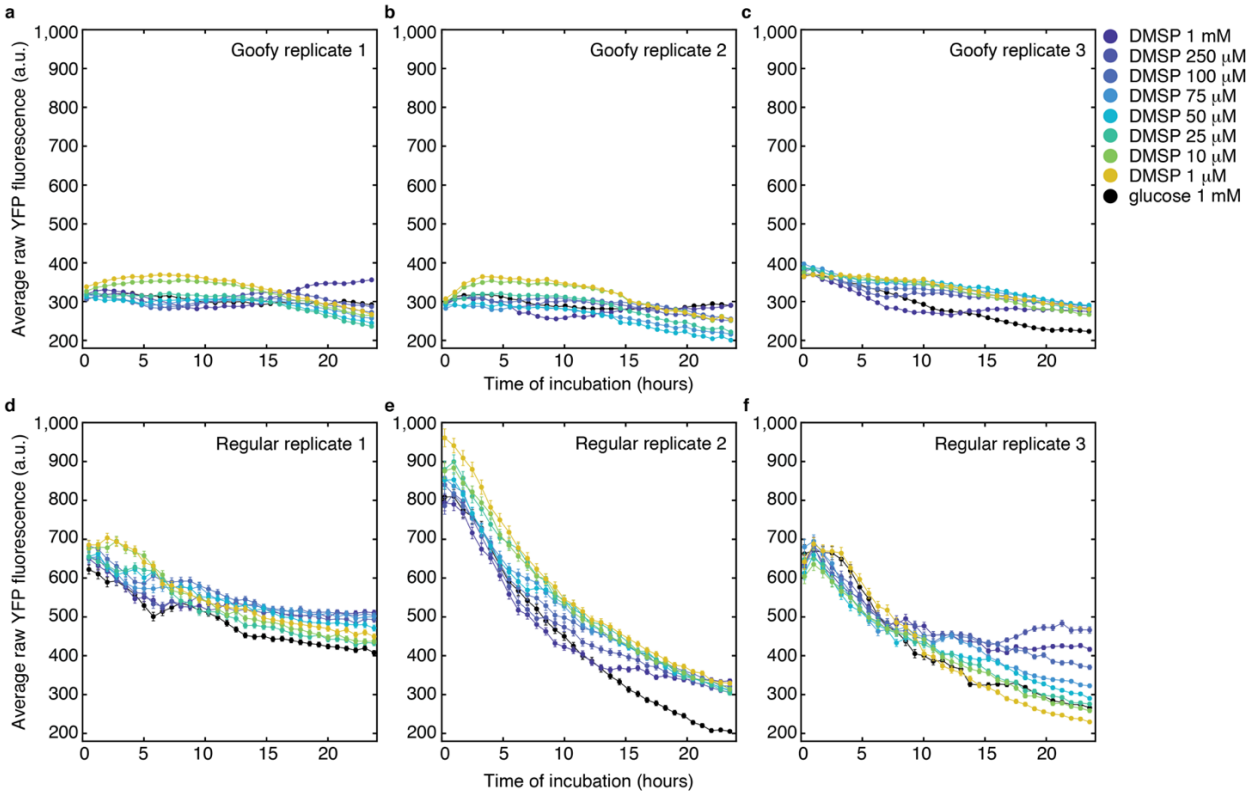

Supplementary Figure 2.15 | YFP fluorescence in time-lapse DMSP experiments performed in microfluidic chips (all replicate experiments). Replicate experiments correspond to those presented in Supplementary Fig. 6. Background subtraction, spectral leakage correction, and YFP intensity thresholding (50 a.u.) were performed. YFP signals decreased over the duration of experiments, which may be due to a number of factors including plasmid-loss by bacteria and fluorescence signal dilution due to cell division. Data points and error bars represent mean ± s.e.m. of fluorescence signals of cells.

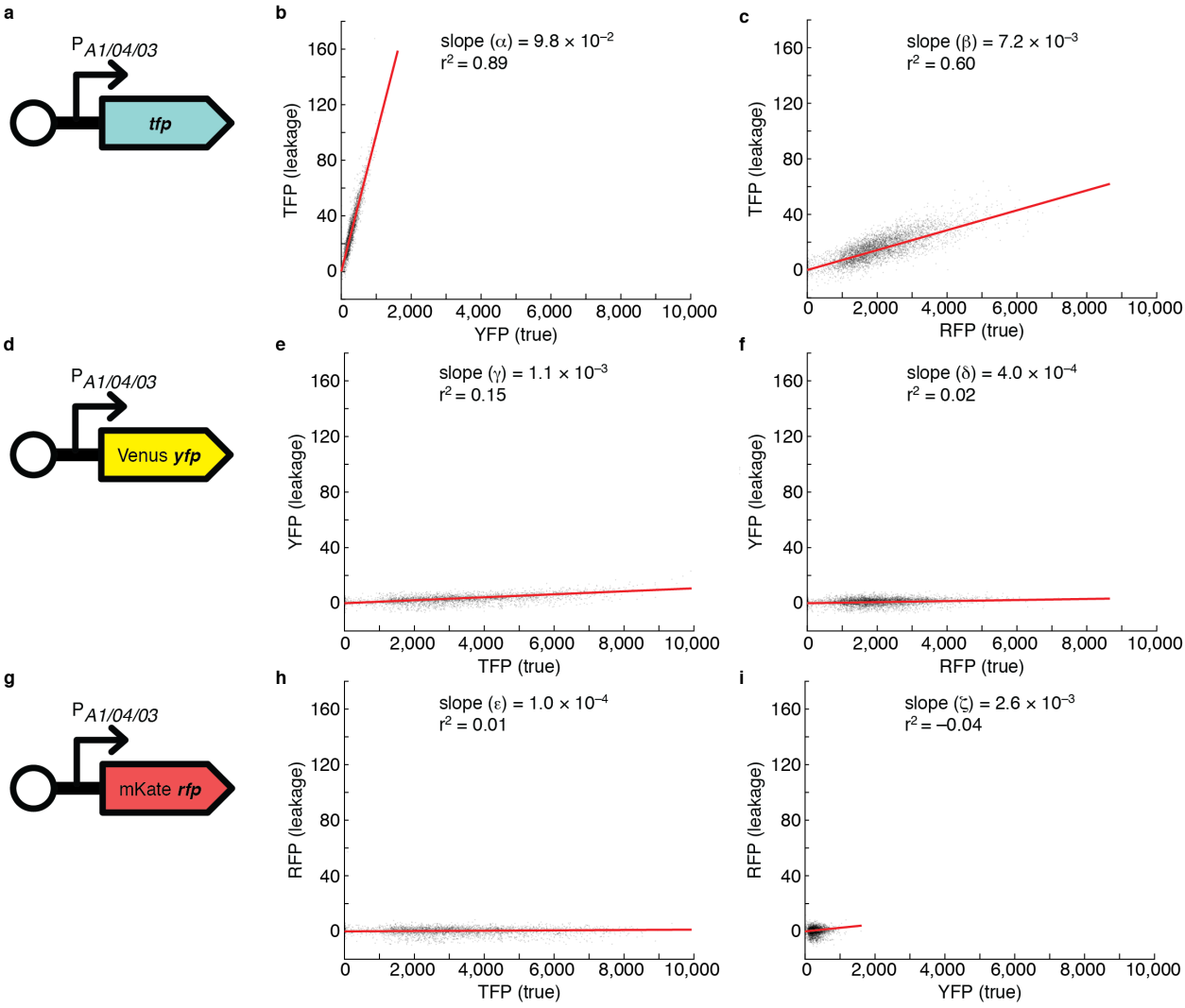

Supplementary Figure 2.16 | Calculation of spectral leakage correction matrix, *B*, with constitutively fluorescent single-color control strains. Each constitutively fluorescent single-color control strain of *R. pomeroyi* (**a**, $P_{A1/04/03}$::mTFP1; **d**, $P_{A1/04/03}$::YFP; **g**, $P_{A1/04/03}$::mKate2) was imaged in its appropriate color channel ('true') and the two inappropriate color channels ('leakage') (n = 10 biological replicates per strain; data point = one cell in **b–c**, **e–f**, **h–i**). Non-fluorescent cells were eliminated from analyses by applying minimum intensity thresholds in the true fluorescence channels (Supplementary Note 1). Only 10% of cells, randomly sampled across ten biological replicates, are plotted for clarity. In images of tricolor reporter strains (Regular or Goofy), recorded fluorescence signals are sums of 'true' and 'leakage' signals (Eq. S1–3). Specifically, recorded teal fluorescence ($\hat{t}$) includes leakage from YFP (αy; **b**) and RFP (βr; **c**); recorded yellow fluorescence ($\hat{y}$) includes leakage from TFP (γt; **e**) and RFP (δr; **f**); recorded red fluorescence ($\hat{r}$) includes leakage from TFP (εt; **h**) and YFP (ζy; **i**). Slopes of linear regressions (α,β,γ,δ,ε,ζ) were used to generate the spectral leakage correction matrix, *B*, which was used for quantification of true fluorescence signals of tricolor reporter strains (Supplementary Note 1).

2.7 Supplementary Tables

Supplementary Table 2.1 | Fluorescent strains constructed in *R. pomeroyi* DSS-3 for this study.

Strain / Plasmid	Description	GenBank Accession #
Regular / pCG301	tricolor reporter (P_{dmdA}::mTFP1, P_{dddW}::mKate2, $P_{A1/04/03}$::YFP)	MN744962
pCG302	single-color reporter (P_{dmdA}::mTFP1)	MN744963
pCG303	single-color reporter (P_{dddW}::mKate2)	MN744964
Goofy / pCG401	tricolor reporter (P_{dmdA}::mKate2, P_{dddW}::mTFP1, $P_{A1/04/03}$::YFP)	MN744965
pCG402	single-color reporter (P_{dmdA}::mKate2)	MN744966
pCG403	single-color reporter (P_{dddW}::mTFP1)	MN744967
pCG101	single-color constitutive control ($P_{A1/04/03}$::mKate2)	MN744959
pCG102	single-color constitutive control ($P_{A1/04/03}$::YFP)	MN744960
pCG103	single-color constitutive control ($P_{A1/04/03}$::mTFP1)	MN744961
pZS2-200	pZS2-123 with replaced promoters (P_{dmdA}, P_{dddW}, P_{lac}) for cloning aid only	MN744968

Supplementary Table 2.2 (Sequences of all oligonucleotide primers used in this study) is in the Excel sheet accompanying the publication.

Supplementary Table 2.3 | Plasmids externally obtained and used in this study.

Plasmid	Description	Source / Reference
pZS2-123	DNA architecture of tricolor reporters; source of Venus YFP and terminators	AddGene #26598 (Reference: [71])
pBBR1MCS-2	vector backbone (Kan^R)	Provided by M.E. Kovach (Reference: [102])
pXGFPC-2 P_{lac}::mKate2	source of mKate2 and $P_{A1/04/03}$ modified *lac* promoter	Provided by G. D'Souza (Reference: [66])
pXGFPC-2 P_{lac}::mTFP1	source of mTFP1	Provided by G. D'Souza (Reference: [66])
pRK415	source of *lac* promoter that is weakly active in DSS-3	Provided by C.R. Reisch (Reference: 4, 5)
pKR600	helper strain (*E. coli*) for triparental mating (Cam^R)	Provided by C.R. Reisch (Reference: [104])

2.8 Supplementary Notes

Supplementary Notes 1 and 3 from the publication are in the Appendix Chapter as sections A1 and A2, respectively, in this Thesis.

2.8.1 Supplementary Note 2: Interpretation of fluorescence results.

Time-lapse DMSP experiments in microfluidic chips.

Results from all replicates of time-lapse DMSP experiments are presented in Supplementary Fig. 6. While the magnitudes of end-point fluorescence intensities (*i.e.*, average fluorescence signals over the final five (~20.4–24 h) time points), and the timepoints of mid-exponential and saturation of fluorescence kinetics curves, were not the same across replicates and strains, other aspects (concentration-dependence of fluorescence intensities and the preservation of slopes of the kinetics curves across concentration) were consistent. The decline in RFP signal after signal saturation may be due to bleaching, plasmid loss, or fluorescent protein degradation. The slight increase in TFP signal in glucose negative control and after signal saturation may be due to a delay in protein folding, or clumping of cells as they reach overgrowth in the experimental chamber, leading to a perceived increase in brightness of cell-containing pixels over time. Due to spectral (*i.e.*, bleaching and effect of cell clumping on signal) and biological (*i.e.*, rate of protein folding and degradation, and effect of plasmid loss) differences between the fluorescent proteins, these phenomena are expected to affect signals detected in red and teal fluorescence channels in different ways. However, these small artefacts did not affect our overall conclusions outlined in the main text.

Temporal evolution of constitutively-expressed YFP fluorescence in all time-lapse DMSP experiments are presented in Supplementary Fig. 15. All experiments were performed with antibiotics (kanamycin) to slow plasmid-loss during experiments, but at a low concentration (10 μg/ml) to minimize interference with biological processes. We observed a 13.4 ± 17.0% (mean ± s.d. of replicate experiments) decay in YFP signals in glucose between 1 h and 10 h of the microfluidic experiments (Supplementary Fig. 15), which may be a predictor of the rate of plasmid-loss in our experiments. Loss of plasmid over the experimental duration may contribute to an underestimation of fluorescence signals reporting *dmdA* and *dddW* expression. However, the relatively small variability in the level of YFP signal decay across replicate experiments

suggests that the rate of plasmid-loss is comparable amongst cells on average. Thus, we conclude that comparisons of cell fluorescence relative to each other (e.g., between different concentrations of DMSP, or between *dddW* and *dmdA*) is valid.

Heterogeneity in DMSP degradation gene expression.

Our single-cell approach revealed the emergence of heterogeneity in the DMSP degradation pathway response within a single bacterial strain (*R. pomeroyi* DSS-3). Underlying the population averages were concentration-dependent shifts in the proportions of cells classified in four discrete categories: (1) *dddW* response only, (2) *dmdA* response only, (3) *dddW* + *dmdA* response, and (4) no response (Supplementary Fig. 9).

End-point expression levels were defined as the average fluorescence signals over the last five time points (*i.e.*, ~20.4–24 h) of a time-lapse DMSP experiment performed in observation chambers, and were used as proxies for maximum gene expression levels that *dddW* and *dmdA* reached as a result of exposure to a DMSP concentration (Fig. 2c,d). For DMSP concentrations ranging between 10–50 μM, the mean end-point cleavage (*dddW*) pathway expression level (shown in Fig. 2d) was driven by a population of cells that solely upregulated the *dddW* gene (the '*dddW* response only' population), which made up nearly half (40.0 ± 21.4% to 44.3 ± 14.9%) of total cells at 10–50 μM (Supplementary Fig. 9g); while the other half of the population maintained baseline expression of the DMSP pathways (the 'no response' population). In contrast, the average end-point demethylation (*dmdA*) pathway expression level (Fig. 2c) was driven by a subpopulation of cells that upregulated both *dmdA* and *dddW* genes (the 'both pathways on' population; Supplementary Fig. 9g). This population grew exponentially between DMSP concentrations of 10 μM (7.0 ± 3.7% of total cells) and 75 μM (28.9 ± 9.3% of total cells), and surpassed all other subpopulations at 250 μM (Supplementary Fig. 9), at which the increase in the maximum gene expression levels with DMSP concentration also dampened (Fig. 2c,d).

Taken together, these results suggest that specific cell subpopulations drove the average increases in *dmdA* and *dddW* gene expression in different DMSP concentration regimes. At the highest DMSP concentrations tested (>100 μM), the majority of cells shifted their metabolic

strategy towards upregulating both pathways (*dddW* + *dmdA*), probably in order to capitalize on the abundance of DMSP. However, upregulation of both pathways came at the expense of the ability to respond sensitively to DMSP concentration, as the positive relationship between end-point gene expression levels and concentration dampened above 100 μM (Fig. 2c,d). Finally, we speculate that the shift in the relative expression towards cleavage pathway with increasing DMSP concentration (Fig. 3) is controlled at two distinct levels: (i) at the single cell level (*i.e.*, individual cells increase *dddW* expression levels), as well as (ii) at the population level (*i.e.*, increasing fractions of '*dddW* only' or '*dddW* + *dmdA*' subpopulations with concentration).
Model of DMSP concentrations in the phycosphere

2.8.2 Supplementary Note 4: Model of DMSP concentrations in the phycosphere

The microenvironment surrounding a unicellular phytoplankton, the 'phycosphere', is often characterized by a concentration gradient of exudates and dissolved organic matter (DOM)[115]. Exudates include DMSP, which comprises up to 10% of fixed carbon in some phytoplankton species[116]. Here, we predict the concentration of exuded DMSP in the phycosphere as a function of the leakage rate, L, and its molecular diffusivity, D (Supplementary Fig. 13).

Experimentally, we simulated a phycosphere by seeding *R. pomeroyi* fluorescent reporter bacteria with *Breviolum* phytoplankton cells on agarose pads, which preserved the spatial arrangement of co-incubated organisms (Methods). We assumed a 30% reduction in diffusivity of DMSP in agarose ($D_{agarose}$) compared to solution ($D_{solution} = 0.5 \times 10^{-5}$ cm^2 s^{-1})[117]. A similar percentage of diffusivity reduction was observed for sucrose in agarose in a previous study[118]. The thickness of agarose (~0.5 mm) was much larger (150×) than the average radius of *Breviolum* cells (3.3 μm); thus, a 3D diffusion model was used to describe the concentration of DMSP in agarose. However, since the phytoplankton cell was immobilized with agarose on one side, diffusion may be more accurately approximated on a half-volume around the cell, instead of its entire volume. Thus, the effective leakage rate would be double of that expected ($2L$). Taken together, the concentration of DMSP in agarose at distance r from the center of a phytoplankton cell is modeled as:

$$C_r = \frac{2L}{4\pi D_{agarose} r} \qquad \text{(Eq. S7)}$$

with L, the constant exudation rate (mol/s) of DMSP, defined as:

$$L = \mu\theta f \qquad \text{(Eq. S8)}$$

where μ is the doubling rate of the *Breviolum* cell, θ is the amount of intracellular DMSP if there were no leakage ($\mu\theta$ is thus the rate of production of DMSP by the cell), and f is the fraction of the production rate that is leaked.

The actual, stable quantity of intracellular DMSP that is maintained by the cell, ϕ, is defined with the following relationship with θ and f:

$$\phi = \theta(1 - f) \qquad \text{(Eq. S9)}$$

Thus, L, the constant exudation rate (mol/s) of DMSP, is described as:

$$L = \frac{\mu\phi f}{1-f} \qquad \text{(Eq. S10)}$$

Breviolum cells in our experiment were most likely under physiological stress, or undergoing senescence, due to immobilization on an agarose pad, proximity to high numbers of bacteria, and exposure to vigorous shaking of cell cultures prior to co-incubation; stress and shaking have been shown to increase intracellular DMSP and exudation rate[119,120]. However, all *Breviolum* cells included in our image analyses maintained high fluorescence signal from photosynthetic pigments to ensure viable phycospheres at the time of imaging. We considered the leakage fraction (f) to be constant and not dependent on cell size; however, in reality, leakage fraction may be expected to decrease with increasing cell size, though little information is available on this issue.

Up to 50% of all organic materials produced can be released by phytoplankton[87,121], and a survey of intracellular DMSP measurements of 55 samples of Symbiodiniaceae found a range of 0.021–

3.831 pmol DMSP per cell[77]. In this model, we assumed a doubling rate (μ) of 1 day^{-1} or 86,400 s^{-1}, a leakage fraction (f) of 1/9 (~11%), and an intracellular content (ϕ) of 1 pmol per cell for a small, spherical phytoplankton (mean radius of *Breviolum* cells in our experiment was 3.3 μm), in the absence of fluid flow.

Two further cases, in which μ, ϕ, $\frac{f}{1-f}$, or $1/D_{agarose}$ by themselves, or the product of these four terms overall, is 3-fold greater or 3-fold smaller, are calculated and shown as upper and lower boundaries compared to the baseline case scenario (the edges of the shaded region in Supplementary Fig. 13). The former case (*i.e.*, upper boundary) represents the scenario in which parameters are as in the baseline case, but leakage or intracellular DMSP content is high (as is the case for stressed cells[119]; in our model, f = 0.25 or ϕ = 3 pmol per cell) or diffusivity is low (*e.g.*, agarose reduces diffusivity by more than 30% of $D_{solution}$; in our model, $D_{agarose} = 0.12 \times 10^{-5}$ cm^2 s^{-1}). The same reasoning applies to the lower boundary. Parameters for the baseline case were chosen to represent realistic values, and the two further curves thus provide a measure of possible DMSP concentration ranges in a phycosphere under different conditions.

2.9 Acknowledgements

The authors thank F. Moser and Prof. C.A. Voigt (MIT) for assisting in reporter construction; Prof. C.R. Reisch (University of Florida) for discussions on genetic design of reporters; G. D'Souza (ETH Zurich) for providing fluorescent protein genes; Prof. M.E. Kovach (Baldwin Wallace University) for providing pBBR1MCS cloning vectors; and A.S. Burns (Georgia Tech) for assisting in *R. pomeroyi* transformations. We thank Prof. L. Behrendt (Uppsala University) for *Breviolum* cell culture; Prof. F. Menolascina (University of Edinburgh) for assisting in development of the image analysis software; and F.J. Peaudecerf for assisting with microscopy imaging. We also thank Prof. D.A. Lauffenburger, Prof. K. Ribbeck (MIT), C.S. Smillie (Broad Institute), and U. Alcolombri (ETH Zurich) for scientific discussions. This research was funded by a Gordon and Betty Moore Foundation Marine Microbiology Initiative Investigator Award (GBMF3783) to R.S., a grant from the Simons Foundation through the Principles of Microbial Ecosystems (PriME) collaboration (542395) to R.S., and a National Science Foundation

Graduate Research Fellowship (Grant No. 1122374) to C.G. J.B.R. was supported by Australian Research Council fellowship DE160100636. We acknowledge the International Max Planck Research School "The Exploration of Ecological Interactions with Molecular and Chemical Techniques" for a fellowship to S.F., and the German Research Foundation for funding within the framework of the Cluster of Excellence Balance of the Microverse EXC 2051 to G.P.

2.10 Author contributions

J.R.S., J.B.R., and R.S. designed the study. C.G. constructed the reporter strains and performed the microfluidic and agarose pad experiments. C.G., and K.S.L. performed the Raman microspectroscopy experiments. C.G., S.F., and G.P. performed the large-volume DMSP concentration measurement experiment. C.G., V.I.F., and R.S. created the image analysis software. C.G., V.I.F., J.R.S., J.B.R., and R.S. wrote the manuscript. All authors edited the manuscript before submission.

Chapter 3.

Coral mucus rapidly induces chemokinesis and genome-wide transcriptome shifts toward pathogenesis in a bacterial coral pathogen

Work presented in this Chapter in in preparation for submission as "Cherry Gao, Melissa Garren, Kevin Penn, Vicente I. Fernandez, Justin R. Seymour, Janelle R. Thompson, Jean-Baptiste Raina, Roman Stocker. Coral mucus rapidly induces chemokinesis and genome-wide transcriptional shifts toward pathogenesis in a bacterial coral pathogen."

3.1 Abstract

Elevated seawater temperatures have contributed to the rise of coral disease mediated by bacterial pathogens, such as the globally distributed *Vibrio coralliilyticus*. This pathogen utilizes coral mucus as a chemical cue to locate stressed corals that are vulnerable to infection. However, the physiological events that follow entry into the host environment remain unknown. Here, we present simultaneous measurements of the behavioral and transcriptional responses of *V. coralliilyticus* BAA-450 incubated in coral mucus. Video microscopy revealed a strong and rapid behavioral response, chemokinesis, corresponding to a two-fold increase in average swimming speed within six minutes of coral mucus exposure. RNA sequencing showed that this behavior was accompanied by equally rapid differential expression of 53% of the genes in the genome. Specifically, transcript abundance ten minutes after mucus exposure suggested upregulation of genes involved in quorum sensing, biofilm formation, and nutrient metabolism, and downregulation of flagella and chemotaxis genes. After 60 minutes, transcript abundance suggested upregulation of genes associated with virulence, including zinc metalloproteases implicated in coral tissue damage and symbiont photoinactivation, and secretion systems that

may export toxins. Together, our results suggest that this bacterial pathogen employs a suite of behavioral and transcriptional responses to rapidly shift into a distinct infection mode within minutes of exposure to the host microenvironment.

3.2 Introduction

Coral reefs are declining worldwide due to rising sea surface temperatures and increasing prevalence of coral disease outbreaks[17–19]. Elevated sea surface temperatures cause physiological stress in corals[122] as well as distinct advantages for some bacterial coral pathogens[123]. One well-studied coral pathogen, *Vibrio coralliilyticus* BAA-450, displays a tightly regulated temperature-dependent virulence against its coral host, *Pocillopora damicornis*. While *V. coralliilyticus* is avirulent at temperatures below 24 °C, it is capable of attacking the coral symbiotic algae[31,124] and lysing coral tissue[125] at temperatures above 27 °C.

V. coralliilyticus displays two distinct behavioral adaptations that enable targeted infection of corals that are physiologically stressed and therefore more vulnerable to pathogenic invasion. First, the bacterial pathogen finds vulnerable corals through chemotaxis toward chemical signatures present in the mucus of stressed corals[27]. Second, *V. coralliilyticus* displays chemokinesis, or swimming speed enhancement, to enable faster environmental exploration in the presence of its host mucus[27,28]. These two behaviors combine to enable efficient and rapid targeting of stressed corals by *V. coralliilyticus*.

While coral mucus triggers increased motility and chemotaxis, which are behaviors necessary for infection by *V. coralliilyticus*[30,35], the mucus also represents the critical interface where pathogen activities can dictate the outcome of an infection. Corals secrete up to half of the carbon assimilated by their algal symbionts as mucus[126,127] and coral mucus represents a sizable energetic investment that is important for nutrient cycling across the entire reef system[26,128–130]. In addition, mucus provides corals with protection against desiccation and is an ancient and evolutionarily conserved first line of defense against pathogens[131]. During infection studies, corals have been observed to actively expel ingested pathogens by spewing out bacteria-laden mucus from the polyps' mouths[132,133]. Furthermore, studies of the human pathogen *Pseudomonas*

aeruginosa have revealed that the chemistry of porcine gastric mucus attenuates the pathogen by altering its swimming behavior[134,135] and gene expression[136,137]. However, entry into host mucus may alternatively signal to the bacterial pathogen that contact with a potential host is imminent. Thus, elucidating the behavioral and transcriptional responses of *V. coralliilyticus* in the context of its coral host environment, and in particular coral mucus, is important in elucidating the mechanisms of *V. coralliilyticus* infection.

Here, we present experiments in which we simultaneously used video microscopy and RNA sequencing to measure the behavioral and transcriptional responses of *V. coralliilyticus* upon a sudden exposure to mucus from its coral host. Chemokinesis, in contrast to chemotaxis, is a rarely studied behavior in bacteria, and one that is almost entirely undescribed in the context of marine disease[138–140]. Thus, to study chemokinesis independently from chemotaxis, we conducted our experiments in the absence of chemical gradients. This represents, to the best of our knowledge, the first investigation that couples behavioral and transcriptomic analyses to decipher the mechanisms promoting coral infection. We show that behavioral and transcriptomic responses occur concomitantly over a surprisingly rapid timescale of only minutes, highlighting the agility of the pathogens in seizing what are likely to be limited windows of opportunity to target and ultimately infect their host.

3.3 Materials and methods

3.3.1 Coral mucus collection

Five small colonies of the coral *Pocillopora damicornis* were collected from Heron Island (23.4423°S, 151.9148°E, Great Barrier Reef, Australia) in April 2015 and maintained in aquaria for two weeks at 25 °C ± 1 °C and 35 ppt salinity on a 12 h light–dark cycle. Mucus was collected with a sterile 1-ml syringe (Becton Dickinson, NJ, USA) from corals subjected to repeated 3-min air exposure, and snap-frozen in a sterile 50 ml tube (Falcon, Corning Life Sciences, MA, USA) in liquid nitrogen and maintained at −80 °C until used in experiments. A total of 55 ml of coral mucus was collected over three consecutive days as three separate samples. Directly before experimentation, a single pool of coral mucus was created by thawing in a room temperature water bath and pooling samples in a sterile glass bottle. Mucus of

Acropora millepora, a coral species that is also vulnerable to *V. coralliilyticus* infection[31] and to whose mucus *V. coralliilyticus* performs chemotaxis[27], was used in a single experiment (Supplementary Fig. 3.4) with similar mucus collection and preservation methods.

3.3.2 Bacterial culture

Vibrio coralliilyticus type strain ATCC BAA-450 was acquired from the American Type Culture Collection (Manassas, VA, USA). A frozen stock (−80 °C, 25% glycerol) of *V. coralliilyticus* was streaked onto a marine broth 2216 (BD Difco, Franklin Lakes, NJ, USA) culture plate and incubated at room temperature for 24–48 h. For liquid culture inoculation, five colonies were resuspended in 20 µl filtered (0.2 µm) artificial sea water (FASW, 35 g/L; Instant Ocean) and 5 µl of this suspension was inoculated into each of three sterile 250-ml Erlenmeyer flasks containing 80 ml of 1% marine broth medium (99% FASW, v/v). The timing of inoculation of the triplicate liquid cultures was staggered to allow 17–18 h of growth (to OD_{600} 0.04) before the start of each replicate experiment. Liquid cultures were incubated at 30 °C in an orbital shaker (250 rpm).

3.3.3 Preparation of filtered spent medium

Experimental controls consisted of *V. coralliilyticus* incubated in their own filtered spent medium, which was prepared immediately prior (≤ 10 min) to the start of each replicate experiment. Approximately 20 ml *V. coralliilyticus* culture was aseptically filtered through a sterile 0.2-µm syringe filter (polyethersulfone membrane; VWR International) attached to a sterile 10-ml syringe, into a sterile 50-ml Falcon tube. Filters were changed every 10 ml of volume filtered to minimize clogging.

3.3.4 Experimental setup

Three biological replicate experiments were sequentially performed on the same day using three independent cultures of *V. coralliilyticus* and their filtered spent media (control) or pooled coral mucus (treatment) (Fig. 3.1). Aliquots of 25 ml of bacteria were placed into each of two RNase-free 50-ml Falcon tubes for the mucus and control treatments. Bacteria, coral mucus, and filtered spent media were maintained at 30 °C ± 1 °C in a water bath for the duration of the experiment. Incubation was initiated by the 1:1 (v/v) addition of coral mucus or filtered spent medium to bacteria, followed by thorough mixing by repeated pipetting to eliminate any chemical gradients.

Bacteria were repeatedly and manually sampled from populations incubated with mucus or filtered spent media. At each time point, 40 µl of the bacteria-containing solution was removed from the top of the incubation tube using a pipette and introduced into a straight microfluidic channel (60 mm × 4 mm, 90 µm depth), followed immediately by video acquisition. A single microfluidic device, fabricated using soft lithography[141] and permanently fixed to a glass microscope slide (75 mm × 25 mm × 1 mm; VWR International) by plasma bonding, contained two identical channels in parallel to accommodate the mucus and the control experimental conditions. A temperature-controlled microscope stage insert (Warner Instruments, Hamden, CT, USA) was used to maintain cells at 30 °C during imaging. After each time point, cells were removed from the device and discarded. Three biological replicate experiments were performed sequentially on the same day, using three different cultures of *V. coralliilyticus* exposed to aliquots of the same pooled coral mucus (Fig. 3.1). A new microfluidic device was used for each replicate experiment.

3.3.5 Microscopy and video analysis

Phase contrast microscopy videos (300 frames at 29.79 fps) were acquired using an inverted epifluorescence TE2000 microscope (Nikon, Tokyo, Japan) controlled through Nikon Elements software, with a 20× objective (S Plan Fluor ELWD ADM Ph1 20×, 0.45 NA; Nikon) and 1.5× optical magnification (combined objective magnification of 30×), and an sCMOS camera (Andor Neo, 2560 × 2160 pixels, 6.5 µm/pixel; Andor, Belfast, Northern Ireland). Videos were acquired at the center of the microfluidic channels, with the focal plane at channel mid-depth to avoid wall effects on motility.

Analysis of microscopy videos was performed in MATLAB (MathWorks, Natick, MA, USA) using an automated image segmentation and trajectory reconstruction software developed in-house (detailed methods in Supplementary Methods). Briefly, cells in each image were identified using a pixel intensity threshold, and their swimming trajectories were reconstructed using their *x,y*-positions in sequential frames (Fig. 3.2a,b). To identify motile and non-motile bacteria, we determined the type of motion (ballistic or diffusive) of each bacterium by calculating the mean squared displacement (MSD) as a function of short time intervals (Δt), and quantifying the exponent α of this dependence ($MSD \sim \Delta t^{\alpha}$). Non-motile bacteria were identified as slow-

moving (median instantaneous speed < 10 μm/s) and displaying purely diffusive motion ($\alpha < 1$). Motile bacteria were instead identified as those cells moving more rapidly (median instantaneous speed ≥ 10 μm/s) and having a higher value of the MSD exponent ($\alpha \geq 1$) (Supplementary Fig. 3.1). A sensitivity analysis showed that our results were robust against the selection of different threshold values (Supplementary Fig. 3.2). Amongst motile bacteria, the swimming speed of each cell was calculated by averaging the instantaneous speed over the duration of its trajectory, and the mean speed of the population was quantified by averaging over all trajectories of motile bacteria detected in each microscopy video (mean ± s.d. of number of trajectories in videos, n = 1298 ± 312 pre-addition, n = 753 ± 230 post-addition; Supplementary Fig. 3.3), representing a single time point in mucus or control conditions (Fig. 3.2).

3.3.6 RNA sampling, isolation, sequencing, and sequence alignment

The incubation tubes containing bacteria were swirled vigorously to mix before taking samples of mucus and control cells at three time points during each replicate experiment (Fig. 3.1). Sample volumes of 8 ml pre-mucus or -filtered spent medium (control) addition, and 16 ml post-addition (10 min and 60 min; larger volume to account for biomass dilution) were each filtered through a 0.22 μm Sterivex-GP filter unit (polyethersulfone membrane; Millipore) attached to a sterile 60-ml syringe to capture bacteria onto the membrane. Subsequently, the filtrate end of the Sterivex filter cartridge was briefly flamed and pinched to close, and 2 ml of RNAlater (Thermo Fisher Scientific) was added with a pipette through the other end of the cartridge to immerse the cell-containing filter membrane in the RNA-stabilizing solution. Sample-containing filter cartridges were incubated at 4 °C for 24 h, then preserved at −80°C until RNA extraction. A sample of coral mucus (~2 ml) was also preserved, and its RNA extraction confirmed that little to no RNA was present in coral mucus.

Total RNA extraction was performed as described previously[142] (detailed description in Supplementary Methods). Depletion of rRNA (using Ribo-Zero rRNA Removal Kit for bacteria (Epicentre Biotechnologies)) and subsequent mRNA sequencing (using Illumina HiSeq2500 sequencer), assembly, and alignment were performed by the Joint Genome Institute (Los Alamos, NM, USA) (detailed description in Supplementary Methods). Due to RNA degradation, mucus-treatment sample at 10 min from replicate 2 could not be sequenced. Thus, 17 samples in total were sequenced. Raw reads from each library were aligned to the reference genome (*V.*

coralliilyticus ATCC BAA-450, NCBI Taxon ID 675814). As a result, 99.48% (5022 genes) of the filtered FASTQ reads mapped to the *V. coralliilyticus* reference genome. GenBank protein IDs (prefix "EEX") were obtained from *V. coralliilyticus* BAA-450 genome assembly ASM17613v1 and matched by locus tags (prefix "VIC_") of each gene.

3.3.7 Differential expression analysis

The DESeq2 package[143] (v1.26.0) in R was used for differential expression analyses for time point-matched, pairwise comparisons (e.g., mucus vs. control at 10 min). The DESeq2 algorithm uses negative binomial generalized linear models to test for differential abundances in raw count data, and controls for differences in sequencing depth between libraries by estimating size and dispersion factors. Adjusted *p*-values are calculated in DESeq2 using the Benjamini-Hochberg procedure, which accounts for multiple comparisons. Statistically significant gene expression differences were assessed using the Wald test with a false discovery rate (FDR) adjusted *p*-value < 0.01. No fold change cutoff was applied. All instances of gene upregulation or downregulation discussed in the text are deduced from statistical tests performed on transcript abundances.

For principal component analysis (PCA) and sample-to-sample distance calculation, raw count data were transformed using the variance stabilizing transformation (VST) method[144] to remove the dependence of the variance on the count mean, especially when count means are low. VST uses the experiment-wide trend of variance over mean in order to transform the data to remove the experiment-wide trend. Transformed values are on the $\log_2$ scale.

3.3.8 Gene Set Enrichment Analysis (GSEA)

Gene set enrichment analysis was performed using the GSEA software[145,146] v4.0.3 to identify differential representation of metabolic pathways in transcripts sequenced in mucus or control conditions. Only genes with significant differential expression determined by DESeq2 was included in the GSEA analyses. Gene sets were defined by KEGG Pathways. Genes were ranked by $\log_2$ fold change values. Further details are described in Supplementary Methods.

3.4 Results

3.4.1 *V. coralliilyticus* exhibits strong chemokinesis within minutes of exposure to coral mucus

Video microscopy observations revealed a strong and rapid behavioral response of *V. coralliilyticus* upon a sudden 1:1 addition (v/v at $t = 0$ min) of *Pocillopora damicornis* coral mucus, relative to controls amended with filtered spent medium (Fig. 3.2). All experiments were performed at 30 °C to capture conditions in which *V. coralliilyticus* is capable of infecting its coral host[125]. The viscosity of coral mucus in our experiments (0.750 cP) was similar to that of filtered artificial seawater (0.731 cP). Thus, bacterial responses measured in this study were assumed to be mostly due to chemical components of coral mucus, rather than hydrodynamic parameters.

V. coralliilyticus responded to coral mucus with strong chemokinesis. Microscopy video analyses revealed that their average swimming speed increased from 48.0 ± 3.4 μm/s (mean ± s.d. of three replicates), measured five minutes before addition of coral mucus, to 81.0 ± 9.6 μm/s within two minutes of coral mucus addition (Fig. 3.2e). The maximum swimming speed (95.5 ± 4.6 μm/s) was reached at six minutes post-addition, representing a two-fold increase compared to the pre-addition swimming speed (Fig. 3.2e). When samples were collected for RNA-seq, at 10- and 60-min post-addition of mucus, swimming speeds were 90.1 ± 2.9 μm/s and 64.5 ± 0.9 μm/s, respectively (Fig. 3.2e). After reaching the maximum speed, the average swimming speed of bacteria in coral mucus gradually decreased over time, but remained significantly higher than the swimming speeds of pre-addition and control cells for the entire experimental duration (65 min) (two-tailed *t*-tests, $p < 0.01$).

Chemokinesis in *V. coralliilyticus* seems to be a temperature-dependent behavior that is caused by a combination of chemical cues, nutrient influx, and environmental change. Coral mucus–induced chemokinesis was attenuated in an experiment conducted at a lower temperature (18.7 °C), in which the observed speed enhancement was only 1.1-fold at 7 min post-mucus-addition (Supplementary Fig. 3.4). In a separate experiment, rich medium (marine broth) and coral mucus both led to a doubling of swimming speeds within 5 min (Supplementary Fig. 3.5),

suggesting that at least initially, *V. coralliilyticus* chemokinesis is a response to an influx of nutrients. Furthermore, control cells, exposed to the addition of filtered spent medium in place of coral mucus, displayed a weak and short-lived increase in swimming speed that peaked at 1.3× the pre-addition speed after 8 min and returned to baseline within 15 min (Fig. 3.2e; two-tailed *t*-test with control speed at −2 min, $p > 0.01$). Results from separate experiments suggested that this short-lived chemokinesis in control cells was caused by oxygenation of the spent medium during filtration (Supplementary Fig. 3.5, Supplementary Discussion). Taken together, our results suggest that the virulent form (30 °C) of *V. coralliilyticus* is highly sensitive to chemical changes in the environment, and that coral mucus induces chemokinesis that is especially rapid, larger in magnitude, and longer in duration than any other conditions tested.

Probability distributions of the swimming speeds of motile cells before and after mucus addition showed that the observed increase in average swimming speed was caused by the shift of the entire motile cell population toward a faster swimming regime (Fig. 3.2c,d, Supplementary Fig. 3.6), rather than the emergence of behaviorally distinct subpopulations. In contrast, only a subset of motile control cells increased swimming speeds upon the addition of filtered spent media (Supplementary Fig. 3.6). Furthermore, the fraction of the population that was motile (as opposed to non-motile) did not change significantly upon exposure to mucus or spent medium: in both treatments, approximately 75% of the population was motile over the whole experimental duration (Supplementary Fig. 3.7). These results suggest that speed enhancement within the motile fraction of the population underlies the increase in average swimming speed observed in coral mucus, and that non-motile cells mostly maintain their non-swimming state upon mucus addition. Taken together, our video microscopy results revealed that coral mucus exposure causes strong chemokinesis in *V. coralliilyticus*, over timescales as short as 2 minutes, with a peak in the response corresponding to a doubling of swimming speed at 6 minutes post-exposure to mucus.

3.4.2 Within minutes of coral mucus exposure, *V. coralliilyticus* initiates a transcriptional infection program

Motivated by the rapid behavioral changes observed in *V. coralliilyticus* upon exposure to coral mucus, we investigated the transcriptional response of the bacteria on the same timescales by

performing RNA sequencing (RNA-seq) on the same *V. coralliilyticus* populations from which samples for tracking by video microscopy were obtained. Sequencing and alignment of mRNA libraries to the *V. coralliilyticus* BAA-450 reference genome (5078 protein-coding sequences[33]) resulted in 5020 genes with non-zero total read count. Differential expression between mucus treatments and controls at each time point was analyzed by using the DESeq2 R package[143] with a false discovery rate (FDR) cutoff of 0.01 (Supplementary Tables 3.1, 3.2). All instances of gene differential expression given in the text are statistically significant (unless otherwise noted), and the fold difference values provided in each case are relative to the control at the same time point. Coral mucus led to a genome-wide response, with significant upregulation of 1379 genes (27% of detected genes) after 10 min, and 1159 genes (23%) after 60 min, compared to controls at the same time points (Fig. 3.3a). In addition, coral mucus exposure was associated with significant downregulation of 1326 genes (26%) after 10 min and 1076 genes (21%) after 60 min (Fig. 3.3a). Of all significantly differentially expressed genes, 1521 genes (30%) were shared between 10 and 60 min (Supplementary Table 3.3). These results suggest that exposure to coral mucus leads to large shifts in the gene expression profile of *V. coralliilyticus*.

The changes in gene expression caused by coral mucus occurred rapidly and on the same timescales as behavioral changes. Principal component analysis (PCA) showed that the transcriptomic shift in mucus-incubated bacteria over time was captured by the first two principal components (collectively accounting for 88.3% of the variance), with the largest differences in the PCA space occurring at 10 min after addition (Fig. 3.3b). Replicate libraries clustered tightly together in the PCA space, indicating that there was little variance amongst replicates (Fig. 3.3b). The transcriptional shifts in control cells were largely captured by shifts along the second component (PC2, 15.9%), which also captured, to a similar magnitude, a portion of the response to mucus at 10 min (Fig. 3.3b), suggesting that the transcriptional changes in control cells were also present in mucus cells. After 60 min of mucus incubation, gene expression shifted back part of the way toward pre-addition conditions on PC1 (72.4%), but occupied a distinct space on PC2 in comparison with other time points, pointing to a potential physiological switch that requires the expression of a different group of genes than the early time point (10 min). Taken together, our results reveal a rapid (within 10 min) transcriptional response of the pathogen to coral mucus that mirrors the timescales of their behavioral changes.

Surprisingly, chemotaxis and flagella genes were downregulated in coral mucus compared to controls at 10 min (Fig. 3.3c), despite the strong increase in swimming speed observed by video microscopy at the same time point (Fig. 3.2). To identify pathways in which genes were collectively up- or downregulated in mucus, Gene Set Enrichment Analysis (GSEA)[145,146] was performed between mucus and control cells at each time point, with significance determined at an FDR *q*-value cut-off of 0.25. Chemotaxis (KEGG 02030) and flagellar assembly (KEGG 02040) gene sets were downregulated within 10 min of incubation with coral mucus (Fig. 3.3c, Supplementary Fig. 3.8). All 17 chemotaxis *che* genes (A, B, D, R, V, W, Y, Z) were downregulated, except *cheX* (EEX30576) (Supplementary Fig. 3.8). Out of the 50 methyl-accepting chemotaxis protein (MCP) genes encoded in the *V. coralliilyticus* genome, 26 were downregulated and only 15 were upregulated (Supplementary Fig. 3.8). Out of the 74 flagellar assembly genes, 31 were downregulated in coral mucus including those encoding polar and lateral flagella, as well as the sigma factor σ28, which directs flagellar promoters (Supplementary Fig. 3.8). Taken together, these patterns of gene expression led us to speculate that – while increasing its swimming speed – *V. coralliilyticus* is already preparing, at the transcriptional level, for a lifestyle in which motility and chemotaxis are no longer important.

Next, we searched for potential mechanisms underpinning the chemokinesis behavior within the RNA-seq data. Our results from differential expression analysis (DESeq2) revealed the upregulation of all six genes of the Na^+-translocating NADH:ubiquinone oxidoreductase (Na^+-NQR) enzyme in coral mucus compared to controls at 10 min (Fig. 3.4a, Supplementary Table 3.4). The Na^+-NQR enzyme is responsible for generating a sodium motive force that drives flagellar rotation in Vibrios[147,148]. Although the rapid onset (within 2 min) of chemokinesis suggests that this behavior is not entirely a result of changes to gene expression (bacterial protein production typically takes 10 minutes or longer[89]), the increase in Na^+-NQR production may have enabled the sustained chemokinesis observed over our experimental duration.

Metabolic pathways involved in the catabolism of natural constituents of mucus were upregulated in coral mucus at 10 min (Fig. 3.3c). Coral mucus, similarly to other animal mucus, is rich in sugars, lipids, peptides, amino acids (especially serine and threonine), and sulfur[24,149–153], on which *V. coralliilyticus* can grow (Supplementary Fig. 3.9). Consistent with the chemical

composition of coral mucus, upregulated pathways included those involved in the metabolism of starch and sucrose (KEGG 00500), glycerophospholipid (KEGG 00564), glycine, serine and threonine (KEGG 00260), and sulfur (KEGG 00920), as well as fatty acid degradation (KEGG 00071) (Fig. 3.3c, Supplementary Discussion). The downregulation of genes involved in the assimilation of inorganic nitrogen (nitrate and nitrite reductases in KEGG 00910; Fig. 3.3c) suggests a metabolic switch toward the utilization of organic nitrogen, which is abundant in coral mucus within amino acids and peptides. Consistent with elevated metabolism, almost all ribosomal protein genes (KEGG 03010) and aminoacyl-tRNA synthetases (KEGG 00970) were upregulated in coral mucus compared to controls at 10 min (Fig. 3.3c, Supplementary Fig. 3.10), as were markers of cell growth, *ftsZ* and *rpoD* (EEX34708 and EEX34866; Supplementary Fig. 3.11). This suite of changes suggests that upon exposure to the nutrient-rich coral mucus, *V. coralliilyticus* rapidly (within 10 min) and substantially alters its transcriptome to increase metabolism, protein production, and growth.

Coral mucus triggered early responses of genes involved in quorum-sensing signal molecule production (*luxM*, *luxS*, *cqsA*) and regulation (*aphA*, *vtpR*), as well as biofilm-related polysaccharide production (*vps* and *rbm* genes) (Fig. 3.4b–d), which are consistent with a transition to a host-associated lifestyle. The *V. coralliilyticus* genes responsible for the production of the quorum-sensing autoinducer molecules (AI-1, AI-2, CAI-1)[33] displayed diverse responses, with *luxM* (AI-1; EEX31502) upregulated and *cqsA* (CAI-1; EEX33462) downregulated in mucus at both 10 and 60 min relative to controls at the same time points (Fig. 3.4c). In contrast, *luxS* (AI-2; EEX35562) was first downregulated at 10 min (0.35×) and subsequently upregulated at 60 min (1.8×) in mucus relative to controls (Fig. 3.4c). Furthermore, the expression patterns of the quorum-sensing master regulators, *aphA* (EEX30687) and *vcpR* (EEX34823; homologous to *luxR* of *V. harveyi* and *hapR* of *V. cholerae*[154]), which operate at low and high cell densities[155,156], respectively, were consistent with the dilution of cells due to the addition of mucus (Fig. 3.4d). At 10 min in coral mucus, *aphA* was upregulated (2.8×) while *vcpR* was downregulated (0.5×) compared to controls (Fig. 3.4d). In Vibrios, quorum sensing is tightly coupled with biofilm formation[155,157–159]. Indeed, the majority of the 18 *vps* (Vibrio polysaccharide) and 5 *rbm* (rugosity and biofilm structure modulator) genes, which are essential for biofilm formation in *V. cholerae*[160–163], were upregulated together in coral mucus at 10 min

(Fig. 3.4b). These early-onset expression changes of specific genes involved in quorum sensing and biofilm formation were followed by the significant upregulation of their entire pathways (39 quorum sensing genes in KEGG 02024; 37 biofilm formation genes in KEGG 05111) at 60 min (Fig. 3.3d). Taken together, these results suggest that upon coral mucus exposure, *V. coralliilyticus* initiates a gene expression program that is consistent with host colonization.

Virulence genes characteristic of *Vibrio* pathogens were amongst the most strongly and significantly upregulated genes in coral mucus (Supplementary Figs. 3.12, 3.13). The master regulator of virulence, ToxR (EEX35320), and its associated stabilizer[164,165], ToxS (EEX35319), were upregulated in coral mucus compared to controls at both the 10- and 60-min time points (Fig. 3.4d). Concurrently, several toxin genes were upregulated in coral mucus compared to controls at both time points (Fig. 3.4e). The important *V. coralliilyticus* virulence factor, VcpB zinc metalloprotease (EEX32371), was one of the most strongly and significantly upregulated genes in coral mucus at both 10 min (8.6×; Supplementary Figure 3.12) and 60 min (53.5×; Supplementary Figure 3.13). In addition, the VchA hemolysin (EEX31069) and the associated putative chaperone VchB (EEX31068), which are homologs of the primary virulence factors for *Vibrio vulnificus*[166,167], were significantly upregulated in coral mucus at 60 min (3.9× and 11.8×, respectively) (Fig. 3.4e, Supplementary Fig. 3.13). Furthermore, the upregulation of other zinc metalloproteases (Supplementary Fig. 3.14) suggests the existence of multiple, as yet uncharacterized, zinc metalloproteases available to *V. coralliilyticus* (Supplementary Discussion). Together, these virulence factors and toxins may be responsible for the tissue lysis of corals previously observed during *V. coralliilyticus* BAA-450 infection at elevated temperatures[125].

The bacterial secretion system (KEGG 03070) and protein export (KEGG 03060) gene sets were significantly upregulated in coral mucus at 60 min (Fig. 3.3d), suggesting elevated secretion of proteins. In particular, types 2, 6 (T2SS, T6SS) and Sec secretion system genes were collectively upregulated in coral mucus (Fig. 3.4f). Indeed, *vipB* (EEX32048) which encodes an essential component of T6SS[168], and *sec* genes were amongst the most significantly and highly upregulated genes in coral mucus at 60 min (Supplementary Fig. 3.13, Supplementary Table 3.5). In addition, the upregulation of β-lactam resistance (KEGG 01501; Fig. 3.3d), as well as

several of the multidrug-resistance efflux pump (*vex*) genes (Supplementary Fig. 3.15), may confer resistance against antibiotic compounds produced by commensal bacteria within coral mucus[169–174]. Taken together, these results suggest that exposure to coral mucus induces *V. coralliilyticus* to upregulate toxin production, secretion and antibiotic resistance genes, which may be important for host damage and for defense and competition against the commensal microbiome during host colonization.

3.5 Discussion

We have reported a rapid behavioral and transcriptional response of *V. coralliilyticus* to coral mucus exposure, which led to a two-fold increase in swimming speed and significant differential expression of 53% of the genes in the genome within 10 minutes. Our findings identify coral mucus as a potential chemical signal that induces pathogens to prepare for host colonization and infection. These responses are in line with the behavioral and physiological versatility characteristic of marine copiotrophic bacteria, which are often adapted to boom and bust lifestyles[40,175], yet the extent and the rapidity of the responses observed here indicate that timeliness is particularly important for coral host colonization by *V. coralliilyticus*.

Chemokinesis upon exposure to coral mucus is likely a strategy for *V. coralliilyticus* to seize a limited window of opportunity to reach the coral surface. By increasing swimming speed, bacteria also enhance their chemotactic velocity, leading to a decrease in the time required to follow a chemical gradient to its source. This was previously shown for *V. coralliilyticus* using microfluidic gradient experiments[27,28] and appears to be a more general feature of Vibrios, having also been observed in *V. alginolyticus* chemotaxing toward amino acids[140]. While swimming fast is expensive in the typically dilute ocean environment[176], energy is no longer limiting once nutrient-rich mucus is available. Instead, what is limiting is the window of time that bacteria can exploit that mucus signal to reach the host. Not only can ambient water currents transport bacteria past the coral surface, but intense vortical flows produced by the corals themselves through cilia on their surfaces – moving at speeds much greater than bacterial swimming speeds – can result in rapid alternation of transport toward and away from the coral surface[177]. In this hydrodynamic environment, the colonization of a host by a bacterial pathogen

is a challenging behavioral feat, a 'landing in a storm', where the opportunity to home in and attach to the coral surface may only last minutes or even less. The rapid response we reported here is consistent with this dynamic environment. In particular, the strong chemokinesis – where bacteria doubled their speed – is consistent with the need to reduce the time required to migrate to the coral surface once the detection of mucus indicates the presence of a coral.

A confluence of environmental and chemical cues, including elevated temperature and nutrient influx, may be responsible for the induction of chemokinesis by *V. coralliilyticus* in coral mucus. Chemokinesis can be considered to represent a virulence trait, since chemokinesis in coral mucus was almost entirely absent at a temperature at which *V. coralliilyticus* is avirulent. This result is consistent with the temperature-dependence of chemokinesis observed in our previous study[28]. Entry into coral mucus represents a dramatic change in nutrient exposure for *V. coralliilyticus* compared to the oligotrophic reef waters. Accordingly, *V. coralliilyticus* rapidly upregulated metabolic pathways of nutrients that are present in coral mucus, which may fuel the energetically expensive chemokinesis trait, as well as protein production (ribosome and tRNA biosynthesis) and cell growth (*ftsZ* and *rpoD*) genes that may enable rapid proliferation and confer a competitive advantage to pathogens as they invade the coral host microbiome[178,179]. Chemokinesis upon homogeneous addition of nutrients has been observed in other bacteria including *Rhodobacter sphaeroides*[180], *E. coli*[181] and *Azospirillum brasilense*[182], and it has been speculated that this swimming speed enhancement is mediated by increasing the proton motive force that is responsible for flagellar rotation[139,182]. In line with this, *V. coralliilyticus* exposed to coral mucus increased the expression, on a similar time scale as the chemokinesis behavior, of genes encoding the Na^+-NQR enzyme, which builds the sodium motive force that drives flagellar rotation[147,148]. The identification of other chemical and environmental cues in coral mucus that induce the chemokinesis behavior is subject to further study.

Flagellar genes were downregulated at the early RNA-seq time point (10 min), when swimming speed was 1.88-fold higher than before mucus addition. The swimming phenotype may thus persist using the existing polar flagellum, while downregulation of flagellar genes may be a strategy to prevent further replenishment of the flagellar apparatus during the transition to a non-motile phase, evidenced by the concurrent upregulation of biofilm genes. This observation has a

parallel in the removal and downregulation of flagella observed in pathogens within the human mucosa, where it is speculated to be a strategy to escape immunological detection by the host, since flagella are strong inducers of pro-inflammatory signaling[183]. While corals possess innate and adaptive-like immunity[21], whether a similar dynamic occurs on the coral surface is currently not known.

The master regulator of *Vibrio* virulence, ToxR, and its associated protein ToxS, were upregulated in coral mucus at 10 min. ToxR is essential for coral infection by *V. coralliilyticus*[32,36], and in *V. cholerae*, the ToxR regulatory system coordinates the transcription of colonization, motility, and virulence genes in response to environmental conditions[184,185]. Indeed, these downstream effects of ToxR were observed in our RNA-seq results. The temporal modulation of quorum-sensing autoinducer molecules (AI-1, AI-2, CAI-1) as seen in our RNA-seq data may be a strategy to coordinate metabolic and lifestyle transitions at the population level, as has been observed in *Vibrio harveyi*[186]. One such lifestyle transition may be biofilm formation, which is tightly regulated by quorum sensing in *Vibrio* pathogens[158,187]. Indeed, we observed the upregulation of biofilm-related *vps* and *rbm* gene clusters in coral mucus at 10 min. Furthermore, we observed the upregulation of important *Vibrio* toxins, VcpB zinc metalloprotease, and VchA and VchB hemolysins, in coral mucus at both 10- and 60-min time points. Similarly, several secretion systems were upregulated, including the Sec-dependent and type 2 secretion systems, which are together responsible for extracellular secretion of a broad range of proteins, including toxins and degradative enzymes involved in the pathogenesis of many Gram-negative bacteria[188–190]. Type 6 secretion systems are responsible for the injection of toxic effector proteins into bacterial cells in antagonistic interactions[191–193]. Taken together, the upregulation of *toxR* and *toxS*, as well as their downstream gene expression effects, suggest that coral mucus serves as an environmental signal for *V. coralliilyticus* to activate host colonization and virulence gene expression programs.

The VcpB zinc metalloprotease is a key virulence factor of *V. coralliilyticus* that causes photoinactivation of coral endosymbionts and coral tissue lesions[31], and its rank as one of the most strongly and significantly upregulated genes in our RNA-seq dataset suggests that the bacterium rapidly responded to coral mucus as a cue to initiate its virulence program. However,

the second zinc metalloprotease that has been implicated in *V. coralliilyticus* infections of corals, VcpA (EEX33179)[125], was downregulated in our experiment. The two zinc metalloproteases (VcpA and VcpB) may thus play redundant roles in *V. coralliilyticus* infections and may be important in different environmental contexts (Supplementary Discussion).

Our results underscore the rapidity of behavioral and transcriptional changes that occur in a coral pathogen upon entry into the host environment (Fig. 3.5). These changes in swimming and gene expression patterns paint a clear sequence of events immediately preceding infection – although further validation with direct phenotypic evidence is required. Upon exposure to coral mucus, the bacterial coral pathogen *V. coralliilyticus* increases swimming speed by up to two-fold within minutes, a response that, in the natural environment, would lead to faster chemotaxis and a halving of the time required for the pathogen to track the coral surface from which the mucus signal originates. Simultaneously, transcriptional changes indicate that upon mucus exposure, the bacteria nearly immediately (10 min) increase nutrient metabolism and prepare for host colonization and damage. The downregulation of motility genes, puzzling at first in view of the strong chemokinetic response, is in fact consistent with the upregulation of quorum sensing and biofilm formation genes, together suggesting a 'final dash' to the coral surface enabled by enhanced swimming speed, followed by a rapid transition to a non-motile, coral surface-associated lifestyle. The upregulation of metabolism, growth, and antibiotic resistance genes suggests that the pathogen takes advantage of mucus as a conspicuous energy source and prepares to colonize the coral surface and compete with commensal bacteria. The upregulation of host damage genes and secretion systems responsible for toxin export suggests preparation for the infection process itself. Precise temporal control of pathogenesis is a hallmark of *Vibrio* pathogens[194,195], which are capable of rapidly modulating their lifestyle between free-swimming and biofilm phases in response to their environment, in particular temperature changes[33,194,196]. The frequency of acute temperature-rise in reef waters is increasing[197], giving additional opportunities for temperature-dependent bacterial pathogens, such as *V. coralliilyticus*, to infect corals[198,199]. In this context, understanding the mechanisms underlying the earliest stages of bacterial infections is critical in anticipating future disease outbreaks and curbing coral mortality to protect the ecosystems that they support.

3.6 Figures

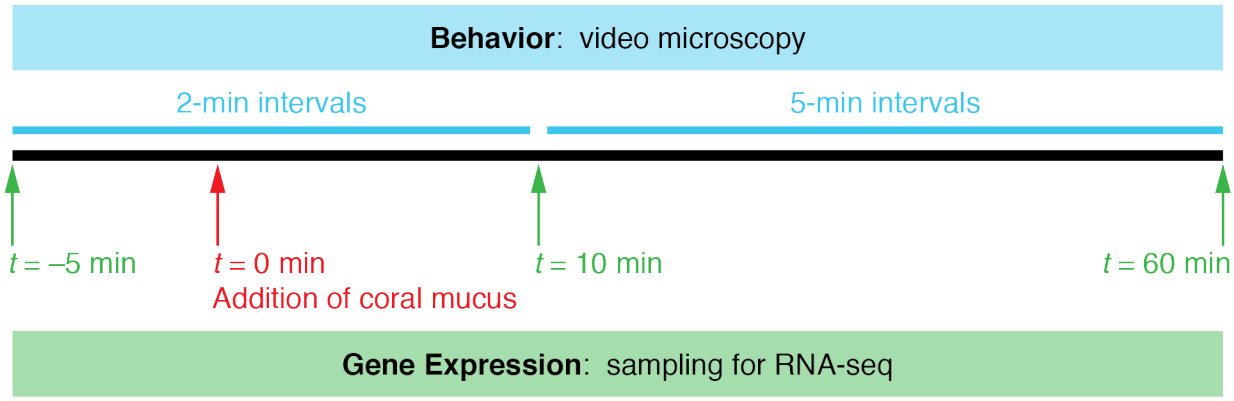

Figure 3.1 | Behavioral and transcriptional measurements of *V. coralliilyticus* in coral mucus. Experimental timeline showing time points for microscopy video acquisition and RNA-seq sampling. At $t = 0$ (red arrow), coral mucus or filtered spent medium (control) was added (1:1, v/v) to *V. coralliilyticus* cultured in 1% marine broth. The experiment was conducted at 30 °C, and repeated three times sequentially in a single day, using three different cultures of *V. coralliilyticus*.

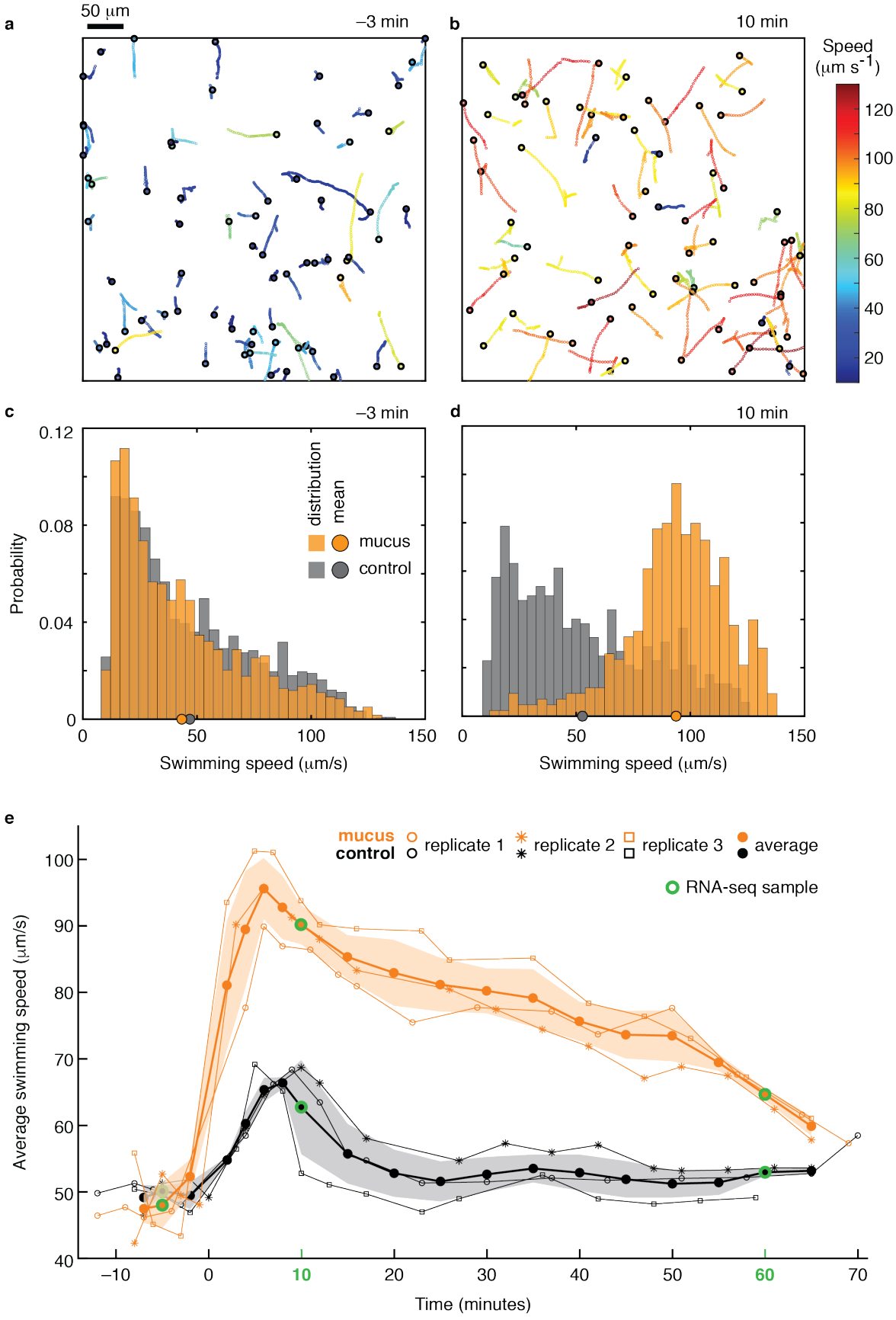
a
50 μm
–3 min
b
10 min
Speed
(μm s-1)
120
100
80
60
40
20
c
–3 min
d
10 min
0.12
0.08
0.04
0
Probability
distribution
mean
mucus
control
0
50
100
150
Swimming speed (μm/s)
e
mucus
control
replicate 1
replicate 2
replicate 3
average
RNA-seq sample
Average swimming speed (μm/s)
100
90
80
70
60
50
40
–10
0
10
20
30
40
50
60
70
Time (minutes)

Figure 3.2 | *V. coralliilyticus* exhibits strong chemokinesis upon exposure to coral mucus. Experiments were conducted at 30 °C. (**a**, **b**) Swimming tracks of *V. coralliilyticus* before (–3 min, **a**) and after (10 min, **b**) addition of coral mucus. Swimming tracks of 70 motile cells were randomly selected for each panel. Open circles represent frames of a microscopy video (0.03 seconds per frame), and black circles mark the start of each swimming track. Colors indicate the mean swimming speed of each track. (**c**, **d**) Probability distributions of swimming speeds of motile cells, before (–3 min, **c**) and after (10 min, **d**) addition of coral mucus (orange) or filtered spent medium (gray). (**e**) Average swimming speeds of motile cells before and after 1:1 addition (v/v at t = 0 min) of coral mucus (orange) or filtered spent medium (black, control). Averages (filled circles) and standard deviation (shaded regions) were calculated using data obtained from three replicate experiments (○, *, □). Data were interpolated to match time points across replicates. RNA-seq samples were taken at −5, 10, and 60 min (green circles). Data from replicate 3 are presented in panels **a–d**.

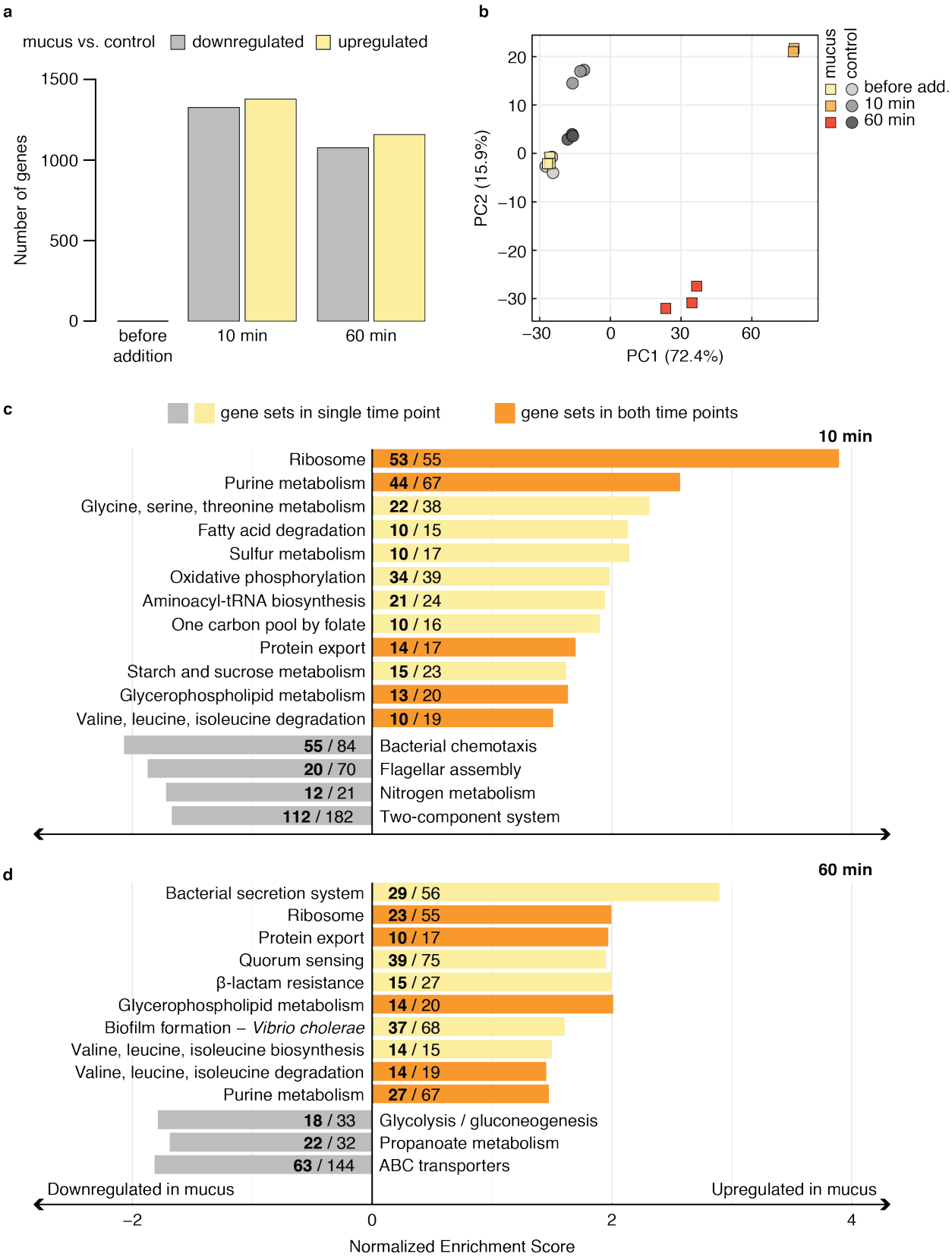
a
mucus vs. control
downregulated
upregulated
Number of genes
1500
1000
500
0
before addition
10 min
60 min
b
PC2 (15.9%)
PC1 (72.4%)
20
10
0
−10
−20
−30
−30
0
30
60
mucus
control
before add.
10 min
60 min
c
gene sets in single time point
gene sets in both time points
10 min
Ribosome 53 / 55
Purine metabolism 44 / 67
Glycine, serine, threonine metabolism 22 / 38
Fatty acid degradation 10 / 15
Sulfur metabolism 10 / 17
Oxidative phosphorylation 34 / 39
Aminoacyl-tRNA biosynthesis 21 / 24
One carbon pool by folate 10 / 16
Protein export 14 / 17
Starch and sucrose metabolism 15 / 23
Glycerophospholipid metabolism 13 / 20
Valine, leucine, isoleucine degradation 10 / 19
55 / 84 Bacterial chemotaxis
20 / 70 Flagellar assembly
12 / 21 Nitrogen metabolism
112 / 182 Two-component system
d
60 min
Bacterial secretion system 29 / 56
Ribosome 23 / 55
Protein export 10 / 17
Quorum sensing 39 / 75
β-lactam resistance 15 / 27
Glycerophospholipid metabolism 14 / 20
Biofilm formation – Vibrio cholerae 37 / 68
Valine, leucine, isoleucine biosynthesis 14 / 15
Valine, leucine, isoleucine degradation 14 / 19
Purine metabolism 27 / 67
18 / 33 Glycolysis / gluconeogenesis
22 / 32 Propanoate metabolism
63 / 144 ABC transporters
Downregulated in mucus
Upregulated in mucus
−2
0
2
4
Normalized Enrichment Score

Figure 3.3 | Exposure to coral mucus leads to genome-wide transcriptional shifts in *V. coralliilyticus*. (**a**) Number of genes that were significantly upregulated or downregulated in coral mucus at each time point (FDR $\alpha < 0.01$). (**b**) Principal component analysis (PCA) plot showing all RNA-seq samples in the 2D plane spanned by the first two principal components. PCA was performed using raw read count data after variance stabilizing transformation. (**c**, **d**) Gene set enrichment analyses (GSEA) on mucus vs. control at 10 min (**c**) and 60 min (**d**). Gene sets (KEGG pathways, bar labels) that were significantly upregulated or downregulated in coral mucus (FDR $q < 0.25$) are shown, and their bars are ordered top to bottom by FDR q-values (smallest to largest; i.e., most significant to least significant) within each expression category (upregulated in mucus, yellow/orange, or downregulated in mucus, gray). Number of significantly differentially expressed genes in mucus that were included in the GSEA (bold), and the total number of genes in the *V. coralliilyticus* genome assigned to the KEGG pathway, are shown. Orange bars represent gene sets that were upregulated in mucus at both 10 and 60 min.

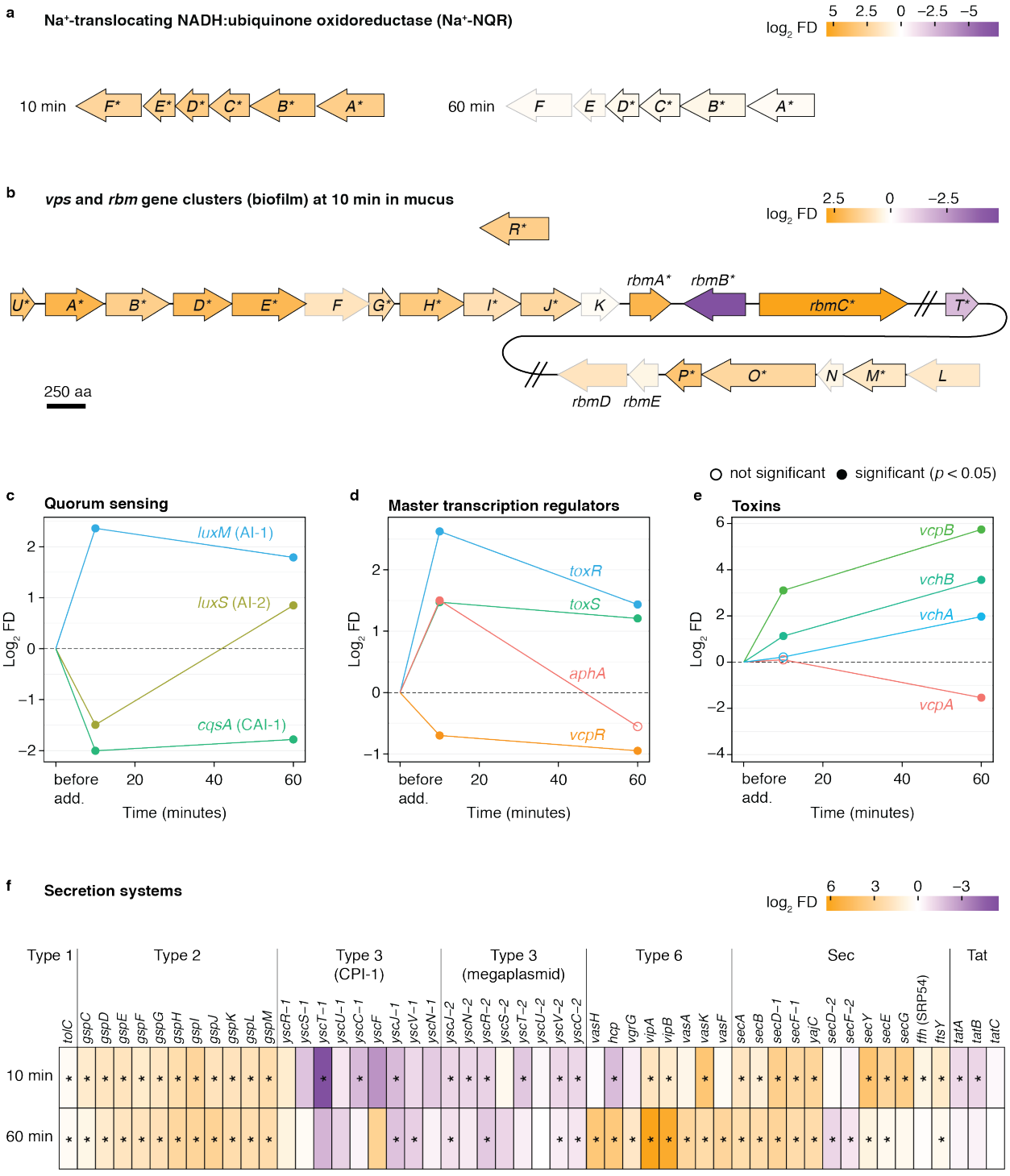
a
Na+-translocating NADH:ubiquinone oxidoreductase (Na+-NQR)
log2 FD 5 2.5 0 −2.5 −5
10 min
F* E* D* C* B* A*
60 min
F E D* C* B* A*
b
vps and rbm gene clusters (biofilm) at 10 min in mucus
log2 FD 2.5 0 −2.5
R*
U* A* B* D* E* F G* H* I* J* K rbmA* rbmB* rbmC* T*
P* O* N M* L
rbmD rbmE
250 aa
not significant significant (p < 0.05)
c
Quorum sensing
luxM (AI-1)
luxS (AI-2)
cqsA (CAI-1)
Log2 FD
before add.
Time (minutes)
d
Master transcription regulators
toxR
toxS
aphA
vcpR
e
Toxins
vcpB
vchB
vchA
vcpA
f
Secretion systems
log2 FD 6 3 0 −3
Type 1
Type 2
Type 3 (CPI-1)
Type 3 (megaplasmid)
Type 6
Sec
Tat
tolC gspC gspD gspE gspF gspG gspH gspI gspJ gspK gspL gspM yscR−1 yscS−1 yscT−1 yscU−1 yscC−1 yscF yscJ−1 yscV−1 yscN−1 yscJ−2 yscN−2 yscR−2 yscS−2 yscT−2 yscU−2 yscV−2 yscC−2 vasH hcp vgrG vipA vipB vasA vasK vasF secA secB secD−1 secF−1 yajC secD−2 secF−2 secY secE secG ffh (SRP54) ftsY tatA tatB tatC
10 min
60 min

Figure 3.4 | Differential expression of Na^+-NQR enzyme, surface association, and host damage genes in coral mucus. Log_2-transformed fold difference between mucus and control (log_2 FD) and their adjusted *p*-values were determined using DESeq2. (**a**) Na^+-NQR genes *nqrA–F* were identified through homology with *nqr* genes of *Vibrio alginolyticus* (Supplementary Table 3.6). (**b**) *Vibrio* biofilm genes in the *vps* and *rbm* gene clusters were identified through homology with *V. cholerae* genes (Supplementary Table 3.7). *Vps* genes (*vpsU, vpsA–P, vpsR, vpsT*) (**a**) and *nqr* genes (*nqrA–F*) (**b**) are labeled with their respective suffix letters. Lengths of arrows are proportional to protein size (scale bar; aa = amino acids). (**c–e**) Log_2 FD of quorum-sensing autoinducer synthase genes (**c**), *Vibrio* master transcription regulators (**d**), and toxins (**e**) at 10 and 60 min. Homology was found with genes in other Vibrios (Supplementary Table 3.8). Fold difference before addition was assumed to be 1:1 (mucus:control, log_2 FD = 0). (**c**) Heatmap showing differential expression of secretion system genes identified through KEGG pathway assignments (Supplementary Table 3.9). The *V. coralliilyticus* genome has two sets of type 3 secretion genes[33]. CPI-1, Coralliilyticus Pathogenicity Island-1. Colors (**a**,**b**,**f**) indicate log_2 FD values. Asterisks (**a**,**b**,**f**), black outlines of arrows (**a–b**), and closed circles (**c–e**) mark genes with significant differential expression (adjusted $p < 0.05$). Open circles, not significant.

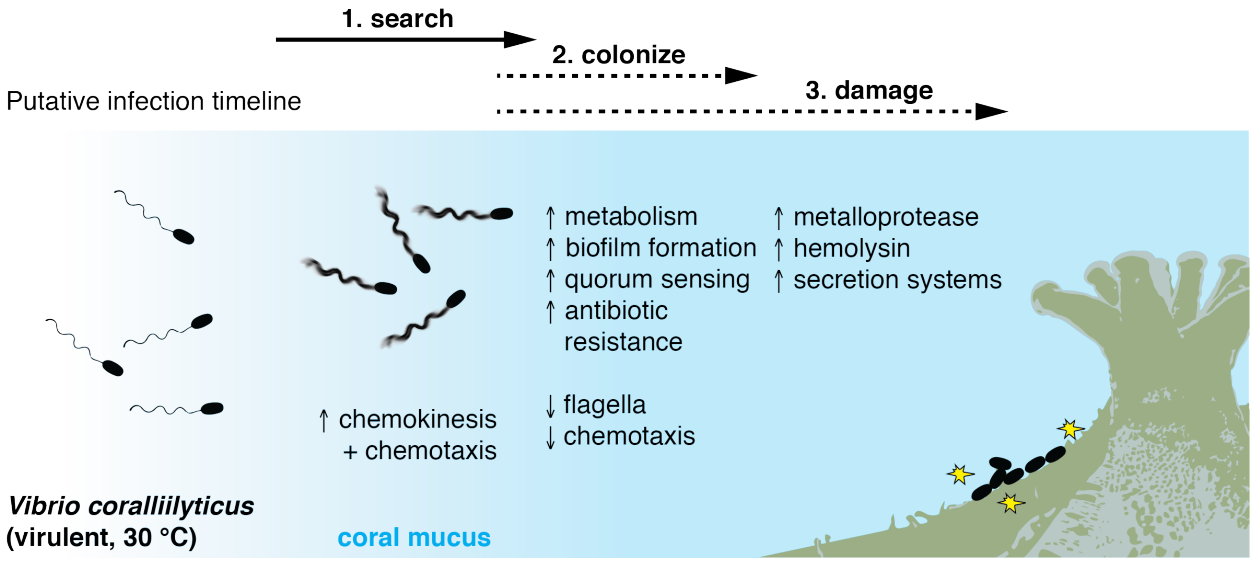

Figure 3.5 | Putative infection timeline of *V. coralliilyticus*. Our results suggest that exposure to coral mucus triggers a suite of behavioral and transcriptomic responses in *V. coralliilyticus* leading up to infection. Within two minutes, coral mucus induces strong chemokinesis, which allows the pathogens a faster final dash toward the coral surface via chemotaxis[27,28]. Early upon coral mucus exposure, upregulation of genes for metabolism of mucus components, biofilm formation, quorum sensing, and antibiotic resistance, and downregulation of flagella- and chemotaxis-related genes, enable host colonization and competition with commensal bacteria. Toxin genes (zinc metalloproteases and hemolysins; yellow stars) and secretion system genes are upregulated in coral mucus, which may lead to host tissue and symbiont damage. Solid arrows indicate bacterial responses for which we have direct observational evidence; dotted arrows indicate hypothesized phenomena based on our RNA-seq data.

3.7 Supplementary Methods

3.7.1 RNA sampling, isolation, sequencing, and sequence alignment

RNA extraction.

For total RNA extraction, each sample was thawed, the closed tip of the filter cartridge was cut open, and the RNAlater solution was removed by filtration through the membrane by attaching a syringe. The filter cartridge was then broken in a sterile Whirl-Pak plastic bag using a hammer to access the filter membrane containing RNA-stabilized cells. The filter membrane was cut into pieces and placed in Eppendorf tubes containing 15 mg/ml lysozyme, vortexed, and incubated at 37 °C for 10 min. Samples were bead-beaten with sterile autoclaved beads for 10 min, with brief submersion of the sample-containing tubes in ice at 2-min intervals to keep cool. Tubes were centrifuged at 1,000 rpm in a microcentrifuge for 1 min and the supernatant was collected into new tubes, which were centrifuged at 14,000 rpm for 3 min. To each pellet, 1 ml TRIzol was added, and the tube was vortexed for 1 min for pellet dissolution, then incubated at room temperature for 5 min. Next, 200 µl chloroform was added to partition RNA into the aqueous supernatant for separation, vortexed to mix, then incubated for 8 min. After centrifuging at 12,000×*g* for 15 min, the aqueous phase was removed. To increase precipitation efficiency from the dilute RNA solutions, 1 µl glycogen (15 mg/ml) was added, followed by 0.5 ml isopropanol to precipitate total RNA. After overnight incubation at −80 °C, samples were centrifuged at 14,000 rpm for 30 min. Pellets were washed with 70% ethanol, centrifuged at 12,000×*g* for 5 min, and air-dried. Extracted total RNA pellets were resuspended in 50 µl DEPC-treated RNase-free water and stored at −80 °C. The coral mucus-only RNA extraction control did not yield any detectable RNA.

Ribosomal RNA removal and mRNA sequencing.

Ribosomal RNA was removed from total RNA using Ribo-Zero rRNA Removal Kit for bacteria (Epicentre Biotechnologies). Due to low RNA yield, all samples from replicates 1 and 2 were sequenced using the ultra-low input protocol (> 10 ng total RNA), while replicate 3 samples were sequenced using the low input protocol (> 100 ng total RNA). The sample-to-sample distance heatmap showed clustering of samples according to time point and condition, confirming that the different sequencing protocols (ultra-low or low inputs), did not affect our

RNA-seq results (Supplementary Fig. 3.16). Due to RNA degradation, the mucus-treatment sample at 10 min from replicate 2 could not be sequenced. Thus, 17 samples in total were sequenced.

Stranded cDNA libraries were generated using the Truseq Stranded RNA LT kit (Illumina). The rRNA-depleted RNA was fragmented and reverse transcribed using random hexamers and SSII (Invitrogen) followed by second strand synthesis. The fragmented cDNA was treated with end-pair, A-tailing, adapter ligation, and 10 cycles (15 cycles for the ultra-low input protocol) of PCR. The prepared libraries were quantified using KAPA Biosystem's next-generation sequencing library qPCR kit and run on a Roche LightCycler 480 real-time PCR instrument. The quantified libraries were then prepared for sequencing on the Illumina HiSeq sequencing platform using a TruSeq paired-end cluster kit, v4, and Illumina's cBot instrument to generate a clustered flow cell for sequencing. Sequencing of the flow cell was performed on the Illumina HiSeq2500 sequencer using HiSeq TruSeq SBS sequencing kits, v4, following a 2x100 indexed run recipe.

Sequence processing and alignment.

Raw FASTQ file reads were filtered and trimmed using the JGI QC pipeline. Using BBDuk (www.sourceforge.net/projects/bbmap), raw reads were evaluated for artifact sequences by kmer matching (kmer = 25), allowing 1 mismatch. Detected artifacts were trimmed from the 3' ends of the reads. RNA spike-in reads, PhiX reads, and reads containing any Ns were removed. Quality trimming was performed using the Phred trimming method set at Q10. Following trimming, reads under the minimum length threshold of 45 bases were removed.

Raw reads from each library were aligned to the reference genome (*V. coralliilyticus* ATCC BAA-450, NCBI Taxon ID 675814) using BWA[200] with only unique mapping allowed (BAMs/directory). If a read mapped to more than one location, it was excluded. As a result, 99.48% (5022 genes) of the filtered FASTQ reads mapped to the *V. coralliilyticus* reference genome. featureCounts[201] was used to generate the raw gene counts. Counts refer to fragments: for example if the library was a paired-end run where both reads aligned to the same feature/gene in the reference genome then it would be represented as a count of 1 in the raw gene counts.

3.7.2 Gene Set Enrichment Analysis (GSEA)

GSEA input table preparation.

The KEGG Pathway assignment database for genes (as KEGG Orthology (KO) identifiers) of *V. coralliilyticus* OCN014 (code vct) was obtained from Kyoto Encyclopedia of Genes and Genomes (www.genome.jp/kegg). No KEGG Pathway assignment database for *V. coralliilyticus* BAA-450 was available. According to this KEGG Pathway assignment database, there are 116 metabolic pathways with at least one gene assignment from the *V. coralliilyticus* genome.

The database containing *V. coralliilyticus* ATCC BAA-450 reference genome information, including KO number assignments of genes, was obtained from the JGI IMG website (https://img.jgi.doe.gov). According to the JGI dataset, 2355 genes in the *V. coralliilyticus* BAA-450 genome did not have a KO number assigned. Most of these genes with no KO number assignment were annotated as "hypothetical proteins" (1089 genes). Of the remaining 2789 genes with KO number assignments, 1375 were not assigned to any KEGG pathways. This may be due to the difference in the strains of *V. coralliilyticus* between the KEGG (OCN014) and JGI (BAA-450) databases, but is more likely due to inadequate information available on the genes for pathway assignment. As a result, 1414 genes that were assigned to at least one KEGG Pathway were included in the GSEA gene matrix table (.gmt file). The majority of the genes (888 genes) were assigned to only one KEGG Pathway. The KEGG Pathways with the greatest number of gene assignments were "two-component system" (KEGG 02020, 182 genes); "ABC transporters" (KEGG 02010; 144 genes); "bacterial chemotaxis" (KEGG 02030; 84 genes); "quorum sensing" (KEGG 02024; 75 genes); and "flagellar assembly" (KEGG 02040; 70 genes).

The ranked gene list (.rnk file) for GSEA was built for each pairwise comparison (e.g., mucus vs. control at 10 min) using the DESeq2 analysis results (containing $\log_2$ fold difference and adjusted *p*-values). The $\log_2$ fold difference values, which are biologically meaningful, were used to rank the genes. To give validity to the $\log_2$ fold difference values in the ranked gene list, only genes with significant differential expression (adjusted *p*-value < 0.01) were included in the ranked gene list. Thus, the size of genes sets (i.e., number of genes in the gene set) varied amongst different pairwise gene set enrichment analyses.

GSEA. The two tables (.gmt and .rnk files) were loaded into the GSEA software (v4.0.3)[145,146], which automatically excluded genes that were not present in the ranked gene list from gene sets. After this exclusion criterion is applied, gene sets that contained less than 10 genes were excluded from the analyses to enable accurate calculation of Enrichment Scores (ES). The following settings were used in the GSEA software: number of permutations (for statistical significance assessment of enrichment score) = 1000; scoring scheme $p = 1$ (weighted); normalization mode = meandiv (default method for normalization of Enrichment Scores across analyzed gene sets, resulting in Normalized Enrichment Score, NES). NES is the primary statistic for examining gene set enrichment results. Given the large variability expression datasets and the small number of gene sets being analyzed, a relatively inclusive FDR q-value cutoff of 0.25 was used to assess significance. All KEGG Pathways that were significantly enriched (FDR $q < 0.25$) are presented in Figure 3.3.

3.7.3 Viscosity measurements

Viscosity measurements were performed at 25.1 °C using a VISCOlab3000 (Cambridge Viscosity) viscometer with a 0.5–10 cP range piston. Estimated error determined by the instrument was 0.3% for mucus, and 2.9% for filtered artificial seawater (FASW).

3.7.4 Growth curves and DAPI-stained cell counts.

Growth curves of *V. coralliilyticus* in coral mucus or 1% marine broth (Supplementary Fig. 3.9) were measured in a sterile clear flat-bottom 48-well plate (Falcon), containing 200 µl volume per well. Coral mucus was collected on two separate days from the same *P. damicornis* coral colony and preserved at –80 °C until experimentation. Mucus was pooled and filter-sterilized (0.2 µm) before inoculation. Each growth condition was prepared in triplicates, with corresponding blank wells in triplicates (1% marine broth) or duplicates (mucus). Several bacterial colonies were picked from a marine broth agar plate, washed twice and suspended in 200 µl FASW for starvation at 30 °C for 6.5 h before it was used for inoculation. Each well was inoculated with 1 µl of prepared bacteria. The 48-well plate was incubated at 30 °C, and optical density was measured at 720 nm (OD_{720}) every 1 h (30 sec of slow orbital shaking before each time point) for 41 h using a Synergy HTX Multi-Mode Microplate Reader (BioTek Instruments).

DAPI staining followed by cell counts were performed to determine concentrations of cells associated with the OD_{720} values. Bacteria were diluted with FASW with a known dilution factor and preserved in 2% final concentration (v/v) of formaldehyde (0.2-µm-filtered). Preserved cells were kept at 4 °C until staining. Preserved cells were filtered onto a 0.2µm, 25 mm polycarbonate filter (Millipore GTBP02500) whose black color is ideal for fluorescence imaging. The DAPI dye is mixed with mounting medium (VECTASHIELD) to a final concentration of 2 µg/ml. The filter containing preserved cells was carefully touched with the DAPI-mounting medium mixture and secured between a glass slide and cover slip. Images were taken using epifluorescence microscopy with 395 nm LED excitation (10% power; Lumencor), DAPI filter cube (350/50 nm excitation; 400 nm longpass dichroic mirror; 420 nm longpass emission), 60× oil objective (CFI Plan Apochromat, numerical aperture 1.40, Nikon), and an sCMOS camera (30 ms exposure; Andor Zyla 4.2; 6.5 µm pixel). Fluorescence images were taken at ten different locations on the filter. Cells were counted manually within a cropped (400 pixels × 400 pixels) region of each image, and the mean ± s.d. cell concentration of images was calculated.

3.8 Supplementary Figures

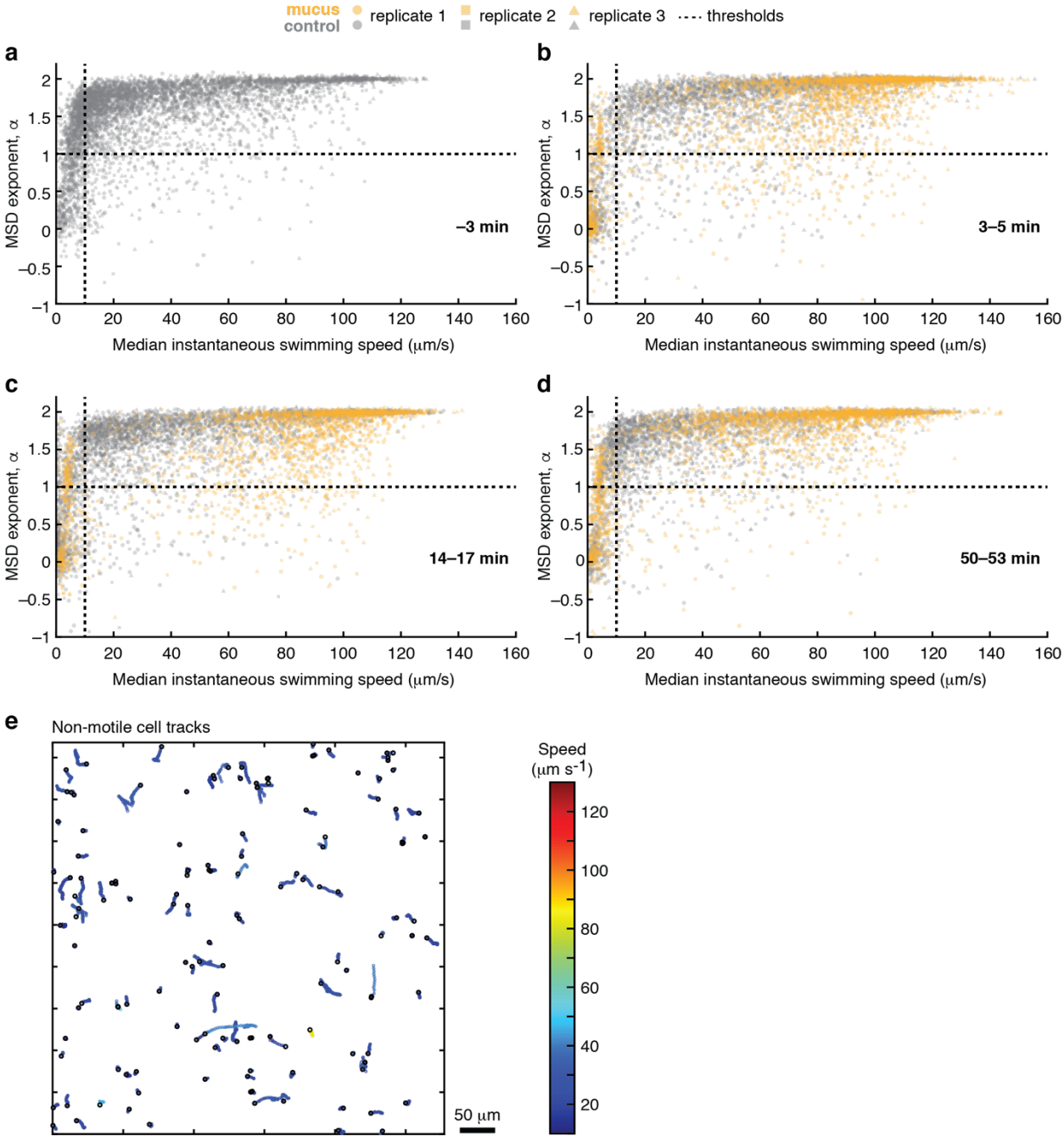

Supplementary Figure 3.1 | Threshold value selection for motile and non-motile cell determination. (**a–d**) Each point represents a single cell's trajectory (before motile or non-motile differentiation), whose median instantaneous swimming speed (V) and MSD exponent (α) are plotted. Panels represent different time points during the experiment, relative to addition of mucus (orange) or filtered spent medium (control, gray) at $t = 0$ min. Before addition, cells designated for mucus-exposure are not differentiated from control cells (**a**). Dotted lines indicate final threshold values used for motile and non-motile cell determination; median $V = 10$ μm/s; $\alpha = 1$. (**e**) Trajectories of non-motile cells determined by the application of final thresholds. A sample of 150 non-motile tracks that are 15 frames or longer (≥ 0.5 s) are presented (from replicate 1, –4 min time point). Colors indicate track swimming speed on a scale that is equal to the color scale shown in Fig. 3.2a,b.

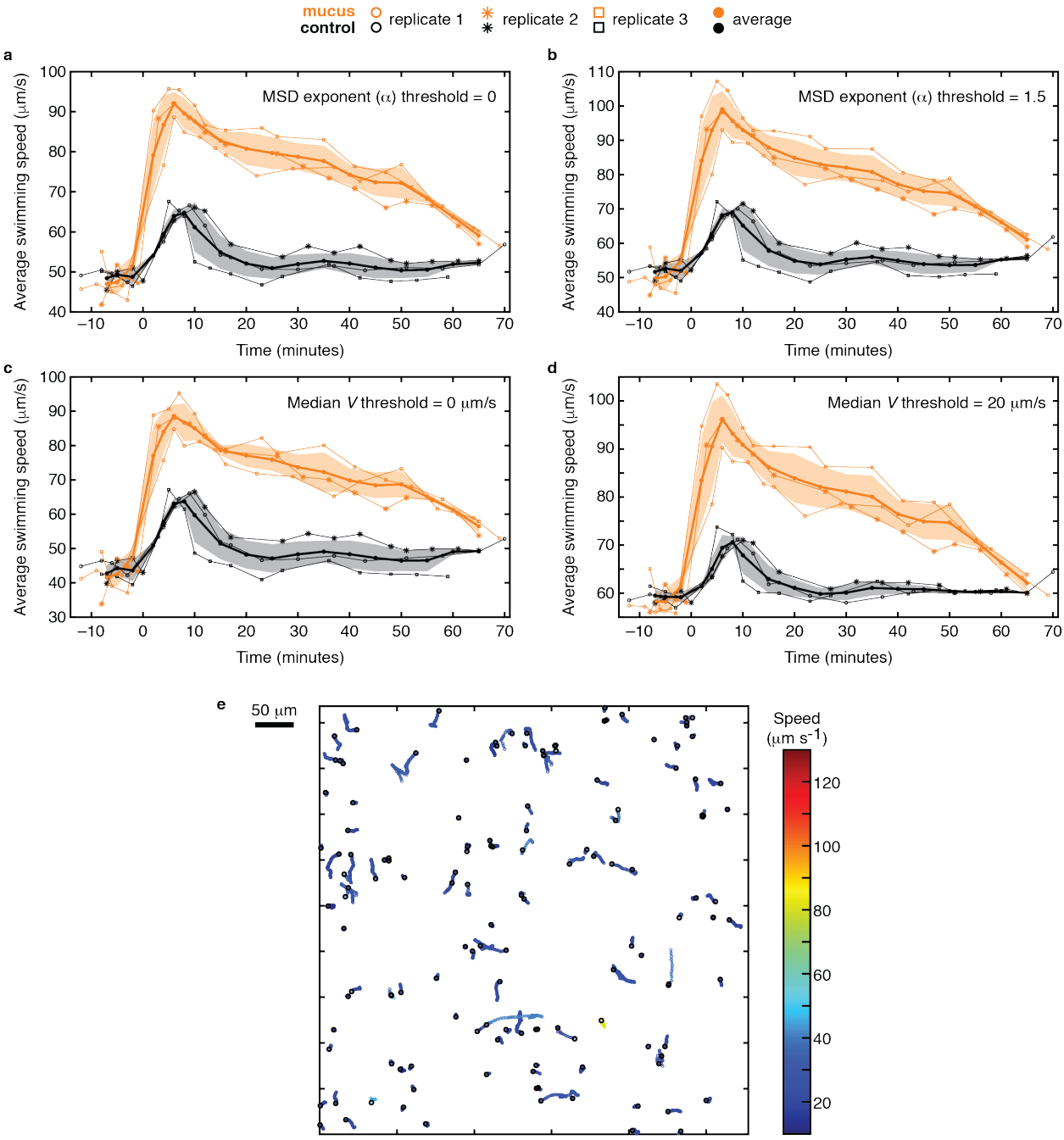

Supplementary Figure 3.2 | Effect of threshold value on swimming speed calculation. In each panel, the video microscopy data presented in Figure 3.2 were analyzed as described in Methods and Supplementary Methods, but while varying a single threshold value (α or median *V*) used to classify bacteria as motile or non-motile. The minimum threshold on MSD exponent α (α ≥ 1 in Figure 3.2) was changed to 0 in (**a**) and 1.5 in (**b**). The minimum threshold on median instantaneous swimming speed (*V*) (median *V* ≥ 10 μm/s in Figure 3.2) was changed to 0 μm/s in (**c**) and 20 μm/s in (**d**). While the range of average swimming speeds (*y*-axis) changed slightly, the main features of the speed time series were conserved regardless of the threshold values applied.

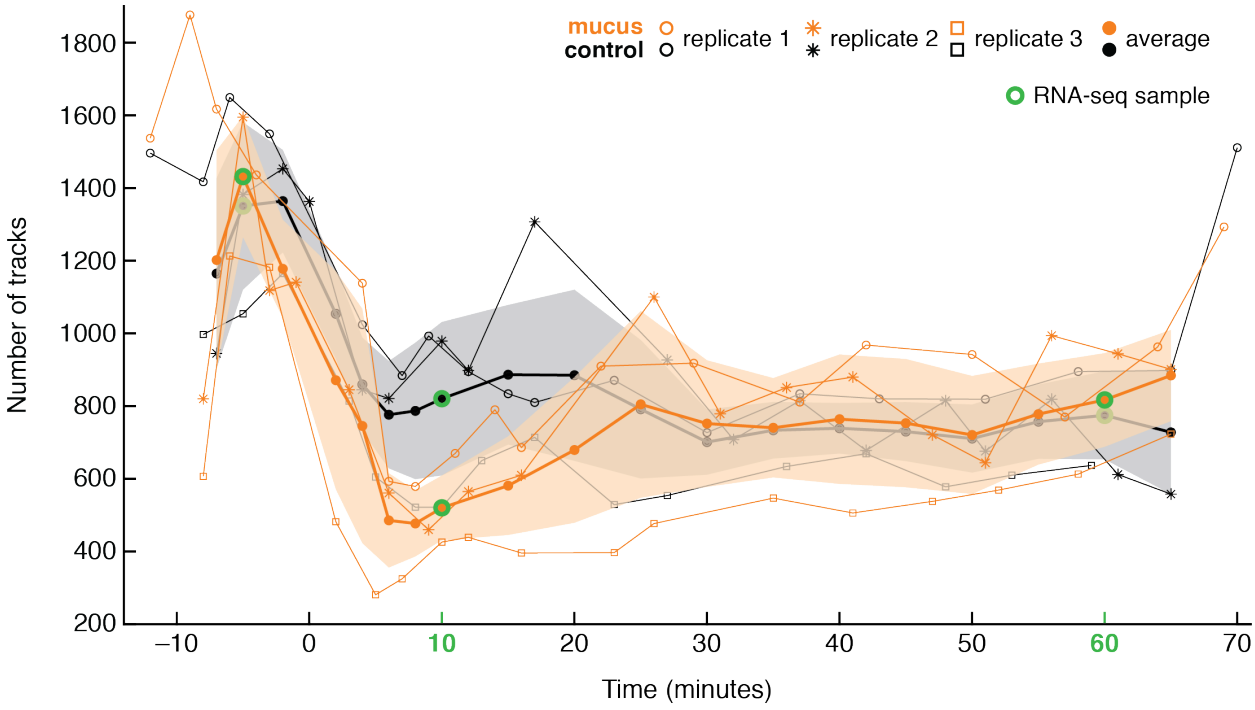

Supplementary Figure 3.3 | Number of motile cell tracks. Number of motile cell tracks that were included in the video analyses and whose results are presented in Fig. 3.2. Shaded regions represent standard deviation of replicates.

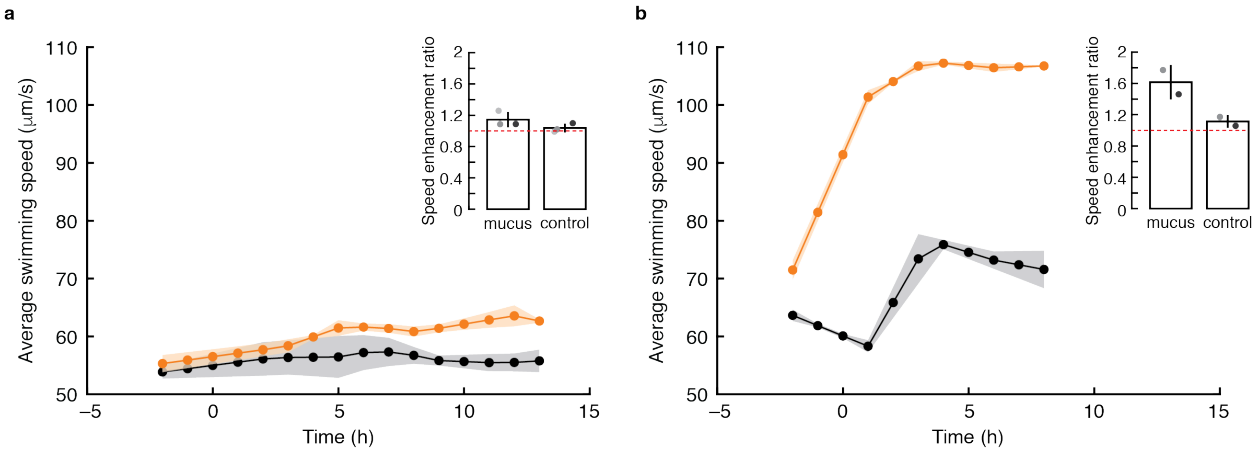

Supplementary Figure 3.4 | Chemokinesis is attenuated at 18.7 °C compared to 30 °C. *V. coralliilyticus* cultures were grown as described in Methods. At $t = 0$ min, filtered spent media (gray, control) or *Acropora millepora* coral mucus (orange) were added to cell cultures at 1:1 ratio (v/v) and incubated and imaged at 18.7 °C (room temperature, **a**) or 30 °C (**b**). Insets show the speed enhancement ratio between the swimming speed at a post-addition (5–8 min) and pre-addition (–2 min) time point (red dotted line marks ratio of 1). Shaded regions (and error bars in inset) represent s.d. of replicates, of which there were three (**a**) or two (**b**) (data points, inset). This represents the only experiment in which *A. millepora* coral mucus was used in this study.

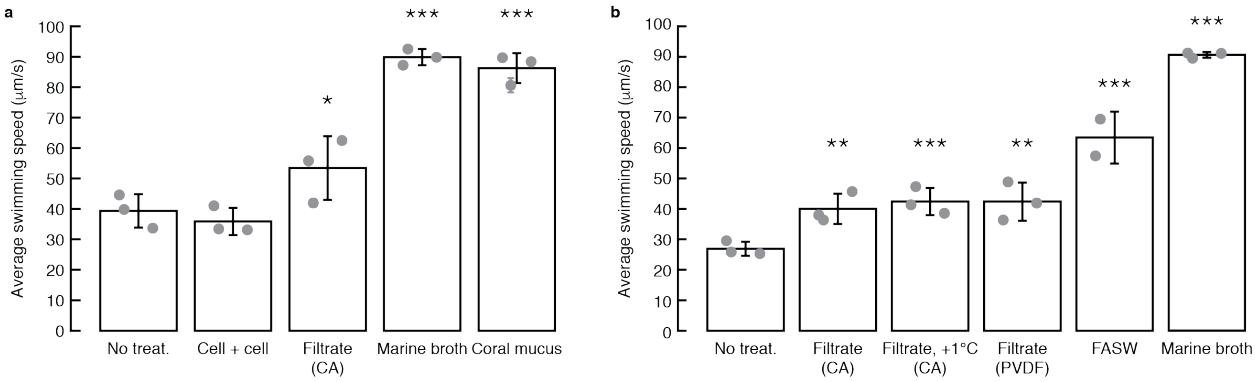

Supplementary Figure 3.5 | Chemokinesis in filtered spent media, sea water, and marine broth. Panels (**a**) and (**b**) represent two separate experiments, conducted at 30 °C. All overnight culture conditions (1% marine broth), filtered spent media preparation (~20 ml through 0.2 μm filters), and imaging setups were the same as the experiment described in the main text (Methods). Treatments were performed by adding 50 μl of each specified solution to 50 μl of cells, followed by repeated pipetting to mix. Treated cells were transferred to a microfluidic device for microscopy observation 5 min after treatment. For the "Cell + cell" condition, bacteria were aliquoted into two tubes and subsequently combined again in order to test whether the act of pipetting would cause a speed enhancement. Filtered spent media ("filtrate") were produced using two different 0.2 μm membrane materials (cellulose acetate (CA) or polyvinylidene fluoride (PVDF)) and filtration surface areas (2.8 cm^2 (CA) or 10 cm^2 (PVDF)). Higher membrane surface areas are expected to reduce the filtration pressure and thus decrease the frequency of cell-bursting that would release intracellular materials into the filtrate. Filtered spent media enhanced swimming speeds consistently (**a**,**b**), and to the same extent regardless of membrane type (CA or PVDF) or a small temperature increase (+1 °C) (**b**; two-tailed *t*-tests amongst filtrate conditions, $p > 0.01$). Chemokinesis was induced to the same extent by both marine broth and coral mucus (**a**; two-tailed *t*-tests, $p > 0.01$). Data points represent replicate treatments performed on different aliquots of cells (error bars = s.e.m. of cells; error bars may be smaller than data points). Bars and error bars represent mean and s.d. of replicate treatments. Two-tailed *t*-tests were performed on all treatment conditions compared to the no treatment condition, with significance indicated by asterisks: * $p < 0.1$; ** $p < 0.05$; *** $p < 0.01$. FASW = filtered (0.2 μm) artificial sea water.

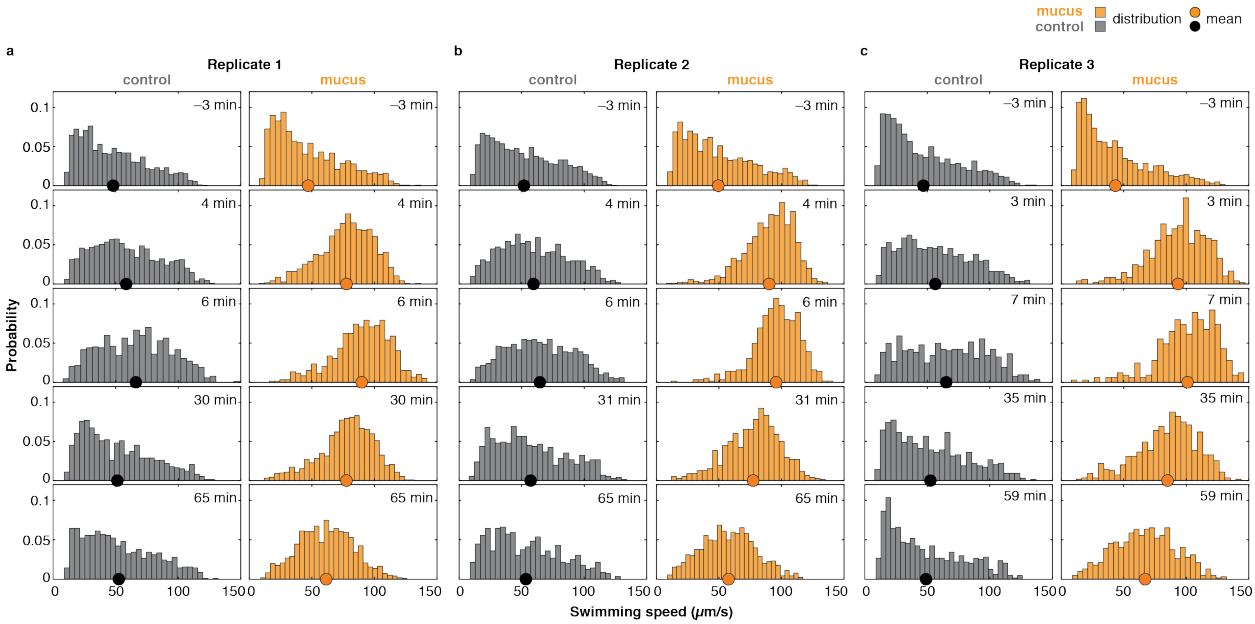

Supplementary Figure 3.6 | Probability distributions of swimming speeds of motile cells over time. Only motile cells were included in the analysis. Probability distributions of swimming speeds at different time points in replicate experiments 1 (**a**), 2 (**b**), and 3 (**c**) (number of bins = 30). Solid circles represent the average swimming speed of the population. Time points are relative to the addition of mucus or filtrate at $t = 0$ min.

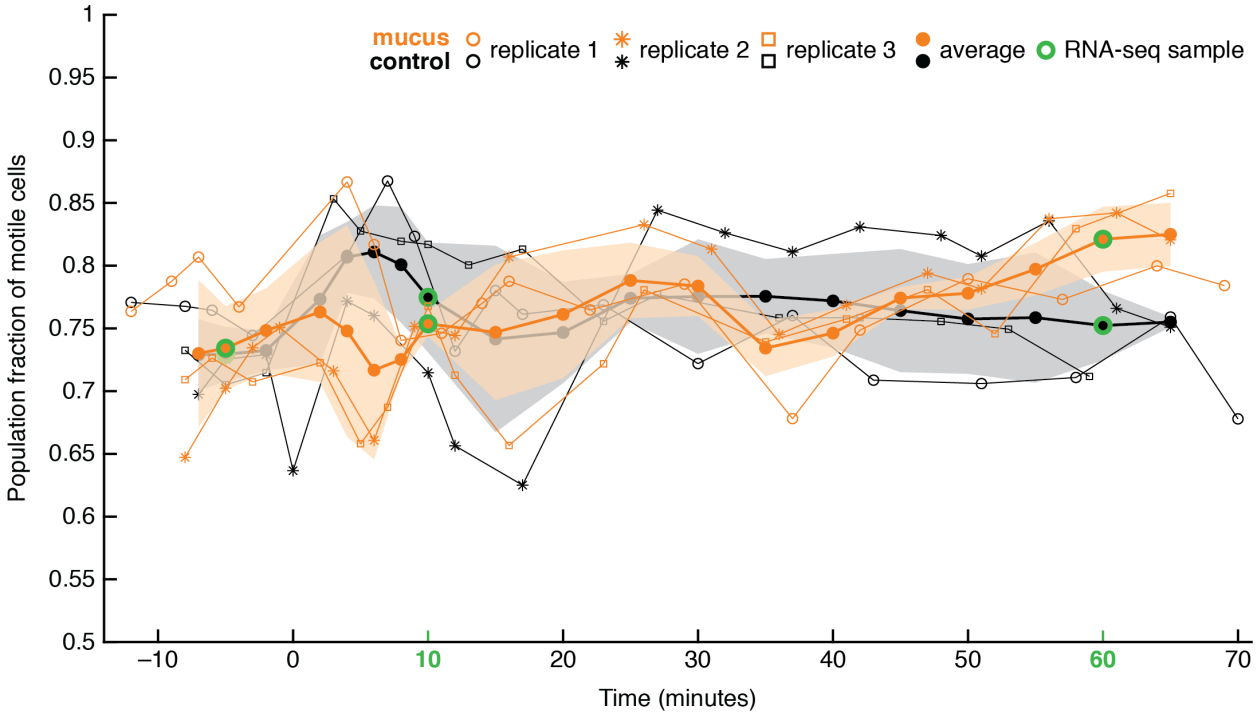

Supplementary Figure 3.7 | Population fraction of motile cells over time. The motile population fraction was calculated by dividing the number of motile cells by the total number of cell trajectories detected in each microscopy video. At all post-addition time points, neither mucus nor control populations deviated significantly from the pre-addition (control at −2 min) motile fraction value (two-tailed *t*-tests, $p > 0.01$). Furthermore, mucus and control populations did not differ significantly from each other at any time point (two-tailed *t*-tests, $p > 0.01$). Shaded regions represent standard deviation of replicates.

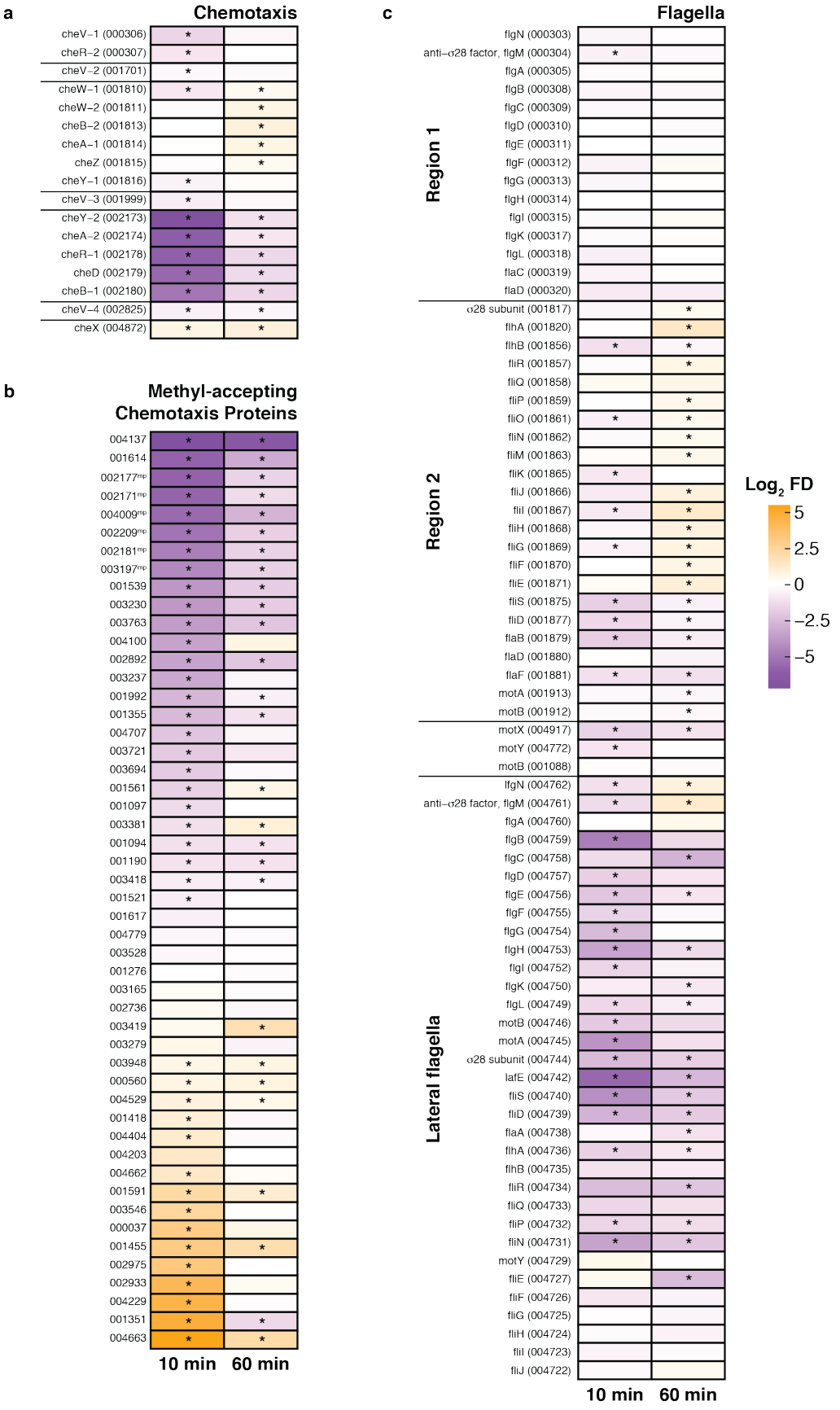
a
Chemotaxis
cheV–1 (000306)
cheR–2 (000307)
cheV–2 (001701)
cheW–1 (001810)
cheW–2 (001811)
cheB–2 (001813)
cheA–1 (001814)
cheZ (001815)
cheY–1 (001816)
cheV–3 (001999)
cheY–2 (002173)
cheA–2 (002174)
cheR–1 (002178)
cheD (002179)
cheB–1 (002180)
cheV–4 (002825)
cheX (004872)
b
Methyl-accepting Chemotaxis Proteins
004137
001614
002177mp
002171mp
004009mp
002209mp
002181mp
003197mp
001539
003230
003763
004100
002892
003237
001992
001355
004707
003721
003694
001561
001097
003381
001094
001190
003418
001521
001617
004779
003528
001276
003165
002736
003419
003279
003948
000560
004529
001418
004404
004203
004662
001591
003546
000037
001455
002975
002933
004229
001351
004663
10 min
60 min
c
Flagella
Region 1
flgN (000303)
anti–σ28 factor, flgM (000304)
flgA (000305)
flgB (000308)
flgC (000309)
flgD (000310)
flgE (000311)
flgF (000312)
flgG (000313)
flgH (000314)
flgI (000315)
flgK (000317)
flgL (000318)
flaC (000319)
flaD (000320)
Region 2
σ28 subunit (001817)
flhA (001820)
flhB (001856)
fliR (001857)
fliQ (001858)
fliP (001859)
fliO (001861)
fliN (001862)
fliM (001863)
fliK (001865)
fliJ (001866)
fliI (001867)
fliH (001868)
fliG (001869)
fliF (001870)
fliE (001871)
fliS (001875)
fliD (001877)
flaB (001879)
flaD (001880)
flaF (001881)
motA (001913)
motB (001912)
motX (004917)
motY (004772)
motB (001088)
Lateral flagella
lfgN (004762)
anti–σ28 factor, flgM (004761)
flgA (004760)
flgB (004759)
flgC (004758)
flgD (004757)
flgE (004756)
flgF (004755)
flgG (004754)
flgH (004753)
flgI (004752)
flgK (004750)
flgL (004749)
motB (004746)
motA (004745)
σ28 subunit (004744)
lafE (004742)
fliS (004740)
fliD (004739)
flaA (004738)
flhA (004736)
flhB (004735)
fliR (004734)
fliQ (004733)
fliP (004732)
fliN (004731)
motY (004729)
fliE (004727)
fliF (004726)
fliG (004725)
fliH (004724)
fliI (004723)
fliJ (004722)
10 min
60 min
Log2 FD
5
2.5
0
–2.5
–5

Supplementary Figure 3.8 | Heatmaps of motility- and chemotaxis-related gene expression. Log_2-transformed fold differences between mucus and control (log_2 FD) and their adjusted *p*-values were determined by using DESeq2. Columns represent time points, colors indicate log_2 FD, and asterisks mark genes with significant differential expression (adjusted $p < 0.05$). Numbers in row labels represent NCBI locus tags, and follow the prefix, "VIC_". Horizontal dividers mark putative operons. Chemotaxis *che* genes (**a**) and methyl-accepting chemotaxis protein (MCP) genes (**b**) were identified through bacterial chemotaxis KEGG 02030 pathway gene assignment. The fifty methyl-accepting chemotaxis protein (MCP) genes are ranked by log_2 FD values at 10 min. Superscripts "MP" in row labels mark the six MCP genes located in the *V. coralliilyticus* megaplasmid. Flagella genes (**c**) were identified through flagellar assembly KEGG 02040 pathway gene assignment. Putative flagellar regions 1 and 2 were determined by comparison with the *V. parahaemolyticus* genome[202]. Putative lateral flagella region[33], VIC_004722–VIC_004762, is also marked.

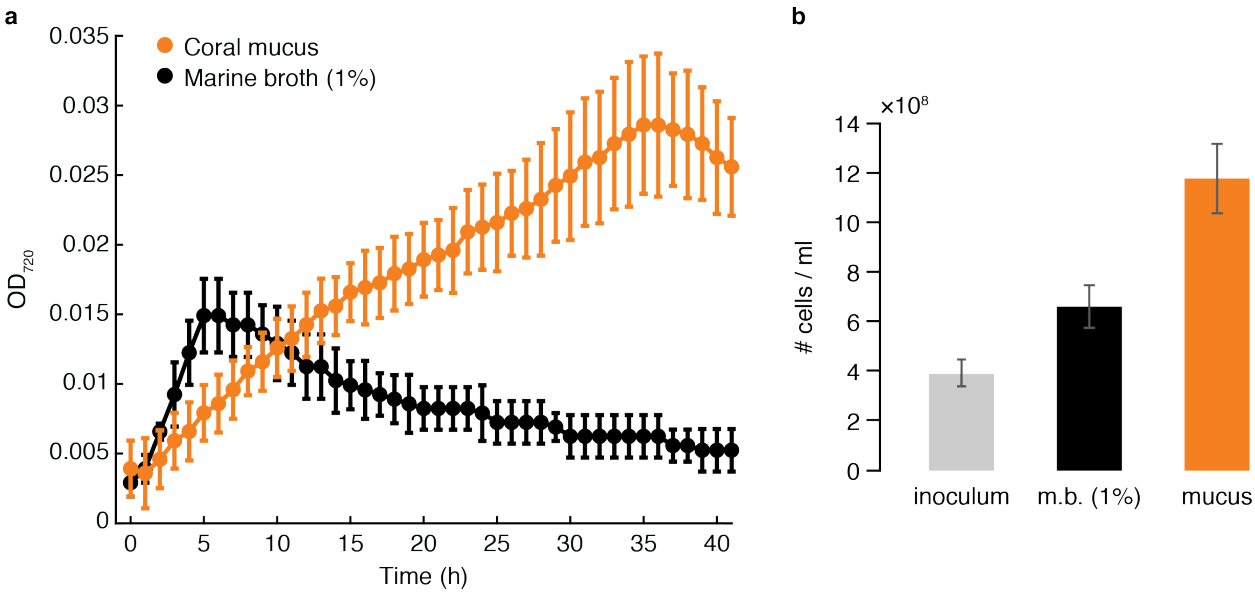

Supplementary Figure 3.9 | Growth curves of *V. coralliilyticus* in coral mucus and marine broth (1%) at 30 °C. (**a**) Optical densities (OD_{720}) of bacteria-free blank wells were subtracted before averaging over triplicate wells. Error bars are s.d. of triplicate wells. (**b**) Since OD measurements may be affected by bacterial attachment to walls, cells were sampled from the growth curve setup at the first and last time points for cell counts. DAPI-stained cells were counted, and cell concentrations were determined at inoculum (gray), and at the last time point of the growth curves for 1% marine broth (m.b., black) and coral mucus (orange). Bars and error bars are mean and s.d. of microscopy images (n = 10 images for inoculum and m.b.; n = 20 images for mucus).

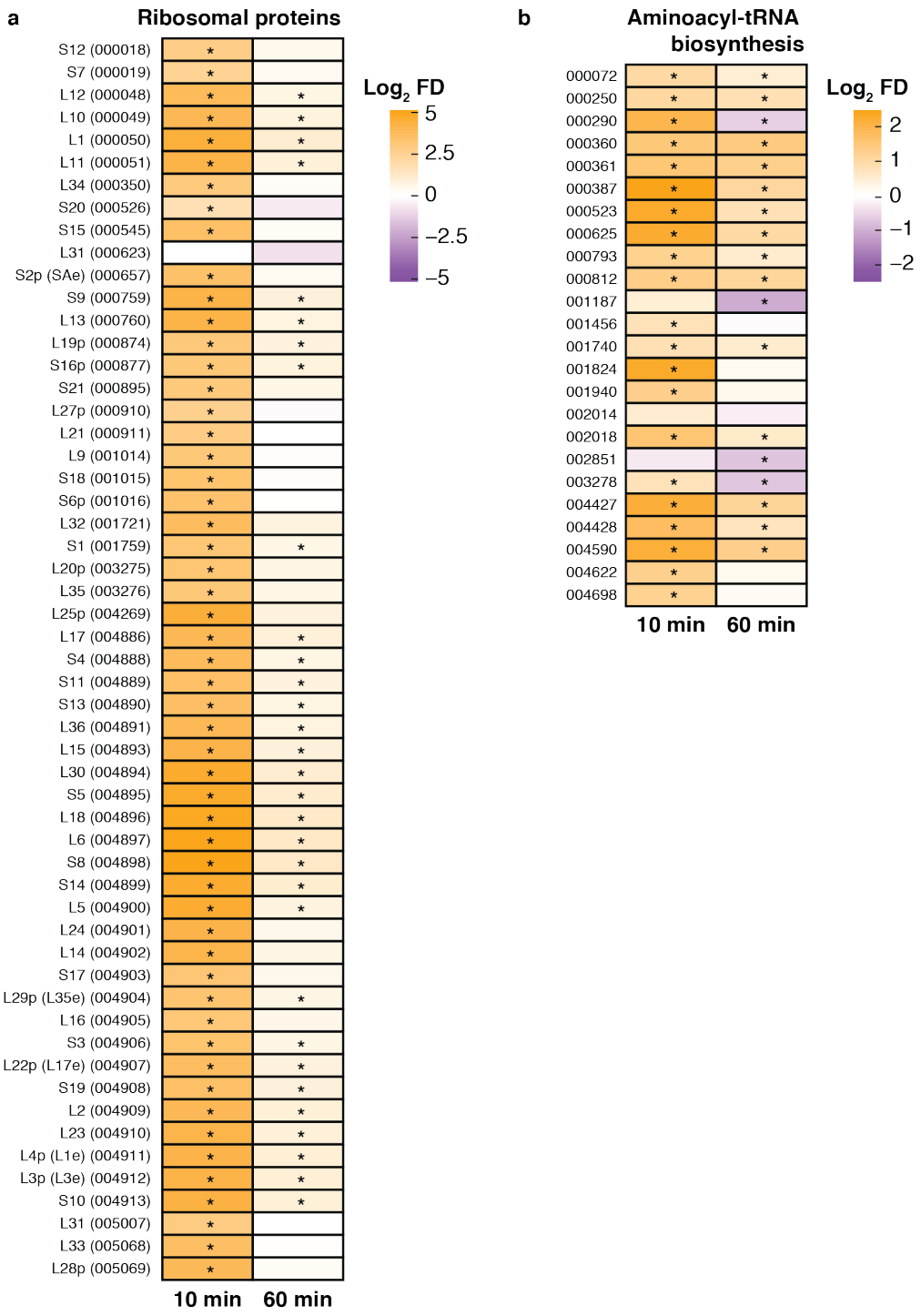

Supplementary Figure 3.10 | Heatmaps of ribosomal protein and aminoacyl-tRNA biosynthesis gene expression. Log_2-transformed fold differences between mucus and control (log_2 FD) and their adjusted *p*-values were determined by using DESeq2. Columns represent time points, colors indicate log_2 FD, and asterisks mark genes with significant differential expression (adjusted $p < 0.05$). Numbers in row labels represent NCBI locus tags, and follow the prefix, "VIC_". Ribosomal protein (**a**) and aminoacyl-tRNA biosynthesis genes (**b**) were identified through KEGG 03010 and KEGG 00970 pathway gene assignments, respectively.

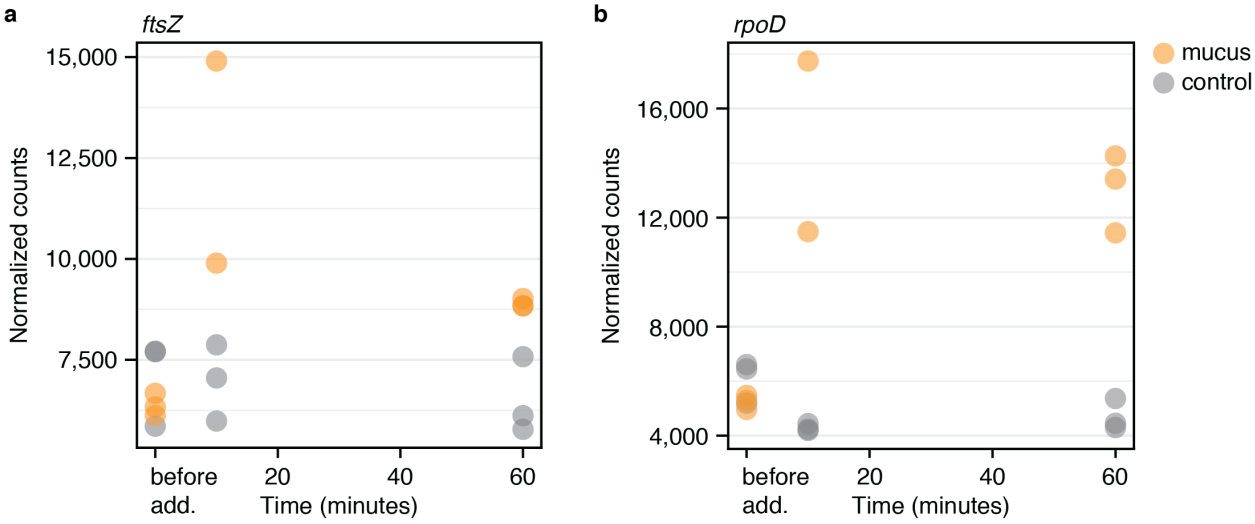

Supplementary Figure 3.11 | Growth-related genes were upregulated in coral mucus. Raw transcript counts were normalized by library size. Each data point represents a replicate experiment. (**a**) FtsZ (EEX34708) is required for bacterial cell division. Differential expression analysis (DESeq2) showed that at 10 min, upregulation of *ftsZ* in mucus was significant at adjusted $p < 0.01$ (fold change mucus vs. control, 1.78×) but at 60 min, upregulation was significant only at adjusted $p < 0.05$ (1.37×). (**b**) RpoD (EEX34866) is the principal RNA polymerase sigma factor for the transcription of growth-related genes. Upregulation of *rpoD* in mucus was significant at both 10 and 60 min (adjusted $p < 0.01$; 3.41× at 10 min and 2.78× at 60 min).

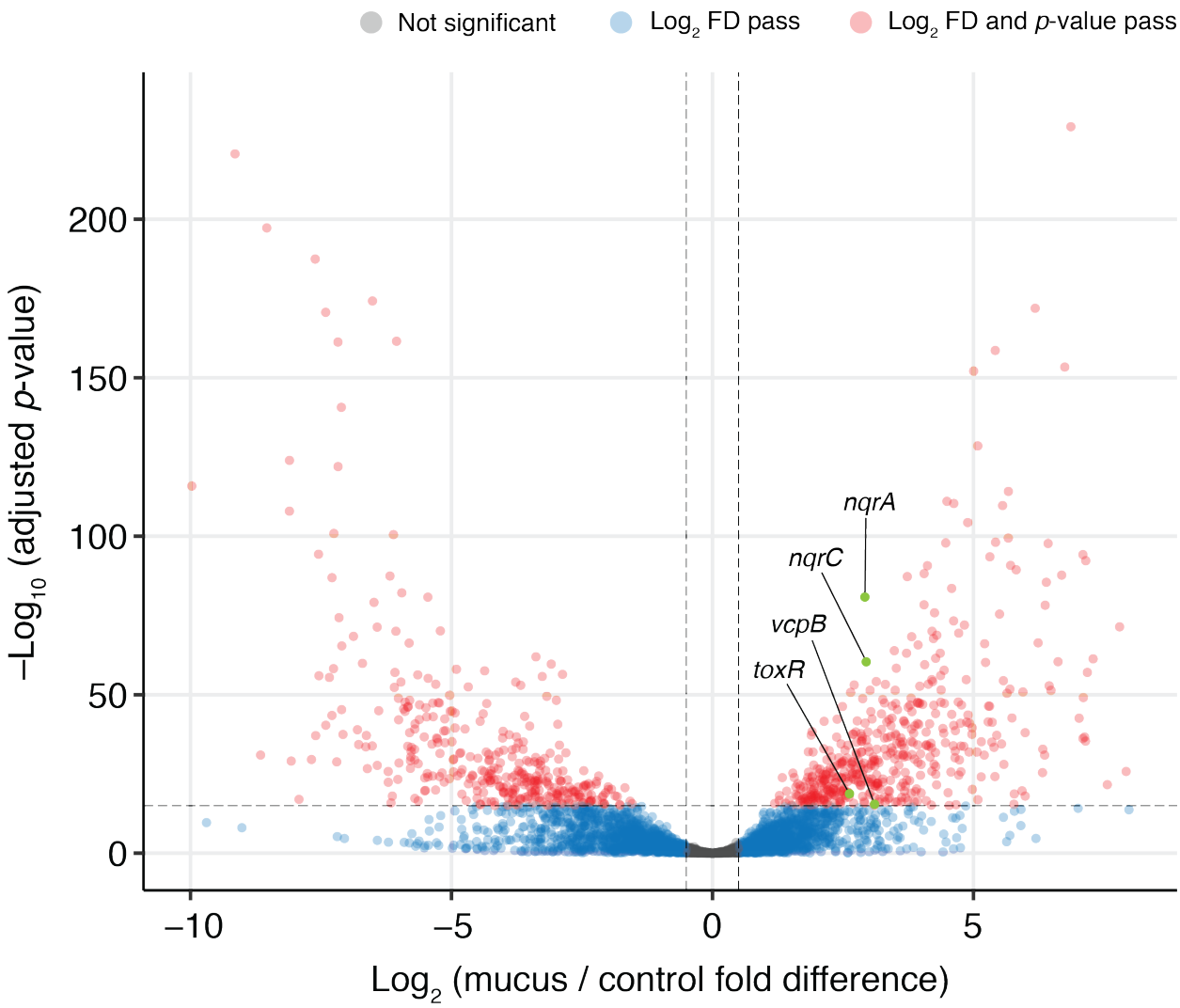

Supplementary Figure 3.12 | Volcano plot of differential expression at 10 minutes. Log_2-transformed fold differences between mucus and control (log_2 FD) at 10 min and their adjusted *p*-values (negative log_{10}-transformed) were determined by using DESeq2. Each point represents a single gene. For visualization only, the plot is segmented by cutoffs on log_2 FD at –0.5 and 0.5, and adjusted *p*-value at 1×10^{-15} (dotted lines; note that these cutoffs differ from thresholds applied in DESeq2 analyses). Four notable genes that are strongly and significantly upregulated are highlighted (green dots): NA^+-NQR genes *nqrA* (EEX34667) and *nqrC* (EEX34665); virulence-implicated zinc metalloprotease *vcpB* (EEX32371); virulence master regulator *toxR* (EEX35320).

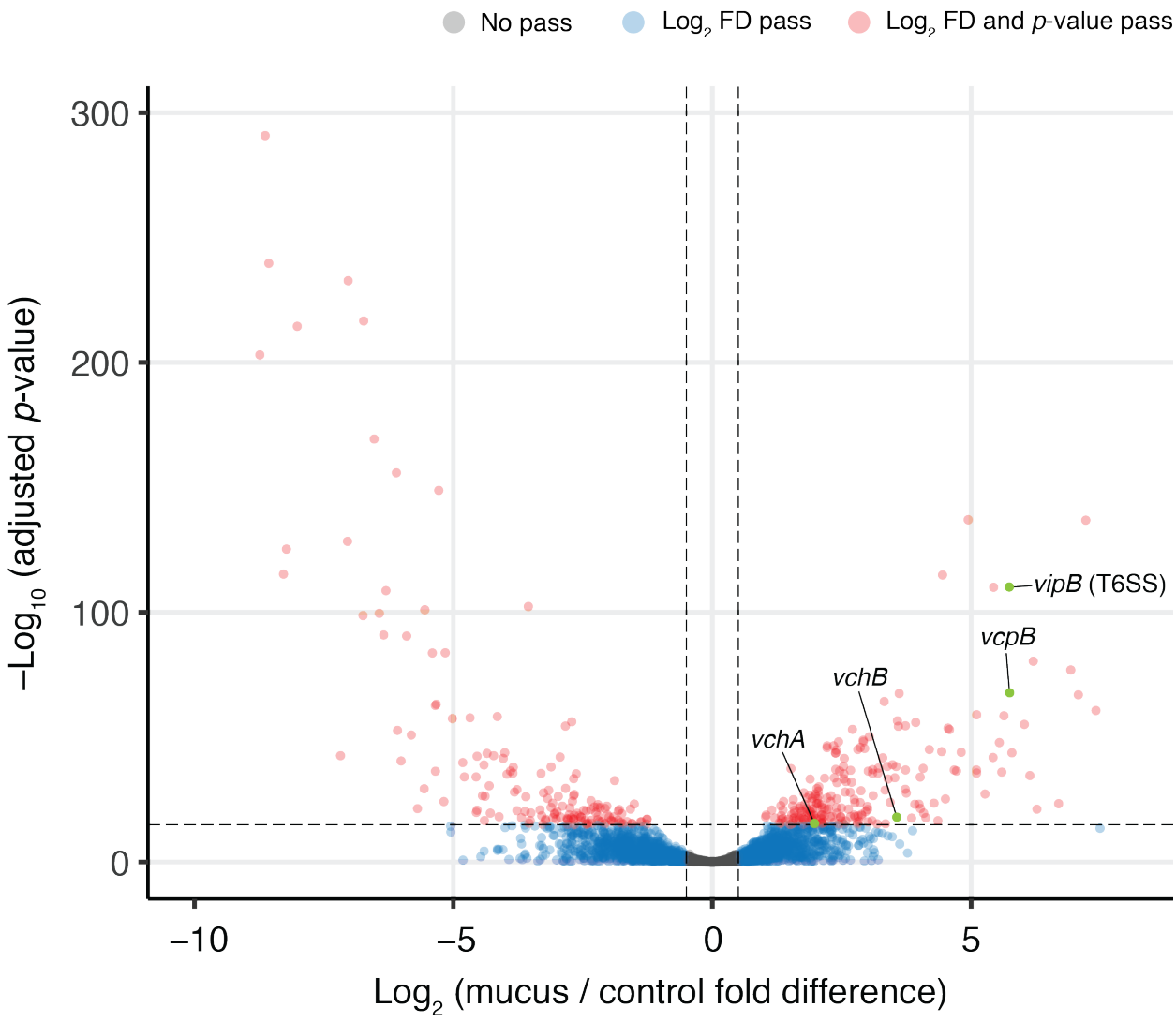

Supplementary Figure 3.13 | Volcano plot of differential expression at 60 minutes. Same as Supplementary Figure 12 except at the 60 min time point. Four notable genes that are strongly and significantly upregulated are highlighted (green dots): Type 6 secretion system gene *vipB* (EEX32048); virulence-implicated zinc metalloprotease *vcpB* (EEX32371); hemolysins *vchA* (EEX31069) and *vchB* (EEX31068).

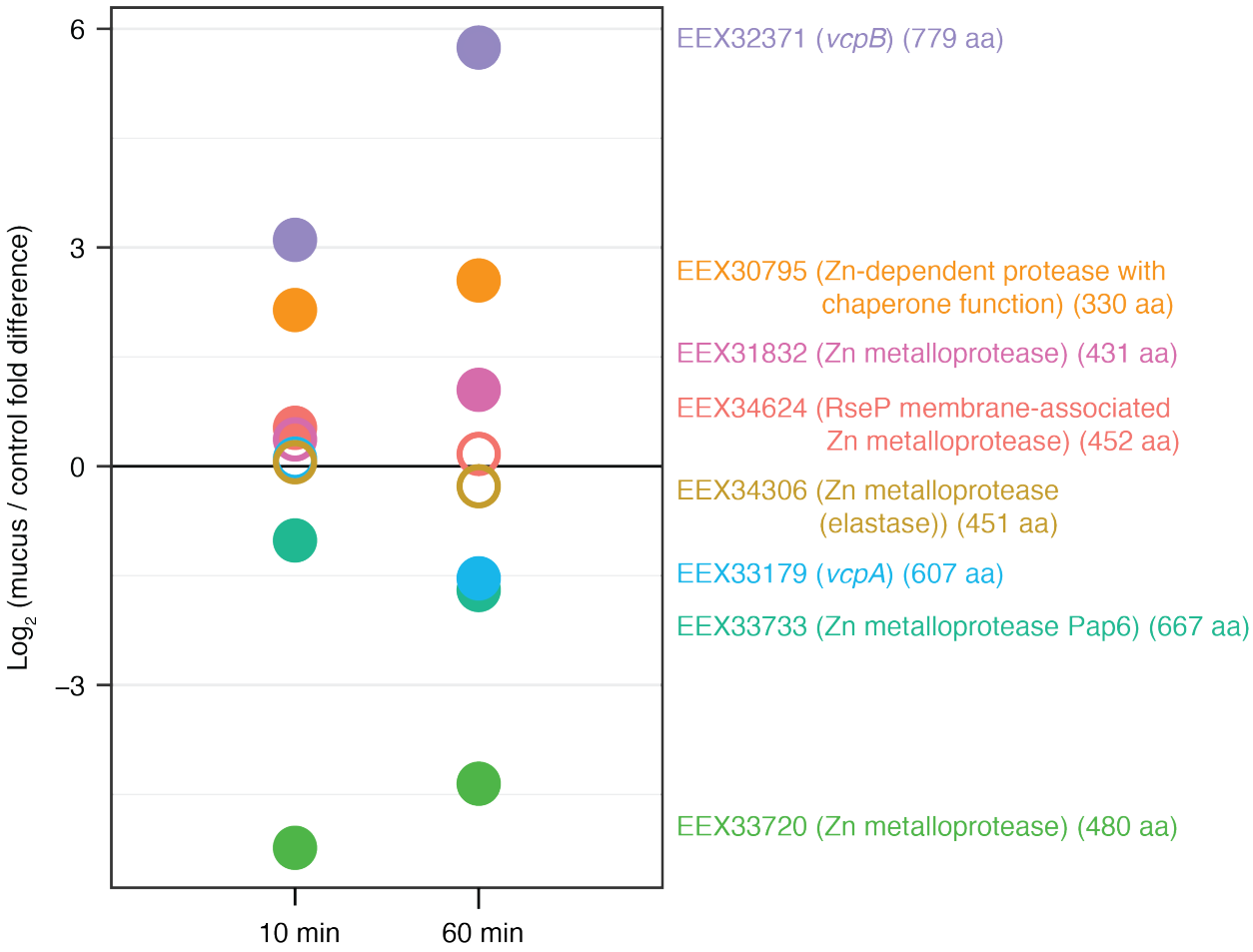

Supplementary Figure 3.14 | Differential expression of zinc metalloprotease genes in the *V. coralliilyticus* genome. Eight zinc metalloproteases are shown and discussed in Supplementary Discussion. Solid circles, statistically significant; open circles, not significant (adjusted p-value < 0.01).

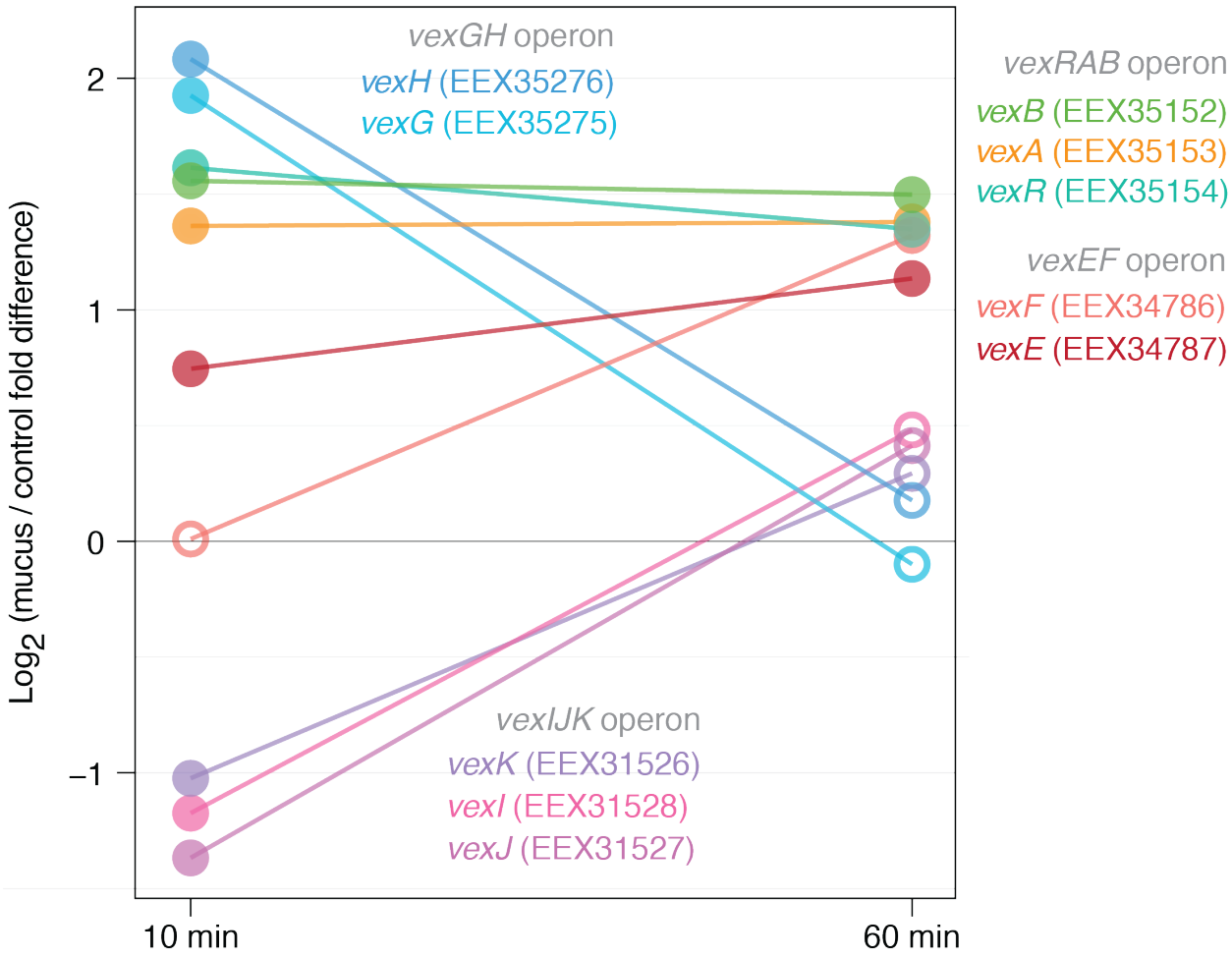

Supplementary Figure 3.15 | Differential expression of genes encoding RND multidrug efflux systems. The *vex* genes encoding RND multidrug efflux pumps were identified in the *V. coralliilyticus* genome through amino acid sequence homology with *vex* genes of *V. cholerae*, in which the RND efflux systems have been found to be required for antimicrobial resistance and optimal virulence factor production [203,204]. Similarly to *V. cholerae*, the *vex* genes are clustered in operons (gray text) in the *V. coralliilyticus* genome. Unlike *V. cholerae*, *vexC* was equivalent to *vexI*, and *vexD* was equivalent to *vexK* in *V. coralliilyticus*. Furthermore, no homology was found for *vexLM* of *V. cholerae*. Solid circles, statistically significant; open circles, not significant (adjusted *p*-value < 0.05).

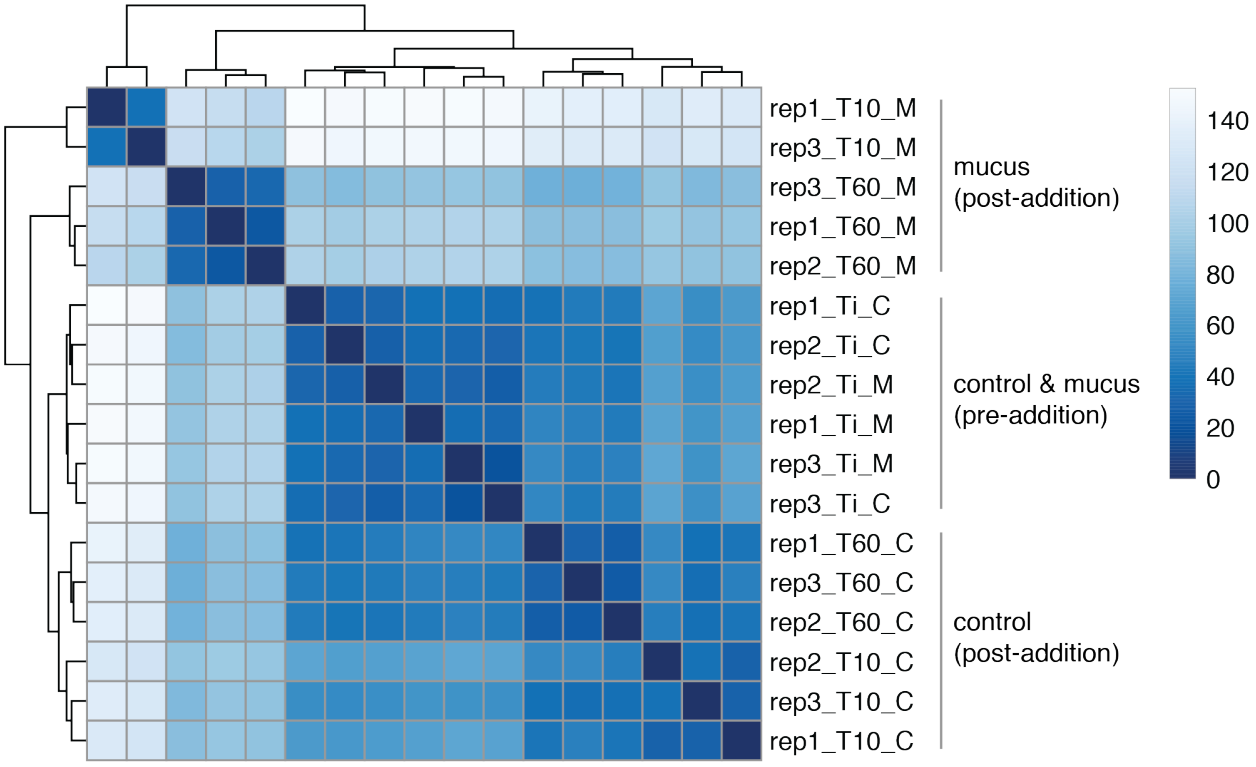

Supplementary Figure 3.16 | Heatmap of sample-to-sample distances. Hierarchical clustering based on sample distances calculated using raw transcript count data that were transformed with the variance stabilizing transformation (VST) method (Methods). The color scale represents sample-to-sample distances. Each row is labeled with the sample name with the following convention: rep, replicate (1–3); T, time point (i, before addition; 10, 10 min; 60, 60 min); M, mucus; C, control.

3.9 Supplementary Tables

Supplementary Table 3.1 | Differential expression analysis results (DESeq2) of pairwise comparison, coral mucus (10 min) vs. control (10 min) (in Excel file accompanying publication).

Supplementary Table 3.2 | Differential expression analysis results (DESeq2) of pairwise comparison, coral mucus (60 min) vs. control (60 min) (in Excel file accompanying publication).

Supplementary Table 3.3 | Summary of differential expression analysis results (DESeq2, FDR $\alpha < 0.01$).

Differential expression at 10 min	**Differential expression at 60 min**	**Number of genes (% of total genes)**
Up	Up	634 (12.6%)
Down	Down	679 (13.5%)
Up	Down	118 (2.4%)
Down	Up	90 (1.8%)
Total number of genes differentially expressed at both 10 and 60 min		**1521 (30.3%)**

Supplementary Table 3.4 | List of 100 *V. coralliilyticus* genes that were most significantly differentially expressed at 10 minutes. Genes are sorted first by adjusted *p*-values, then by log_2 fold difference from pairwise comparison of coral mucus (10 min) vs. control (10 min).

#	GenBank accession	Gene product name	Log_2 fold difference	Adjusted *p*-value
Upregulated in mucus				
1	EEX33015.1	cobalt-zinc-cadmium resistance protein czcA	10.6566036	9.93E-99
2	EEX34074.1	proton/glutamate symport protein	9.16765548	2.21E-230
3	EEX33014.1	hypothetical protein	8.68655938	6.13E-124
4	EEX32322.1	maltoporin	8.51898588	1.53E-150
5	EEX30917.1	imidazolonepropionase	7.79929087	3.80E-72
6	EEX32286.1	permease	7.29195188	4.92E-62
7	EEX35011.1	carbon starvation protein A	7.18158551	9.27E-58
8	EEX30915.1	urocanate hydratase	7.15083777	5.19E-93
9	EEX30914.1	histidine ammonia-lyase	7.09646689	6.42E-95
10	EEX32326.1	serine hydroxymethyltransferase	6.86563018	6.38E-230
11	EEX32328.1	glycine dehydrogenase (decarboxylating)	6.74844777	4.20E-154
12	EEX34598.1	multidrug efflux pump component MtrF	6.68917031	1.89E-88
13	EEX34604.1	acyl-CoA dehydrogenase short-chain specific	6.61989584	3.79E-61
14	EEX30923.1	formate-dependent phosphoribosylglycinamide formyltransferase	6.42949641	1.98E-98
15	EEX31998.1	glycerol kinase	6.39580172	3.29E-86
16	EEX32016.1	putative NADH oxidase	6.37357105	5.80E-79
17	EEX35442.1	xanthine/uracil/thiamine/ascorbate permease family protein	6.23865965	4.43E-67
18	EEX32298.1	putative pullulanase precursor	6.1816164	1.19E-172
19	EEX33239.1	maltose/maltodextrin transport ATP-binding protein MalK	5.81901806	3.86E-90
20	**EEX32739.1**	**macrophage infectivity potentiator-related protein**	**5.71059916**	**1.57E-91**
21	EEX33580.1	hypothetical protein	5.66880306	7.23E-115
22	EEX32841.1	proton/glutamate symporter	5.66706003	3.77E-100
23	EEX33240.1	maltooligosaccharide-binding protein	5.55807483	2.08E-110
24	EEX33022.1	predicted arginine uptake transporter	5.49896441	3.68E-76
25	**EEX31713.1**	**methyl-accepting chemotaxis protein**	**5.42372756**	**8.43E-99**
26	EEX33579.1	cysteine desulfurase	5.41707269	2.48E-159
27	EEX33840.1	2,4-dienoyl-CoA reductase [NADPH]	5.31382424	3.08E-94
28	EEX33898.1	3-ketoacyl-CoA thiolase	5.2315967	6.56E-61
29	EEX34106.1	D-amino acid dehydrogenase small subunit	5.21387567	8.24E-67
30	EEX35229.1	amino acid ABC transporter substrate-binding protein	5.08280362	3.14E-129
31	EEX33177.1	predicted transcriptional regulator	5.0029201	7.91E-153
32	EEX33897.1	enoyl-CoA hydratase/delta(3)-cis-delta(2)-trans-enoyl-CoA isomerase/3-hydroxyacyl-CoA dehydrogenase/3-hydroxybutyryl-CoA epimerase	4.88878765	4.84E-105
33	EEX32397.1	hypothetical protein	4.82656344	1.03E-72
34	EEX33044.1	periplasmic alpha-amylase	4.71699406	3.75E-70
35	EEX31285.1	ribonucleotide reductase of class Ia (aerobic) alpha subunit	4.62330791	4.58E-111
36	EEX32329.1	hypothetical protein	4.61972112	5.25E-74

37	**EEX31282.1**	**methyl-accepting chemotaxis protein (Cache sensor)**	**4.5823632**	**2.89E-84**
38	EEX33702.1	alanine dehydrogenase	4.49076586	9.60E-112
39	EEX32321.1	maltose operon periplasmic protein MalM	4.46891373	1.36E-98
40	EEX31583.1	transcriptional regulator, TetR family	4.43805121	1.85E-58
41	EEX30617.1	SSU ribosomal protein S10P	4.3703164	9.46E-57
42	EEX31837.1	xanthine/uracil permease	4.36342242	8.08E-64
43	EEX35227.1	amino acid ABC transporter ATP-binding protein	4.2975494	1.69E-69
44	EEX32241.1	glycosidase	4.27467001	3.27E-62
45	EEX33241.1	maltooligosaccharide ABC transporter membrane protein	4.25343375	1.45E-76
46	**EEX33475.1**	**methyl-accepting chemotaxis protein (Pas/Pac sensor)**	**4.23252507**	**1.94E-68**
47	EEX33830.1	sulfate permease	4.2055486	9.29E-71
48	EEX32327.1	glycine cleavage system H protein	4.1178951	1.96E-91
49	EEX34056.1	phosphoribosylformylglycinamidine cyclo-ligase	4.06505349	3.35E-60
50	EEX33555.1	L-serine dehydratase	4.0548527	6.14E-89
51	EEX32740.1	l-2-haloalkanoic acid dehalogenase HAD superfamily protein	4.0533089	4.22E-79
52	EEX33936.1	amidophosphoribosyltransferase	3.93862721	2.00E-66
53	EEX34013.1	[ThiS-adenylate] sulfurtransferase	3.81586261	5.02E-69
54	EEX31286.1	ribonucleotide reductase of class Ia (aerobic) beta subunit	3.73231893	5.36E-88
55	EEX33832.1	long-chain-fatty-acid--CoA ligase	3.71761202	8.06E-64
56	EEX35268.1	5-(carboxyamino)imidazole ribonucleotide synthase	3.52135049	4.42E-59
57	EEX32044.1	transcriptional regulator, AsnC family	3.48360993	1.33E-64
58	**EEX34665.1**	**Na(+)-translocating NADH-quinone reductase subunit C (NqrC)**	**2.94495236**	**4.19E-61**
59	**EEX34667.1**	**Na(+)-translocating NADH-quinone reductase subunit A (NqrA)**	**2.92008554**	**1.53E-81**
Downregulated in mucus				
1	EEX34882.1	putative hemolysin	-11.224845	6.40E-136
2	EEX35096.1	glycosyltransferase	-10.032939	1.41E-194
3	EEX35097.1	membrane-associated phospholipid phosphatase	-9.9752612	1.46E-116
4	EEX32760.1	putative phosphatase	-9.1475814	2.33E-221
5	EEX33354.1	ABC transporter, periplasmic substrate-binding protein	-8.5387418	5.39E-198
6	EEX33158.1	hypothetical protein	-8.1050309	1.24E-108
7	EEX33200.1	UDP-glucose dehydrogenase	-8.1036764	1.20E-124
8	**EEX32441.1**	**phosphate ABC transporter substrate-binding protein (PstS)**	**-7.6113156**	**3.60E-188**
9	EEX33364.1	transcriptional regulator	-7.5476702	4.75E-95
10	**EEX30802.1**	**PhoH-like ATPase**	**-7.5397774**	**1.04E-56**
11	EEX32754.1	phosphoglycolate phosphatase	-7.4101961	2.29E-171
12	EEX32881.1	C4-dicarboxylate-binding protein	-7.3397322	3.57E-56
13	EEX32017.1	alkaline phosphatase	-7.2886016	1.18E-87
14	EEX32259.1	phosphoserine phosphatase	-7.2600894	5.83E-59
15	EEX32752.1	carbohydrate ABC transporter substrate-binding protein	-7.2532991	1.30E-101
16	**EEX31192.1**	**methyl-accepting chemotaxis protein**	**-7.1755851**	**5.50E-162**
17	**EEX34149.1**	**phosphate regulon transcriptional regulatory protein (PhoB)**	**-7.1733708**	**1.07E-122**
18	EEX32818.1	hypothetical protein	-7.1551303	4.86E-75
19	EEX32755.1	carbohydrate ABC transporter ATP-binding protein	-7.1102302	2.17E-141
20	EEX32937.1	microbial collagenase secreted	-7.1018711	4.00E-66

21	EEX34285.1	hypothetical protein	-6.8779039	3.88E-69
22	EEX32753.1	putative secreted protein	-6.7062364	1.31E-60
23	**EEX32440.1**	**phosphate ABC transporter membrane protein 1 (PstC)**	**-6.5141418**	**6.01E-175**
24	**EEX34148.1**	**phosphate regulon sensor protein (PhoR)**	**-6.4849994**	**7.43E-80**
25	EEX31160.1	staphylolysin. Metallo peptidase. MEROPS family M23A	-6.4240748	4.73E-72
26	EEX32765.1	hypothetical protein	-6.1787542	3.61E-88
27	**EEX32439.1**	**phosphate ABC transporter membrane protein 2 (PstA)**	**-6.1117239**	**3.05E-101**
28	**EEX32726.1**	**chemotaxis protein CheA**	**-6.0838184**	**9.27E-58**
29	EEX33717.1	glutamate decarboxylase	-6.0650682	9.31E-71
30	**EEX32438.1**	**phosphate ABC transporter ATP-binding protein (PstB)**	**-6.0524215**	**3.00E-162**
31	EEX31686.1	alkaline phosphatase	-5.9527367	7.27E-83
32	**EEX33718.1**	**methyl-accepting chemotaxis protein (Cache sensor)**	**-5.8120389**	**5.17E-67**
33	EEX33725.1	hypothetical protein	-5.6464007	5.42E-57
34	EEX32024.1	hypothetical protein	-5.4533219	1.64E-81
35	**EEX32733.1**	**Che cluster related two-component response regulator**	**-5.2133035**	**7.29E-71**
36	**EEX33217.1**	**phosphate ABC transporter substrate-binding protein**	**-4.9045433**	**9.26E-59**
37	EEX33095.1	hypothetical protein	-4.3650866	2.90E-58
38	EEX35279.1	hypothetical protein	-3.3823566	1.13E-62
39	EEX35185.1	transcriptional regulator AraC/XylS family	-3.2612591	1.76E-56
40	EEX35184.1	threonine efflux protein	-3.0892819	2.20E-60
41	EEX35194.1	hypothetical protein	-2.8734852	3.85E-57

Red Putative virulence-related genes
Bold Chemotaxis-related genes
Purple Na^+-NQR enzyme genes
Green Phosphate regulation genes with putative connections to virulence

Supplementary Table 3.5 | List of 100 *V. coralliilyticus* genes that were most significantly differentially expressed at 60 minutes. Genes are sorted first by adjusted *p*-values, then by log_2 fold difference from pairwise comparison of coral mucus (60 min) vs. control (60 min).

#	GenBank accession	Gene product name	Log_2 fold difference	Adjusted *p*-value
Upregulated in mucus				
1	EEX31999.1	glycerol uptake facilitator protein	7.40848654	2.30E-61
2	EEX31998.1	glycerol kinase	7.21332462	1.44E-137
3	EEX35090.1	glycerol-3-phosphate transporter	7.06957256	1.19E-67
4	EEX31989.1	homodimeric glycerol 3-phosphate dehydrogenase (quinone)	6.92333158	1.33E-77
5	EEX33444.1	hypothetical protein	6.19910525	4.23E-81
6	EEX32058.1	ClpB protein	6.02673103	8.52E-56
7	EEX33015.1	cobalt-zinc-cadmium resistance protein czcA	5.78661754	1.98E-44
8	**EEX32371.1**	**zinc metalloprotease (VcpB)**	**5.74273607**	**1.78E-68**
9	**EEX32048.1**	**uncharacterized protein ImpC (VipB of T6SS)**	**5.73561841**	**7.84E-111**
10	**EEX32353.1**	**protease**	**5.63236912**	**2.96E-59**
11	**EEX32019.1**	**metalloprotease**	**5.54347655**	**1.55E-48**
12	**EEX34099.1**	**alkaline serine protease**	**5.43283505**	**1.04E-110**
13	**EEX32370.1**	**aminopeptidase**	**5.421236**	**1.43E-42**
14	EEX33014.1	hypothetical protein	5.10638813	1.16E-59
15	EEX32041.1	hypothetical protein	5.10265631	1.46E-37
16	EEX33885.1	UPF0061 domain-containing protein	4.94128021	9.81E-138
17	EEX31899.1	Phosphocarrier protein HPr/PTS system D-fructose-specific IIA component	4.80734402	1.19E-44
18	EEX33901.1	long-chain fatty acid transport protein	4.71619906	3.62E-37
19	EEX31898.1	1-phosphofructokinase	4.67180086	1.48E-37
20	EEX32000.1	glycerol 3-phosphate dehydrogenase (quinone) subunit A	4.58023526	1.00E-53
21	EEX32322.1	maltoporin	4.55237858	2.52E-54
22	EEX32298.1	putative pullulanase precursor	4.44666553	1.26E-115
23	EEX31648.1	aldehyde dehydrogenase	4.43044939	6.39E-45
24	EEX32113.1	betaine aldehyde dehydrogenase	4.1917458	9.39E-46
25	**EEX33113.1**	**aminopeptidase Y (Arg Lys Leu preference)**	**4.07209529**	**3.44E-38**
26	EEX34954.1	aspartate kinase	3.92897031	1.36E-56
27	EEX32114.1	transcriptional regulator, TetR family	3.73131125	1.45E-37
28	EEX32112.1	choline dehydrogenase	3.72914504	2.89E-55
29	EEX31647.1	choline dehydrogenase	3.60929868	3.43E-68
30	EEX35321.1	chaperone protein HtpG	3.59435654	5.01E-55
31	EEX32471.1	putative periplasmic substrate-binding protein	3.5756782	3.00E-57
32	EEX30735.1	hypothetical protein	3.55109177	5.81E-39
33	EEX30720.1	heat shock protein 60 family co-chaperone GroES	3.48014351	1.08E-39
34	EEX32472.1	L-proline Glycine Betaine ABC transport system permease proW	3.37742632	5.84E-39
35	EEX32109.1	L-proline Glycine Betaine ABC transport ATP-binding protein proV	3.32015589	5.70E-65
36	EEX34073.1	chaperone protein DnaK	3.29161547	1.99E-42
37	**EEX32739.1**	**macrophage infectivity potentiator-related protein**	**3.21027974**	**2.44E-38**

38	EEX30705.1	ATP-dependent hsl protease ATP-binding subunit HslU	3.09672866	9.94E-38
39	EEX30719.1	heat shock protein 60 family chaperone GroEL	3.03216849	7.15E-51
40	**EEX35183.1**	**gamma-glutamyltranspeptidase**	**2.94236444**	**3.65E-46**
41	EEX34072.1	chaperone protein DnaJ	2.91701728	7.56E-49
42	**EEX34157.1**	**protein-export membrane protein SecD**	**2.91377221**	**1.74E-49**
43	EEX32202.1	pentapeptide repeat family protein	2.85785441	1.46E-46
44	EEX35091.1	glycerophosphoryl diester phosphodiesterase	2.80854053	9.48E-46
45	EEX32044.1	transcriptional regulator, AsnC family	2.70701783	8.23E-54
46	EEX30796.1	membrane protein	2.67090846	1.98E-37
47	**EEX30795.1**	**Zn-dependent protease with chaperone function**	**2.54844484**	**3.50E-42**
48	EEX33871.1	cell division trigger factor	2.53288819	5.51E-39
49	EEX35368.1	type III restriction enzyme res subunit	2.43867985	7.82E-49
50	EEX32473.1	L-proline Glycine Betaine ABC transport ATP-binding protein proV	2.39323275	1.50E-45
51	**EEX34158.1**	**protein translocase subunit yajC**	**2.38450408**	**2.27E-44**
52	**EEX34156.1**	**protein translocase subunit secF**	**2.38285125**	**8.39E-38**
53	**EEX30690.1**	**protein translocase subunit secB**	**2.37785509**	**2.27E-44**
54	**EEX34706.1**	**protein translocase subunit secA**	**2.34129002**	**3.28E-47**
55	EEX30698.1	YjbH outer membrane lipoprotein	2.21671352	3.28E-47
56	EEX33177.1	predicted transcriptional regulator	2.21413958	1.87E-46
57	EEX32908.1	chromosome segregation ATPase	1.51818514	4.12E-38
Downregulated in mucus				
1	EEX33074.1	hypothetical protein	-2.7149682	7.23E-57
2	EEX35185.1	transcriptional regulator AraC/XylS family	-2.837767	3.88E-55
3	EEX33357.1	ABC transporter, permease protein	-2.9392167	9.41E-43
4	EEX33073.1	multidrug resistance protein D	-3.1138029	8.46E-39
5	EEX35184.1	threonine efflux protein	-3.5521563	4.99E-103
6	EEX34475.1	hypothetical protein	-3.8430412	1.12E-38
7	**EEX34148.1**	**phosphate regulon sensor protein (PhoR)**	**-4.0082037**	**1.74E-44**
8	EEX30987.1	transcriptional regulator, GntR family	-4.0384179	3.46E-42
9	EEX31335.1	hypothetical protein	-4.1526739	6.00E-59
10	EEX33356.1	ABC transporter, ATP-binding protein	-4.2238716	2.72E-43
11	**EEX33720.1**	**zinc metalloprotease**	**-4.3527684**	**3.26E-44**
12	EEX32753.1	putative secreted protein	-4.4104483	1.38E-39
13	EEX32259.1	phosphoserine phosphatase	-4.5430871	4.58E-43
14	EEX32818.1	hypothetical protein	-4.6800137	1.97E-58
15	EEX32751.1	carbohydrate ABC transporter membrane protein 2, CUT1 family	-4.8199352	1.57E-40
16	EEX30988.1	methylisocitrate lyase	-5.0190929	3.98E-58
17	**EEX34149.1**	**phosphate regulon transcriptional regulatory protein (PhoB)**	**-5.1578667**	**1.76E-84**
18	**EEX32438.1**	**phosphate ABC transporter ATP-binding protein (PstB)**	**-5.2829748**	**1.71E-149**
19	EEX30990.1	2-methylcitrate dehydratase FeS dependent	-5.3310035	6.77E-64
20	EEX30991.1	2-methylaconitate cis-trans isomerase	-5.3501319	2.03E-63
21	EEX30989.1	2-methylcitrate synthase	-5.4068002	2.09E-84
22	**EEX32439.1**	**phosphate ABC transporter membrane protein 2 (PstA)**	**-5.5524533**	**1.01E-101**
23	EEX33360.1	hypothetical protein	-5.813381	1.50E-51

24	EEX32752.1	carbohydrate ABC transporter substrate-binding protein, CUT1 family	-5.9032963	3.41E-91
25	EEX32750.1	carbohydrate ABC transporter membrane protein 1, CUT1 family	-6.011247	3.59E-41
26	EEX30992.1	propionyl-CoA synthetase	-6.0804617	2.11E-53
27	EEX32755.1	carbohydrate ABC transporter ATP-binding protein, CUT1 family	-6.1019383	1.50E-156
28	EEX33200.1	UDP-glucose dehydrogenase	-6.3025751	2.30E-109
29	EEX31160.1	staphylolysin. Metallo peptidase. MEROPS family M23A	-6.3471964	1.29E-91
30	**EEX33217.1**	**phosphate ABC transporter substrate-binding protein**	**-6.431385**	**2.99E-100**
31	**EEX31192.1**	**methyl-accepting chemotaxis protein**	**-6.5310413**	**4.50E-170**
32	EEX32754.1	phosphoglycolate phosphatase	-6.7327592	2.47E-217
33	EEX33158.1	hypothetical protein	-6.7454801	2.28E-99
34	**EEX32440.1**	**phosphate ABC transporter membrane protein 1 (PstC)**	**-7.0333295**	**2.01E-233**
35	EEX33364.1	transcriptional regulator	-7.0455797	4.15E-129
36	EEX31630.1	hypothetical protein	-7.179953	2.75E-43
37	EEX33354.1	ABC transporter, periplasmic substrate-binding protein	-8.0163816	3.34E-215
38	EEX35097.1	membrane-associated phospholipid phosphatase	-8.2248773	5.37E-126
39	EEX32017.1	alkaline phosphatase	-8.2823799	5.81E-116
40	EEX32760.1	putative phosphatase	-8.5664181	2.03E-240
41	**EEX32441.1**	**phosphate ABC transporter substrate-binding protein (PstS)**	**-8.6359639**	**1.47E-291**
42	EEX35096.1	glycosyltransferase	-8.7388328	9.47E-204
43	EEX34882.1	putative hemolysin	-10.711944	2.70E-158

Red Putative virulence-related genes, including secretion systems
Orange Proteases
Bold Chemotaxis-related genes
Green Phosphate regulation genes with putative connections to virulence

Supplementary Table 3.6 | Na^+-NQR genes shown in Fig. 3.4a.

Gene	*V. alginolyticus* gene*	*V. coralliilyticus* gene	*V. coralliilyticus* gene locus	Identity (%)	Coverage (%)
nqrA	GAD71943	EEX34667	VIC_000693	92.52	89
nqrB **	GAD71712	EEX34666	VIC_000692	67.48	99
nqrC	GAD71945	EEX34665	VIC_000691	80.08	100
nqrD	GAD71946	EEX34664	VIC_000690	98.57	100
nqrE	GAD71947	EEX34663	VIC_000689	98.48	100
nqrF	GAD71948	EEX34662	VIC_000688	97.05	100

* *nqr* genes were identified in the *V. coralliilyticus* genome through high amino acid homology (queried on BLASTp) with *nqr* genes of *V. alginolyticus*[205].
** Two genes with high homology to *nqrB* was found in the *V. coralliilyticus* genome (EEX32277, not shown). Only the gene (EEX34666) that is adjacent to the other *nqr* genes is shown.

Supplementary Table 3.7 | Biofilm (*vps* and *rbm*) genes shown in Fig. 3.4b.

Gene	*V. cholerae* gene*	*V. coralliilyticus* gene	*V. coralliilyticus* gene locus	Identity (%)	Coverage (%)
vpsR	AWB73202	EEX35032	VIC_000540	86.39	99
vpsU	AWK28764	EEX33051	VIC_002501	43.57	83
vpsA	AWB73428	EEX33052	VIC_002502	77.09	99
vpsB	AWB73429	EEX33053	VIC_002503	83.05	100
vpsC	AWB73430	-	-	-	-
vpsD	AWB73431	EEX33054	VIC_002504	37.31	99
vpsE	AWB73432	EEX33055	VIC_002505	36.23	99
vpsF	AWB73433	EEX33056	VIC_002506	46.41	89
vpsG	AWB73434	EEX33057	VIC_002507	41.22	91
vpsH	AWB73435	EEX33058	VIC_002508	57.76	93
vpsI	AWB73436	EEX33059	VIC_002509	54.49	99
vpsJ	AWB73437	EEX33060	VIC_002510	58.95	97
vpsK	AWB73438	EEX33061	VIC_002511	77.59	98
vpsT	AWB76290	EEX33067	VIC_002517	57.28	91
vpsL	AWB73444	EEX33156	VIC_002610	77.16	100
vpsM	AWB73445	EEX33155	VIC_002609	56.85	98
vpsN	AWB73446	EEX33154	VIC_002608	67.82	99
vpsO	AWB73447	EEX33153	VIC_002607	68.18	98
vpsP	AWB73448	EEX33152	VIC_002606	31.28	88
vpsQ	AWB73449	-	-	-	-
rbmA	AAF94090 (VC_0928)	EEX33062	VIC_002512	41.28	85
rbmB	AAF94091 (VC_0929)	EEX33063	VIC_002513	47.62	92
rbmC	AAF94092 (VC_0930)	EEX33064	VIC_002514	66.42	99
rbmD	AAF94093 (VC_0931)	EEX33150	VIC_002604	59.29	97
rbmE	AAF94094 (VC_0932)	EEX33151	VIC_002605	67.86	88
rbmF	AAF94095 (VC_0933)	-	-	-	-

***** *vps* and *rbm* genes were identified in the *V. coralliilyticus* genome through high amino acid homology (queried on BLASTp) with *vpsA–Q*, *vpsR*, *vpsT* and *rbmABCDEF* genes of *V. cholerae*[161,206]. Additional information is available in Supplementary Discussion.

Supplementary Table 3.8 | Quorum sensing, transcription regulator, and toxin genes shown in Fig. 3.4c–e.

Gene	*V. coralliilyticus* gene	Homologous genes in other Vibrios	References
Quorum sensing autoinducer synthases			
luxM (AI-1 synthase)	EEX31502	*luxM*	33
luxS (AI-2 synthase)	EEX35562	*luxS*	33
cqsA (CAI-1 synthase)	EEX33462	*cqsA*	33
Master transcription regulators			
toxR	EEX35320	*toxR*	32,36,183,207
toxS	EEX35319	*toxS*	196
aphA	EEX30687	*aphA*	159
vcpR	EEX34823	*hapR, luxR*	154,155
Toxins			
vcpA	EEX33179	*hapA*	29,31,33,34,125,154
vcpB	EEX32371	*hapA*	29,31,33,154
vchA	EEX31069	*vvhA*	33,154
vchB	EEX31068	*vvhB*	33,154

Supplementary Table 3.9 | Secretion system genes shown in Fig. 4f.

Gene	*V. coralliilyticus* gene locus*	KO number
Type 1 Secretion System		
tolC	VIC_000771	K12340 tolC; outer membrane protein
Type 2 Secretion System		
gspC	VIC_000133	K02452 gspC; general secretion pathway protein C
gspD	VIC_000132	K02453 gspD; general secretion pathway protein D
gspE	VIC_000131	K02454 gspE; general secretion pathway protein E
gspF	VIC_000130	K02455 gspF; general secretion pathway protein F
gspG	VIC_000129	K02456 gspG; general secretion pathway protein G
gspH	VIC_000128	K02457 gspH; general secretion pathway protein H
gspI	VIC_000127	K02458 gspI; general secretion pathway protein I
gspJ	VIC_000126	K02459 gspJ; general secretion pathway protein J
gspK	VIC_000125	K02460 gspK; general secretion pathway protein K
gspL	VIC_000124	K02461 gspL; general secretion pathway protein L
gspM	VIC_000123	K02462 gspM; general secretion pathway protein M
Type 3 Secretion System (located on Coralliilyticus Pathogenicity Island-1)		
yscR-1	VIC_004064	K03226 yscR; type III secretion protein R
yscS-1	VIC_004063	K03227 yscS; type III secretion protein S
yscT-1	VIC_004062	K03228 yscT; type III secretion protein T
yscU-1	VIC_004061	K03229 yscU; type III secretion protein U
yscC-1	VIC_004057	K03219 yscC; type III secretion protein C
yscF	VIC_004032	K03221 yscF; type III secretion protein F
yscJ-1	VIC_004029	K03222 yscJ; type III secretion protein J
yscV-1	VIC_004022	K03230 yscV; type III secretion protein V
yscN-1	VIC_004021	K03224 yscN; ATP synthase in type III secretion protein N
Type 3 Secretion System (located on Megaplasmid)		
yscJ-2	VIC_001055	K03222 yscJ; type III secretion protein J
yscN-2	VIC_001050	K03224 yscN; ATP synthase in type III secretion protein N
yscR-2	VIC_001046	K03226 yscR; type III secretion protein R
yscS-2	VIC_001045	K03227 yscS; type III secretion protein S
yscT-2	VIC_001044	K03228 yscT; type III secretion protein T
yscU-2	VIC_001043	K03229 yscU; type III secretion protein U
yscV-2	VIC_001039	K03230 yscV; type III secretion protein V
yscC-2	VIC_001022	K03219 yscC; type III secretion protein C
Type 6 Secretion System		
vasH	VIC_003158	-
hcp	VIC_003156	-
vgrG	VIC_003155	-
vipA	VIC_003148	-

vipB	VIC_003147	-
vasA	VIC_003145	-
vasK	VIC_003142	-
vasF	VIC_003136	-
Sec Secretion System		
secA	VIC_000732	K03070 secA; preprotein translocase subunit SecA
secB	VIC_004986	K03071 secB; preprotein translocase subunit SecB
secD-1	VIC_002055	K03072 secD; preprotein translocase subunit SecD
secF-1	VIC_002054	K03074 secF; preprotein translocase subunit SecF
yajC	VIC_002056	K03210 yajC; preprotein translocase subunit YajC
secD-2	VIC_002788	K03072 secD; preprotein translocase subunit SecD
secF-2	VIC_002789	K03074 secF; preprotein translocase subunit SecF
secY	VIC_004892	K03076 secY; preprotein translocase subunit SecY
secE	VIC_000053	K03073 secE; preprotein translocase subunit SecE
secG	VIC_000786	K03075 secG; preprotein translocase subunit SecG
ffh (SRP54)	VIC_000878	K03106 SRP54; signal recognition particle subunit SRP54
ftsY	VIC_000196	K03110 ftsY; fused signal recognition particle receptor
Tat Secretion system		
tatA	VIC_000431	K03116 tatA; sec-independent protein translocase protein TatA
tatB	VIC_000432	K03117 tatB; sec-independent protein translocase protein TatB
tatC	VIC_000433	K03118 tatC; sec-independent protein translocase protein TatC

***** List of genes in types 1, 2, 3, Sec, and Tat secretion systems were obtained from the Bacterial Secretion System KEGG 03070 pathway gene assignment. Type 6 secretion genes were obtained from Guillemette, Ushijima et al.[208].

Supplementary Table 3.10 | Zinc metalloprotease genes shown in Supplementary Figure 3.14 and discussed in Supplementary Discussion.

V. coralliilyticus **gene**	***V. coralliilyticus*** **locus tags**	**Gene name**	**Length (aa)**	**Identity (%) HapA***	**References**
EEX33179	VIC_002633	*vcpA*	607	69.41	[31,33,34,125,154]
EEX32371	VIC_003472	*vcpB*	779	49.11	[29,31,33,154]
EEX33720	VIC_001616	Zinc metalloprotease	480	48.42	NCBI annotation
EEX33733	VIC_001629	Zinc metalloprotease Pap6	667	41.65	NCBI annotation
EEX31832	VIC_004782	Zinc metalloprotease	431	39.13	NCBI annotation
EEX34624	VIC_000650	Membrane-associated zinc metalloprotease (RseP)	452	33.33	NCBI annotation
EEX30795	VIC_004815	Zn-dependent protease with chaperone function (YfgC)	330	33.33	NCBI annotation
EEX34306	VIC_001102	Zinc metalloprotease (elastase)	451	28.30	NCBI annotation

* Amino acid (aa) sequence identity with *V. cholerae* HapA gene (AVK79064).

3.10 Supplementary Discussion

3.10.1 Investigation of swimming speed enhancement by control cells.

We observed a weak and short-lived increase in swimming speed in *V. coralliilyticus* control cells that were exposed to the addition of filtered spent medium in place of coral mucus. This unexpected enhancement of swimming speed in control cells peaked at 66.3 ± 0.9 μm/s after 8 minutes, representing 1.3× the pre-addition speed (Fig. 3.2e). Swimming speeds returned to baseline within 15 minutes (two-tailed *t*-test with control speed at −2 min, $p > 0.01$).

This speed enhancement in filtered spent medium (also referred to as "filtrate") was observed consistently across experiments and regardless of the filter material used (cellulose acetate or polyvinylidene fluoride), the amount of pressure applied (2.8 cm^2 or 10 cm^2 filtration area) during filtrate production, or the use of slightly warmer (+1 °C) filtrate (Supplementary Fig. 3.5), indicating that chemicals leaching from the filter membranes, bursting of cells due to high pressure, or a small elevation in temperature upon filtrate addition are unlikely to be the cause of the increase in swimming speed in control cells. Furthermore, vigorous and repeated pipetting of cells did not cause any speed enhancement, suggesting that hydrodynamic stimuli, specifically shear forces, were not responsible for the changes in swimming speed in control cells (Supplementary Fig. 3.5). In contrast, separate experiments in which we probed the addition of filtered artificial sea water (FASW) to *V. coralliilyticus* caused a speed increase of 2.4-fold (marine broth caused a 3.4-fold speed enhancement in the same experiment; Supplementary Fig. 3.5), leading us to hypothesize that chemokinesis in control cells was partially caused by oxygenation of the spent medium during filtration. Indeed, oxygen has been shown to affect swimming speeds of *V. coralliilyticus*, with faster swimming speeds recorded under oxic (~65 μm/s) compared to anoxic conditions (~25 μm/s)[209].

Importantly, the speed enhancement caused by coral mucus was higher in magnitude and longer in duration than that observed in control cells (Fig. 3.2e). Furthermore, the addition of filtered spent medium seems to induce speed enhancement only in a subset of the control population, observed as the mere flattening of the speed distribution histogram, compared to the whole-

population shift towards faster swimming speeds observed in coral mucus-exposed populations (Supplementary Fig. 3.6).

3.10.2 Release from phosphate starvation.

Release from phosphate limitation upon coral mucus addition was likely responsible for the strong and highly statistically significant downregulation of the two-component system PhoBR, and the associated ABC-type phosphate transporter, Pst at both 10 and 60 min (Supplementary Tables 3.4 and 3.5). Inactivation of the PhoBR system has been connected to the induction of biofilm formation and virulence gene expression in *V. cholerae*[210–212]. Thus, the upregulation of biofilm and virulence genes observed in our RNA-seq results (Fig. 3.4) may have been the result of the strong downregulation of PhoBR and Pst systems in coral mucus.

3.10.3 Further evidence for *V. coralliilyticus* growth and physiological transformation in coral mucus.

In addition to elevated metabolism, gene sets involved in protein production, cell membrane generation, cell growth, and energy production were significantly upregulated in coral mucus at 10 min (Fig. 3.3c). Almost all ribosomal protein genes (KEGG 03010) and tRNA synthetases (KEGG 00970) were significantly upregulated within 10 min of incubation with coral mucus (Fig. 3.3c, Supplementary Fig. 3.10), which suggests a rapid increase in protein production. The sustained high expression of ribosomal protein genes (KEGG 03010) at 60 min, despite the downregulation of nutrient acquisition genes (ABC transporters, KEGG 02010) in coral mucus (Fig. 3.3d), suggests that the bacteria may be undergoing a physiological transformation that required continued protein production, such as a transition towards host-association and virulence. Upregulation of gene sets important for cell membrane generation (fatty acid degradation (KEGG 00071) and glycerophospholipid metabolism (KEGG 00564)), and amino acid precursors for membrane fatty acids (KEGG 00280; valine, leucine, isoleucine degradation) (Fig. 3.3c,d) may be caused by the elevated production of cell membranes during growth. The upregulation of oxidative phosphorylation (KEGG 00190) (Fig. 3.3c) suggests increased energy generation as a result of incubation with coral mucus at 10 min.

3.10.4 *vps* and *rbm* (biofilm) gene expression.

Homologs of *V. cholerae vps* and *rbm* biofilm-related genes were found in the *V. coralliilyticus* genome through amino acid sequence similarity (Supplementary Table 3.7). Similarly to the *V. cholerae* genome, the *rbmA–E* gene cluster of *V. coralliilyticus* was in the intergenic region between the two clusters *vpsU,A–K* and *vpsL–P* (Fig. 3.4b).

Three genes present in the *V. cholerae* genome did not lead to significant matches in the *V. coralliilyticus* genome: *vpsQ*, *vpsC*, and *rbmF* (Supplementary Table 3.7). VpsQ may share functional redundancy with VpsP, as mutants of *vpsP* and *vpsQ* were both found to produce biofilms similar to wildtype in *V. cholerae*[161]. Similarly, *vpsC* mutants did not display compromised VPS production or biofilm formation[161], suggesting that it shares functional redundancy with other genes. Finally, *rbmE* and *rbmF* genes of *V. cholerae* share an 88-bp overlapping region and are predicted to be an operon[163], suggesting that they may serve similar functions. Thus, while *rbmF* was not found in the *V. coralliilyticus* genome, its function may be fulfilled by *rbmE*.

In the *V. cholerae* genome, genes *rbmC* (AAF94092, VC0930) and *bap1* (AAF95036, VC1888), encode secreted proteins that modulate the development of corrugated colonies, and are critical for pellicle and biofilm formation[163]. An amino acid sequence homology search of the *V. cholerae* genes *bap1* and *rbmC* against the *V. coralliilyticus* genome yielded the same, single gene, EEX33064, which likely satisfy the function of both *rbmC* and *bap1* in *V. coralliilyticus* biofilms.

Homologs of both *V. cholerae* biofilm transcriptional activators, *vpsR* and *vpsT*, were found in the *V. coralliilyticus* genome (Supplementary Table 3.7), but while *vpsR* was significantly upregulated in coral mucus, *vpsT* was significantly downregulated. Furthermore, it has been found that *rbmA*, which is required for rugose colony formation and biofilm structure integrity in *V. cholerae*, is positively regulated by VpsR but not VpsT[162]. Consistently, we observed the upregulation of both *rbmA* and its positive regulator, *vpsR*, in coral mucus (Fig. 3.4b). The divergent expression patterns of the biofilm transcriptional regulators *vpsR* and *vpsT* in coral

mucus suggest that their activation may be temporally separated in orchestrating the multi-step process of biofilm formation.

A single *rbm* gene, *rbmB*, was significantly downregulated in coral mucus (Fig. 3.4b). RbmB is a putative lyase whose function may be to degrade biofilm-related polysaccharides during the development of colony corrugation and biofilm formation[163]. It is possible that the function of RbmB is important at the later stages of biofilm formation, and thus is initially downregulated in coral mucus.

3.10.5 Zinc metalloprotease gene expression.

Zinc metalloproteases or their homologs have been identified as key virulence factors for many *Vibrio* pathogens[213–216], including *V. coralliilyticus* during coral infection[31,125,217]. In the *V. coralliilyticus* genome, several zinc metalloproteases have been identified through genomic[29,33], and biochemical or phenotypic[31,34,125,218] studies. We focused on 8 zinc metalloproteases and their expression patterns in coral mucus (Supplementary Figure 3.14, Supplementary Table 3.10), though other zinc metalloproteases likely exist in the *V. coralliilyticus* genome.

The most well-studied zinc metalloproteases of *V. coralliilyticus* are VcpA (EEX33179, VIC_002633) and VcpB (EEX32371, VIC_003472), which only share 48% amino acid sequence identity with each other. VcpA (69%) and VcpB (49%) share the highest homology with *V. cholerae*'s Zn-dependent hemagglutinin protease, HapA or vibriolysin (Supplementary Table 3.10), which is an important virulence factor attributed to multiple pathogenic activities, including degradation of mucus barriers in human intestines[213,219,220]. Thus, the high amino acid sequence homology with HapA point to their possible importance in *V. coralliilyticus* pathogenicity.

VcpA is likely the zinc metalloprotease characterized by Ben-Haim et al., who observed that the protease purified from *V. coralliilyticus* BAA-450 led to tissue damage in coral tissue (*P. damicornis*)[125]. VcpA was found to have 100% identify with the 17 amino acid sequence published by Ben-Haim et al.[125], while VcpB only had partial identity. VcpA was further characterized as a major virulence factor of *V. coralliilyticus* in oysters by Hasegawa et al.[34]

(note that *V. tubiashii* has now been re-identified as *V. coralliilyticus*). In the present study, however, we observed a significant downregulation of the *vcpA* gene in coral mucus (Fig. 3.4e), despite other gene expression patterns in *V. coralliilyticus* that point to virulence. This suggests the existence of functional redundancies amongst the many zinc metalloproteases that are encoded in the *V. coralliilyticus* genome. Indeed, it has previously been found that a Δ*vcpA* mutation did not compromise coral infection by the *V. coralliilyticus* P1 strain[29], and both VcpA and VcpB were undetectable at any temperature (avirulent 24 °C or virulent 27 °C) by Kimes et al.[33]. Finally, the mean nucleotide divergence of the *vcpA* gene amongst *V. coralliilyticus* isolates was found to be 3.7% compared to only 0.2% in the 16S rRNA gene[221], pointing to the possibility that protein functions may differ even within the single species of *V. coralliilyticus*.

The second, highly studied zinc metalloprotease in *V. coralliilyticus* virulence is VcpB. The *vcpB* gene has been found to be co-regulated with *vcpA* by VcpR (shown in Fig. 3.4d)[154]. Sussman et al. partially sequenced the putative zinc metalloprotease suspected to cause photoinactivation of coral symbionts[31]. According to our amino acid sequence homology analyses of the Sussman et al. fragment sequences, both VcpA and VcpB have 100% identity with some, but mutually exclusive, fragments. Thus, it is plausible that the symbiont photoinactivation and coral tissue lesions observed by Sussman et al. was mediated by a mixture of the two zinc metalloproteases (VcpA and VcpB). Notably, *vcpB* was one of the most significantly and strongly upregulated genes in coral mucus compared to control at 60 min (Supplementary Fig. 3.13, Supplementary Table 3.5), suggesting that its function is especially important for *V. coralliilyticus* in coral mucus. Similarly, the transcription of a metalloprotease by the fish pathogen *V. anguillarum* was induced by mucus[222]. Furthermore, the *V. cholerae* zinc metalloprotease HapA has been observed to degrade mucin as well as other physiological substrates[213,219,220]. Thus, a more detailed investigation of this second, less studied zinc metalloprotease may yield novel insights into the mechanisms of coral infection by *V. coralliilyticus*.

The gene annotated as “Zn-dependent protease with chaperone function” (EEX30795) was also amongst the top upregulated genes with high statistical significance (Supplementary Table 3.5). NCBI annotation suggests that this gene may encode YfgC, which has been found to maintain integrity of the outer membrane of *E. coli*[223]. Thus, it is plausible that EEX30795 may act in

concert with the growth- and biofilm-related activities suggested by the gene expression patterns of *V. coralliilyticus* in coral mucus.

RseP (EEX34624) was weakly upregulated in coral mucus at 10 min but not at 60 min (Supplementary Fig. 3.14), and was also detected at elevated levels at the virulent temperature of 27 °C (compared to 24 °C) by Kimes et al.[33]. RseP is characterized as an inner membrane-localized zinc metalloprotease that proteolyzes the master virulence regulator, ToxR, in response to nutrient limitation[165,224]. Thus, the reversal of nutrient limitation upon exposure to coral mucus may have led to the return of RseP expression to baseline levels at 60 min (Supplementary Fig. 3.14), and as a result, the accumulation of ToxR through its upregulation is expected (Fig. 3.4d).

Little information is available on the three zinc metalloproteases (aside from VcpA) that were downregulated (EEX33733, EEX33720) or not differentially expressed (EEX34306) in coral mucus compared to control. These, like some zinc metalloproteases, may serve biological functions that are not virulence-related, as suggested by a previous study of coral pathogens[217].

3.11 Acknowledgements

This research was funded by a Gordon and Betty Moore Foundation Marine Microbiology Initiative Investigator Award (GBMF3783) and Symbiosis in Aquatic Systems Initiative Investigator Award (GBMF9197) to R.S., a U.S. Department of Energy Joint Genome Institute Emerging Technologies Opportunity grant (DE-AC02-05CH11231) to R.S., a grant from the Simons Foundation through the Principles of Microbial Ecosystems (PriME) collaboration (542395) to R.S., and the National Science Foundation Graduate Research Fellowship (Grant No. 1122374) to C.G. The authors thank K.M. Wheeler (MIT), Dr. B. Ushijima (Smithsonian Marine Station), C. McLean (MIT/WHOI), Dr. U. Pfreundt (ETH Zurich), Dr. C. Martinez-Pérez (ETH Zurich), Dr. C.S. Smillie (Broad Institute/MGH), Eric Hill (NU Singapore) for discussions on RNA-seq analyses and interpretations; Dr. T. Kassis (MIT) for providing computational resources; Prof. J.S. Guasto (Tufts University) for insights and scripts on particle tracking; Prof. D.A. Lauffenburger (MIT) and Prof. K. Ribbeck (MIT) for scientific discussions; and Dr. R. Naisbit for editing this manuscript.

3.12 Author contributions

C.G., M.G., K.P., and R.S. designed the study. C.G., M.G., K.P. performed experiments. J.B.R. collected coral mucus. C.G., V.I.F., and R.S. created the video analysis software. C.G. performed RNA-seq data analyses with J.R.T.'s input. J.R.S. provided conceptual guidance. C.G., J.B.R., and R.S. wrote the manuscript. All authors edited the manuscript before submission.

Conclusions and Future Directions

In this Thesis, I combined diverse experimental techniques from biological engineering to connect marine microbial behavior and gene expression to ecosystem- and global-scale processes. In **Chapters 1** and **2**, the development of new genetic engineering tools for the manipulation of a marine microorganism, *R. pomeroyi*, afforded a novel opportunity to measure the expression of DMSP-degradation genes at the single-cell level. In **Chapter 3**, the first simultaneous measurements of behavior (video microscopy) and gene expression (RNA-seq) performed on the coral pathogen *V. coralliilyticus* enabled the observation of the sequence of events leading to infection. While this work gives us a peek into the marine microbial world, it also opens up several future directions of research.

In **Chapters 1** and **2**, I developed fluorescent reporter strains of *R. pomeroyi* to quantitatively measure, and visually differentiate between, the expression of demethylation or cleavage pathways. These reporter strains now enable researchers to test other environmental conditions that are relevant for DMSP catabolism. For example, measuring the effects of climate change on the relative expression of DMSP pathways could provide insights into future scenarios of climate-relevant DMS gas emission by marine bacteria.

The long timescales of fluorescent protein maturation (tens of minutes in *E. coli* at 37 °C)[89,225] and degradation (half-lives of hours to more than a day)[73,226] were a major design challenge of the fluorescent reporter strains, which prevented the real-time measurements of DMSP pathway expression. These challenges can by overcome with the combination of (i) decreasing the temporal gap between gene expression and fluorescence output by utilizing fluorescent proteins with fast maturation times (fastest maturation time of 6.4 ± 0.5 min reported in literature[70,225]), (ii) speed up fluorescent protein degradation by appending a short peptide sequence to mark them for protease degradation[73], and (iii) superior sensitivity of fluorescence signal detector that can measure dim signals due to fast fluorescent protein strains. The development of such a temporally faithful and responsive fluorescent reporter would require rigorous testing to validate precise signal measurements and quantification. If achieved, and if coupled with microfluidic

designs to simulate microscale hotspot conditions of DMSP, such as the microfluidic signal generator (MSG) that can rapidly deliver pulses of elevated solute concentrations to cells under microscopic observation[227], these fluorescent reporter strains could enable the truly real-time observation of intracellular gene expression changes in response to the heterogeneous exposure to DMSP or other solutes relevant in the marine environment.

In **Chapter 3**, I present the first investigation that couples behavioral and transcriptomic analyses of a bacterial pathogen to decipher the mechanisms promoting coral infection. The transcriptomic results generated several hypotheses regarding molecular mechanisms of disease progression, such as motility downregulation, biofilm formation, and toxin secretion in coral mucus, which must be tested in phenotypic experiments for confirmation.

Heterogeneous outcomes have been observed in coral colonies challenged with *V. coralliilyticus*, and the mechanisms behind coral survival or death post-infection remains elusive[133]. One possibility is that the chemical heterogeneity of mucin molecules leads to resistance in some coral colonies, while not in others. In the healthy human host, mucin glycoproteins have been shown to chemically attenuate bacterial pathogens by downregulating the expression of virulence genes[136,137] and preventing their biofilm formation[134,135]. While the mucus tested in the present study was collected from healthy corals, it is likely that the concentration of mucins, which underlie the high viscosity of mucus and whose glycans components are responsible for pathogen attenuation[134,136,137], was low due to contamination from surrounding seawater. Other studies that collected coral mucus through similar methodologies (i.e., dripping through air exposure), also reported low mucin concentrations and the lack of gel-like properties[24,131,228], which has been speculated to significantly alter the anti-microbial properties of the coral mucus[131]. In future studies, it would be of significant interest to test whether purified and concentrated coral mucin molecules, and their glycan components, can also attenuate *V. coralliilyticus* pathogenesis and prevent coral disease.

For billions of people around the world, the ocean provides food security, economic empowerment, and climate stability. Understanding how microbes mediate ecological processes,

from biogeochemical cycles to disease in a changing environment, holds the key to the future health of our oceans.

Appendix.

Quantitative microscopy and image analysis

This Appendix describes the following custom-built image processing pipelines used to analyze the microscopy image and video data presented in this Thesis:

A1. Image analysis for cellular fluorescence quantification
A2. Image analysis for phytoplankton-bacteria co-incubation experiment
A3. Video analysis for cell segmentation, swimming track reconstruction, and speed calculation
A4. Motile and non-motile cell determination

Sections A1 and A2 have been published as Supplementary Notes 1 and 3, respectively, in the publication presented in **Chapter 2**. Sections A3 and A4 represent text in the Supplementary Methods of the manuscript prepared for publication in **Chapter 3**.

MATLAB scripts for image processing and data analyses are available in the GitHub repository: https://github.com/cherryag

A1. Image analysis for cellular fluorescence quantification

A1.1. Cell segmentation, thresholding, and generation of 'cell mask' and 'background mask'

Analysis of fluorescence images was performed in MATLAB (MathWorks) using an automated image segmentation and fluorescence quantification software developed in-house. First, cell-containing pixels were recognized by applying a threshold (determined manually for each replicate experiment) on pixel intensity in phase contrast images, in which cells appear as dark (*i.e.*, low intensity) pixels. Subsequently, cells were segmented by grouping cell-containing pixels that were in contact with each other.

Not all recognized cells were suitable for further analyses due to their orientation or size. Cells that were positioned perpendicular to the glass slide, which contained high intensity pixels in phase contrast images, were not suitable for quantification due to the larger integration distance in the z-direction for fluorescence signals. These perpendicular cells were eliminated from further analyses by applying a threshold (determined manually for each replicate experiment) on the upper quartile pixel intensity within each cell in phase contrast images, whereby cells containing many high intensity (*i.e.*, white) pixels were eliminated from further analyses. Furthermore, thresholds on maximum and minimum size (*i.e.*, number of pixels within a segmented cell; pixel size = 0.2 μm × 0.2 μm) eliminated aggregates of many cells (large size; maximum area threshold = 200 pixels), or other particles (small size; minimum area threshold = 10 pixels). The average size of a cell was 39.0 ± 4.02 pixels (mean ± s.d. of cells in replicate experiments). As a result of thresholding, ~20% of originally recognized cells were eliminated from further analyses. The position of each cell was recorded, and a 'cell mask' was generated from each phase contrast image. Appropriate cell segmentation and thresholding were visually inspected and confirmed for each image. In some images, a small offset (*e.g.*, by 1–5 pixels) between 'cell masks' and fluorescence images were manually corrected.

Background fluorescence was defined as the average intensity of pixels that do not contain cells, within a fluorescence channel image. Cell-containing areas of 'cell masks' were dilated by a radius of 20–30 pixels, and the negatives of these expanded 'cell masks' served as 'background masks'. Representative samples of 'background masks' were visually inspected for appropriate background pixel identification. The background intensity for each fluorescence image was calculated as the average intensity of pixels containing no cells, labeled in 'background masks'.

Cell and background masks were applied to fluorescence images for cellular and background fluorescence intensity quantification. Fluorescence intensity (TFP, YFP, or RFP) of each cell was defined as the mean intensity of pixels contained within a recognized cell. Background fluorescence was subtracted from each cell to account for variation in background signal levels in different images.

A1.2. Spectral leakage correction in image processing and analyses

Our tricolor reporter strains (Fig. 1a,b) expressed three fluorescent proteins (TFP, YFP, and RFP) which were chosen for maximum spectral separation. However, the wide excitation and emission spectra of fluorescent proteins, combined with the range of wavelengths that pass through emission filters of filter cubes, led to some fluorescence emission signals leaking into inappropriate channels (*e.g.*, fluorescence emission from YFP leaking into the teal channel). Thus, spectral leakage correction was applied during image processing and analyses for accurate quantification of true fluorescence intensities. True fluorescence intensities expressed by the tricolor reporter strains are represented in the following equations:

$$\hat{t} = \boldsymbol{t} + \alpha y + \beta r \qquad \text{(Eq. S1)}$$

$$\hat{y} = \gamma t + \boldsymbol{y} + \delta r \qquad \text{(Eq. S2)}$$

$$\hat{r} = \varepsilon t + \zeta y + \boldsymbol{r} \qquad \text{(Eq. S3)}$$

where $\hat{t}$, $\hat{y}$, and $\hat{r}$ represent the recorded intensities in teal, yellow, and red channels, respectively. The recorded intensity ($\hat{t}$, $\hat{y}$, or $\hat{r}$) of each fluorescent protein was expressed as a sum of (i) the *true* intensity (t, y, or r) in the color channel that match the fluorescent protein of interest and (ii) *leakage* intensities from the other two fluorescent proteins, which were represented as fractions (α, β, γ, δ, ε, and ζ) of the true intensities of the two auxiliary fluorescent proteins. Equations S1–S3 can also be represented in aggregate:

$$\begin{bmatrix} \widehat{t} \\ y \\ r \end{bmatrix} = B \times \begin{bmatrix} \boldsymbol{t} \\ \boldsymbol{y} \\ \boldsymbol{r} \end{bmatrix} \qquad \text{(Eq. S4)}$$

where

$$B = \begin{bmatrix} 1 & \alpha & \beta \\ \gamma & 1 & \delta \\ \varepsilon & \zeta & 1 \end{bmatrix} \qquad \text{(Eq. S5)}$$

Thus, B is the spectral leakage correction matrix that enabled us to solve for the true intensities (t, y, and r) from recorded intensities ($\hat{t}$, $\hat{y}$, and $\hat{r}$).

A1.3. Calculation of spectral leakage correction matrix, *B*

To calculate the spectral leakage correction matrix, B, the intensities of signals that leaked into inappropriate channels were quantified for each fluorescent protein (Supplementary Fig. 16). Constitutively fluorescent single-color control strains (TFP-, YFP-, or RFP-expressing strains) were grown as described in Methods. These control strains were placed in separate observation chambers of a microfluidic device, allowed to settle for ~30 minutes, and imaged in every fluorescence color channel with microscopy specifications as described in Methods. Images were obtained from ten biological replicates (*i.e.*, from overnight cultures prepared on 10 different days) of each single-color control strain.

Cells in images were segmented by thresholding on pixel intensity in phase contrast images, followed by background fluorescence subtraction. Only cells with fluorescence intensity values above 0 a.u. in the true fluorescent color channel were included for calculation of B (mean ± s.d. number of cells included for analysis in a biological replicate were n = 4,765 ± 1,955; n = 3,246 ± 1,938; n = 3,367 ± 1,952 for RFP, YFP, and TFP single-color strains, respectively). All cells across all biological replicates (n = 10) were pooled, and the signals of each cell measured in all three fluorescence channels were plotted on pairs of axes each representing a color channel (n = 47,648; n = 32,458; n = 33,672 cells after pooling, for RFP, YFP, and TFP single-color strains, respectively) (Supplementary Fig. 16). Linear least squares regression, assuming an intercept at x = 0 and y = 0, was performed on the pooled fluorescence signal data for the calculation of B (Supplementary Fig. 16):

$$B = \begin{bmatrix} 1 & 9.8 \times 10^{-2} & 7.2 \times 10^{-3} \\ 1.1 \times 10^{-3} & 1 & 4.0 \times 10^{-4} \\ 1.0 \times 10^{-4} & 2.6 \times 10^{-3} & 1 \end{bmatrix}$$

The spectral leakage correction matrix, B, was used to solve for the true fluorescence intensities (t, y, or r) of each cell in microfluidic experiments using Equation S4.

A similar method, with images of single-color strains grown on agarose pads, was used to calculate a different spectral leakage correction matrix, $B_{agarose}$, for the phytoplankton-bacteria co-incubation experiment:

$$B_{agarose} = \begin{bmatrix} 1 & 8.9 \times 10^{-2} & 1.9 \times 10^{-3} \\ 6.0 \times 10^{-4} & 1 & 1.0 \times 10^{-4} \\ -2.0 \times 10^{-4} & 1.1 \times 10^{-2} & 1 \end{bmatrix}$$

A1.4. Spectral leakage correction, and thresholding and normalization by constitutive YFP

True fluorescence intensities of each cell were solved for by using the spectral leakage correction matrix, B. The largest correction occurred with teal fluorescence signals, into which YFP leaked significantly (Supplementary Fig. 16). After spectral leakage correction, dim or non-fluorescent (*i.e.*, low metabolic activity or dead) cells were eliminated from further analyses by applying a threshold (50 a.u.) on constitutive YFP fluorescence. The distribution of cellular YFP signals revealed a bimodal distribution: one population with a sharp peak near 0 a.u. containing non-fluorescent or dim cells, and a second, larger population consisting of bright cells. A cutoff YFP intensity of 50 a.u. was applied to all replicate experiments of time-lapse DMSP experiments in microfluidic chips (Supplementary Fig. 6) to eliminate non-fluorescent or dim cells. As a result of thresholding on YFP intensity, 6–33% of recognized cells were eliminated from further analyses.

Finally, RFP and TFP signals of each cell were normalized by YFP fluorescence, which served as a proxy for metabolic activity level and plasmid number. Fluorescence signals in red and teal channels of each cell were normalized by the mean YFP signal at the corresponding time point and experimental condition (Supplementary Fig. 15).

A1.5. Calculation of theoretical 'off' fluorescence intensity

Due to detector noise, a non-zero signal was detected even in the absence of fluorescence expression by cells. Thus, the theoretical 'off' intensity value of cells had to be determined to differentiate absence of fluorescence (*e.g.*, promoters that are turned off) from weak signal intensities (*e.g.*, leaky promoters).

The theoretical 'off' fluorescence intensities were defined as the values of signal leakage detected in the red and teal fluorescence channels while imaging the single-color YFP control strain, after background subtraction, and spectral-leakage correction using *B*. Only YFP cells whose true fluorescence intensities in the yellow channel were above 30 a.u. were included in the analysis.

To calculate the average theoretical 'off' fluorescence intensities, signals in red and teal channels were first averaged across cells in each image, then subsequently averaged across images within a replicate, and normalized by the average YFP intensity of the corresponding replicate. Finally, normalized leakage intensities were averaged across all replicate experiments ($n = 10$). The values (mean ± s.d.) of the theoretical 'off' fluorescence were $-1.6 \pm 0.37 \times 10^{-3}$ a.u. (red channel) and $2.5 \pm 4.1 \times 10^{-3}$ a.u. (teal channel) (Supplementary Fig. 5).

A2. Image analysis for phytoplankton-bacteria co-incubation experiment

A2.1. Segmentation of *Breviolum* cells and identification of concentric rings

Phycosphere images were analyzed using a similar MATLAB software as that described for the analysis of observation chamber experiments (Supplementary Note 2). Additional steps and differences in image processing of phycosphere images are described below.

Due to spectral leakage in the red channel by photosynthetic pigments (which masked any RFP signals from bacteria), only signals in the teal (reporting *dmdA* in strain Regular and *dddW* in strain Goofy) and yellow (constitutive YFP expression) channels were quantified, while the red channel was used only to assess the fluorescence signal of *Breviolum* photosynthetic pigments. Images were selected for analysis by screening for bright photosynthetic pigment fluorescence in the red channel (*Breviolum* cells with diffuse, low-intensity pigment fluorescence were excluded from analysis). Furthermore, images with only one phytoplankton cell per field of view (80 μm × 80 μm) were selected. These selection criteria yielded 15 images for strain Regular (reporting *dmdA* with TFP) and 18 images for strain Goofy (reporting *dddW* with TFP), with a combined total of 33 phycosphere images for further analyses.

Segmentation of *Breviolum* cells was achieved through pixel intensity thresholding on photosynthetic pigment signal in the red channel, and approximating *Breviolum* cells as circles. Concentric rings with 20 pixels width (1.6 μm), emanating from the surface of circularly approximated *Breviolum* cells, were used to bin distances within phycospheres. Since the radii of *Breviolum* cells slightly differed across 33 cells (3.3 ± 0.9 μm; mean radius ± s.d.), the distance of concentric rings from the center of *Breviolum* cells varied slightly from image to image. The largest concentric ring (*i.e.*, the farthest distance within the phycosphere) was determined to be the ring before the one that contacted any edge of the image.

A2.2. Uneven illumination correction, background fluorescence subtraction, and spectral leakage correction with $B_{agarose}$

Uneven illumination across the field of view was observed at high magnification (100×), probably due to factors related to the light path between the camera and the microscope. To quantitatively correct for uneven illumination, images of agarose pads in the absence of cells were taken in each channel at different stage positions (n = 4). At each pixel position, intensities were averaged across the 4 images to create a master 'uneven illumination correction' image. Phycosphere images in teal and yellow channels were corrected by division, at each pixel position, by the master 'uneven illumination correction' image at the corresponding pixel position in corresponding channels. The effect of uneven illumination was small: as an estimate of the magnitude of the maximum correction, the ratio of minimum and maximum intensities in the 'uneven illumination correction' images were 0.81 in teal and 0.87 in yellow.

Background fluorescence intensity was calculated by first roughly identifying *Breviolum*- and bacteria-containing regions by thresholding on pixel intensity in the phase contrast channel (to identify dark/low- and bright/high-intensity pixels), then expanding the region by a distance of 35 pixels. The negative of this expanded area generated the 'background masks'. Average intensities of background pixels were calculated in teal and yellow fluorescence channels for each phycosphere image, and were subtracted from each non-background pixel.

Phycosphere experiment-specific spectral leakage correction matrix, $B_{agarose}$, was generated by analyzing images of constitutively fluorescent single-color control strains (RFP, YFP, or TFP)

grown on agarose pads in the absence of phytoplankton. Single-color bacteria-containing pixels were identified by thresholding on fluorescence intensity, and linear regression on pixel intensities were performed to calculate the spectral leakage correction matrix, $B_{agarose}$. The spectral leakage correction matrix was applied to each pixel of co-incubation images to solve for the true fluorescence intensities in teal and yellow channels.

A2.3. Quantification of bacterial *dmdA* and *dddW* gene expression in phycospheres

After background subtraction and spectral leakage correction, pixels containing *R. pomeroyi* cells were identified by thresholding for high YFP fluorescence (proxy for metabolic activity), and for positive teal fluorescence values. Due to differences in magnification and experimental setups, different fluorescence intensity thresholds were chosen for the phycosphere experiments than those applied in the time-lapse DMSP experiments performed in observation chambers. Constitutive YFP was brighter in strain Goofy than in strain Regular, reporting *dddW* and *dmdA* in TFP, respectively, probably due to slight differences in growth phase in each bacterial culture. As such, different thresholds of YFP intensity (>0.08 a.u. for *dmdA* and >0.23 a.u. for *dddW* reporters) were chosen through visual inspection of resulting images, whereby appropriate YFP intensity thresholds accepted cell-containing pixels but excluded background pixels. The YFP intensity threshold values were roughly in the same place in the distribution of pixel intensities for the two reporter strains. Finally, pixels that passed the YFP intensity threshold had to also have positive teal fluorescence values (>0 a.u.) for inclusion in further analyses. Appropriate cell-associated pixel identification and thresholding were visually inspected and confirmed for each image.

Rather than segmenting each bacterial cell, each bacteria-containing pixel was independently quantified. In each phycosphere, only distances at which the area of 20-pixel-width concentric rings contained at least 500 bacteria-associated pixels (equivalent area of a 6.3 μm × 6.3 μm square, or approximately 3 cells) were included for further analyses. Despite this 500-pixel threshold, at least 10 images (out of 15, for *dmdA*) and 14 images (out of 18, for *dddW*) were included for analyses at any given concentric ring distance within the phycosphere. Fluorescence intensity values at each concentric ring were aggregated across images to calculate the average values presented in Fig. 4c,d.

A2.4. Calculation of relative expression of *dmdA* and *dddW* in phycospheres

To compare *dmdA* and *dddW* expression levels, TFP intensity (reporting *dmdA* or *dddW*) of each pixel was normalized by its own YFP intensity (Fig. 4e). Cleavage-to-demethylation ratio (*dddW* / *dmdA*) was calculated as the product of the mean normalized TFP intensity of strain Goofy (*dddW*, $n = 18$) and the mean of the inverse of normalized TFP intensity of strain Regular (*dmdA*, $n = 15$) at each distance within the phycosphere (Fig. 4f). Error bars represent the variance of the cleavage-to-demethylation ratio, or the product of cleavage and inverse of demethylation gene expression ($\mu_W \cdot \mu_{\frac{1}{A}}$), and was calculated with the following equation at each distance within the phycosphere:

$$Var\left(\mu_W \cdot \mu_{\frac{1}{A}}\right) = \sigma^2{}_W \cdot \sigma^2{}_{\frac{1}{A}} + \sigma^2{}_W \cdot \mu^2{}_{\frac{1}{A}} + \sigma^2{}_{\frac{1}{A}} \cdot \mu^2{}_W \qquad \text{(Eq. S6)}$$

where μ_W and σ_W represent the mean and standard deviation of *dddW* expression level at a concentric ring; and $\mu_{\frac{1}{A}}$ and $\sigma_{\frac{1}{A}}$ are the mean and standard deviation of the inverse of *dmdA* expression levels at a concentric ring.

A3. Video analysis for cell segmentation, swimming track reconstruction, and speed calculation

Each frame of a video was processed independently for bacterial cell segmentation. First, images were smoothed by applying a Gaussian spatial filter to reduce the background signal noise and increase contrast. Next, putative cell-containing pixels were recognized by applying a threshold on pixel intensity (determined manually for each experiment) to phase contrast images, in which cells appear as dark (i.e., low intensity) pixels. Images were converted to binary by assigning 0 to putative cell-containing pixels and 1 to all other pixels. Putative cell-containing pixels that were in contact with each other were grouped together as putative cells (particles). To remove unwanted particles, thresholds on diameter and average pixel intensity of particles were applied.

Threshold values were manually determined through visual inspection for each experiment, and typically categorized particles as cells if they possessed 1 μm ≤ diameter ≤ 4 μm, and particle intensity ≤ –500 a.u.

Individual trajectories (*x,y*-coordinates vs. time), each representing the swimming path of a single cell, were reconstructed from identified cell positions through subsequent frames using a particle tracking routine. Cells tracked for less than four consecutive frames (< 0.1 s) were excluded from trajectory reconstruction, as were cells with displacements exceeding 6 μm between two consecutive frames (equivalent swimming speed of ≥ 180 μm/s). The success of cell segmentation and swimming track reconstruction was manually assessed by visualizing 40 frames of each video with swimming track information overlaid.

A swimming trajectory was sometimes inappropriately broken into two or more tracks, for example due to a motile cell going into and out of focus between frames. To reconnect broken trajectories, the future position of a bacterium was predicted using its direction and speed (i.e., velocity) at the end of its track, which was locally smoothed over 3 frames (0.1 s) using a linear fit. Subsequently, if another track with a similar velocity began within 8 μm distance from the end of the first track, and within the next 1–3 frames, the two tracks were reconnected as one. Application of this trajectory reconnection algorithm led to an average reduction to 83% ± 6% (mean ± s.d.) of the original number of tracks.

Finally, we discarded short swimming tracks from further analyses by applying a minimum track length threshold of 10 frames (0.33 s), inclusive, to enable accurate calculation of swimming speeds. From these reconstructed trajectories that passed the minimum track length threshold, we calculated the swimming speed of each cell by averaging the instantaneous speed over the duration of that cell's trajectory. The mean speed of the population was quantified by averaging over all trajectories detected in each microscopy video, representing a single time point in mucus or control condition.

A4. Motile and non-motile cell determination

To differentiate between motile and non-motile cells, two types of thresholds (speed and extent of ballistic motion) were applied to each swimming trajectory. First, slow bacteria (median instantaneous speed < 10 μm/s) were categorized as non-motile cells. The median instantaneous speed, rather than the mean, was used to avoid disproportionate influence of extreme instantaneous swimming speeds, which are more likely to occur in longer swimming tracks. Subsequently, we fine-tuned the categorization of motile and non-motile cells by characterizing their motility as ballistic or diffusive.

Motile bacteria display ballistic motion over short time intervals, while non-motile bacteria display diffusive motion. To determine the type of motility (ballistic or diffusive) of a bacterium, we calculated the mean squared displacement (MSD) as a function of short time intervals (Δt) ranging from 1 frame (0.03 s) to 9 frames (0.3 s) at 1-frame intervals, and quantified the exponent α of this dependence (MSD ~ Δt^{α}). The maximum Δt of 9 frames (0.3 s) was chosen as a time window that is short enough to only observe one ballistic motion, but long enough to differentiate between diffusive and ballistic motion. The MSD of particles such as bacterial cells is described by a power law, (MSD ~ Δt^{α}), where $\alpha = 2$ for ballistic motion, $\alpha = 1$ for diffusive motion, and $\alpha = 0$ for non-motile cells. Thus, we determined the MSD exponent, α, for each bacterium as the slope of the linear fit of $\log_{10}$-transformed Δt and MSD.

Since *V. coralliilyticus* bacteria do not swim ballistically throughout their entire trajectories, but rather display a run-reverse-flick mode of swimming with intermittent ballistic motion[229,230], the MSD exponent of motile cells is expected to fall in the range $1 < \alpha \leq 2$. Thresholds were determined by inspection of the scatter plot of median instantaneous velocities and MSD exponents of all swimming tracks (Supplementary Fig. 3.1). Subsequently, cells with MSD exponent $\alpha \geq 1$, in addition to median instantaneous speed ≥ 10 μm/s, were categorized as motile. A sensitivity analysis was performed that showed how the precise value of the selected parameter thresholds did not substantially affect results (Supplementary Fig. 3.2).

References

1. Field, C. B., Behrenfeld, M. J., Randerson, J. T. & Falkowski, P. Primary production of the biosphere: Integrating terrestrial and oceanic components. *Science* **281**, 237–240 (1998).
2. Li, W. K. W. *et al.* Autotrophic picoplankton in the tropical ocean. *Science* **12**, 1987 (1983).
3. Falkowski, P. *et al.* The global carbon cycle: A test of our knowledge of earth as a system. *Science* **290**, 291–296 (2000).
4. Azam, F. *et al.* The ecological role of water-column microbes in the sea. *Mar. Ecol. Prog. Ser.* **10**, 257–263 (1983).
5. Pomeroy, L. R. The Ocean's Food Web, A Changing Paradigm. *Bioscience* **24**, 499–504 (1974).
6. Bar-On, Y. M., Phillips, R. & Milo, R. The biomass distribution on Earth. *Proc. Natl. Acad. Sci. USA* **115**, 6506–6511 (2018).
7. Whitman, W. B., Coleman, D. C. & Wiebe, W. J. Prokaryotes: The unseen majority. *Proc. Natl. Acad. Sci. USA* **95**, 6578–6583 (1998).
8. Burke, L., Reytar, K., Spalding, M. & Perry, A. *Reefs at risk revisited*. *Word Resources Institute* (World Resources Institute, 2011).
9. Archer, S. D., Widdicombe, C. E., Tarran, G. A., Rees, A. P. & Burkill, P. H. Production and turnover of particulate dimethylsulphoniopropionate during a coccolithophore bloom in the northern North Sea. *Aquat. Microb. Ecol.* **24**, 225–241 (2001).
10. Howard, E. C. *et al.* Bacterial taxa that limit sulfur flux from the ocean. *Science* **314**, 649–652 (2006).
11. Moran, M. A. & Durham, B. P. Sulfur metabolites in the pelagic ocean. *Nat. Rev. Microbiol.* **17**, 665–678 (2019).
12. Zubkov, M. V. *et al.* Linking the composition of bacterioplankton to rapid turnover of dissolved dimethylsulphoniopropionate in an algal bloom in the North Sea. *Environ. Microbiol.* **3**, 304–311 (2001).
13. Simó, R., Archer, S. D., Pedrós-Alió, C., Gilpin, L. & Stelfox-Widdicombe, C. E. Coupled dynamics of dimethylsulfoniopropionate and dimethylsulfide cycling and the microbial food web in surface waters of the North Atlantic. *Limnol. Oceanogr.* **47**, 53–61 (2002).
14. Kiene, R. P., Linn, L. J. & Bruton, J. A. New and important roles for DMSP in marine microbial communities. *J. Sea Res.* **43**, 209–224 (2000).
15. Vallina, S. M. & Simó, R. Strong relationship between DMS and the solar radiation dose over the global surface ocean. *Science* **315**, 506–508 (2007).
16. Charlson, R. J., Lovelock, J. E., Andreae, M. O. & Warren, S. G. Oceanic phytoplankton, atmospheric sulphur, cloud albedo and climate. *Nature* **326**, 655–661 (1987).
17. Maynard, J. *et al.* Projections of climate conditions that increase coral disease susceptibility and pathogen abundance and virulence. *Nat. Clim. Chang.* **5**, 688–695 (2015).
18. De'Ath, G., Fabricius, K. E., Sweatman, H. & Puotinen, M. The 27-year decline of coral cover on the Great Barrier Reef and its causes. *Proc. Natl. Acad. Sci. USA* **109**, 17995–17999 (2012).
19. Randall, C. J. & van Woesik, R. Contemporary white-band disease in Caribbean corals driven by climate change. *Nat. Clim. Chang.* **5**, 375–379 (2015).
20. Ben-Haim, Y. *et al. Vibrio coralliilyticus* sp. nov., a temperature-dependent pathogen of the coral *Pocillopora damicornis*. *Int. J. Syst. Evol. Microbiol.* **53**, 309–315 (2003).
21. Reed, K. C., Muller, E. M. & van Woesik, R. Coral immunology and resistance to disease. *Dis. Aquat. Organ.* **90**, 85–92 (2010).
22. Mao-Jones, J., Ritchie, K. B., Jones, L. E. & Ellner, S. P. How microbial community composition regulates coral disease development. *PLoS Biol.* **8**, 22–26 (2010).
23. Rosado, P. M. *et al.* Marine probiotics: increasing coral resistance to bleaching through microbiome manipulation. *ISME J.* **13**, 921–936 (2019).
24. Brown, B. E. & Bythell, J. C. Perspectives on mucus secretion in reef corals. *Mar. Ecol. Prog. Ser.* **296**, 291–309 (2005).
25. Garren, M. & Azam, F. New method for counting bacteria associated with coral mucus. *Appl. Environ. Microbiol.* **76**, 6128–6133 (2010).
26. Wild, C. *et al.* Coral mucus functions as an energy carrier and particle trap in the reef ecosystem. *Nature* **428**, 66–70 (2004).
27. Garren, M. *et al.* A bacterial pathogen uses dimethylsulfoniopropionate as a cue to target heat-stressed

corals. *ISME J.* **8**, 999–1007 (2014).
28. Garren, M., Son, K., Tout, J., Seymour, J. R. & Stocker, R. Temperature-induced behavioral switches in a bacterial coral pathogen. *ISME J.* **10**, 1363–1372 (2016).
29. de O Santos, E. *et al.* Genomic and proteomic analyses of the coral pathogen *Vibrio coralliilyticus* reveal a diverse virulence repertoire. *ISME J.* **5**, 1471–1483 (2011).
30. Ushijima, B. & Häse, C. C. Influence of chemotaxis and swimming patterns on the virulence of the coral pathogen *Vibrio coralliilyticus*. *J. Bacteriol.* **200**, 1–16 (2018).
31. Sussman, M. *et al. Vibrio* zinc-metalloprotease causes photoinactivation of coral endosymbionts and coral tissue lesions. *PLoS One* **4**, (2009).
32. Ushijima, B. *et al.* Mutation of the *toxR* or *mshA* genes from *Vibrio coralliilyticus* strain OCN014 reduces infection of the coral *Acropora cytherea*. *Environ. Microbiol.* **18**, 4055–4067 (2016).
33. Kimes, N. E. *et al.* Temperature regulation of virulence factors in the pathogen *Vibrio coralliilyticus*. *ISME J.* **6**, 835–846 (2012).
34. Hasegawa, H., Lind, E. J., Boin, M. A. & Häse, C. C. The extracellular metalloprotease of *Vibrio tubiashii* is a major virulence factor for pacific oyster (*Crassostrea gigas*) larvae. *Appl. Environ. Microbiol.* **74**, 4101–4110 (2008).
35. Meron, D. *et al.* Role of Flagella in Virulence of the Coral Pathogen *Vibrio coralliilyticus*. *Appl. Environ. Microbiol.* **75**, 5704–5707 (2009).
36. Ushijima, B., Richards, G. P., Watson, M. A., Schubiger, C. B. & Häse, C. C. Factors affecting infection of corals and larval oysters by Vibrio coralliilyticus. *PLoS One* **13**, e0199475 (2018).
37. Stocker, R. Marine microbes see a sea of gradients. *Science* **338**, 628–633 (2012).
38. Azam, F. Microbial control of oceanic carbon flux: the plot thickens. *Science* **280**, 694–696 (1998).
39. Stocker, R. The 100 µm length scale in the microbial ocean. *Aquat. Microb. Ecol.* **76**, 189–194 (2015).
40. Stocker, R., Seymour, J. R., Samadani, A., Hunt, D. E. & Polz, M. F. Rapid chemotactic response enables marine bacteria to exploit ephemeral microscale nutrient patches. *Proc. Natl. Acad. Sci. USA* **105**, 4209–4214 (2008).
41. Stepanauskas, R. & Sieracki, M. E. Matching phylogeny and metabolism in the uncultured marine bacteria, one cell at a time. *Proc. Natl. Acad. Sci. USA* **104**, 9052–9057 (2007).
42. Zhao, W. & Andersson, S. G. E. Single cell genomics of deep ocean bacteria. *Trends Microbiol.* **22**, 233–234 (2014).
43. Koch, L. Plenty of single cells in the sea. *Nat. Rev. Genet.* **21**, 70 (2020).
44. Kashtan, N. *et al.* Single-cell genomics reveals hundreds of coexisting subpopulations in wild *Prochlorococcus*. *Science* **344**, 416–420 (2014).
45. Smriga, S., Fernandez, V. I., Mitchell, J. G. & Stocker, R. Chemotaxis toward phytoplankton drives organic matter partitioning among marine bacteria. *Proc. Natl. Acad. Sci.* **113**, 1576–1581 (2016).
46. Lambert, B. S. *et al.* A microfluidics-based in situ chemotaxis assay to study the behaviour of aquatic microbial communities. *Nat. Microbiol.* **2**, 1344–1349 (2017).
47. Olson, R. J. & Sosik, H. M. A submersible imaging-in-flow instrument to analyze nano-and microplankton: Imaging FlowCytobot. *Limnol. Oceanogr. Methods* **5**, 195–203 (2007).
48. González, J. M., Kiene, R. P. & Moran, M. a. Transformation of sulfur compounds by an abundant lineage of marine bacteria in the alpha-subclass of the class Proteobacteria. *Appl. Environ. Microbiol.* **65**, 3810–9 (1999).
49. José M González *et al. Silicibacter pomeroyi* sp. nov. and *Roseovarius nubinhibens* sp. nov., dimethylsulfoniopropionate-demethylating bacteria from marine environments. *Int. J. Syst. Evol. Microbiol.* **53**, 1261–1269 (2003).
50. Moran, M. A. *et al.* Genome sequence of *Silicibacter pomeroyi* reveals adaptations to the marine environment. *Nature* **432**, 910–913 (2004).
51. Henriksen, J. R. Physiology of DMSP metabolism in a model marine Roseobacter, *Silicibacter pomeroyi*. (University of Georgia, 2008).
52. Reisch, C. R. *et al.* Novel pathway for assimilation of dimethylsulphoniopropionate widespread in marine bacteria. *Nature* **473**, 208–211 (2011).
53. Todd, J. D., Curson, A. R. J., Sullivan, M. J., Kirkwood, M. & Johnston, A. W. B. The *Ruegeria pomeroyi acuI* Gene Has a Role in DMSP Catabolism and Resembles *yhdH* of *E. coli* and Other Bacteria in Conferring Resistance to Acrylate. *PLoS One* **7**, e35947 (2012).
54. Lidbury, I., Murrell, J. C. & Chen, Y. Trimethylamine N-oxide metabolism by abundant marine heterotrophic bacteria. *Proc. Natl. Acad. Sci. USA* **111**, 2710–2715 (2014).

55. Reisch, C. R. *et al.* Metabolism of dimethylsulphoniopropionate by *Ruegeria pomeroyi* DSS-3. *Mol. Microbiol.* **89**, 774–791 (2013).
56. Keen, N. T., Tamaki, S., Kobayashi, D. & Trollinger, D. Improved broad-host-range plasmids for DNA cloning in Gram-negative bacteria. *Gene* **70**, 191–197 (1988).
57. Piekarski, T. *et al.* Genetic tools for the investigation of Roseobacter clade bacteria. *BMC Microbiol.* **9**, 265 (2009).
58. Burns, A. S. *et al.* Small RNAs expressed during dimethylsulfoniopropionate degradation by a model marine bacterium. *Environ. Microbiol. Rep.* **00**, (2016).
59. Sebastian, M. & Ammerman, J. W. The alkaline phosphatase PhoX is more widely distributed in marine bacteria than the classical PhoA. *ISME J.* **3**, 563–72 (2009).
60. Lambertsen, L., Sternberg, C. & Molin, S. Mini-Tn7 transposons for site-specific tagging of bacteria with fluorescent proteins. *Environ. Microbiol.* **6**, 726–732 (2004).
61. Koch, B., Jensen, L. E. & Nybroe, O. A panel of Tn7-based vectors for insertion of the *gfp* marker gene or for delivery of cloned DNA into Gram-negative bacteria at a neutral chromosomal site. *J. Microbiol. Methods* **45**, 187–195 (2001).
62. Bürgmann, H. *et al.* Transcriptional response of *Silicibacter pomeroyi* DSS-3 to dimethylsulfoniopropionate (DMSP). *Environ. Microbiol.* **9**, 2742–2755 (2007).
63. Lanzer, M. & Bujard, H. Promoters largely determine the efficiency of repressor action. *Proc. Natl. Acad. Sci. USA* **85**, 8973–8977 (1988).
64. Croxatto, A., Lauritz, J., Chen, C. & Milton, D. L. *Vibrio anguillarum* colonization of rainbow trout integument requires a DNA locus involved in exopolysaccharide transport and biosynthesis. *Environ. Microbiol.* **9**, 370–382 (2007).
65. Antje Stahl. Interaction of the Marine Bacterium *Marinobacter adhaerens* HP15 with the Diatom *Thalassiosira weissflogii* Analyzed by Proteomics Approaches. (Jacobs University, 2015).
66. Persat, A., Stone, H. A. & Gitai, Z. The curved shape of *Caulobacter crescentus* enhances surface colonization in flow. *Nat. Commun.* **5**, 3824 (2014).
67. D'Alvise, P. W. *et al. Phaeobacter gallaeciensis* reduces *Vibrio anguillarum* in cultures of microalgae and rotifers, and prevents Vibriosis in cod larvae. *PLoS One* **7**, e43996 (2012).
68. Pédelacq, J.-D., Cabantous, S., Tran, T., Terwilliger, T. C. & Waldo, G. S. Engineering and characterization of a superfolder green fluorescent protein. *Nat. Biotechnol.* **24**, 79–88 (2006).
69. Miyawaki, A., Sawano, A. & Kogure, T. Lighting up cells: Labelling proteins with fluorophores. *Nat. Rev. Mol. Cell Biol.* **4**, 1–7 (2003).
70. Lambert, T. J. FPbase: a community-editable fluorescent protein database. *Nat. Methods* **16**, 277–278 (2019).
71. Cox III, R. S., Dunlop, M. J. & Elowitz, M. B. A synthetic three-color scaffold for monitoring genetic regulation and noise. *J. Biol. Eng.* **4**, 10 (2010).
72. Haugen, S. P., Ross, W. & Gourse, R. L. Advances in bacterial promoter recognition and its control by factors that do not bind DNA. *Nat. Rev. Microbiol.* **6**, 507–519 (2008).
73. Andersen, J. B. *et al.* New unstable variants of green fluorescent protein for studies of transient gene expression in bacteria. *Appl. Environ. Microbiol.* **64**, 2240–2246 (1998).
74. Simó, R. Production of atmospheric sulfur by oceanic plankton: biogeochemical, ecological and evolutionary links. *Trends Ecol. Evol.* **16**, 287–294 (2001).
75. Kettle, A. J. *et al.* A global database of sea surface dimethylsulfide (DMS) measurements and a procedure to predict sea surface DMS as a function of latitude, longitude, and month. *Global Biogeochem. Cycles* **13**, 399–444 (1999).
76. Malin, G., Turner, S., Liss, P., Holligan, P. & Harbour, D. Dimethylsulphide and dimethylsulphoniopropionate in the Northeast Atlantic during the summer coccolithophore bloom. *Deep Sea Res. I* **40**, 1487–1508 (1993).
77. Caruana, A. M. N. & Malin, G. The variability in DMSP content and DMSP lyase activity in marine dinoflagellates. *Prog. Oceanogr.* **120**, 410–424 (2014).
78. Landa, M., Burns, A. S., Roth, S. J. & Moran, M. A. Bacterial transcriptome remodeling during sequential co-culture with a marine dinoflagellate and diatom. *ISME J.* **11**, 2677–2690 (2017).
79. Varaljay, V. A. *et al.* Single-taxon field measurements of bacterial gene regulation controlling DMSP fate. *ISME J.* **9**, 1677–1686 (2015).
80. Rinta-Kanto, J. M. *et al.* Analysis of sulfur-related transcription by Roseobacter communities using a taxon-specific functional gene microarray. *Environ. Microbiol.* **13**, 453–467 (2011).

81. Moran, M. A., González, J. M. & Kiene, R. P. Linking a bacterial taxon to sulfur cycling in the sea: studies of the marine Roseobacter group. *Geomicrobiol. J.* **20**, 375–388 (2003).
82. Curson, A. R. J., Todd, J. D., Sullivan, M. J. & Johnston, A. W. B. Catabolism of dimethylsulphoniopropionate: microorganisms, enzymes and genes. *Nat. Rev. Microbiol.* **9**, 849–859 (2011).
83. Young, J. W. *et al.* Measuring single-cell gene expression dynamics in bacteria using fluorescence time-lapse microscopy. *Nat. Protoc.* **7**, 80–88 (2012).
84. Locke, J. C. W. & Elowitz, M. B. Using movies to analyse gene circuit dynamics in single cells. *Nat. Rev. Microbiol.* **7**, 383–392 (2009).
85. Kentner, D. & Sourjik, V. Use of fluorescence microscopy to study intracellular signaling in bacteria. *Annu. Rev. Microbiol.* **64**, 373–390 (2010).
86. Kiene, R. P. Production of methanethiol from dimethylsulfoniopropionate in marine surface waters. *Mar. Chem.* **54**, 69–83 (1996).
87. Seymour, J. R., Amin, S. A., Raina, J.-B. & Stocker, R. Zooming in on the phycosphere: the ecological interface for phytoplankton-bacteria relationships. *Nat. Microbiol.* **2**, 17065 (2017).
88. Seymour, J. R., Simó, R., Ahmed, T. & Stocker, R. Chemoattraction to dimethylsulfoniopropionate throughout the marine microbial food web. *Science* **329**, 342–345 (2010).
89. Milo, R. & Phillips, R. *Cell Biology By The Numbers*. (Garland Science, 2016).
90. Sun, J. *et al.* The abundant marine bacterium *Pelagibacter* simultaneously catabolizes dimethylsulfoniopropionate to the gases dimethyl sulfide and methanethiol. *Nat. Microbiol.* **1**, 16065 (2016).
91. Tripp, H. J. *et al.* SAR11 marine bacteria require exogenous reduced sulphur for growth. *Nature* **452**, 741–744 (2008).
92. Broadbent, A. D. & Jones, G. B. DMS and DMSP in mucus ropes, coral mucus, surface films and sediment pore waters from coral reefs in the Great Barrier Reef. *Mar. Freshw. Res.* **55**, 849–855 (2004).
93. Wilson, W. H., Turner, S. & Mann, N. H. Population dynamics of phytoplankton and viruses in a phosphate-limited mesocosm and their effect on DMSP and DMS production. *Estuar. Coast. Shelf Sci.* **46**, 49–59 (1998).
94. Malin, G., Wilson, W. H., Bratbak, G., Liss, P. S. & Mann, N. H. Elevated production of dimethylsulfide resulting from viral infection of cultures of *Phaeocystis pouchetii*. *Limnol. Oceanogr.* **43**, 1389–1393 (1998).
95. Reisch, C. R., Moran, M. A. & Whitman, W. B. Dimethylsulfoniopropionate-dependent demethylase (DmdA) from *Pelagibacter ubique* and *Silicibacter pomeroyi*. *J. Bacteriol.* **190**, 8018–8024 (2008).
96. Brummett, A. E., Schnicker, N. J., Crider, A., Todd, J. D. & Dey, M. Biochemical, kinetic, and spectroscopic characterization of *Ruegeria pomeroyi* DddW—a mononuclear iron-dependent DMSP lyase. *PLoS One* **10**, e0127288 (2015).
97. Azam, F. & Hodson, R. Multiphasic kinetics for D-glucose uptake by assemblages of natural marine bacteria. *Mar. Ecol.* **6**, 213–222 (1981).
98. Ai, H., Henderson, J. N., Remington, S. J. & Campbell, R. E. Directed evolution of a monomeric, bright and photostable version of *Clavularia* cyan fluorescent protein: structural characterization and applications in fluorescence imaging. *Biochem. J.* **400**, 531–540 (2006).
99. Griesbeck, O., Baird, G. S., Campbell, R. E., Zacharias, D. A. & Tsien, R. Y. Reducing the environmental sensitivity of yellow fluorescent protein. *J. Biol. Chem.* **276**, 29188–29194 (2001).
100. Kremers, G.-J., Goedhart, J., van Munster, E. B. & Gadella Jr., T. W. J. Cyan and yellow super fluorescent proteins with improved brightness, protein folding, and FRET Förster radius. *Biochemistry* **45**, 6570–6580 (2006).
101. Shcherbo, D. *et al.* Far-red fluorescent tags for protein imaging in living tissues. *Biochem. J.* **418**, 567–574 (2009).
102. Kovach, M. E. *et al.* Four new derivatives of the broad-host-range cloning vector pBBR1MCS, carrying different antibiotic-resistance cassettes. *Gene* **166**, 175–176 (1995).
103. Antoine, R. & Locht, C. Isolation and molecular characterization of a novel broad-host-range plasmid from *Bordetella bronchiseptica* with sequence similarities to plasmids from Gram-positive organisms. *Mol. Microbiol.* **6**, 1785–1799 (1992).
104. Kessler, B., de Lorenzo, V. & Timmis, K. N. A general system to integrate *lacZ* fusions into the chromosomes of Gram-negative eubacteria: regulation of the *Pm* promoter of the *TOL* plasmid studied with all controlling elements in monocopy. *Mol. Genet. Genomics* **233**, 293–301 (1992).
105. Taylor, D. E. Bacterial tellurite resistance. *Trends in Microbiology* **7**, 111–115 (1999).
106. Ollivier, P. R. L. *et al.* Volatilization and precipitation of tellurium by aerobic, tellurite-resistant marine

microbes. *Appl. Environ. Microbiol.* **74**, 7163–7173 (2008).
107. González, J. M., Mayer, F., Moran, M. A., Hodson, R. E. & Whitman, W. B. *Microbulbifer hydrolyticus* gen. nov., sp. nov., and *Marinobacterium georgiense* gen. nov., sp. nov., two marine bacteria from a lignin-rich pulp mill waste enrichment community. *Int. J. Syst. Bacteriol.* **47**, 369–376 (1997).
108. Thume, K. *et al.* The metabolite dimethylsulfoxonium propionate extends the marine organosulfur cycle. *Nature* **563**, 412–415 (2018).
109. Xia, Y. & Whitesides, G. M. Soft lithography. *Annu. Rev. Mater. Sci.* **28**, 153–184 (1998).
110. LaJeunesse, T. C. *et al.* Systematic revision of Symbiodiniaceae highlights the antiquity and diversity of coral endosymbionts. *Curr. Biol.* **28**, 2570–2580 (2018).
111. Spielmeyer, A. & Pohnert, G. Direct quantification of dimethylsulfoniopropionate (DMSP) with hydrophilic interaction liquid chromatography/mass spectrometry. *J. Chromatogr. B* **878**, 3238–3242 (2010).
112. Chrimes, A. F., Khoshmanesh, K., Stoddart, P. R., Mitchell, A. & Kalantar-zadeh, K. Microfluidics and Raman microscopy: current applications and future challenges. *Chem. Soc. Rev.* **42**, 5880–5906 (2013).
113. Lee, K. S. *et al.* An automated Raman-based platform for the sorting of live cells by functional properties. *Nat. Microbiol.* **4**, 1035–1048 (2019).
114. Berry, D. *et al.* Tracking heavy water (D_2O) incorporation for identifying and sorting active microbial cells. *Proc. Natl. Acad. Sci. USA* **112**, E194–E203 (2015).
115. Mitchell, J. G., Okubo, A. & Fuhrman, J. A. Microzones surrounding phytoplankton form the basis for a stratified marine microbial ecosystem. *Nature* **316**, 58–59 (1985).
116. Matrai, P. A. & Keller, M. D. Total organic sulfur and dimethylsulfoniopropionate in marine phytoplankton: intracellular variations. *Mar. Biol.* **119**, 61–68 (1994).
117. Spiese, C. E. Determination of the diffusion constants of dimethylsulfide and dimethylsulfoniopropionate by diffusion-ordered nuclear magnetic resonance spectroscopy. *Mar. Chem.* **207**, 77–83 (2018).
118. Lundberg, P. & Kuchel, P. W. Diffusion of solutes in agarose and alginate gels: ^{1}H and ^{23}Na PFGSE and ^{23}Na TQF NMR studies. *Magn. Reson. Med.* **37**, 44–52 (1997).
119. Stefels, J. Physiological aspects of the production and conversion of DMSP in marine algae and higher plants. in *Journal of Sea Research* **43**, 183–197 (2000).
120. Berdalet, E., Llaveria, G. & Simó, R. Modulation of dimethylsulfoniopropionate (DMSP) concentration in an *Alexandrium minutum* (Dinophyceae) culture by small-scale turbulence: a link to toxin production? *Harmful Algae* **11**, 88–95 (2011).
121. Thornton, D. C. O. Dissolved organic matter (DOM) release by phytoplankton in the contemporary and future ocean. *Eur. J. Phycol.* **49**, 20–46 (2014).
122. Cziesielski, M. J., Schmidt-Roach, S. & Aranda, M. The past, present, and future of coral heat stress studies. *Ecol. Evol.* **9**, 10055–10066 (2019).
123. Bourne, D., Iida, Y., Uthicke, S. & Smith-Keune, C. Changes in coral-associated microbial communities during a bleaching event. *ISME J.* **2**, 350–363 (2008).
124. van de Water, J. A. J. M. *et al.* Antimicrobial and stress responses to increased temperature and bacterial pathogen challenge in the holobiont of a reef-building coral. *Mol. Ecol.* **27**, 1065–1080 (2018).
125. Ben-Haim, Y., Zicherman-Keren, M. & Rosenberg, E. Temperature-regulated bleaching and lysis of the coral *Pocillopora damicornis* by the novel pathogen *Vibrio coralliilyticus*. *Appl. Environ. Microbiol.* **69**, 4236–4241 (2003).
126. Crossland, C. J., Barnes, D. J. & Borowitzka, M. A. Diurnal Lipid and Mucus Production in Coral *Acropora acuminata*. *Mar. Biol.* **60**, 81–90 (1980).
127. Davies, P. S. The role of Zooxanthellae in the nutritional energy requirements of *Pocillopora eydouxi*. *Coral Reefs* **2**, 181–186 (1984).
128. Rix, L. *et al.* Coral mucus fuels the sponge loop in warm-and cold-water coral reef ecosystems. *Sci. Rep.* **6**, 1–11 (2016).
129. Naumann, M. S. *et al.* Organic matter release by dominant hermatypic corals of the Northern Red Sea. *Coral Reefs* **29**, 649–659 (2010).
130. Bythell, J. C. & Wild, C. Biology and ecology of coral mucus release. *J. Exp. Mar. Bio. Ecol.* **408**, 88–93 (2011).
131. Bakshani, C. R. *et al.* Evolutionary conservation of the antimicrobial function of mucus: a first defence against infection. *npj Biofilms Microbiomes* **14**, 1–12 (2018).
132. Gibbin, E. *et al. Vibrio coralliilyticus* infection triggers a behavioural response and perturbs nutritional exchange and tissue integrity in a symbiotic coral. *ISME J.* (2018). doi:10.1038/s41396-018-0327-2
133. Gavish, A. R., Shapiro, O. H., Kramarsky-Winter, E. & Vardi, A. Microscale tracking of coral disease

reveals timeline of infection and heterogeneity of polyp fate. *bioRxiv* (2018). doi:10.1101/302778
134. Caldara, M. *et al.* Mucin biopolymers prevent bacterial aggregation by retaining cells in the free-swimming state. *Curr. Biol.* **22**, 2325–2330 (2012).
135. Co, J. Y. *et al.* Mucins trigger dispersal of *Pseudomonas aeruginosa* biofilms. *npj Biofilms Microbiomes* **23**, 1–8 (2018).
136. Wheeler, K. M. *et al.* Mucin glycans attenuate the virulence of *Pseudomonas aeruginosa* in infection. *Nat. Microbiol.* **4**, 2146–2154 (2019).
137. Wang, B. *et al.* Mucin glycans signal through the sensor kinase RetS to inhibit virulence-associated traits in *Pseudomonas aeruginosa*. *bioRxiv* (2020). doi:10.1101/2020.03.31.018614
138. Barbara, G. M. & Mitchell, J. G. Marine bacterial organisation around point-like sources of amino acids. *FEMS Microbiol. Ecol.* **43**, 99–109 (2003).
139. Seymour, J. R., Marcos & Stocker, R. Resource patch formation and exploitation throughout the marine microbial food web. *Am. Nat.* **173**, E15–E29 (2009).
140. Son, K., Menolascina, F. & Stocker, R. Speed-dependent chemotactic precision in marine bacteria. *Proc. Natl. Acad. Sci. USA* **113**, 8624–8629 (2016).
141. Seymour, J. R., Ahmed, T. & Stocker, R. A microfluidic chemotaxis assay to study microbial behavior in diffusing nutrient patches. *Limnol. Oceanogr. Methods* **6**, 477–488 (2008).
142. Penn, K., Wang, J., Fernando, S. C. & Thompson, J. R. Secondary metabolite gene expression and interplay of bacterial functions in a tropical freshwater cyanobacterial bloom. *ISME J.* **8**, 1866–1878 (2014).
143. Love, M. I., Huber, W. & Anders, S. Moderated estimation of fold change and dispersion for RNA-seq data with DESeq2. *Genome Biol.* **15**, 1–34 (2014).
144. Anders, S. & Huber, W. Differential expression analysis for sequence count data. *Genome Biol.* **11**, (2010).
145. Subramanian, A. *et al.* Gene set enrichment analysis: A knowledge-based approach for interpreting genome-wide expression profiles. *Proc. Natl. Acad. Sci. USA* **102**, 15545–15550 (2005).
146. Mootha, V. K. *et al.* PGC-1α-responsive genes involved in oxidative phosphorylation are coordinately downregulated in human diabetes. *Nat. Genet.* **34**, 267–273 (2003).
147. Kojima, S., Yamamoto, K., Kawagishi, I. & Homma, M. The polar flagellar motor of *Vibrio cholerae* is driven by an Na^+ motive force. *J. Bacteriol.* **181**, 1927–1930 (1999).
148. Sowa, Y., Hotta, H., Homma, M. & Ishijima, A. Torque-speed relationship of the Na^+-driven flagellar motor of *Vibrio alginolyticus*. *J. Mol. Biol.* **327**, 1043–1051 (2003).
149. Ducklow, H. W. & Mitchell, R. Composition of mucus released by coral reef coelenterates. *Limnol. Oceanogr.* **24**, 706–714 (1979).
150. Crossland, C. J. In situ release of mucus and DOC-lipid from the corals *Acropora variabilis* and *Stylophora pistillata* in different light regimes. *Coral Reefs* **6**, 35–42 (1987).
151. Meikle, P., Richards, G. N. & Yellowlees, D. Structural determination of the oligosaccharide side chains from a glycoprotein isolated from the mucus of the coral *Acropora formosa*. *J. Biol. Chem.* **262**, 16941–16947 (1987).
152. Coddeville, B., Maes, E., Ferrier-Pagès, C. & Guerardel, Y. Glycan profiling of gel forming mucus layer from the scleractinian symbiotic coral *Oculina arbuscula*. *Biomacromolecules* **12**, 2064–2073 (2011).
153. Benson, A. A. & Muscatine, L. Wax in coral mucus: Energy transfer from corals to reef fishes. *Limnol. Oceanogr.* **19**, 810–814 (1974).
154. Hasegawa, H. & Häse, C. C. TetR-type transcriptional regulator VtpR functions as a global regulator in *Vibrio tubiashii*. *Appl. Environ. Microbiol.* **75**, 7602–7609 (2009).
155. Ball, A. S., Chaparian, R. R. & van Kessel, J. C. Quorum Sensing Gene Regulation by LuxR/HapR Master Regulators in Vibrios. *J. Bacteriol.* **199**, e00105-17 (2017).
156. Rutherford, S. T., Van Kessel, J. C., Shao, Y. & Bassler, B. L. AphA and LuxR/HapR reciprocally control quorum sensing in vibrios. *Genes Dev.* **25**, 397–408 (2011).
157. Hammer, B. K. & Bassler, B. L. Quorum sensing controls biofilm formation in *Vibrio cholerae*. *Mol. Microbiol.* **50**, 101–104 (2003).
158. Waters, C. M., Lu, W., Rabinowitz, J. D. & Bassler, B. L. Quorum sensing controls biofilm formation in *Vibrio cholerae* through modulation of cyclic Di-GMP levels and repression of *vpsT*. *J. Bacteriol.* **190**, 2527–2536 (2008).
159. Burger, A. H. Quorum Sensing in the Hawai`ian Coral Pathogen *Vibrio coralliilyticus* strain OCN008. (University of Hawaii at Manoa, 2017).
160. Yildiz, F. H. & Schoolnik, G. K. *Vibrio cholerae* O1 El Tor: Identification of a gene cluster required for the rugose colony type, exopolysaccharide production, chlorine resistance, and biofilm formation. *Proc. Natl.*

Acad. Sci. USA **96**, 4028–4033 (1999).
161. Fong, J. C. N., Syed, K. A., Klose, K. E. & Yildiz, F. H. Role of *Vibrio* polysaccharide (*vps*) genes in VPS production, biofilm formation and *Vibrio cholerae* pathogenesis. *Microbiology* **156**, 2757–2769 (2010).
162. Fong, J. C. N., Karplus, K., Schoolnik, G. K. & Yildiz, F. H. Identification and characterization of RbmA, a novel protein required for the development of rugose colony morphology and biofilm structure in *Vibrio cholerae*. *J. Bacteriol.* **188**, 1049–1059 (2006).
163. Fong, J. C. N. & Yildiz, F. H. The *rbmBCDEF* gene cluster modulates development of rugose colony morphology and biofilm formation in *Vibrio cholerae*. *J. Bacteriol.* **189**, 2319–2330 (2007).
164. DiRita, V. J. & Mekalanos, J. J. Periplasmic interaction between two membrane regulatory proteins, ToxR and ToxS, results in signal transduction and transcriptional activation. *Cell* **64**, 29–37 (1991).
165. Almagro-Moreno, S., Root, M. Z. & Taylor, R. K. Role of ToxS in the proteolytic cascade of virulence regulator ToxR in *Vibrio cholerae*. *Mol. Microbiol.* **98**, 963–976 (2015).
166. Lee, S. E. *et al.* Production of *Vibrio vulnificus* hemolysin in vivo and its pathogenic significance. *Biochem. Biophys. Res. Commun.* **324**, 86–91 (2004).
167. Senoh, M., Okita, Y., Shinoda, S. & Miyoshi, S. The crucial amino acid residue related to inactivation of *Vibrio vulnificus* hemolysin. *Microb. Pathog.* **44**, 78–83 (2008).
168. Bröms, J. E., Ishikawa, T., Wai, S. N. & Sjöstedt, A. A functional VipA-VipB interaction is required for the type VI secretion system activity of *Vibrio cholerae* O1 strain A1552. *BMC Microbiol.* **13**, 1–12 (2013).
169. Vizcaino, M. I. *et al.* Antimicrobial resistance of the coral pathogen *Vibrio coralliilyticus* and Caribbean sister phylotypes isolated from a diseased octocoral. *Microb. Ecol.* **59**, 646–657 (2010).
170. Ritchie, K. B. Regulation of microbial populations by coral surface mucus and mucus-associated bacteria. *Mar. Ecol. Prog. Ser.* **322**, 1–14 (2006).
171. Nissimov, J., Rosenberg, E. & Munn, C. B. Antimicrobial properties of resident coral mucus bacteria of *Oculina patagonica*. *FEMS Microbiol. Lett.* **292**, 210–215 (2009).
172. Shnit-Orland, M. & Kushmaro, A. Coral mucus-associated bacteria: A possible first line of defense. *FEMS Microbiol. Ecol.* **67**, 371–380 (2009).
173. Rypien, K. L., Ward, J. R. & Azam, F. Antagonistic interactions among coral-associated bacteria. *Environ. Microbiol.* **12**, 28–39 (2010).
174. Alagely, A., Krediet, C. J., Ritchie, K. B. & Teplitski, M. Signaling-mediated cross-talk modulates swarming and biofilm formation in a coral pathogen *Serratia marcescens*. *ISME J.* **5**, 1609–1620 (2011).
175. Polz, M. F., Hunt, D. E., Preheim, S. P. & Weinreich, D. M. Patterns and mechanisms of genetic and phenotypic differentiation in marine microbes. *Philos. Trans. R. Soc. B Biol. Sci.* **361**, 2009–2021 (2006).
176. Taylor, J. R. & Stocker, R. Trade-Offs of Chemotactic Foraging in Turbulent Water. *Science* **338**, 675–679 (2012).
177. Shapiro, O. H. *et al.* Vortical ciliary flows actively enhance mass transport in reef corals. *Proc. Natl. Acad. Sci. USA* **111**, 13391–13396 (2014).
178. Krediet, C. J. *et al.* Utilization of mucus from the coral *Acropora palmata* by the pathogen *Serratia marcescens* and by environmental and coral commensal bacteria. *Appl. Environ. Microbiol.* **75**, 3851–3858 (2009).
179. Krediet, C. J., Ritchie, K. B., Alagely, A. & Teplitski, M. Members of native coral microbiota inhibit glycosidases and thwart colonization of coral mucus by an opportunistic pathogen. *ISME J.* **7**, 980–990 (2013).
180. Packer, H. L. & Armitage, J. P. The chemokinetic and chemotactic behavior of *Rhodobacter sphaeroides*: two independent responses. *J. Bacteriol.* **176**, 206–212 (1994).
181. Deepika, D., Karmakar, R., Tirumkudulu, M. S. & Venkatesh, K. V. Variation in swimming speed of *Escherichia coli* in response to attractant. *Arch. Microbiol.* **197**, 211–222 (2015).
182. Zhulin, I. B. & Armitage, J. P. Motility, Chemokinesis, and methylation-independent chemotaxis in *Azospirillum brasilense*. *J. Bacteriol.* **175**, 952–958 (1993).
183. Ramos, H. C., Rumbo, M. & Sirard, J.-C. Bacterial flagellins: mediators of pathogenicity and host immune responses in mucosa. *Trends Microbiol.* **12**, 509–517 (2004).
184. Peterson, K. M. & Mekalanos, J. J. Characterization of the *Vibrio cholerae* ToxR regulon: Identification of novel genes involved in intestinal colonization. *Infect. Immun.* **56**, 2822–2829 (1988).
185. Provenzano, D. & Klose, K. E. Altered expression of the ToxR-regulated porins OmpU and OmpT diminishes *Vibrio cholerae* bile resistance, virulence factor expression, and intestinal colonization. *Proc. Natl. Acad. Sci. USA* **97**, 10220–10224 (2000).
186. Waters, C. M. & Bassler, B. L. The *Vibrio harveyi* quorum-sensing system uses shared regulatory

components to discriminate between multiple autoinducers. *Genes Dev.* **20**, 2754–2767 (2006).
187. Mukherjee, S. & Bassler, B. L. Bacterial quorum sensing in complex and dynamically changing environments. *Nature Reviews Microbiology* **17**, 371–382 (2019).
188. Sikora, A. E., Zielke, R. A., Lawrence, D. A., Andrews, P. C. & Sandkvist, M. Proteomic analysis of the *Vibrio cholerae* type II secretome reveals new proteins, including three related serine proteases. *J. Biol. Chem.* **286**, 16555–16566 (2011).
189. Korotkov, K. V., Sandkvist, M. & Hol, W. G. J. The type II secretion system: biogenesis, molecular architecture and mechanism. *Nat. Rev. Microbiol.* **10**, 336–351 (2012).
190. Stathopoulos, C. *et al.* Secretion of virulence determinants by the general secretory pathway in Gram-negative pathogens: An evolving story. *Microbes Infect.* **2**, 1061–1072 (2000).
191. Hood, R. D. *et al.* A Type VI Secretion System of *Pseudomonas aeruginosa* Targets a Toxin to Bacteria. *Cell Host Microbe* **7**, 25–37 (2010).
192. Zheng, J., Ho, B. & Mekalanos, J. J. Genetic Analysis of Anti-Amoebae and Anti-Bacterial Activities of the Type VI Secretion System in *Vibrio cholerae*. *PLoS One* **6**, e23876 (2011).
193. MacIntyre, D. L., Miyata, S. T., Kitaoka, M. & Pukatzki, S. The *Vibrio cholerae* type VI secretion system displays antimicrobial properties. *Proc. Natl. Acad. Sci. USA* **107**, 19520–19524 (2010).
194. Lee, S. H., Hava, D. L., Waldor, M. K. & Camilli, A. Regulation and Temporal Expression Patterns of *Vibrio cholerae* Virulence Genes during Infection. *Cell* **99**, 625–634 (1999).
195. Pennetzdorfer, N. *et al.* Regulated proteolysis in *Vibrio cholerae* allowing rapid adaptation to stress conditions. *Front. Cell. Infect. Microbiol.* **9**, 1–9 (2019).
196. Liu, R. *et al.* Comparative transcriptome analysis of *Vibrio splendidus* JZ6 reveals the mechanism of its pathogenicity at low temperatures. *Appl. Environ. Microbiol.* **82**, 2050–2061 (2016).
197. Hughes, T. P. *et al.* Spatial and temporal patterns of mass bleaching of corals in the Anthropocene. *Science* **359**, 80–83 (2018).
198. Vezzulli, L. *et al.* Vibrio infections triggering mass mortality events in a warming Mediterranean Sea. *Environ. Microbiol.* **12**, 2007–2019 (2010).
199. Zaneveld, J. R. *et al.* Overfishing and nutrient pollution interact with temperature to disrupt coral reefs down to microbial scales. *Nat. Commun.* **7**, 1–12 (2016).
200. Li, H. & Durbin, R. Fast and accurate short read alignment with Burrows-Wheeler transform. *Bioinformatics* **25**, 1754–1760 (2009).
201. Liao, Y., Smyth, G. K. & Shi, W. featureCounts: an efficient general purpose program for assigning sequence reads to genomic features. *Bioinformatics* **30**, 923–930 (2014).
202. Kim, Y.-K. & McCarter, L. L. Analysis of the polar flagellar gene system of *Vibrio parahaemolyticus*. *J. Bacteriol.* **182**, 3693–3704 (2000).
203. Bina, X. R., Provenzano, D., Nguyen, N. & Bina, J. E. *Vibrio cholerae* RND family efflux systems are required for antimicrobial resistance, optimal virulence factor production, and colonization of the infant mouse small intestine. *Infect. Immun.* **76**, 3595–3605 (2008).
204. Bina, J. E., Provenzano, D., Wang, C., Bina, X. R. & Mekalanos, J. J. Characterization of the *Vibrio cholerae vexAB* and *vexCD* efflux systems. *Arch. Microbiol.* **186**, 171–181 (2006).
205. Hayashi, M., Nakayama, Y. & Unemoto, T. Recent progress in the Na^+-translocating NADH-quinone reductase from the marine *Vibrio alginolyticus*. *Biochimica et Biophysica Acta* **1505**, 37–44 (2001).
206. Matthey, N., Drebes Dörr, N. C. & Blokesch, M. Long-Read-Based Genome Sequences of Pandemic and Environmental *Vibrio cholerae* Strains. *Microbiol. Resour. Announc.* **7**, 1–3 (2018).
207. Skorupski, K. & Taylor, R. K. Control of the ToxR virulence regulon in *Vibrio cholerae* by environmental stimuli. *Mol. Microbiol.* **25**, 1003–1009 (1997).
208. Guillemette, R., Ushijima, B., Jalan, M., Häse, C. C. & Azam, F. Insight into the resilience and susceptibility of marine bacteria to T6SS attack by *Vibrio cholerae* and *Vibrio coralliilyticus*. *PLoS One* **15**, e0227864 (2020).
209. Winn, K. M., Bourne, D. G. & Mitchell, J. G. *Vibrio coralliilyticus* Search Patterns across an Oxygen Gradient. *PLoS One* **8**, 1–8 (2013).
210. Sultan, S. Z., Silva, A. J. & Benitez, J. A. The PhoB regulatory system modulates biofilm formation and stress response in El Tor biotype *Vibrio cholerae*. *FEMS Microbiol. Lett.* **302**, 22–31 (2010).
211. Pratt, J. T., McDonough, E. K. & Camilli, A. PhoB regulates motility, biofilms, and cyclic di-GMP in *Vibrio cholerae*. *J. Bacteriol.* **191**, 6632–6642 (2009).
212. Pratt, J. T., Ismail, A. M. & Camilli, A. PhoB regulates both environmental and virulence gene expression in *Vibrio cholerae*. *Mol. Microbiol.* **77**, 1595–1605 (2010).

213. Benitez, J. A. & Silva, A. J. *Vibrio cholerae* hemagglutinin(HA)/protease: An extracellular metalloprotease with multiple pathogenic activities. *Toxicon* **115**, 55–62 (2016).
214. Binesse, J. *et al.* Metalloprotease Vsm is the major determinant of toxicity for extracellular products of *Vibrio splendidus*. *Appl. Environ. Microbiol.* **74**, 7108–7117 (2008).
215. Aguirre-Guzmán, G., Ruíz, H. M. & Ascencio, F. A review of extracellular virulence product of *Vibrio* species important in diseases of cultivated shrimp. *Aquac. Res.* **35**, 1395–1404 (2004).
216. Norqvist, A., Norrman, B. & Wolf-Watz, H. Identification and characterization of a zinc metalloprotease associated with invasion by the fish pathogen *Vibrio anguillarum*. *Infect. Immun.* **58**, 3731–3736 (1990).
217. Sussman, M., Willis, B. L., Victor, S. & Bourne, D. G. Coral pathogens identified for White Syndrome (WS) epizootics in the Indo-Pacific. *PLoS One* **3**, (2008).
218. Delston, R. B., Kothary, M. H., Shangraw, K. A. & Tall, B. D. Isolation and characterization of a zinc-containing metalloprotease expressed by *Vibrio tubiashii*. *Can. J. Microbiol.* **49**, 525–529 (2003).
219. Booth, B. A., Boesman-Finkelstein, M. & Finkelstein, R. A. *Vibrio cholerae* soluble hemagglutinin/protease is a metalloenzyme. *Infect. Immun.* **42**, 639–644 (1983).
220. Hase, C. & Finkelstein, R. A. Bacterial extracellular zinc-containing metalloproteases. *Microbiol. Rev.* **57**, 823–837 (1993).
221. Pollock, F. J. *et al.* Phylogeny of the coral pathogen *Vibrio coralliilyticus*. *Environ. Microbiol. Rep.* **2**, 172–178 (2010).
222. Denkin, S. M. & Nelson, D. R. Induction of protease activity in *Vibrio anguillarum* by gastrointestinal mucus. *Appl. Environ. Microbiol.* **65**, 3555–3560 (1999).
223. Narita, S. -i., Masui, C., Suzuki, T., Dohmae, N. & Akiyama, Y. Protease homolog BepA (YfgC) promotes assembly and degradation of -barrel membrane proteins in *Escherichia coli*. *Proc. Natl. Acad. Sci. USA* **110**, E3612–E3621 (2013).
224. Almagro-Moreno, S., Kim, T. K., Skorupski, K. & Taylor, R. K. Proteolysis of Virulence Regulator ToxR Is Associated with Entry of *Vibrio cholerae* into a Dormant State. *PLOS Genet.* **11**, e1005145 (2015).
225. Balleza, E., Kim, J. M. & Cluzel, P. Systematic characterization of maturation time of fluorescent proteins in living cells. *Nat. Methods* **15**, 47–51 (2018).
226. Corish, P. & Tyler-Smith, C. Attenuation of green fluorescent protein half-life in mammalian cells. *Protein Eng.* **12**, 1035–1040 (1999).
227. Nguyen, J. K. T. Rapid nutrient fluctuations and their implications for bacterial growth. (Massachusetts Institute of Technology, 2020).
228. Jatkar, A. A. *et al.* Coral mucus: The properties of its constituent mucins. *Biomacromolecules* **11**, 883–888 (2010).
229. Xie, L., Altindal, T., Chattopadhyay, S. & Wu, X.-L. Bacterial flagellum as a propeller and as a rudder for efficient chemotaxis. *Proc. Natl. Acad. Sci. USA* **108**, 2246–2251 (2011).
230. Son, K., Guasto, J. S. & Stocker, R. Bacteria can exploit a flagellar buckling instability to change direction. *Nat. Phys.* **9**, 494–498 (2013).